



Theses and Dissertations

2011-09-23

Effects of Pressure on the Properties of Coal Char Under Gasification Conditions at High Initial Heating Rates

Randy C. Shurtz
Brigham Young University - Provo

Follow this and additional works at: <https://scholarsarchive.byu.edu/etd>



Part of the [Chemical Engineering Commons](#)

BYU ScholarsArchive Citation

Shurtz, Randy C., "Effects of Pressure on the Properties of Coal Char Under Gasification Conditions at High Initial Heating Rates" (2011). *Theses and Dissertations*. 2877.
<https://scholarsarchive.byu.edu/etd/2877>

This Dissertation is brought to you for free and open access by BYU ScholarsArchive. It has been accepted for inclusion in Theses and Dissertations by an authorized administrator of BYU ScholarsArchive. For more information, please contact scholarsarchive@byu.edu, ellen_amatangelo@byu.edu.

Effects of Pressure on the Properties of Coal Char
Under Gasification Conditions at High
Initial Heating Rates

Randy Clark Shurtz

A dissertation submitted to the faculty of
Brigham Young University
in partial fulfillment of the requirements for the degree of
Doctor of Philosophy

Thomas H. Fletcher, Chair
Larry L. Baxter
Ronald J. Pugmire
David O. Lignell
Thomas A. Knotts

Department of Chemical Engineering
Brigham Young University

December 2011

Copyright © 2011 Randy Shurtz

All Rights Reserved

ABSTRACT

Effects of Pressure on the Properties of Coal Char Under Gasification Conditions at High Initial Heating Rates

Randy Clark Shurtz
Department of Chemical Engineering, BYU
Doctor of Philosophy

The effects of elevated pressure and high heating rates on coal pyrolysis and gasification were investigated. A high-pressure flat-flame burner (HPFFB) was designed and built to conduct these studies. The HPFFB was designed to provide an environment with laminar, dispersed entrained flow, with particle heating rates of $\sim 10^5$ K/s, pressures of up to 15 atm, and gas temperatures of up to 2000 K. Residence times were varied from 30 to 700 ms in this study.

Pyrolysis experiments were conducted at particle heating rates of $\sim 10^5$ K/s and maximum gas temperatures of ~ 1700 K at pressures of 1 to 15 atm. A new coal swelling correlation was developed that predicts the effects of heating rate, pressure, and coal rank on the swelling ratio at heating rates above $\sim 10^4$ K/s. A coal swelling rank index system based on ^{13}C -NMR chemical structural parameters was devised. The empirical swelling model requires user inputs of the coal ultimate and proximate analyses and the use of a transient particle energy balance to predict the maximum particle heating rate. The swelling model was used to explain differences in previously reported bituminous coal swelling ratios that were measured in facilities with different heating rates.

Char gasification studies by CO_2 were conducted on a subbituminous coal and 4 bituminous coals in the HPFFB. Pressures of 5, 10, and 15 atmospheres were used with gas compositions of 20, 40, and 90 mole % CO_2 . Gas conditions with peak temperatures of 1700 K to 2000 K were used, which resulted in char particle temperatures of 1000 K to 1800 K. Three gasification models were developed to fit and analyze the gasification data. A simple 1st-order model was used to show that the measured gasification rates were far below the film-diffusion limit. The other two models, designated CCK and CCK^{N} , were based on three versions of the CBK models. CCK^{N} used an n^{th} -order kinetic mechanism and CCK used a semi-global Langmuir-Hinshelwood kinetic mechanism. The two CCK models fit the HPFFB gasification data better than the 1st-order model. The fits of the gasification data with CCK and CCK^{N} were comparable to each other. The fit of the data in CCK suggests that Knudsen diffusion may have influenced the gasification rates in the HPFFB experiments. The gasification rate parameters in each of the three models were correlated with coal rank. ^{13}C -NMR parameters were used to estimate a structural parameter of the coal char. Char- CO_2 gasification rate coefficients correlated better with this NMR-based char structure index than it did with the carbon and oxygen content of the parent coal.

Keywords: Randy Shurtz, coal, gasification, pyrolysis, swelling, pressure, heating rate, soot

ACKNOWLEDGMENTS

I would like to thank my wife Alyson for the great support and encouragement she gave me during the pursuit of my doctoral studies. I would also like to thank my other family members for their encouragement. I thank Dr. Thomas H. Fletcher for his positive attitude, friendship, and mentorship. I am grateful that he provided direction and correction when needed, and he also taught me to take more responsibility for my own learning and come to my own conclusions. I am particularly grateful for his constructive criticism that helped me to become a better writer. I am also grateful to my graduate committee for their time and ideas.

I would like to thank the many undergraduate assistants and fellow graduate students who helped me to do the experimental and modeling work and provided ideas and feedback that were very helpful. I am especially grateful for the friendship and valuable contributions of John Sowa, Aaron Lewis, Jamis Hillier, Dallan Prince, Brady Burgener, David Johnson, Kolbein Kolste, Jeffrey van Wagoner, Gregory Sorensen, Samuel Goodrich, Kade Fowers, and Joseph Hogge. I am grateful I had the opportunity to exercise a leadership role among them so that I could learn to have greater trust in the abilities of others as well as myself.

I would like to thank both Dr. Fletcher and Dr. Ronald J. Pugmire of the University of Utah for the great efforts they made to ensure that we had the funds required to carry on with this research. I would like to thank providers of funding, including GE Global Research and the U.S. Department of Energy (DOE). I appreciate the research fellowship from the BYU Office of Research and Creative Activities (ORCA), and also funds left by the late James J. Christensen. Last but certainly not least, I thank God, who blessed me with the talents, persistence, and inspiration needed to accomplish all that is good or creative in this dissertation.

TABLE OF CONTENTS

LIST OF TABLES	x
LIST OF FIGURES	xvi
NOMENCLATURE.....	xxiv
Chapter 1. Introduction.....	1
Chapter 2. Literature Review	3
2.1 Chemical Structure of Coal.....	4
2.2 Primary Pyrolysis.....	5
2.2.1 Network Devolatilization Models.....	6
2.2.2 Coal Char Characteristics	7
2.2.3 Effect of Heating Rate on Volatiles Yield and Swelling during Coal Pyrolysis	9
2.2.4 Effect of Pyrolysis Pressure on Volatiles Yield and Coal Swelling	13
2.3 Secondary Pyrolysis.....	14
2.4 Gasification.....	15
2.4.1 Three-Zone Theory	16
2.4.2 Recent Gasification Experiments.....	19
2.4.3 Reaction Chemistry.....	21
2.4.4 Advanced CBK Combustion and Gasification Models	27
2.5 Summary.....	34
Chapter 3. Objectives.....	37
Chapter 4. Experimental Equipment and Procedures	41

4.1	Description of HPFFB Features and Development	43
4.1.1	Coal Feeding System	47
4.1.2	Nichrome Wire Heaters	49
4.1.3	Molybdenum Disilicide Heaters	49
4.1.4	Quartz Tubing	51
4.1.5	Ignition System	51
4.1.6	Quench Probe	53
4.2	Product Separation and Collection System.....	54
4.2.1	Char Fragmentation	54
4.2.2	Soot Contamination	55
4.3	Development of Viable Fuel Mixtures	60
4.4	Temperature Measurement	61
4.5	Determination of Residence Times.....	63
4.6	Sample Characterization	66
4.6.1	Swelling Ratio Measurement	70
4.6.2	Measurement of Mass Release.....	70
4.6.3	Surface Area Measurements	74
Chapter 5.	Particle Swelling during Coal Pyrolysis.....	77
5.1	Experimental Investigation of the Effect of Heating Rate at Atmospheric Pressure....	79
5.2	Experimental Investigation of the Effect of Pressure at High Heating Rates.....	84
5.2.1	Fuel-Rich Pyrolysis Conditions	85
5.2.2	Oxidizer-Rich Pyrolysis Conditions	88

5.3	Calculation of Particle Heating Rates	91
5.4	High Heating Rate Swelling Model Development	94
5.4.1	Comparison to Additional Data at Atmospheric Pressure	101
5.5	Low Heating Rate Correlation	106
5.6	Pressurized Swelling Model Development.....	110
5.7	Discussion of Model Application	120
5.8	Summary and Conclusions	125
Chapter 6. Gasification Experiments and Modeling		129
6.1	First-Order Gasification Model	130
6.2	Advanced CBK-Based Gasification Models	132
6.2.1	Physical Properties.....	133
6.2.2	Calculation Methods	135
6.2.3	Effectiveness Factors and Kinetic Mechanism	137
6.2.4	Kinetic Parameters	140
6.2.5	Options and Outputs Included in CCK	142
6.2.6	N^{th} -Order Gasification Model.....	143
6.3	CO_2 Gasification Data with 1^{st} -Order Model	144
6.3.1	Comparison of 1^{st} -Order Rate Parameters to Literature	154
6.3.2	Correlation of 1^{st} -Order Model with Coal Rank.....	162
6.4	CO_2 Gasification Data with the CCK^N Model.....	166
6.4.1	Correlation of CCK^N Model with Coal Rank	171
6.5	CCK Parametric Studies	175

6.6	CO ₂ Gasification Data with the CCK Model.....	185
6.6.1	Correlation of CCK Model with Coal Rank	188
6.7	Summary and Conclusions	190
Chapter 7. Summary and Conclusions		195
7.1	Coal Swelling During Pyrolysis at High Heating Rates.....	196
7.2	Experimental Studies and Modeling of CO ₂ -Char Gasification.....	197
7.3	Experimental Recommendations	200
7.4	Modeling Recommendations	202
REFERENCES.....		205
Appendix A. Soot Studies.....		219
Appendix B. Additional Details Regarding HPFFB Development		245
Appendix C. Particle Velocity Calculations		251
Appendix D. HPFFB Stepper Motor Electronics and Software.....		255
Appendix E. Char Separation Procedure.....		257
Appendix F. Radiation Temperature Correction.....		261
Appendix G. Experimental Gas Conditions and Particle Sizes.....		267
Appendix H. Pyrolysis Data for Pressurized Swelling Model.....		279
Appendix I. Gasification Data.....		283
Appendix J. 1st-Order Model with Steam Gasification Data		291
Appendix K. Effectiveness Factors From CCK^N		297
Appendix L. Correlations for NMR Parameters.....		301
Appendix M. Additional Details Regarding CCK Development.....		303

Appendix N. Thermogravimetric Analysis.....	305
Appendix O. HPFFB Operating Manual.....	307

LIST OF TABLES

Table 2.1. Chemical structural parameters derived from ^{13}C -NMR measurements used in the CPD model	7
Table 2.2. Three-fold char classification system	9
Table 2.3. Recent pyrolysis and gasification studies	20
Table 2.4. Summary of differences between versions of the CBK model.....	29
Table 4.1. Properties of coals studied in this work.....	68
Table 5.1. Experimental conditions for Eastern Bituminous A at 0.84 atm	80
Table 5.2. Coal properties for correlation of s_{var} with rank	97
Table 5.3. Coal properties for correlation of c_{HR} with rank	100
Table 5.4. Correlations for s_{var} and c_{HR} with NMR-based rank index $(\sigma+I)/M_{\delta}$	101
Table 5.5. Heating rates in Regimes 1 and 2 with equivalent model swelling ratios	108
Table 5.6. Heating rates and chemical structure information for coals in Figure 5.14.....	113
Table 5.7. Scaling factors for pressure function assuming $c_{visc} = 7.77$ and $c_{ext} = 3.47$	117
Table 5.8. Correlations of c_{scale} for use in the pressure function $f(P)$	119
Table 6.1. Rate parameter correlations used in the CCK and CBK/G models	141
Table 6.2. 1 st -order CO ₂ gasification kinetic parameters	152
Table 6.3. Coal rank correlations for CO ₂ gasification rate parameters in the 1 st -order model	165
Table 6.4. CO ₂ gasification kinetic parameters for the CCK ^N model.....	167

Table 6.5. Coal rank correlations for CO ₂ gasification parameters in the CCK ^N model with $T_{ref} = 1450$ K	174
Table 6.6. Surface areas and pore diameters from adsorption measurements of HPFFB chars	182
Table 6.7. Optimized CO ₂ gasification $A_{7,0}$ with the CCK model using $E_7 = 35$ kcal/mol, $\psi_0 = 0$, and $\tau/f = 12$	186
Table 6.8. Correlations for $A_{7,0}$ with coal rank for CO ₂ gasification with the CCK model.....	189
Table A.1. Model compounds previously investigated in soot formation studies.....	221
Table A.2. Average measured tar properties compared to properties of suggested average tar molecules.....	225
Table A.3. Additional compounds used as coal-tar surrogates in pyrolysis experiments.....	226
Table A.4. Measured NMR parameters for 2 coals from this study.....	229
Table A.5. EBA coal and two tar/soot samples collected at 3 inches in the atmospheric FFB.....	234
Table A.6. EBA coal and pyrolysis products collected at 1 3/8 inches in the atmospheric FFB.....	234
Table A.7. Wyodak coal and tar/soots collected at 3 inches in the atmospheric FFB	235
Table A.8. Wyodak coal with tar/soots and chars collected at 1 3/8 inches on the atmospheric FFB.....	235
Table A.9. Gas flow rates and post-flame gas compositions for soot formation studies	242

Table A.10. Radiation-corrected HPFFB temperature profiles for soot formation studies	242
Table A.11. Estimated particle velocity profiles and residence times for soot formation studies.....	243
Table A.12. Radiation-corrected FFB temperature profiles for soot formation studies	243
Table G.1. Gas flow rates and post-flame gas compositions with ~20% CO ₂	267
Table G.2. Residence times with ~20% CO ₂	267
Table G.3. Particle velocity profiles with ~20% CO ₂	268
Table G.4. Radiation-corrected HPFFB temperature profiles with ~20 % CO ₂ with probe at 3 inches above burner	268
Table G.5. Radiation-corrected HPFFB temperature profiles with ~20 % CO ₂ and curve-fits with probe at 10 inches.....	269
Table G.6. Radiation-corrected HPFFB temperature profiles with ~20 % CO ₂ with probe at 16.25 inches	270
Table G.7. Gas flow rates and post-flame gas compositions with enhanced CO ₂	271
Table G.8. Particle velocity profiles with enhanced CO ₂	271
Table G.9. Residence times with enhanced CO ₂	272
Table G.10. Radiation-corrected HPFFB temperature profiles with enhanced CO ₂ , 7.5-inch probe height, no heaters	272
Table G.11. Radiation-corrected HPFFB temperature profiles with enhanced CO ₂ and heaters	273
Table G.12. Gas flow rates and post-flame gas compositions with ~2% O ₂	274
Table G.13. Particle velocity profiles and residence times with ~2% O ₂	274
Table G.14. Radiation-corrected HPFFB temperature profiles with ~2 % O ₂	275

Table G.15. Gas flows, compositions, and temperatures for atmospheric FFB coal swelling experiments	275
Table G.16. Standard particle velocity profile used for 0.84 atm FFB pyrolysis experiments	276
Table G.17. Particle size distributions for coals	276
Table G.18. Particle size distributions for reinjected chars sieved to 75-106 μm	278
Table H.1. Wyodak pyrolysis data with 0% O_2	279
Table H.2. Dietz pyrolysis data with ~2% O_2	279
Table H.3. Illinois #6 pyrolysis data with ~2% O_2	280
Table H.4. Kentucky #9 pyrolysis data with ~2% O_2	280
Table H.5. Pittsburgh #8 pyrolysis data with ~2% O_2	280
Table H.6. Lower Kittanning pyrolysis data with ~2% O_2	281
Table I.1. Wyodak 2010 gasification data with ~20% CO_2 used for kinetic modeling	284
Table I.2. Wyodak 2011 gasification data used for kinetic modeling, mostly with enhanced CO_2	285
Table I.3. Illinois #6 reinjection gasification data with enhanced CO_2	286
Table I.4. Kentucky #9 CO_2 gasification data with in-situ pyrolysis	287
Table I.5. Kentucky #9 CO_2 gasification data with char reinjection	288
Table I.6. Kentucky #9 CO_2 gasification data omitted from kinetic analysis	288
Table I.7. EBA CO_2 gasification data with in-situ pyrolysis	289
Table I.8. EBB CO_2 gasification data with in-situ pyrolysis	290
Table J.1. Ultimate analysis of Wyodak coal and chars produced at 2.5 atm and 1698 K (daf wt%)	293

Table J.2. Mass release, apparent particle densities and swelling ratios of Wyodak coal and chars.....	293
Table J.3. Steam gasification gas flow rates and post-flame gas compositions from the NASA-CEA code.....	294
Table J.4. Residence times for 2.5 atm HPFFB steam gasification experiments	295
Table J.5. Radiation-corrected HPFFB temperature profiles with steam and Nichrome wire heaters at 2.5 atm	295
Table L.1. Coefficients used to predict NMR parameters	302

LIST OF FIGURES

Figure 2.1. Structure of a hypothetical coal molecule	4
Figure 2.2. Pyrolysis processes and products	5
Figure 2.3. Effect of initial heating rate on particle swelling ratio	11
Figure 2.4. Swelling ratio versus pressure from pulverized coal experiments and a model.....	14
Figure 2.5. Secondary pyrolysis processes and products.....	15
Figure 2.6. Three-zone theory for heterogeneous reactions on porous particles.....	16
Figure 2.7. Intrinsic gasification rates of a German bituminous coal char at 900°C.	22
Figure 2.8. Effect of temperature and gas composition on gasification rates for 500 µm metallurgical coke in mixtures of CO ₂ and CO at 0.96 atm total pressure.	25
Figure 2.9. Inhibited gasification rates at 900°C and 40 bar.....	27
Figure 4.1. HPFFB cross-section illustration (left), burner face (bottom right), and operating burner (top right).....	42
Figure 4.2. Moveable clamp system and water-cooled fitting for the 1-inch flat-flame burner.	44
Figure 4.3. Illustration of stainless steel HPFFB pressure vessel with dimensions.....	45
Figure 4.4. Collection probe with aerodynamic separation system for char and soot collection.	46
Figure 4.5. Illustration of HPFFB coal feeder system, excluding vibrators on coal plunger and feeder tube.....	48
Figure 4.6. Glow plug ignition system and brass insert in top cap of pressure vessel.....	52

Figure 4.7. SEM images of fragmented EBB char produced at 10 atm, 1722 K, 42 ms.....	55
Figure 4.8. SEM images of EBB char. Note that soot (with a fuzzy/clumpy texture compared to char) occurred in very large soot agglomerates and sometimes as a coating on the char particles or as an adhesive that bound char fragments together in clumps.....	56
Figure 4.9. Illinois 6 char pyrolyzed with 2% O ₂ at a collection height of 1.5 inches.....	59
Figure 4.10. New centerline thermocouple fitting (top) and assembly of a similar fitting in the vessel wall (bottom).....	62
Figure 4.11. Velocity profiles at 2.5 atm (left) and 10 atm (right), both at ~1700 K peak temperature.....	64
Figure 5.1. Illinois #6 conversion profiles for different swelling ratios at $T_g = 1700$ K, $P = 15$ atm, 20% CO ₂	78
Figure 5.2. Atmospheric swelling as a function of heating rate, denoting regimes of increasing/decreasing swelling.....	81
Figure 5.3. SEM images of Eastern Bituminous A chars produced at different heating rates (scales differ).....	82
Figure 5.4. SEM images of Eastern Bituminous A chars produced at different heating rates (scales differ).....	83
Figure 5.5. HPFFB swelling ratios at peak gas temperatures of ~1700 K and residence times of ~40 ms.....	85
Figure 5.6. Wyodak chars produced at 2.5 atm, 33 ms (left) and 15 atm, 44 ms (right).....	87
Figure 5.7. Swelling ratios in 2% O ₂ with peak gas temperatures of 1700-1900 K and residence times of ~60 ms.....	90
Figure 5.8. Illinois #6 temperature measurements and predictions in Sandia CDL drop-tube furnace at 1050 K.....	93

Figure 5.9. Correlation of s_{var} with NMR-based rank index using Sandia combustion data.	98
Figure 5.10. Heating rate exponent fitted to Sandia pyrolysis data.	101
Figure 5.11. Bituminous coal validation data sets compared to model.	103
Figure 5.12. Swelling parity plot at heating rates above $\sim 10^4$ K/s. CBK swelling model also shown.	104
Figure 5.13. Complete swelling model for Illinois #6 data of Zygourakis.	108
Figure 5.14. Effect of pressure on swelling for bituminous coals in previous studies.	112
Figure 5.15. Pressure factors from HPFFB and FFB data, including curve-fits extrapolated to 60 atm.	116
Figure 5.16. Correlations of c_{scale} versus coal rank.	117
Figure 5.17. Pressure factor from fits of c_{scale} versus $(\sigma+1)$ (left) and C/O (right) compared to experimental values.	119
Figure 5.18. Heating rate and volatiles yield predicted for Illinois #6 coal with 3.3% moisture in a drop-tube furnace at ~ 1050 K peak centerline gas temperature.	121
Figure 5.19. CPD predictions of volatiles yield and heating rate for Illinois #6 pyrolysis at 15 atm in the HPFFB.	123
Figure 6.1. Algorithm for determining T_p and $P_{i,s}$ at each time step in CCK.	136
Figure 6.2. Parity plot of HPFFB gasification data with 1 st -order model.	145
Figure 6.3. Comparison of gas and particle temperature profiles for Illinois #6 char gasification conditions.	146
Figure 6.4. 1 st -order fit of CO ₂ gasification data with Wyodak 2010 subjected to different gas conditions.	148

Figure 6.5. CO ₂ and H ₂ O gasification χ -factors versus particle temperature from 1 st -order model of HPFFB data.....	154
Figure 6.6. HPFFB 1 st -order CO ₂ gasification rate parameters for Wyodak subbituminous coal (top) and 4 bituminous coals (bottom).....	156
Figure 6.7. CO ₂ gasification rates for Wyodak with particle size error bars and comparison to literature.	157
Figure 6.8. CO ₂ gasification rates for bituminous coals with particle size error bars and comparison to literature.	159
Figure 6.9. Correlations of kinetic parameters with coal rank for 1 st -order CO ₂ gasification model.....	163
Figure 6.10. Fit of HPFFB data with 1st-order model using $E = 123$ kJ/mol and A from correlation with $Char_{Ar}$	166
Figure 6.11. Parity plot of HPFFB gasification data with optimized CCK ^N model predictions.....	169
Figure 6.12. Correlations of kinetic parameters with coal rank for CCK ^N gasification model.....	173
Figure 6.13. Parity plot of HPFFB CO ₂ gasification data with CCK ^N predictions using $Char_{Ar}$ kinetic correlation.....	175
Figure 6.14. Effect of gas composition on conversion of Wyodak char at $T_g = 1500$ K, $P = 15$ atm, $T_{surr} = 1000$ K.	176
Figure 6.15. Effect of ψ_0 , τ/f , and α on Wyodak 2010 char conversion at $T_g = 1500$ K, $P = 15$ atm, $T_{surr} = 1000$ K.	177
Figure 6.16. CO ₂ gasification for Illinois #6 (top) and Wyodak (bottom) with different variable parameters.	179
Figure 6.17. Combined diffusivity compared to molecular diffusivity as a function of pore diameter and pressure.....	181

Figure 6.18. Effect of annealing mechanisms on rate and temperature at $T_g = 1500$ K, $P = 15$ atm, $T_{surr} = 1000$ K.	184
Figure 6.19. Parity plot of HPFFB gasification data with optimized CCK model predictions.	187
Figure 6.20. Correlations of kinetic parameter $A_{7,0}$ with coal composition and NMR parameters.	189
Figure 6.21. Parity plot of HPFFB gasification data with CCK predictions from quadratic $Char_{Ar}$ kinetic correlation.	190
Figure A.1. NMR spectra of soots produced on the FFB from 2,6-dimethylnaphthalene (dmn).	223
Figure A.2. Illustrations A, B, and C (from left to right) of suggested average tar molecules.	225
Figure A.3. ^{13}C -NMR spectra of 6-5(H)-phenanthridinone and its solid pyrolysis products at 1450 K and 19 ms.	227
Figure A.4. C-13 CPMAS NMR spectra of the original EBA coal (bottom) and two tar/soots made at 1100 K (middle) and 1300 K (Top) from the coal.	230
Figure A.5. C-13 CPMAS spectra of the EBA coal (bottom), a matched tar/soot and char pair in the two (middle) spectra and a tar/soot at 1450 K (top) spectrum.	231
Figure A.6. C-13 CPMAS spectra the Wyodak coal (bottom) and tar/soots made at 1150 K (middle) and 1300 K (top).	232
Figure A.7. C-13 CPMAS spectra of the Wyodak coal (bottom) and 1350 K tar/soot and char pairs (2 and 3 from bottom) and 1450 K tar/soot and char pairs (4 and 5 from bottom).	233
Figure A.8. FTIR spectra from pyrolysis of 6-5(H)-phenanthridinone, showing data reduction technique.	237

Figure A.9. Two spectra of a tar/soot made from biphenyl at 5 atm, 1539 K. The (bottom) spectrum shows all carbon types and the (top) short contact time spectrum shows mostly carbons types that are protonated.	239
Figure A.10. A single pulse spectrum of a highly carbonized char made at 5 atm, 1539 K from the EBA.	240
Figure A.11. C-13 CPMAS spectra of EBA tar/soot at 5 atm, 1539 K, collected at 2-inches above the burner. The short contact time (bottom) spectrum shows mostly protonated carbons and the (top) spectrum shows all carbon types.	241
Figure B.1. Burner-to-quartz tube mounting systems: quartz collars (left and center) and steel ring (right).	245
Figure B.2. Photograph of reacting coal stream exhibiting undesired transition to turbulence with 2-inch burner.	247
Figure B.3. Heat damage to sintered steel tubes: old tube (top) and new tube with more large holes (bottom).	250
Figure C.1. Force balance on particle entrained with upward-flowing gas.	251
Figure D.1. HPFFB stepper motor driver circuit diagram and graphical user interface.	256
Figure E.1. SEM images of a separated Eastern Bituminous A char produced at 5 atm, 1702 K, 38 ms.	258
Figure E.2. SEM images of separated Eastern Bituminous B char produced at 15 atm, 1918 K, 660 ms.	259
Figure F.1. Radiation-corrected centerline gas temperatures in the HPFFB at 5 atm with a maximum temperature of 1702 K at two probe heights. The 16.25-inch profile consists of a single collection of measurements and the 10-inch profile uses measurements from a 3-inch profile near the burner.	265
Figure J.1. Gasification of Wyodak 2010 coal in 0.68 atm steam with predicted 1 st -order rate.	292

Figure J.2. Wyodak coal (top left) and chars produced at peak centerline temperature of 1698 K, pressure of 2.5 atm, residence times of 76 ms (top right) 147 ms (bottom left) and 548 ms (bottom right).....	294
Figure K.1. Wyodak 2010 η and χ factors from CCK ^N with $n = 0.5$, indicating Zone II behavior.....	297
Figure K.2. Wyodak 2011 η and χ factors from CCK ^N with $n = 0.5$, indicating Zone II behavior above ~1400 K.	298
Figure K.3. Illinois #6 η and χ factors from CCK ^N with $n = 0.5$, indicating Zone II behavior above ~1500 K.	298
Figure K.4. Kentucky #9 η and χ factors from CCK ^N with $n = 0.5$, indicating Zone II behavior above ~1500 K.	299
Figure K.5. EBA η and χ factors from CCK ^N with $n = 0.5$, indicating Zone II behavior above ~1500 K.	299
Figure K.6. EBB η and χ factors from CCK ^N with $n = 0.5$, indicating Zone II behavior above ~1500 K.	300
Figure M.1. Log-normal annealing distribution from CBK and corrected CCK version.....	304
Figure O.1. Piping flow diagram of HPFFB.....	314
Figure O.2. Piping diagram for gas outlets on HPFFB.....	315
Figure O.3. Gas supply system for the HPFFB.	316

NOMENCLATURE

A	pre-exponential factor [<i>units vary</i>], or external surface area [m^2]
A_{ASTM}	the ASTM ash fraction on a dry basis [<i>dimensionless</i>]
ASTM	American Society for Testing and Materials
a	quadratic coefficient in velocity scaling factor equation
a_{net}	net particle acceleration [m/s^2]
B	mass flux term in the blowing parameter [<i>dimensionless</i>]
BSG	bench-scale gasifier
b	linear coefficient in velocity scaling factor equation
C	concentration [mol/cm^3]
C_D	drag coefficient [<i>dimensionless</i>]
C_{fas}	carbon free active site
$Char_{Ar}$	estimated aromatic cluster mass without attachments: $MW - M_{\delta}(\sigma + 1)$ [<i>amu</i>]
c	constant coefficient in velocity scaling factor equation
c_0	fraction of thermally stable bridges in coal; used in CPD model
c_{ext}	parameter related to the extent to which the external pressure force restrains coal swelling [<i>dimensionless</i>]
c_{HR}	parameter related to the effect of heating rate in the coal swelling model [<i>dimensionless</i>]
c_p	specific heat of the reacting coal or char [$cal/(g \cdot K)$]
c_{scale}	parameter used to scale the maximum magnitude of the effect of pressure in the swelling model [<i>dimensionless</i>]
c_{visc}	parameter representing changes in viscoelastic properties of the metaplast that allow increased swelling with increasing pressure [<i>dimensionless</i>]
CBK	Carbon Burnout Kinetics model
CCK	Char Conversion Kinetics model
CCK ^N	n th -order Char Conversion Kinetics model
CCS	carbon capture and sequestration
CPD	chemical percolation devolatilization model
D	binary or pseudo-binary diffusivity [cm^2/s]
d/d_0	particle diameter swelling ratio [<i>dimensionless</i>]
d	diameter [m], derivative
daf	dry, ash-free
dm/dt	mass reaction rate of carbon [kg/s]
DTF	drop-tube furnace

E	activation energy [J/mol or cal/mol]
EBA	Eastern Bituminous A
EBB	Eastern Bituminous B
EFR	entrained-flow reactor
F_i	View factor for radiation heat transfer calculations
FC_{ASTM}	the ASTM fixed carbon fraction
FFB	flat-flame burner
FG-DVC	functional-group-depolymerization, vaporization, and cross-linking model
f_{CO_2}	the fraction of carbon oxidized that becomes CO_2 [$dimensionless$]
f_{RPM}	internal surface area change factor [$dimensionless$]
g	acceleration due to gravity [$9.8 m/s^2$]
GRG	generalized reduced gradient
h	convection heat transfer coefficient [$W/(m^2K)$]
h_m	mass-transfer coefficient [$units depend on definition where used$]
HPFFB	high-pressure flat-flame burner
ICP-AES	inductively coupled plasma-atomic emission spectroscopy
ID	inner diameter [m]
IGCC	integrated gasification combined cycle
$k_{D,i}$	reactant mass transfer coefficient [$units depend on definition where used$]
k	gasification or Arrhenius-form rate constant
k'	rate constant for a reverse reaction
\mathcal{L}	labile bridge fraction in the polymer network of the coal or char
\mathcal{L}^*	labile bridge that has been converted to a reactive intermediate state
L-H	a Langmuir-Hinshelwood rate expression
l	the height where maximum optical velocity was measured [m]
M_W	the molecular weight of the gas [amu]
M_δ	average molecular weight of an attachment [amu]
MR	mass release, $1-m/m_0$
MW	average aromatic cluster molecular weight with associated attachments [amu]
m	intrinsic reaction order [$dimensionless$], or mass [kg], or scaling factor at the height where maximum optical velocity was measured
m/m_0	residual mass ratio [$dimensionless$]
N_i	molar flux [$mol/(cm^2 \cdot s)$]
NMR	nuclear magnetic resonance
NPT	National Pipe Thread
n	apparent reaction order [$dimensionless$], or total number of data points

n_{Coals}	the number of coals for which parameters were fit
n_j	the effective or observed reaction order with respect to the partial pressure of species j
OD	outer diameter [m]
P	total pressure [atm], or partial pressure (with a subscript) [atm]
PAH	polycyclic aromatic hydrocarbons
PDTF	pressurized drop-tube furnace
PEFR	pressurized entrained-flow reactor
Pr	the Prandtl number [$dimensionless$]
PTGA	pressurized thermogravimetric analyzer
p_0	fraction of attachments that are intact loops or bridges [$dimensionless$]
q_i	rate of mass transfer in the boundary layer, or the net depletion flux [due to reaction] of species i [$mol/(cm^2 \cdot s)$]
q_{tot}	total reaction rate calculated from oxidation and gasification kinetics [$g/(cm^2 \cdot s)$]
R	reaction rate or universal gas constant
R_g	the universal gas constant [$8.314 J/(mol \cdot K)$ or $1.987 cal/(mol \cdot K)$]
$Re_{d,sphere}$	the Reynolds number based on a spherical bead diameter [$dimensionless$]
r	reaction rate [kg/s]
r_p	particle radius [cm]
SEM	scanning electron microscope
SF	scaling factor [$dimensionless$]
Sh	the Sherwood number [$dimensionless$]
SSE	sum of squared errors in mass release
SSE_R	percent increase in SSE when correlated rate parameters are used compared to SSE with optimal rate parameters
s_{min}	theoretical lower limit of swelling at infinitely high heating rates [$dimensionless$]
s_{var}	swelling model parameter most strongly influenced by coal rank [$dimensionless$]
$swell$	fractional swelling parameter defined as $d/d_0 - 1$
T	temperature [K]
TGA	thermogravimetric analyzer
t	time [s]
U	overall heat transfer coefficient that accounts for effects of the boundary layer and an ash film (if present) [$W/(m^2 K)$]
v	velocity [m/s]
WMR	Wire Mesh Reactor
X	the fractional carbon conversion [$dimensionless$]
x	mass fraction [$dimensionless$]

y	mole fraction [<i>dimensionless</i>]
z	height above the burner [<i>m</i>]
α	mode of burning parameter [<i>dimensionless</i>]
γ_i	volume expansion factor defined by the stoichiometry of the reaction [<i>dimensionless</i>]
ΔH	enthalpy of reaction and phase change [<i>J</i>]
ΔH_{rxn}	enthalpy of reaction [<i>J</i>]
δ_f	thickness of ash film [<i>cm</i>]
ε	packing factor [<i>dimensionless</i>], or emissivity [<i>dimensionless</i>]
ε_s	the porosity of the carbonaceous core of the particle [<i>dimensionless</i>]
η	effectiveness factor [<i>dimensionless</i>]
θ	blowing parameter, porosity
μ	gas viscosity [<i>Pa·s</i>]
ν_i	stoichiometric coefficient relating the moles of reactant i transferred to the mass of char reacted [<i>mol/g</i>]
ρ	density [<i>kg/m²</i>]
p_0	Fraction of attachments that are intact loops or bridges
ρ/ρ_0	ratio of apparent densities
σ	Stefan-Boltzmann constant [$5.67 \times 10^{-8} \text{ W m}^{-2} \text{ K}^{-4}$]
$\sigma+1$	coordination number; average number of attachments per aromatic cluster
τ/f	the tortuosity divided by the fraction of the total porosity in the macropores [<i>dimensionless</i>]
Φ	Thiele modulus [<i>dimensionless</i>]
χ	ratio of the observed rate to the maximum film diffusion-limited rate [<i>dimensionless</i>]
ψ_0	structural parameter in the random pore model [<i>dimensionless</i>]

Subscripts

0	initial or previous state
A	ash
a	apparent, ash fraction, or soot agglomeration from primary soot
af	ash film
avg	average
b	thermocouple bead, or bulk
C	carbonaceous
base	base case
bulk	in the bulk
C	carbonaceous portion of the particle
CO	carbon monoxide
CO ₂	carbon dioxide
char	char
coal	coal
comb	combined
daf	dry, ash-free
eff	effective
f	formation rate, ash film
fit	from a correlation or curve-fit
g	in the gas, gasification
HHR	high heating rate [$>8.5 \times 10^3$ K/s]
H ₂	hydrogen
H ₂ O	water
i	reaction or species <i>i</i>
LHR	low heating rate [$<8.5 \times 10^3$ K/s]
Low	low value
<i>j</i>	reaction or species <i>j</i>
K	Knudsen
m	mean, mass, or film
max	maximum
Mid	mid-range value
mix	in the mixture
O ₂	oxygen
obs	observed

p	particle
pore	pore
P ₁	char produced at atmospheric pressure
P ₂	char produced at high pressure
Peak	peak value
R	overall reaction rate
rxn	reaction
S	external particle surface
surr	surrounding surface
t	terminal
Ti	titanium
true	true
∞	in the bulk

Superscripts

E	experimental
n	apparent reaction order
P	predicted

Units

atm	atmospheres [<i>Pressure</i>]
K/s	the basic unit of heating rate
SLPM	standard liter per minute
MPa	megapascal (10 ⁶ Pascals) [<i>Pressure</i>]
ms	millisecond (10 ⁻³ seconds) [<i>time</i>]
μm	micrometer [<i>length</i>]

CHAPTER 1. INTRODUCTION

Coal gasification is an area of much industrial interest today, since it provides a way to make cleaner electricity, liquid fuels, or chemicals. Although coal gasification has been used for many years, in today's energy market it is desirable to obtain additional information to optimize gasifier performance, both for efficiency and reliability. Recent spikes in oil prices and the probable need for carbon capture and sequestration (CCS) to comply with environmental regulations have increased interest in the development of advanced gasification models. It is expected (Liu et al., 2010) that integrated gasification combined cycle (IGCC) technology will be one of several technologies used to raise the standard for efficient and clean use of coal, particularly if CCS is required.

Advanced models of coal gasification processes can be used to improve gasifier designs if such models can be calibrated and/or validated with appropriate experimental data. Some of the physical mechanisms that influence gasification rates and products remain unclear and require investigation. The pyrolysis pressure and initial particle heating rate strongly influence the size and physical structure of chars produced from bituminous coals. These effects should be taken into account to accurately model combustion and gasification behavior. Conventional drop-tube furnaces operating at $\sim 10^4$ K/s often yield char with particle sizes far larger than would be typical at industrial heating rates of $\sim 10^6$ K/s. In this work, the extent of coal swelling during pyrolysis was measured at heating rates of 10^5 K/s and pressures of up to 15 atm. An empirical

model was developed to predict char particle size as a function of coal rank, heating rate, and pressure.

Most gasification kinetic studies have been performed in thermogravimetric analyzers (TGAs), at very low heating rates and temperatures limited to about 1000°C. However, pulverized coal gasifiers operate with initial particle heating rates of up to 10^6 K/s and temperatures of up to 2000°C. Char samples for TGA experiments are often generated at atmospheric pressure, while commercial gasifiers operate at 30 to 60 atm. In this work, gasification kinetics of coal chars with CO₂ were investigated using a new high-pressure flat-flame burner (HPFFB) facility operating at temperatures, pressures, and heating rates that are more representative of industrial entrained-flow facilities. A simple 1st-order model fit the HPFFB gasification data. Advanced models that account for decreasing reactivity with increasing conversion were also developed to produce improved fits of the HPFFB gasification data and to allow further analysis.

CHAPTER 2. LITERATURE REVIEW

Entrained-flow gasifiers feed pulverized coal into a pressurized gasification chamber. Many designs feed the coal as a slurry with water, but some recent designs have begun to incorporate dry-feed systems (Liu et al., 2010). High gasification rates are achieved by using high partial pressures of gaseous reactants; total pressures are typically 30 atm or higher. O_2 is injected to combust some of the gaseous products of pyrolysis and thereby ensure that the heterogeneous gasification reactions occur at high temperatures. The high-temperature combustion also supplies CO_2 , which is one of the gasification reactants. The other major gasification reactant is H_2O , which may be injected as steam with a dry-feed system or as liquid water in a coal slurry (which vaporizes quickly after injection). In any case, steam is also a combustion product from the coal. Many experimental and modeling approaches developed for utility boiler applications may be used directly or modified for entrained-flow gasification because the coal reaction mechanisms are similar in the two types of systems.

The term “combustion” typically encompasses both pyrolysis and the subsequent oxidation reactions. The term “gasification” typically refers to the heterogeneous reactions that occur after pyrolysis has run its course. Pyrolysis and heterogeneous reaction processes are often treated as sequential, although this is not strictly true in all cases. However, it is a better approximation for gasifying conditions compared to oxidizing conditions because gasification reactions are much slower than both pyrolysis and oxidation reactions.

2.1 Chemical Structure of Coal

Coal may be viewed as a polymer network (Figure 2.1) consisting of aromatic clusters with aliphatic bridges, loops and side chains (Smith et al., 1994). Nitrogen occurs primarily in pyrrolic and pyridinic forms rather than in the aliphatic groups. Oxygen occurs in some of the aliphatic groups, commonly at least once per aromatic cluster (Perry et al., 2000). The C-C bonds in the aromatic clusters are very stable even at high temperatures (Yu et al., 2007). The energy required to break the bonds in the aliphatic bridges and side chains is very low compared to the energy required to break C-C bonds in the aromatic clusters. Consequently, the polymer network in the coal usually undergoes thermal decomposition processes known as pyrolysis before the particle temperature becomes high enough to allow heterogeneous reactions (oxidation or gasification) to occur at significant rates.

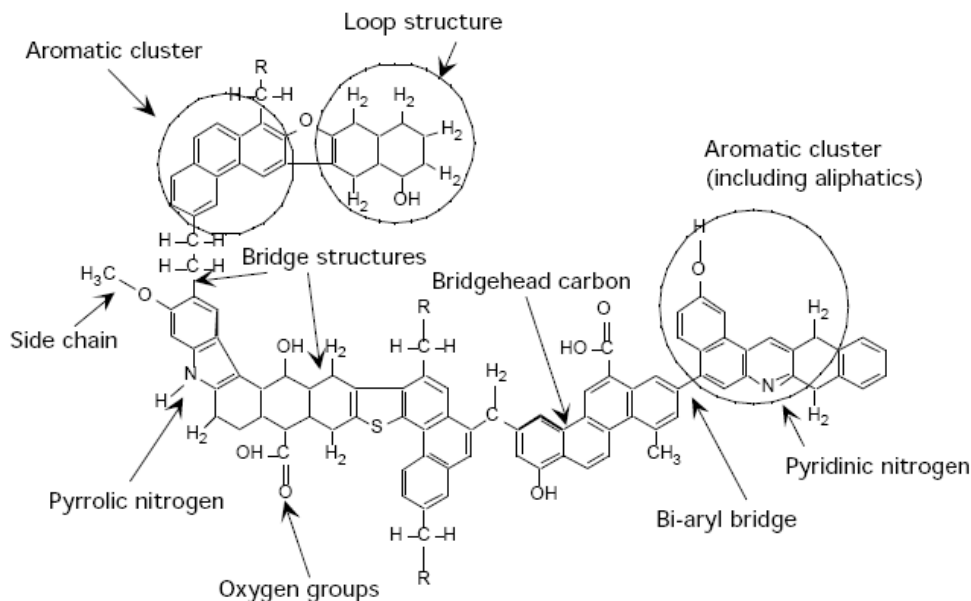


Figure 2.1. Structure of a hypothetical coal molecule, adapted from Serio et al., (1987).

2.2 Primary Pyrolysis

Devolatilization or pyrolysis may be classified into two stages. The first stage is primary pyrolysis. Primary pyrolysis consists of thermal cracking and polymerization processes that liberate volatile matter from the coal particle and reorganize the remaining structure into char (Figure 2.2).

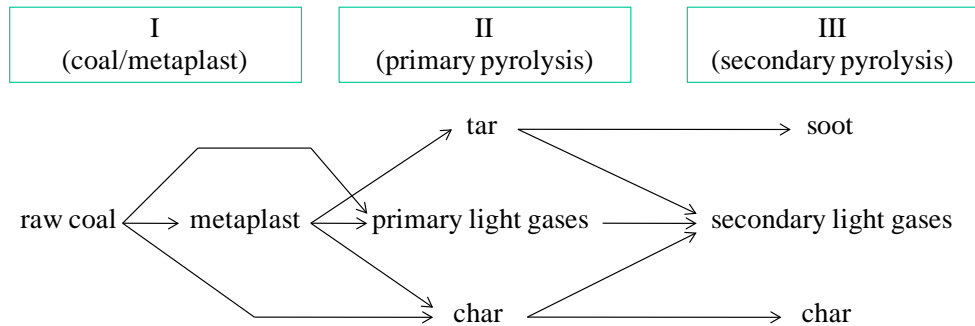


Figure 2.2. Pyrolysis processes and products, adapted from Serio et al., (1987).

After water evaporates, the coal particles experience very high initial heating rates ($\sim 10^6$ K/s in a utility boiler or gasifier). When low experimental heating rates are employed the breaking of C-C aliphatic bonds begins to occur at ~ 670 K and some vaporization of free matter will occur below this temperature (Yu et al., 2007). The breaking of bridges forms radical groups such as CH_2 and O. These form light gases such as CH_4 and water. Fragments that break off the polymer network form the metaplast, which is a viscoelastic fluid. Molecules in the metaplast that have high mobility and vapor pressure will diffuse out of the particle and into the surrounding gas (Smith et al., 1994). If these liberated molecules have high enough molecular weight to condense to liquids or solids at room temperature they are called tar; the rest are defined as light gases. The bulk of the volatile matter is released below ~ 820 K (Yu et al., 2007)

at low initial heating rates, but devolatilization occurs at higher temperatures when the initial heating rate is increased. Metaplast molecules that remain in the char cross-link back into the polymer network until no metaplast remains. The resulting solid network is char.

2.2.1 Network Devolatilization Models

Network statistical devolatilization models have been used successfully to model the volatiles yield, devolatilization rates, and chemical transformations that occur in primary pyrolysis. These include the functional-group-depolymerization, vaporization, and cross-linking (FG-DVC) model (Serio et al., 1987; Solomon et al., 1988a, b; Solomon et al., 1990), the FLASHCHAIN model (Niksa, 1991a, b; Niksa and Kerstein, 1991), and the chemical percolation devolatilization (CPD) model (Grant et al., 1989; Fletcher et al., 1990; Fletcher et al., 1992). For the purposes of this work, the CPD model was used.

The CPD model uses ^{13}C -nuclear magnetic resonance (NMR) structural parameters as inputs along with heating information which may take the form of particle temperature histories or particle velocity and gas temperature histories. The CPD model can be used to calculate pyrolysis rates, pyrolysis yields, and the initial distribution of products between tar and light gases. It has been applied in computational fluid dynamics (CFD) codes such as FLUENT (2007) and STARCD (Price, 2007). Correlations have been developed relating the ^{13}C -NMR structural parameters to the proximate and ultimate analyses (Genetti et al., 1999). These correlations facilitate application of the CPD model to coals outside the NMR database. The ^{13}C -NMR structural parameters used in the CPD model are listed in Table 2.1.

Table 2.1. Chemical structural parameters derived from ^{13}C -NMR measurements used in the CPD model

Structural Parameter	Description
$\sigma+1$	Coordination number; average number of attachments per aromatic cluster
p_0	Fraction of attachments that are intact loops or bridges
M_δ	Average molecular weight of an attachment
MW	Average aromatic cluster molecular weight, including associated attachments

Additionally, the CPD model uses the empirical parameter c_0 for coals of very high or low ranks. The parameter c_0 is typically calculated from a correlation or adjusted to fit pyrolysis data. This parameter represents the fraction of thermally stable bridges in the parent coal or that form early in the pyrolysis process. This parameter has been used to represent early cross-linking in lignites and subbituminous coals. The parameter c_0 represents biaryl linkages in low-volatile bituminous coals and anthracites. The parameter c_0 is typically assigned a value of zero for most bituminous coals.

2.2.2 Coal Char Characteristics




The chemical and physical structure of coal char varies significantly with coal rank and with pyrolysis reaction conditions such as temperature, initial heating rate, and pressure (Solomon and Fletcher, 1994; Yu et al., 2007). The chemical heterogeneity of the parent coal as measured through maceral analysis or other methods also has pronounced effects. Many of these differences have been qualitatively explained in terms of the viscoelastic properties of the metaplast and the competition between the release of volatile mater and cross-linking to form char. The original pore structure of softening coals disappears as the metaplast becomes fluid (Yu et al., 2007). New pore structure is generated as gases are transported out of the particles. If the initial coal structure has many thermally stable cross-links or if such cross-links form during the earliest stages of pyrolysis then the fluidity of the metaplast will be quite limited. For this

reason only bituminous rank coals develop significant fluidity at moderate initial heating rates. Coals that do not undergo softening release their volatiles through their existing pore structures, thereby increasing the size and extent of the pores. Very high-rank coals such as anthracites have little volatile matter, so changes in particle structure during pyrolysis are more limited.

Volatile matter collects in bubbles within the condensed phase that grow and coalesce. Depending on the viscoelastic properties of the metaplast one or several large voids may be present in the char. Fragmentation of particles may occur, which further increases the accessibility of the surface area for gasification and oxidation reactions. (Liu et al., 2000; Ma and Mitchell, 2009). At conditions found in pulverized coal boilers and gasifiers the effect of ambient gas composition on swelling is probably small because the blowing effect inhibits transport of surrounding gases to the surface of pyrolyzing coal particles (Fletcher, 1993).

Descriptions of char structure include various measures of surface area, pore structure, and internal voids caused by bubble growth. Several detailed morphological classification systems have been developed for char. A three-fold classification system is coming into common usage because of its relative simplicity (Benfell et al., 2000). This system has three char types distinguished by three classification parameters, namely porosity, sphericity, and wall thickness (Table 2.2). The number fraction of Group I chars (cenospheres) produced in drop-tube furnaces operating near 10^4 K/s has been correlated with maceral composition and pyrolysis pressure (Benfell et al., 2000; Yu et al., 2007). The effect of heating rate on swelling was not included in these correlations. For highly swollen cenospheres, the particle wall thickness is very small compared to the particle diameter. Therefore, the volume of the internal void may be only slightly less than the total volume of the particle. Knowledge of the particle size and the pyrolysis yield can be used to estimate the wall thickness for cenospheres (Benfell et al., 2000).

Table 2.2. Three-fold char classification system (Benfell et al., 2000; Yu et al., 2007; Ma and Mitchell, 2009)

Char type	Group I: Cenospherical Char	Group II: Mixed Char	Group III: Dense Char
Illustration			
Porosity	>80%	>50%	~50%
Wall Thickness	<5 μm	Variable	>5 μm
Shape Factor	>0.85	>0.8	<0.7
Void Size	\approx Particle	5 μm < Void < Particle	< 5 μm
Swelling Ratio	>1.3	>1	>0.9

The coal swelling ratio or swelling parameter is defined for pulverized coal as the char particle diameter after pyrolysis divided by the initial coal particle diameter. The swelling ratio is the simplest and perhaps the most useful measure of char structure. It is a critical parameter for practically all combustion and gasification models, regardless of the level of sophistication. Other structural characteristics of char, including total porosity and wall thickness, can be estimated using the swelling ratio, volatiles yield, and the density of the solid material (Hurt et al., 1998; Benfell et al., 2000).

2.2.3 Effect of Heating Rate on Volatiles Yield and Swelling during Coal Pyrolysis

The heating rate that has been observed to correlate best with pyrolysis behavior is the maximum derivative of particle temperature with respect to residence time, assuming lumped capacitance (Fletcher, 1993). Maximum temperature and initial particle size influence swelling mainly through their effect on the heating rate (Fletcher, 1989a). In a modeling study of drop-tube reactor conditions, calculated differences between the particle surface and center temperatures were small (< 40 K), and the calculations agreed well with measured particle temperatures (Fletcher, 1989a; Fletcher and Hardesty, 1992). The authors concluded that the

lumped capacitance model was adequate for entrained-flow conditions with particles of 100 μm and heating rates of 10^4 K/s. The physical significance of the lumped-capacitance heating rate gradually breaks down as particle size and heating rate increase.

The volatiles yield for high-temperature applications is higher than the volatiles yield from the American Society for Testing and Materials (ASTM) standard proximate analysis (Yu et al., 2007). The excess volatiles yield is most pronounced for coals with maximum tar yields. Part of this difference is due to mass transfer limitations in the bed of particles used in the ASTM test. Some of the excess volatiles yield is attributable to the heating rate. The higher particle temperatures that are achieved at high heating rates increase the devolatilization rate and total volatiles yield by increasing the rates of bridge-breaking reactions and vaporization of tar faster than the rates of cross-linking reactions. Network devolatilization models such as the CPD model capture the effects of heating rate and temperature on devolatilization rates and yields.

Studies at low heating rates used in TGAs and Wire Mesh Reactors (WMRs) indicate that swelling increases with increasing heating rate (Figure 2.3) (Zygourakis, 1993). This can be attributed to the higher devolatilization rates that occur at higher temperatures, and perhaps also differences in viscoelastic properties. However, experiments with these types of facilities are often performed with coal particles larger than 200 μm (Khan and Jenkins, 1986; Zygourakis, 1993), where internal mass transfer limitations begin to be influential (Solomon and Fletcher, 1994). The observed trend of increased swelling with increasing heating rate should be generally valid, but swelling measurements of large particles do not apply quantitatively to particles of ~ 50 μm mean diameter used in utility boilers and gasifiers.

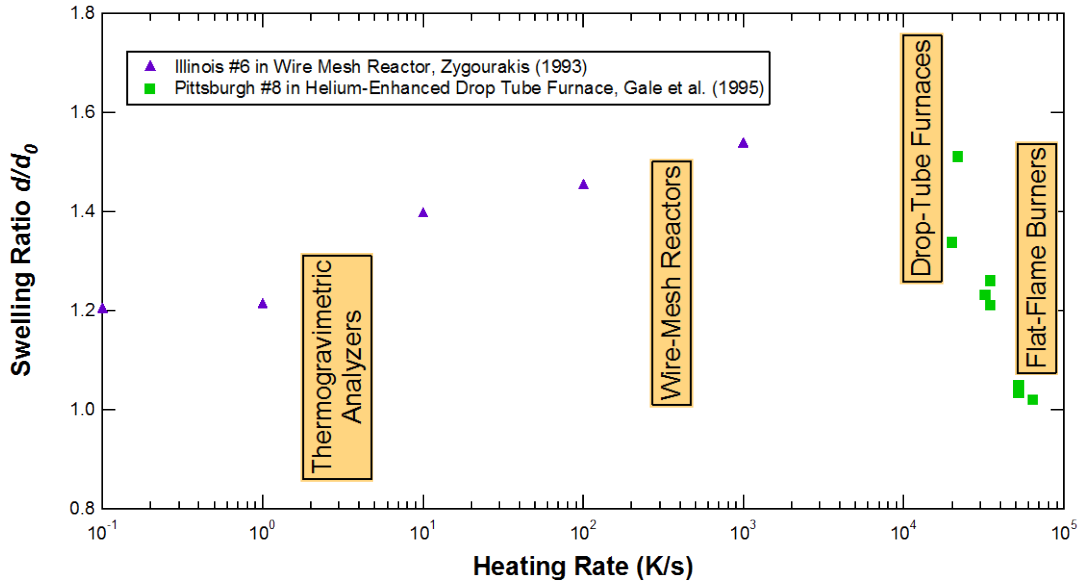


Figure 2.3. Effect of initial heating rate on particle swelling ratio, adapted from Gale et al. (1995)

The influence of heat and mass transfer limitations on coal swelling appears to have a complex dependence on heating rate. At higher heating rates internal temperature gradients in large particles would cause material near the surface to generate volatiles faster than material near the center of the particle. Internal temperature gradients may also cause internal gradients in viscoelastic properties. The interplay between these and other transport effects could cause swelling to be enhanced or inhibited with increasing particle size, depending on the details of particle size, coal type, and heating rate. Swelling data obtained from Pittsburgh #8 coal in a fixed bed at heating rates of 0.4 K/s and 1.1 K/s indicated that the effects of pressure and heating rate on swelling can have very different trends for particles smaller than 75 μm compared to particles of 250-425 μm (Khan and Jenkins, 1984).

Studies with modified drop-tube furnaces and flat-flame burners at atmospheric pressure have shown that the bituminous coal swelling ratios may decrease from greater than 1.5 to less than 1.05 at initial heating rates on the order of 10^5 K/s (Figure 2.3) (Gale et al., 1995). This

decrease in swelling at high heating rates has been attributed to a characteristic devolatilization time that is shorter than the characteristic relaxation time of the viscous coal melt. The bubbles burst at very high heating rates, followed by cross-linking.

The most advanced swelling models based on the physics of bubble formation predict increased swelling with increasing heating rate, but fail to predict decreased swelling at heating rates above 10^4 K/s (Oh et al., 1989; Yu et al., 2004b). There is some indication that different formulations may allow mechanistic models to predict decreased swelling with increasing heating rate (Melia and Bowman, 1983; Sheng and Azevedo, 2000), at least on a qualitative level. Advanced swelling models (Oh et al., 1989; Yu et al., 2004b) are inconvenient for most practical applications because the computational burden is high and input parameters can be difficult to obtain. It is extremely difficult to measure physical properties such as viscosity in reacting metaplast. Other detailed inputs such as density distributions are inconvenient to measure. Existing empirical swelling models also fail to properly capture the effect of heating rate (Niksa et al., 2003; Sun et al., 2003; Kidena et al., 2007).

Swelling is most pronounced for bituminous coals at initial heating rates slightly below 10^4 K/s (Figure 2.3), which is the regime where measurements are most conveniently made for drop-tube furnaces or other entrained-flow reactors. Because highly swollen particles have large internal voids, the porosity follows a trend very similar to the swelling ratio (Gale et al., 1995). Since utility boilers and gasifiers operate at initial particle heating rates of about 10^6 K/s, flat-flame burners are the most industrially representative laboratory-scale equipment available to study coal swelling behavior during pyrolysis. Swelling measurements at heating rates lower than 10^5 K/s may only be appropriate for the largest particles of the distributions used in industrial pulverized coal boilers and gasifiers.

2.2.4 Effect of Pyrolysis Pressure on Volatiles Yield and Coal Swelling

For softening coals at higher pressures, vaporization of the tar is inhibited; only the very lightest molecules have a high enough vapor pressure to leave the particle. This decreases the yield of tar. The retained tar is cross-linked back into the polymer network to become part of the char; aliphatic attachments from molecules that remain in the metaplast increase the yield of light gases. The net effect of higher pyrolysis pressure is to decrease the total yield of volatiles and decrease the average molecular weight of the tar (Solomon and Fletcher, 1994). The effect of total pressure on pyrolysis yield has been captured in network pyrolysis models by treating tar vaporization as a flash-distillation process.

At elevated pressures the metaplast is enriched in lighter molecules, which act as plasticizers, enhancing bubble growth. Greater swelling and higher porosity have been observed at elevated pressures because bubbles are able to grow to larger sizes without popping (Lee et al., 1991; Wu et al., 2000). Group I chars have been found to be more prevalent (Wu et al., 2000; Yu et al., 2004a). However, swelling cannot increase without bound as pressure increases. Very high external pressures are better able to counteract the lower pressure generated inside the bubbles due to lower volatiles release. A recent model includes the competition of these two effects of increasing pressure and predicts that the swelling ratio decreases slowly as total pressure increases beyond 8-10 atm (Figure 2.4) (Yu et al., 2004b).

When swelling data obtained in a pressurized drop-tube furnace at 10^4 K/s (Lee et al., 1991) are compared to data from facilities that enhance the particle heating rates using O_2 (Wu et al., 2000), or flat-flame burners (Zeng et al., 2005), as in Figure 2.4, it becomes apparent that the effect of heating rate on coal swelling is very important for pyrolysis at elevated pressures. The maximum reported swelling ratio for Illinois #6 is more than twice as high at 10^4 K/s compared

to 10^5 K/s. Existing swelling models do not predict the combined effects of pressure and heating rate.

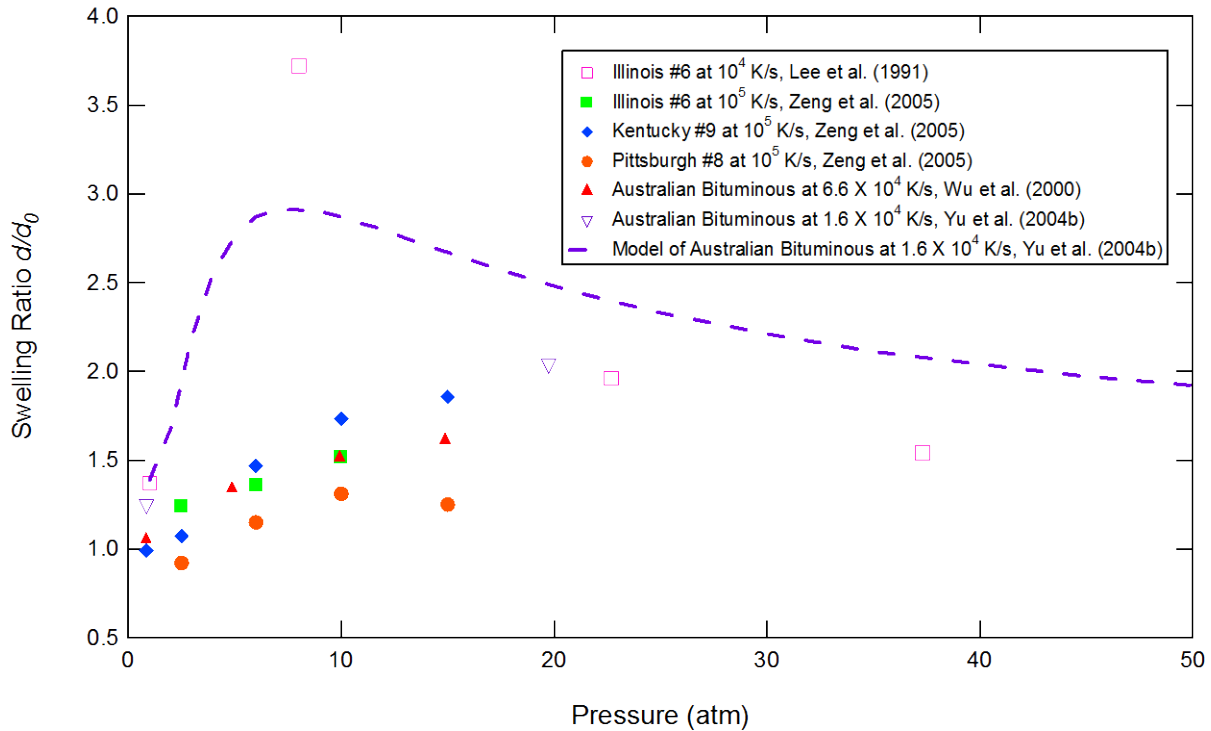


Figure 2.4. Swelling ratio versus pressure from pulverized coal experiments and a model

2.3 Secondary Pyrolysis

Secondary pyrolysis consists of the processes that determine the fate of the volatiles while they are still in a fuel-rich zone, particularly the tar (See Figures 2.2 and 2.5). Previous studies have shown that the sum of the mass of tar and soot remains nearly constant during secondary pyrolysis (Chen, 1991; Smith et al., 1994). The increase of soot as tar decreases indicates that tar is the primary precursor of soot. The conversion of tar to soot tends to become more complete with increasing total pressure due to the increase in the tar concentration.

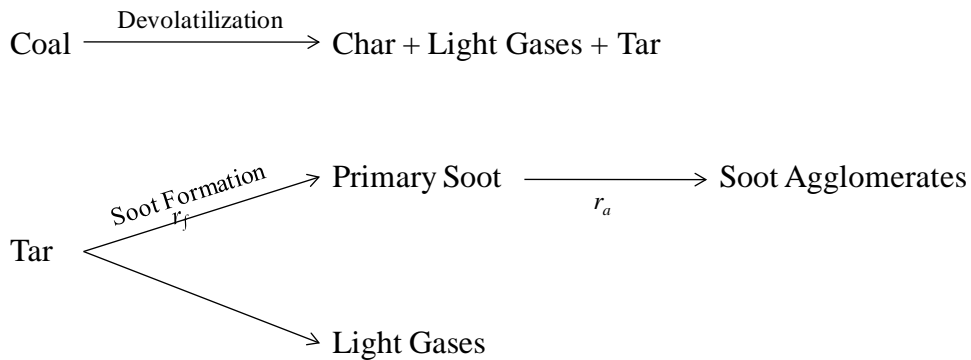


Figure 2.5. Secondary pyrolysis processes and products (Ma, 1996)

On the chemical level soot consists of polycyclic aromatic hydrocarbons (PAH) of very high molecular weight. It is much more graphitic in nature than coal, tar, or char and as such it has fewer functional groups and is less reactive (Wornat et al., 1987; Wornat et al., 1988; Smith et al., 1994). However, soot still contains many defects and some heteroatoms, particularly nitrogen. A considerable portion of the nitrogen in the coal can end up in the soot (Zhang and Fletcher, 2001; Manton et al., 2004). Additional review of the soot literature and secondary pyrolysis experiments conducted in this work are documented in Appendix A.

2.4 Gasification

As primary pyrolysis in a gasifier nears completion the char, tar, and soot begin to undergo heterogeneous oxidation and gasification. Changes in the structure of a coal particle during pyrolysis influence the subsequent char reaction history in various ways. The magnitude and accessibility of surface area for heterogeneous reaction on the interior surfaces of the char particles determine the reaction rate at a given temperature.

2.4.1 Three-Zone Theory

The temperatures at which different physical processes dominate the observed reaction rate have been described in terms of three zones (Figure 2.6) (Smoot and Smith, 1985). At low temperatures (Zone I), oxidation or gasification kinetics are rate-limiting, while diffusion of reactants through the particle boundary layer is rate-limiting at very high temperatures (Zone III). At intermediate temperatures (Zone II) both reaction kinetics and diffusion through pores determine the observed reaction rates. Practical applications of combustion and gasification of pulverized coal typically occur in Zone II, where the particle size and pore structure strongly influence the rates at which gaseous reactants are transported to the internal surfaces of the char.

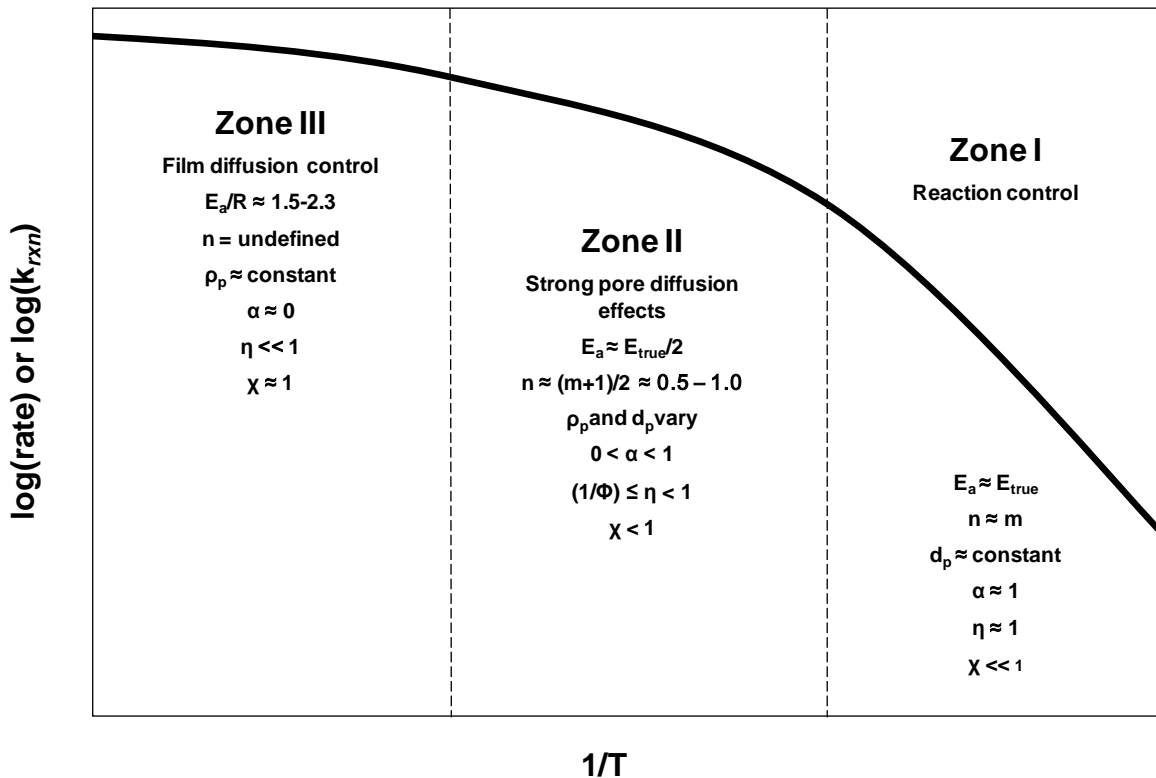


Figure 2.6. Three-zone theory for heterogeneous reactions on porous particles.

The heterogeneous reaction zones have different characteristic changes in particle diameter and density. The mode-of-burning parameter α is commonly used to quantify these changes (Hurt et al., 1998). This parameter relates the particle mass and density to their initial values via the following relationships:

$$\frac{\rho_C}{\rho_{C,0}} = \left(\frac{m_C}{m_{C,0}} \right)^\alpha \quad (2.1)$$

$$\frac{1}{\rho} = \frac{1-x_A}{\rho_C} + \frac{x_A}{\rho_A} \quad (2.2)$$

where ρ is the apparent density, m is mass, and x is a mass fraction. The subscript C refers to the organic portion of the particle, A refers to ash, and 0 refers to either an initial or previous state (e.g., fully pyrolyzed). In the ideal case of zero ash content, Equation 2.1 can be combined with geometric considerations to yield:

$$\frac{d}{d_0} = \left(\frac{m}{m_0} \right)^{(1-\alpha)/3} \quad (2.3)$$

where d is the particle diameter. The empirical mode-of-burning parameter varies with coal type and reaction conditions, but it is commonly assigned a uniform value for a given reactor type to simplify analysis and/or modeling (Hurt et al., 1998; Liu and Niksa, 2004).

Zone III behavior can be computed simply as the mass transfer rate through the boundary layer with a surface reactant concentration of zero. The χ parameter (Smith, 1982) is the ratio of the observed rate to the film diffusion-limited rate (i.e., the maximum possible rate):

$$\chi_j = \frac{r_{obs}}{r_{max}} = \frac{\nu_j r_{obs}}{A_p h_m P_j} \quad (2.4)$$

where r is a reaction rate with units of mass/time. The parameter ν_j is a stoichiometric conversion factor relating the mass of organic matter gasified to the moles of reactant species j that are consumed. A_p is the external surface area of the particle, h_m is a mass-transfer coefficient, and P_j

is the partial pressure of species j in the bulk. The subscripts *obs* and *max* distinguish the observed rate from the maximum diffusion-limited rate. A χ factor with a value close to unity indicates that diffusion through the boundary layer is rate-limiting.

The effectiveness factor η is typically correlated with a Thiele modulus Φ and has been used for many years to model behavior in porous catalysts (Carberry, 1962; Bischoff, 1965). The effectiveness factor accounts for intra-particle concentration gradients and is dependent on reaction kinetics, particle size, temperature, pore structure, gas concentrations, and diffusivities. In the absence of large intra-particle temperature gradients the effectiveness factor typically has a value less than unity. Derivations of the Thiele modulus assume that a static pore structure exists, which is reasonable for catalysts but is not realistic for char over large ranges of conversion.

In codes used to model large-scale devices (i.e. CFD), a high computational cost is already associated with the fluid dynamics and heat transport calculations. The large number of particles found in boilers and gasifiers can significantly increase the computational cost. Also, the local environments of individual particles in large-scale facilities are typically not known with enough accuracy to justify the use of complex models. Therefore, simple pyrolysis and gasification models are typically preferred for CFD applications. The Zone II rates that are thought to be common in industry are influenced by many physical phenomena, which make them difficult to predict accurately (effectiveness factors are embedded in the observed rates). The evaluation of new gasifier designs can best be accomplished through the use of relatively simple gasification kinetic mechanisms that have been fit to data obtained at high temperatures, high heating rates, and high pressures. Such data may also be used to validate more sophisticated kinetic models.

2.4.2 Recent Gasification Experiments

For the development of advanced gasification models, pyrolysis and gasification experiments should be conducted at temperatures, initial heating rates, and pressures that are typical of industrial gasifiers. A representative list of recent experiments is found in Table 2.3, where the char formation conditions for each gasification experiment are indicated (pyrolysis conditions). Many gasification studies conducted at “high heating rates” occur in drop-tube furnaces (DTF) or other entrained-flow reactors (EFR) that are limited to initial heating rates on the order of 10^4 K/s, which is where maximum swelling seems to occur (as shown earlier in Figure 2.3). Wire mesh reactors (WMR) and especially thermogravimetric analyzers (TGA) achieve much lower initial heating rates and are more suitable for measuring intrinsic Zone I rates. WMRs and TGAs often use large individual particles or a bed of particles that experience significant transport limitations. For these reasons, experimental data from these devices are not thought to be representative of industrial entrained-flow conditions.

In most practical gasifiers, pyrolysis and gasification occur in the same vessel and hence at the same pressure, but chars are sometimes pyrolyzed and gasified at different conditions in the laboratory (see Table 2.3). For high-temperature rate measurements (Zone II), the char size and physical structure formed at a given pressure and heating rate will strongly influence the observed rate. Therefore, pyrolysis and gasification experiments conducted at identical elevated pressures and heating rates of at least 10^5 K/s provide the most valuable reaction rates for the design of pulverized-coal gasifiers. There is some indication that the intrinsic (Zone I) char reactivities are not strongly dependent on pyrolysis pressure and initial heating (Wall et al., 2002; Roberts et al., 2003). However, more experimental data is needed at very high initial heating rates and elevated pressures to determine whether this result applies to industrial gasifiers.

Table 2.3. Recent pyrolysis and gasification studies

Source	Coal Particle Size, Pyrolysis System, Initial Heating Rate	Pyrolysis Temperature, Pressure	Gasification System & Reactants	Gasification Temperature, Total Pressure
Industrial PC Gasifiers	50 – 150 μm entrained flow at $\sim 10^6$ K/s	Up to 2000°C 2.5 – 3.0 MPa	Entrained Flow O ₂ , H ₂ O, CO ₂	up to 2000°C; Zone II-Zone III 2.5 – 3.0 MPa
(Peng et al., 1995)	149 – 210 μm TGA at $10^2 - 10^3$ K/s	1000 – 1400°C 0.1 MPa	TGA, H ₂ O	1000 – 1400°C 0.1 MPa
(Lim et al., 1997)	106 – 150 μm WMR at 10^3 K/s Fixed Bed at 10 K/s	1000°C 0.1 – 3.0 MPa	WMR, Fixed Bed O ₂ , CO ₂	850°C, 1000°C 0.1 – 3.0 MPa
(Messenböck et al., 1999; Messenböck et al., 2000)	106 – 150 μm , WMR at 10^3 K/s	1000°C 0.1 – 3.0 MPa	WMR, TGA O ₂ , H ₂ O, CO ₂	1000°C 0.1 – 3 MPa
(Roberts and Harris, 2000, 2006)	1000 – 6000 μm Crucibles at 0.17 K/s	1100°C 0.1 MPa	PTGA O ₂ , H ₂ O, CO ₂	500 – 940°C 0.1 – 3 MPa
(Wu et al., 2000)	63 – 90 μm DTF, PDTF at $\sim 10^4$ K/s	1300°C 0.1 – 1.5 MPa	N/A N/A	N/A N/A
(Ahn et al., 2001)	45 – 64 μm PDTF at 10^4 K/s	1400°C 0.1 MPa	PDTF, TGA CO ₂	900 – 1400°C 0.5 – 1.5 MPa
(Kajitani et al., 2002; Kajitani et al., 2006)	26 – 39 μm DTF at $\sim 10^4$ K/s	1100 – 1500°C 0.1 MPa	PDTF, PTGA CO ₂ , H ₂ O	1100 – 1500°C 0.2 – 2.0 MPa
(Roberts et al., 2003)	N/A PEFR, PDTF at $\sim 10^4$ K/s Crucibles at 0.17 K/s	1100°C 0.1 – 1.5 MPa	PTGA O ₂ , H ₂ O, CO ₂	Zone I (low) 0.1 – 1.5 MPa
(Yu et al., 2004a)	45 – 185 μm , 63 – 95 μm PEFR, DTF at $\sim 10^4$ K/s	1100 – 1400°C 0.1 – 2.0 MPa	PEFR H ₂ O, CO ₂ , O ₂	1100°C, 1400°C 0.1 - 2.0 MPa
(Zeng and Fletcher, 2005)	44 – 90 μm HPFFB at $\sim 10^5$ K/s	1027°C, 1300°C 0.085 – 1.5 MPa	HPFFB, PTGA O ₂	1150°C, 500°C 0.25 – 1.5 MPa
(Harris et al., 2006)	45 – 180 μm WMR at 10^3 K/s PEFR at $\sim 10^4$ K/s	1100°C, 1500°C 1.5 MPa	PEFR, PTGA H ₂ O, CO ₂ , some O ₂ in PEFR	800°C, 900°C 1.5 MPa
(Roberts and Harris, 2007)	1000 – 6000 μm Crucibles at 0.17 K/s	1100°C 1 – 5 MPa	PTGA mixed H ₂ O, CO ₂	850°C, 900°C 1 – 5 MPa
(Yang et al., 2007)	<152 μm PTGA at 0.17 K/s	1000°C 0.1 – 5 MPa	TGA CO ₂	1000°C 0.1 MPa
(Chen et al., 2008)	<152 μm PTGA at 0.17 K/s	1000°C 0.1 and 3.0 MPa	TGA CO ₂	1000°C 0.1 MPa
(Hodge et al., 2010; Roberts et al., 2010)	45 – 180 μm PEFR at $\sim 10^4$ K/s	1000 – 1400°C 1.0 – 2.0 MPa	PEFR, PTGA CO ₂	1000-1400°C 1.0-2.0 MPa

2.4.3 Reaction Chemistry

Coal combustion and gasification models focus primarily on reactions with solid carbon because it is the most abundant element. The global oxidation and gasification reactions include the following (Laurendeau, 1978; Smith et al., 1994):



The char oxidation reaction (Global Reaction 1) proceeds at $\sim 10^5$ times the rate of CO_2 gasification (Global Reaction 3, also known as the reverse Boudouard reaction) and H_2O gasification (Global Reaction 2) at 800 K and 0.1 atm (Simons, 1983; Smith et al., 1994). H_2O gasification rates have been found to exceed CO_2 gasification rates at temperatures of 800 K to 1173 K and reactant partial pressures of 0.1 atm to 60 atm (Simons, 1983; Mühlen et al., 1985), as shown in Figure 2.7. H_2 gasification (Global Reaction 4) is often not considered because its rate is ~ 300 times lower than that of CO_2 gasification at 800 K and 0.1 atm (Smith et al., 1994), although Figure 2.7 shows that the H_2 gasification rate exceeds the CO_2 gasification rate at 900°C and pure reactant partial pressures above 40 atm (Mühlen et al., 1985). Due to the high rate of oxidation compared to gasification, the Zone transitions in Figure 2.6 occur at higher temperatures for gasification when compared to combustion (Roberts and Harris, 2000).

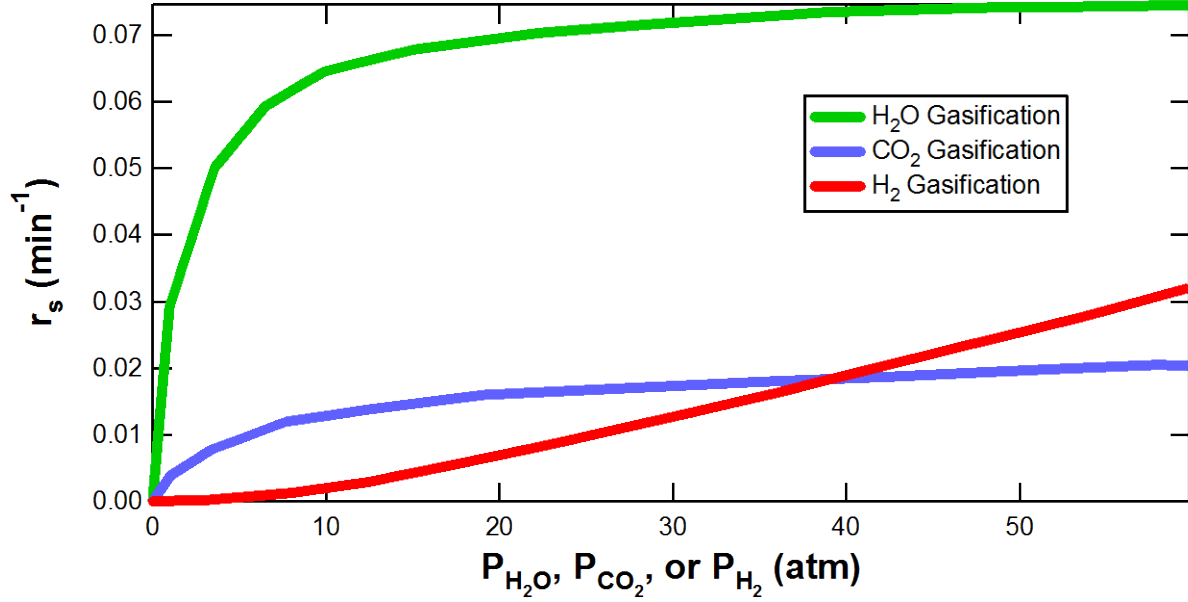


Figure 2.7. Intrinsic gasification rates of a German bituminous coal char at 900°C (Mühlen et al., 1985).

An empirical n^{th} -order Arrhenius form with the global reactions is commonly used to calculate combustion and gasification rates (Hurt et al., 1998; Roberts et al., 2010):

$$\frac{1}{A_p} \frac{dm}{dt} = -k_{rxn,j} P_{j,S}^n \quad (2.5)$$

where A_p is the external surface area of the particle, dm/dt is the mass reaction rate of carbon, $k_{rxn,j}$ is an Arrhenius-form rate constant, n is the apparent reaction order, and $P_{j,S}$ is the partial pressure of gaseous reactant j with at the external particle surface. The n^{th} -order approach has the advantage of being mathematically simple, with only the reaction order and the two Arrhenius rate parameters to fit to experimental data. Intuitively useful descriptions of reaction behavior such as the three-zone theory (Figure 2.6) come from the n^{th} -order model. When the reaction order is assumed to be unity, only two fitted parameters are required and a closed-form solution can be used for the reactant surface partial pressure (Goetz et al., 1982; Ma and Mitchell, 2009). More sophisticated n^{th} -order models account for internal surface area and may use effectiveness

factors and pore development models (Mitchell, 2000; Sun and Hurt, 2000; Roberts et al., 2010). The apparent reaction order n should not be confused with the intrinsic reaction order, which is denoted as m in this work (Figure 2.6). Likewise, the Arrhenius rate parameters used in the n^{th} -order approach should be fit to data from the same temperature zone where the model is to be applied. This means that the apparent activation energy E_a is not the same as the true activation energy E_{true} , except in Zone I (refer to Figure 2.6).

Multi-step reaction mechanisms allow reaction rates to be accurately calculated over a greater range of experimental conditions, including temperature, total pressure, and partial pressures of reactants. Elementary-step mechanisms offer the most rigorous approach, but they are often mathematically cumbersome to implement in practical codes. They usually involve a large number of rate parameters to fit to experimental data. A proposed mechanism for CO₂ gasification is (Ergun, 1956):



In this mechanism, C_{fas} is a carbon free active site. Other authors have proposed mechanisms with at least one additional reaction (Gadsby et al., 1948). A Langmuir-Hinshelwood (L-H) rate expression based on these reactions is (Roberts and Harris, 2006):

$$R_{CO_2} = \frac{k_1 P_{CO_2}}{1 + \frac{k_1}{k_3} P_{CO_2} + \frac{k_2}{k_3} P_{CO}} \quad (\text{2.6})$$

where P is the partial pressure of each species at the surface where the reaction occurs and Elementary Reaction 2 is the rate-limiting step. The L-H form allows Equation 2.6 to predict CO inhibition, which is not possible when traditional n^{th} -order rate models are used. The effect of

CO inhibition for 500 μm carbonaceous particles (coconut charcoal, graphite, and metallurgical coke) has been found to decrease with increasing temperature (Figure 2.8). The observed reaction order was found to change from 0.5 in pure CO_2 to 1.0 for mixtures containing more than 10% CO at a fixed partial pressure (Turkdogan and Vinters, 1970). It was shown that this phenomenon could be explained in terms of a two-step mechanism involving dissociation of CO_2 and formation of CO.

Elementary Reactions 1 and 2 have been used to explain apparent shifts in reaction order with changes in CO_2 partial pressure (Roberts and Harris, 2000, 2006). As CO_2 partial pressure increases, the char surface becomes more saturated with $C(O)$ complexes, which increases the rate and hence the apparent reaction order. Observations of this effect have been most pronounced for partial pressures in the range of 1 to 10 atm CO_2 , where the reaction order increased from 0.5 to 0.7 for the coals investigated (Roberts and Harris, 2000). As the CO_2 partial pressure continues to increase, the surface becomes saturated with $C(O)$ complexes, so the rate becomes insensitive to further increases in partial pressure. At CO_2 partial pressures above 20 atm, reaction orders have been observed to decrease to nearly zero (Roberts and Harris, 2000). Similar trends in apparent order with reactant partial pressure have been observed for H_2O gasification (Mühlen et al., 1985; Roberts and Harris, 2000). Gasification rates in pure H_2O and CO_2 at moderate temperatures increased rapidly with increasing partial pressure up to ~ 10 atm, with little increase at higher pressures, as shown in Figure 2.7 (Mühlen et al., 1985).

There is no strong experimental evidence or theory supporting a significant effect of total pressure on intrinsic reaction kinetics. Effects of total pressure on observed gasification rates at high temperatures have been attributed to the effect of pressure on transport processes (Roberts et al., 2000). The most significant effect of pressure on observed reaction rates in Zone II is

through the physical (and perhaps chemical) structures formed during pyrolysis. The relative contributions of molecular diffusivity (which is inversely proportional to pressure) vs. Knudsen diffusivity (which is independent of pressure) to the effective diffusivity in the porous char determine whether total pressure has a significant effect on observed reaction rates at high temperatures (Hong et al., 2000a; Roberts et al., 2010).

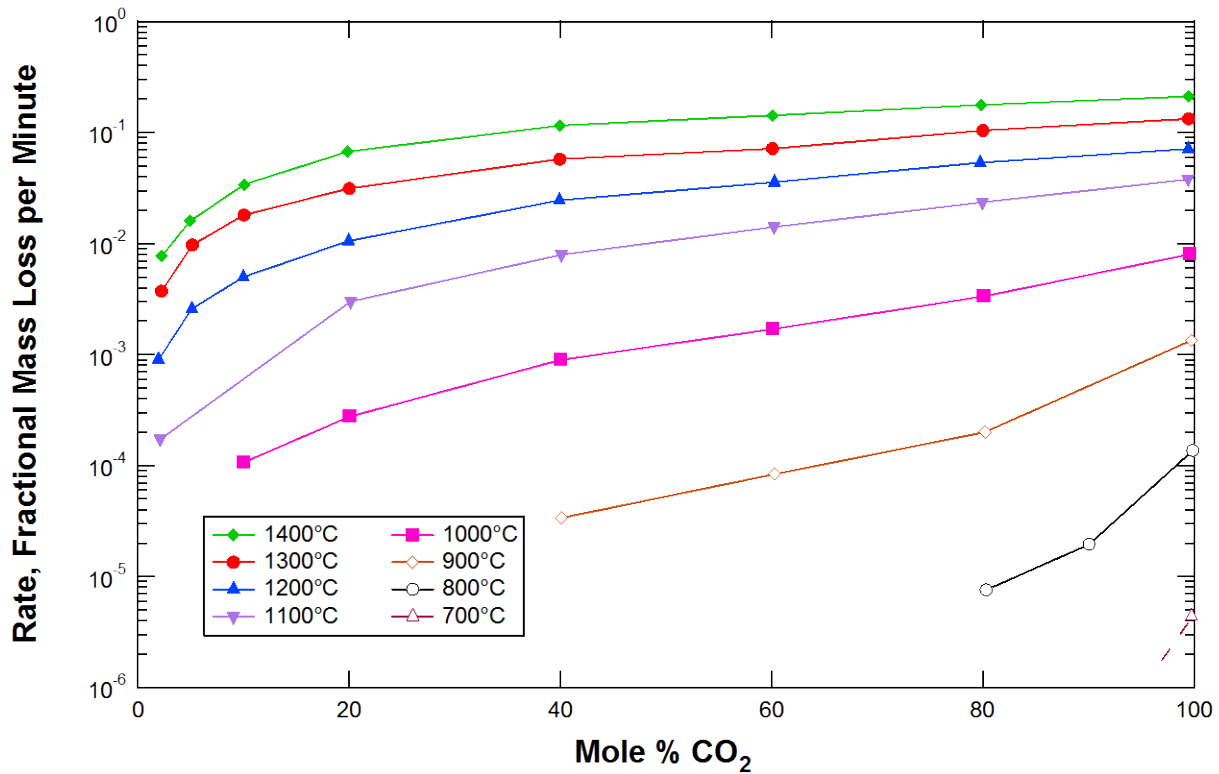
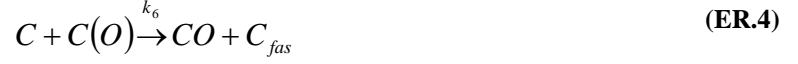


Figure 2.8. Effect of temperature and gas composition on gasification rates for 500 μm metallurgical coke in mixtures of CO_2 and CO at 0.96 atm total pressure (Turkdogan and Vinters, 1970).

Mechanisms with several variations have been proposed for H_2O gasification. One such mechanism for H_2O gasification is (Liu et al., 2010):





With Elementary Reaction 4 as the rate-determining step (Roberts and Harris, 2006; Liu et al., 2010), the resulting L-H rate expression is:

$$R_{H_2O} = \frac{k_4 P_{H_2O} + k_8 P_{CO_2}}{1 + \frac{k_4}{k_6} P_{H_2O} + \frac{k_5}{k_6} P_{H_2} + \frac{k_7}{k_6} P_{CO} + \frac{k_8}{k_6} P_{CO_2}} \quad (2.7)$$

In Equation 2.7, both CO and H₂ inhibit steam gasification. Other derivations omit Elementary Reaction 5, and hence exhibit no inhibition of steam gasification by CO (Roberts and Harris, 2000, 2006). In alternate proposed mechanisms, Elementary Reaction 3 is not reversible and an extra step forming a hydrogen surface complex is included. Depending on whether H₂ adsorption is dissociative, H₂ inhibition may have a different form (Roberts and Harris, 2006; Liu et al., 2010). Larger rate expressions with quadratic and mixed partial pressure terms in the numerator have been derived by including more reactions with the C(O) complex (Mühlen et al., 1985).

Langmuir-Hinshelwood expressions like Equations 2.6 and 2.7 are sometimes needed to model experimentally observed inhibition effects. For example, L-H kinetics have been used to show that CO₂ inhibits H₂O gasification by competing for surface sites (Roberts and Harris, 2007). This means that char in the presence of H₂O and CO₂ reacts at a rate intermediate between the rates observed with the pure gaseous reactants at the same partial pressures. Other investigators have shown that the effect of H₂ inhibition on H₂O gasification is not as strong as inhibition of CO₂ gasification by CO, as shown in Figure 2.9 (Mühlen et al., 1985).

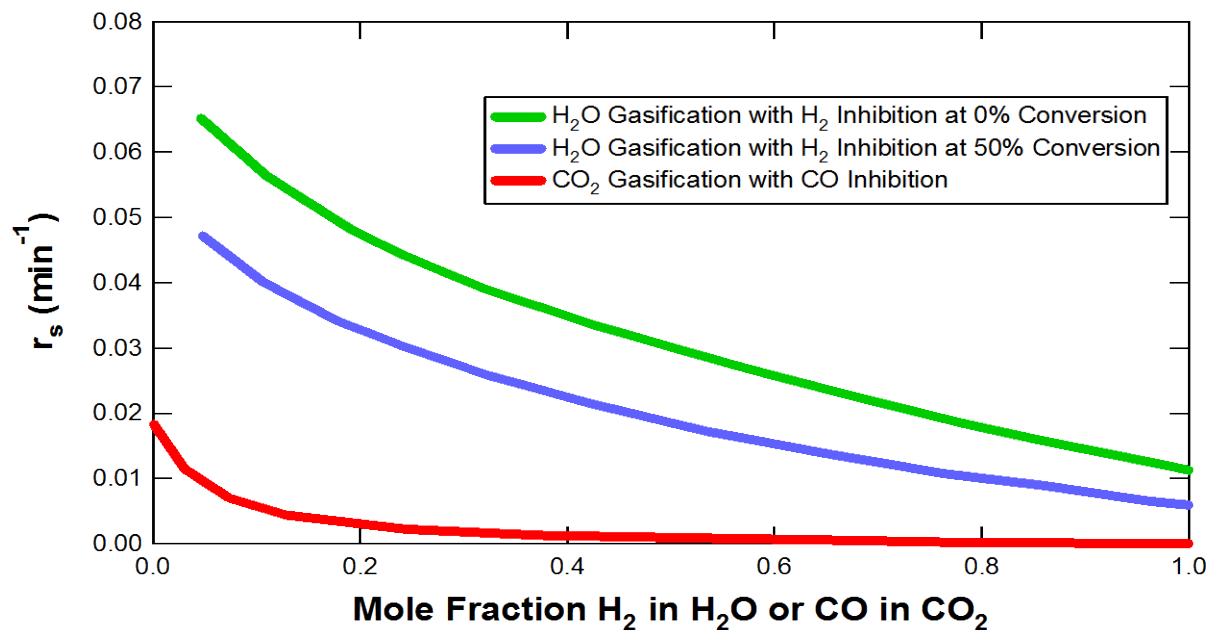


Figure 2.9. Inhibited gasification rates at 900°C and 40 bar (Mühlen et al., 1985).

Depending on the experimentally available range of conditions and the degree to which mass transport limitations are known, obtaining a statistically significant fit of all parameters in an elementary-step mechanism may not be practical. This is especially true for highly heterogeneous systems, (i.e. coal). Semi-global reaction models are sometimes used as a tractable compromise between the purely empirical n^{th} -order models and elementary-step reaction mechanisms (Hurt and Calo, 2001; Liu and Niksa, 2004).

2.4.4 Advanced CBK Combustion and Gasification Models

The Carbon Burnout Kinetics (CBK) model has been used to interpret research data and model industrial applications for more than a decade (Hurt et al., 1998). It is recognized as one of the most advanced combustion models available. The original version and several of the successor models were developed by Robert Hurt's research group at Sandia National

Laboratories and later at Brown University. The distinctive feature of the CBK model is that it allows experimentally observed low rates in late burnout to be modeled. As originally formulated when published as CBK6, the code had 4 essential features (Hurt et al., 1998):

1. A single-film char oxidation model
2. Preferential consumption of the most reactive material through statistical kinetics
3. Thermal deactivation through an annealing mechanism
4. Altered transport of energy and reactant species within char particles through ash inhibition mechanisms

The expressions for the reactant mass transfer coefficient $k_{D,i}$ and the rate of mass transfer in the boundary layer q_i , in CBK are (Mitchell, 1991; Hurt et al., 1998):

$$k_{D,i} = \frac{ShD_{i,mix}\theta_{af}^{2.5}d_p}{R_g T_m \nu_i (Sh\delta_f d_c + \theta_{af}^{2.5} d_c^2)} \quad (2.8)$$

$$q_i = \frac{k_{D,i}P}{\gamma_i} \ln \left(\frac{1 - \gamma_i \frac{P_{i,S}}{P}}{1 - \gamma_i \frac{P_{i,\infty}}{P}} \right) \quad (2.9)$$

where $Sh = 2$ is the Sherwood number, d_p is the particle diameter, R_g is the gas constant, T_m is film temperature (the mean of bulk gas and particle temperatures), and ν_i is a stoichiometric coefficient relating the moles of reactant i (O_2 for oxidation) transferred to the mass of char reacted. The parameter θ_{af} is the porosity of the ash film, d_f is the thickness of the ash film, and d_c is the diameter of the carbonaceous core within the ash film. These terms account for the effect of an ash film on mass transfer rates through the boundary layer. P is the total pressure and $P_{i,S}$ and $P_{i,\infty}$ are the partial pressures of reactant i at the external particle surface and in the bulk,

respectively. γ_i is an expansion factor defined by the stoichiometry of the reaction that allows this formulation to account for Stefan flow.

The CBK model has been adapted for different purposes over the years. The different versions have different features that are summarized in Table 2.4. CBK6 was first modified to include an effectiveness factor and Langmuir kinetics at BYU (Hong et al., 2000b; Hong et al., 2000a). These features allowed the resulting HP-CBK code to fit oxidation rate data at elevated pressures. The Langmuir kinetic form yielded a better fit of experimental data over a larger range of particle temperatures and oxygen partial pressures compared to nth-order kinetics. The corresponding effectiveness factor was derived to correct the reaction rate for intra-particle variation in oxygen concentration (Bischoff, 1965). Under the conditions investigated, the Langmuir rate expression reduced to an intrinsic order of $m = 0$, which implies an apparent order of $n = 0.5$ in Zone II.

Table 2.4. Summary of differences between versions of the CBK model

Name and Publication	Statistical Kinetics Option	Effective Diffusivity Model	Char Structure Model	Kinetic Mechanism
CBK6 (Hurt et al., 1998)	Yes	None	No	N^{th} -order oxidation
HP-CBK (Hong et al., 2000a)	Yes	Random pore model	No	Langmuir oxidation
CBK8 (Sun and Hurt, 2000)	No	Parallel path pore model	No	N^{th} -order oxidation
(Benfell et al., 2000)	Unknown	Unknown	Yes	N^{th} -order oxidation
(Clove et al., 2003)	No	Parallel path pore model	Yes	N^{th} -order oxidation
CBK/E (Niksa et al., 2003)	No	Parallel path pore model	No	3-step Langmuir-Hinshelwood (L-H) oxidation
CBK/G (Liu and Niksa, 2004)	No	Parallel path pore model	No	3-step L-H oxidation, 5-step L-H gasification

Effectiveness factors are correlated with a Thiele modulus, which requires calculation of an effective diffusivity of reactant species through the porous char. A random pore model (Wakao

and Smith, 1962; Wakao and Smith, 1964) was used in the HP-CBK model (Hong et al., 2000a) to calculate the effective diffusivity. This random pore model requires 4 experimentally measured input parameters, including total porosity, macroporosity, average micropore radius, and average macropore radius. However, the microporosity was found to make negligible contributions to the effective diffusivity under the conditions investigated (Hong et al., 2000a), and the Knudsen diffusivity made a negligible contribution to the effective diffusivity in macropores. This result implies that only the macroporosity and macropore radius terms would be required as inputs in a simplified diffusivity model. However, other investigators have shown that Knudsen diffusion may be more important for gasification than it is for the much faster oxidation reactions (Roberts et al., 2010).

Regardless of the pore model used, the effective diffusivity is properly calculated from the combined diffusivity $D_{i,comb}$, which is defined as:

$$D_{i,comb} = \frac{1}{\frac{1}{D_{i,mix}} + \frac{1}{D_K}} \quad (2.10)$$

where the Knudsen diffusivity D_K is proportional to the diameter of the pores through which the gasification reactant is diffusing. $D_{i,mix}$ is the molecular diffusivity of reactant i in the gas mixture. The molecular diffusivity is inversely proportional to total pressure, and the Knudsen diffusivity is independent of pressure, so the relative importance of the two diffusivities largely determine the effect of total pressure on gasification rates for a given char structure. Knudsen diffusion was neglected in all of the CBK codes except HP-CBK (Hong et al., 2000a).

Another modified version of CBK added pressure effects and a simplified char morphology model (Benfell et al., 2000). This Australian version included a correlation for the number percent of char cenospheres based on drop-tube furnace experiments. The char structural

sub-model calculates the diffusion rate of oxygen into the interior void(s) and treats the burning rate of the cenosphere as the sum of the burning rate on the interior and exterior surfaces. When compared to drop-tube data, the char structural model yields a slight improvement in total burnout predictions vs. residence time for the range of 60-90% burnout at 15 atm. In recent years other attempts have been made to model the effects of char morphology on gasification behavior using a modified version of CBK (Cloke et al., 2003) and other advanced models (Ma and Mitchell, 2009; Hodge et al., 2010).

The most widely accepted version of the CBK model in the coal combustion industry is CBK8 (Sun and Hurt, 2000). CBK8 differs from CBK6 in two important respects. First, the calculation of interactions between transport effects and surface reactions was upgraded. The most significant upgrade is an effectiveness factor based on nth-order kinetics, which allows explicit calculation of all three combustion zones and the inter-zone transition regions (Smoot and Smith, 1985). The effect of an ash film on heat transfer was also included. The second major difference between CBK8 and CBK6 is the omission of the statistical kinetic mechanism in CBK8. Preferential consumption of the most reactive char has a strong theoretical and experimental background (Hurt et al., 1996), but implementation was found to be computationally cumbersome and unnecessary in this model. The explicit calculation of reaction behavior in all three combustion zones allows CBK8 to give reasonable results even for atmospheric TGA data.

CBK8 and all later versions of CBK use a parallel-path pore model for the effective diffusivity, neglecting the effect of microporosity and Knudsen diffusion (Wheeler, 1951; Carberry, 1962). The tortuosity parameter was combined with the fraction of the porosity in the feeder pores (macropores) and assigned a uniform value for all coals. This modeling approach

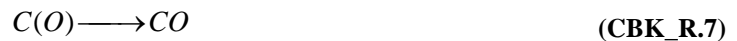
was found to be successful in practice and has the convenient advantage of eliminating the need for experimental measurements of surface area.

The most mechanistic CBK model used exclusively for oxidation is CBK/E (Niksa et al., 2003). CBK/E was developed from CBK8 using three-step semi-global kinetics to describe experimentally observed changes in reaction order (Hurt and Calo, 2001). The three-step mechanism is:



CBK/E also included an optional swelling correlation (Niksa et al., 2003) that dates back at least as far as CBK8, but was upgraded to include pressure effects based on drop-tube measurements. The simple pressure term came from experiments with Australian bituminous coals (Benfell, 2001). The CBK swelling correlation did not consider effects of heating rate.

The next version of CBK to be developed was CBK/G (Liu and Niksa, 2004). This version was an upgrade of CBK/E for gasification. Five reaction steps were added to account for gasification by H_2O , CO_2 , and H_2 . These steps are:



In the complete eight-step mechanism, Reactions 3, 5, and 7 all represent desorption of CO from a surface complex. The surface oxides produced in heterogeneous reactions with O₂, H₂O, and CO₂ are treated as chemically distinct from each other in this semi-global model. This approach was considered necessary to model observed differences in experimental desorption rates (Liu and Niksa, 2004). The gasification rate constants were written as ratios of the CO-desorption rate constant from the H₂O-gasification mechanism (k_7) to simplify the process of fitting gasification rate data. These ratios of rate constants were correlated with coal composition, leaving only a single adjustable pre-exponential factor. The annealing sub-model was applied to reduce the pre-exponential factor of Reaction 7 (A_7) as gasification proceeds so that all reaction rates decrease simultaneously. A similar strategy was used in CBK/E to scale all reactions with the pre-exponential factor of step 3.

A random pore model was included in CBK/G to account for development of surface area during reaction; this approach allowed for a better fit of fluidized bed data, but was not expected to be as important for gasification at the higher temperatures occurring in a pulverized coal gasifiers (Liu and Niksa, 2004). The expression for surface area used in the CBK/G publication was incomplete. The complete form is (Bhatia and Perlmutter, 1980; Gavalas, 1980; Bhatia and Perlmutter, 1981):

$$f_{RPM} = (1 - X) \sqrt{1 - \psi_0 \ln(1 - X)} \quad (2.11)$$

where X is the fractional carbon conversion and ψ_0 is an empirical structural parameter, which was assigned an average value of 4.6 in CBK/G (Liu and Niksa, 2004).

In CBK/G, the value of the mode-of-burning parameter α was changed from an average experimental value of 0.2 (Hurt et al., 1998) to a theoretical value of 0.95 (Essenhigh, 1994; Liu and Niksa, 2004). Transport of all gaseous reactants from the bulk to the surface of the particle

was included. Separate effectiveness factors were used for each gaseous reactant to account for internal concentration gradients. The effectiveness factor for H₂ gasification was assigned a value of unity due to the very low rate of Reaction 8.

2.5 Summary

The understanding of the chemical changes that occur during primary pyrolysis is sufficiently advanced to allow prediction of devolatilization rates and yields of char, tar, and light gas species via network devolatilization models. These models can also predict effects of coal rank, temperature, heating rate, and pressure on pyrolysis behavior. However, coal particles of many ranks also undergo swelling due to bubble formation in the metaplast. Attempts have been made to describe the changes in particle size and physical structure via mechanistic swelling models. Limited success has been achieved in predicting the effects of pressure on swelling of bituminous coals, but existing models cannot make quantitative predictions of the effects of coal rank, pressure and especially heating rate on the swelling ratio. An accurate swelling model that has been calibrated with high-pressure, high-heating rate experimental data is needed to accurately predict gasification rates in advanced CFD-based gasifier design codes.

Low-temperature gasification data are fairly common, but it is difficult to extrapolate Zone I rates to Zone II because of the complex interactions between the many phenomena involved. Chars produced at low heating rates and pressures have different physical structures from chars found in industrial pulverized-coal gasifiers. Hence, much of the limited Zone II gasification data that are available may yield gasification rates that are not applicable to industrial conditions. Experiments that quantify effects of pressure and complex gas compositions on gasification rates of industrially representative chars are also needed.

A variety of combustion and gasification models with different advanced features have been developed in recent years. Prominent among these are the CBK models, some of which have gained wide acceptance in the combustion industry. The only version of CBK that has been developed for gasification is CBK/G, which has not been distributed for in-depth evaluation and general use. A model with features comparable to CBK/G is needed to enable more detailed analysis of experimentally observed gasification behavior and allow accurate prediction of gasification rates over a wide variety of conditions.

CHAPTER 3. OBJECTIVES

The objective of this work was to characterize coal pyrolysis and gasification behavior at elevated pressures, temperatures, and heating rates that are more representative of industrial entrained-flow gasifiers than has been typical in laboratory settings. The ultimate goal was to improve gasification modeling capabilities. The results of this work will be useful in characterizing the performance of existing gasifiers and evaluating alternative features in new gasifier designs. The design process for other coal conversion systems such as utility boilers will also benefit from the results of this work. This project is divided into the following tasks:

1. *Develop an improved high-pressure flat-flame burner to enable studies of coal pyrolysis and gasification at industrially-relevant conditions.* Due to its nature as a large, custom-built pressure vessel, the previously developed high-pressure flat-flame burner (HPFFB) facility (Zeng, 2005) was found to be in violation of state pressure vessel regulations. Since the previous HPFFB was a retrofitted drop-tube furnace (Monson, 1992), there were also many features that were not optimal for the intended gasification studies. The new HPFFB was designed to operate at high heating rates with an enhanced range of temperatures and improved reliability and safety. Operation of the HPFFB was simplified and characterization procedures were improved.

2. *Produce chars from coals at high heating rates and elevated pressures to characterize coal swelling during pyrolysis.* Swelling was characterized for one bituminous coal as a function of heating rate in an atmospheric flat-flame burner (FFB). Swelling was measured initially for 3 bituminous coals and 1 subbituminous coal at 4 pressures from 2.5 atm to 15 atm under reducing conditions in the HPFFB at $\sim 10^5$ K/s. Subsequently, swelling was measured for 4 bituminous coals and 1 subbituminous coal at 3 pressures from 5 atm to 15 atm in the HPFFB under slightly oxidizing conditions to eliminate soot contamination. The latter experiments were supplemented with experiments in the atmospheric FFB, yielding a total of 4 pressures.
3. *Develop a coal swelling model that can predict effects of coal rank, heating rate, and pressure.* The empirical swelling model was calibrated with atmospheric swelling data from Sandia National Laboratories and pressurized swelling data from this work (see Task 2). NMR parameters describing the chemical structure of the coal were used to correlate rank effects. The use of an existing correlation for the NMR parameters (Genetti et al., 1999) limited the required model inputs to the coal ultimate and proximate analyses and the maximum particle heating rate obtained from a transient energy balance.
4. *Measure coal gasification rates at high temperatures with high pyrolysis heating rates and elevated pressures.* The HPFFB was used to gasify 5 coals and also reinjected chars in CO₂ gasification environments at pressures of up to 15 atm and maximum gas temperatures that exceeded 1900 K. Early scoping experiments with a H₂O gasification environment resulted in burner damage and condensation management problems. Therefore, the simpler CO₂ gasification experiments were pursued while safe and reliable operating procedures were developed for the new HPFFB.

5. *Model the experimental gasification rates and correlate them with coal rank.* A simple 1st-order model and two advanced models with different kinetic mechanisms were developed to fit and analyze the CO₂ gasification data from the HPFFB. The resulting kinetic parameters were correlated with char properties that were estimated from the coal properties using correlations for NMR parameters (Genetti et al., 1999).

The development and characterization of a new high-pressure flat-flame burner (HPFFB, Task 1) are discussed in Chapter 4. The coals and experimental procedures used in Tasks 2 and 4 are also documented in Chapter 4. The pyrolysis experiments (Task 2) and the associated swelling model (Task 3) are documented in Chapter 5. The results of the CO₂ gasification experiments (Task 4) are presented in Chapter 6, along with the model development (Task 5) and the associated analysis and correlation of the gasification data. Chapter 7 contains a summary, conclusions, and recommendations for further research.

The appendices contain more extensive tables of the raw pyrolysis and gasification data from Tasks 2 and 4 and characterization of the gasification conditions in the HPFFB. The appendices also contain additional information regarding Task 1 that was not central to the discussion in Chapter 4, including the operating manual for the HPFFB. Thermogravimetric analysis of the HPFFB chars is documented in an appendix because it was not central to the objectives set forth in this chapter. Secondary pyrolysis (soot formation) experiments with coals and coal tar surrogates were initially part of this project. The soot results are documented in an appendix because results were not as productive as had been hoped and because the written dissertation was focused on pyrolysis and gasification to reduce length.

CHAPTER 4. EXPERIMENTAL EQUIPMENT AND PROCEDURES

At the commencement of this work, it was found that the previous version of the BYU high-pressure flat-flame burner (HPFFB) facility (Zeng, 2005) needed to be replaced due to state legal requirements for pressure vessels. The previous facility was a modified version of a pressurized drop-tube furnace designated as the high-pressure, controlled-profile (HPCP) reactor (Monson, 1992; Zeng, 2005). As part of this study, the HPFFB was redesigned and rebuilt to be more suitable for pyrolysis and gasification studies of coal at pressures of up to 15 atm and heating rates of $\sim 10^5$ K/s. Some components of the previous HPFFB were used, especially near the beginning of this work, but significant changes were ultimately made to the facility.

Flat-flame burners consist of an array of tubes that deliver a gaseous fuel to a surface (Figure 4.1). An oxidizer-rich gas is fed through the spaces in between the tubes. The resulting flat flame is ~ 1 mm thick. A larger tube at the center of the array contains coal entrained in a stream of N_2 at solid feed rates of ~ 1 gram/hr or less to ensure single-particle behavior. Coal particles are heated convectively by the post-flame gases at heating rates on the order of 10^5 K/s for particles smaller than ~ 100 μm . These particle heating rates are 2-10 times higher than a more conventional electrically heated drop-tube furnace. Increasing the particle heating rate from 10^4 K/s to 10^5 K/s in this regime has been observed to significantly decrease coal swelling at atmospheric pressure (Gale et al., 1995). The HPFFB facility allows gasification studies to be conducted on chars that have physical structures that are more representative of industrial

gasifiers compared to chars generated at lower pressures and heating rates. The flame stoichiometry can be altered to produce an oxidizing or gasifying environment. Pressure, peak centerline gas temperature (up to 2000 K), post-flame CO₂ and H₂O mole fractions, and residence time are the available experimental variables.

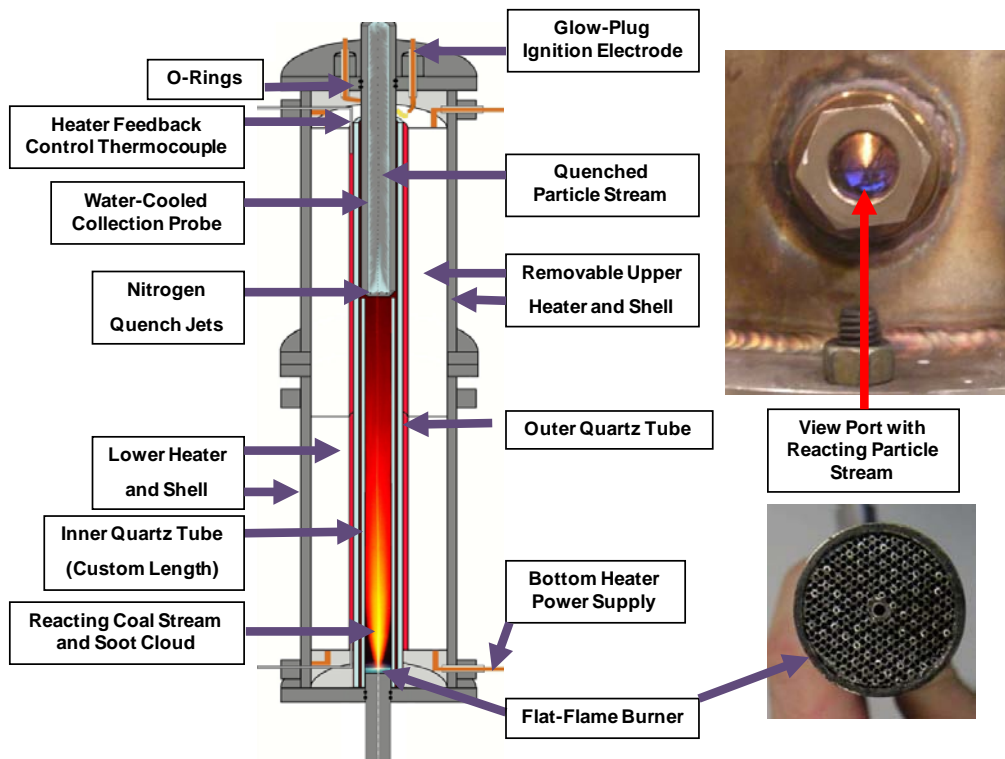


Figure 4.1. HPFFB cross-section illustration (left), burner face (bottom right), and operating burner (top right).

The post-flame gases in the HPFFB flowed through a quartz tube where reactions with coal took place. At the end of the quartz reaction tube there was a water-cooled collection probe that quenched the hot gases and particles with jets of N₂ (Figure 4.1).

The collection probe could be moved up and down on a track system to adjust residence time (up to 800 ms). The burner also had a more limited range of motion that allowed for residence times as low as 30 ms, corresponding to particle collection heights of less than 1 inch.

4.1 Description of HPFFB Features and Development

The previous version of the HPFFB facility included a down-flow burner with a 2-inch diameter (Zeng, 2005). An up-flow burner configuration was chosen for the new HPFFB to reduce wear on the burner and prevent buoyancy effects from disturbing the particle flow. The change to a smaller pressure vessel required that the gas flow path (reaction zone) be slightly reduced in diameter. The flow path was enclosed by a tube of fused quartz. The 2-inch burner was used in the earliest experiments in this study, but a 1-inch diameter burner was used for the bulk of the experiments (Appendix B).

A clamp with a screw and crank system was installed to allow the burner's vertical position to be changed during operation (Figure 4.2). The 1-inch burner was designed to slide freely within the quartz tube. The burner's maximum useful range of motion inside the vessel was ~3 inches. In practice the burner was only moved to achieve residence times of less than ~100 ms. For longer residence times the burner was placed well below the heaters (0.5 inch below the low-temperature heaters or 2 inches below the new high-temperature heaters) to maintain visibility of the coal stream and to avoid damaging the burner. The new clamp system also allowed a single person to remove the burner from the vessel for inspection and cleaning in a matter of seconds. The equivalent task took several minutes and required 2-3 people when the large burner was in use, and the risk of breaking quartz tubing was much greater.

Using the 1" burner required changes in the flow path of the reaction zone. It was found that reducing the ID of the quartz tube from 1.75 inches to 1 inch made collection of the coal and soot particles more efficient because the flow path was a better match for the 3/4-inch ID collection probe. The disadvantage of this design change was that the collection probe would no longer fit inside the quartz reactor tube. A fixed length of quartz was required for each

experimental residence time. The collection probe was lowered until it nearly touched the quartz (~0.125 inch clearance).

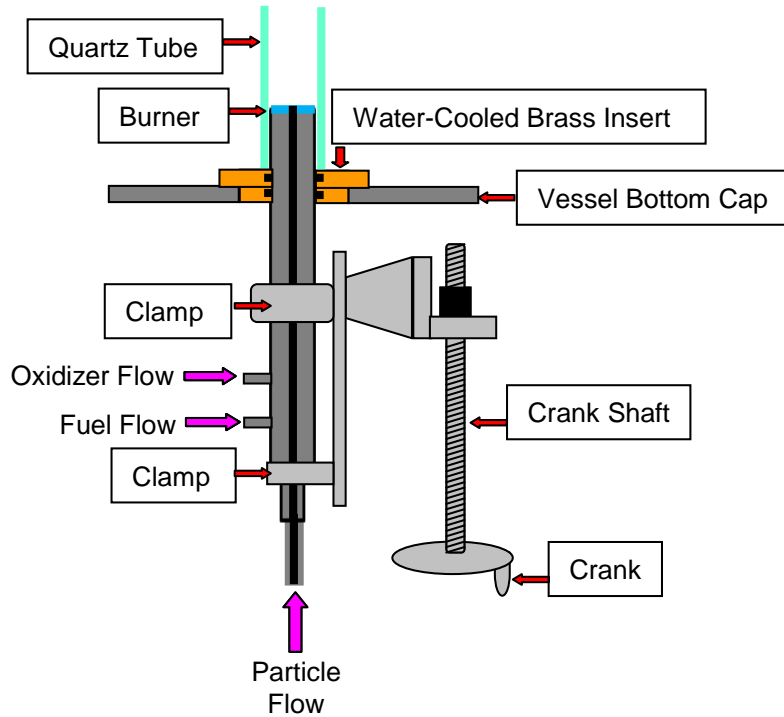


Figure 4.2. Moveable clamp system and water-cooled fitting for the 1-inch flat-flame burner.

The HPFFB vessel design is illustrated in Figure 4.3 with the associated dimensions included. The stainless steel shell was built with an ID of 6 inches to make it exempt from future regulatory problems. The top and bottom caps were both secured using 12 equally spaced bolts on an 8.5-inch diameter circle. This design was adopted to allow operation at pressures of up to 30 atm, but other components of the system limited the safe operating pressure to 15 atm. Two stackable vessel sections were built to allow extended residence times, as shown in Figures 4.1 and 4.3. However, the top vessel extension section was not put into service because of large heat losses experienced at extended residence times.

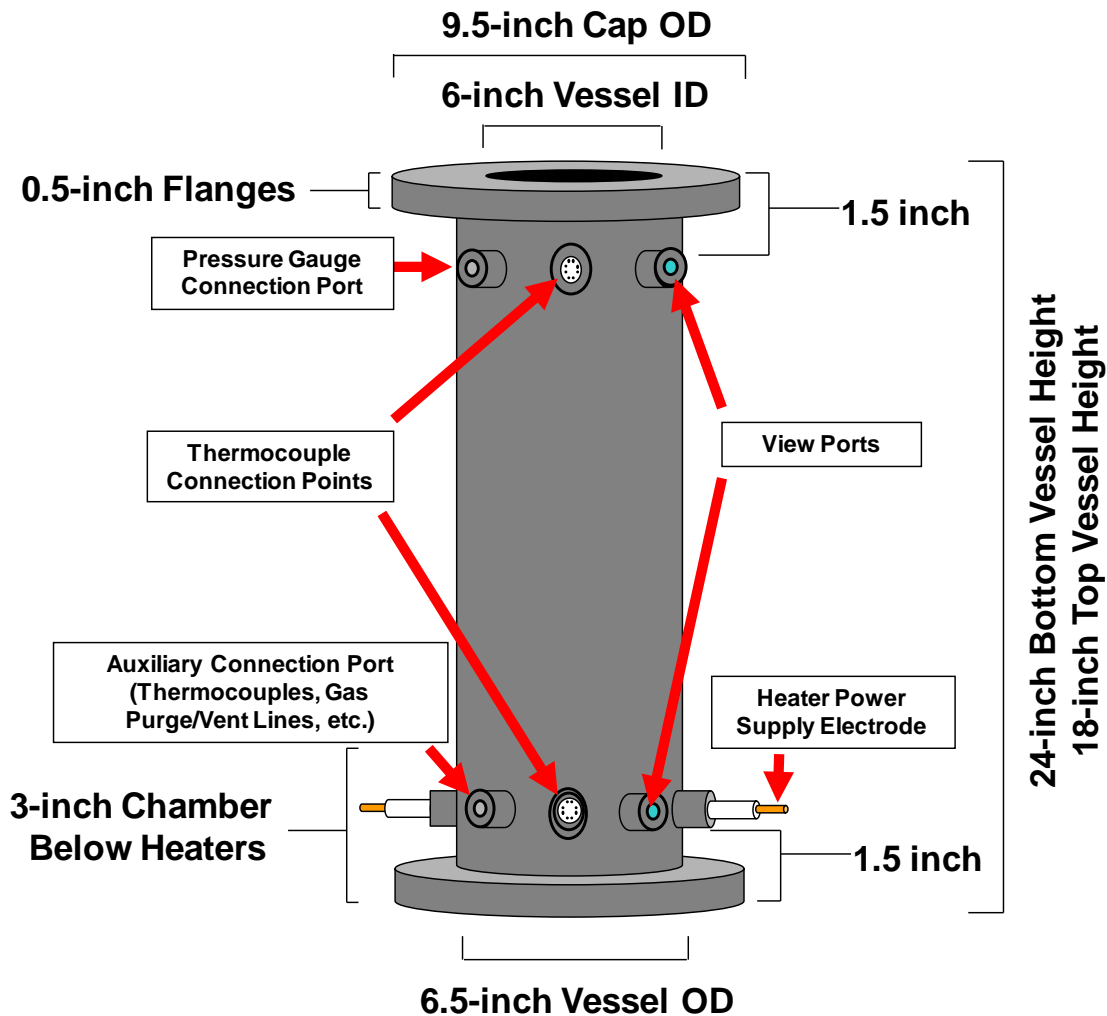


Figure 4.3. Illustration of stainless steel HPFFB pressure vessel with dimensions.

In the new HPFFB, the reacting particle stream and the associated soot cloud were visible through a view port near the bottom of the vessel that was rated at 260°C (Figure 4.1). The view port was mounted in 1 of 4 NPT (0.5-inch) fittings in the lower vessel wall (Figure 4.3). The projecting NPT fittings acted as fins; they protected windows and instrumentation through local convective cooling. The lower view port allowed for verification of proper particle feeding and limited measurements of optical particle velocities. An identical window installed in 1 of the 3 NPT fittings near the top of the vessel allowed ignition to be monitored (Figure 4.3).

The aerodynamic product separation system is illustrated in Figure 4.4. Soot was separated from char in a virtual impactor and a cyclone, which were taken from the previous facility (Daines, 1990; Monson, 1992; Zeng, 2005). Tar and soot were collected on polycarbonate filters.

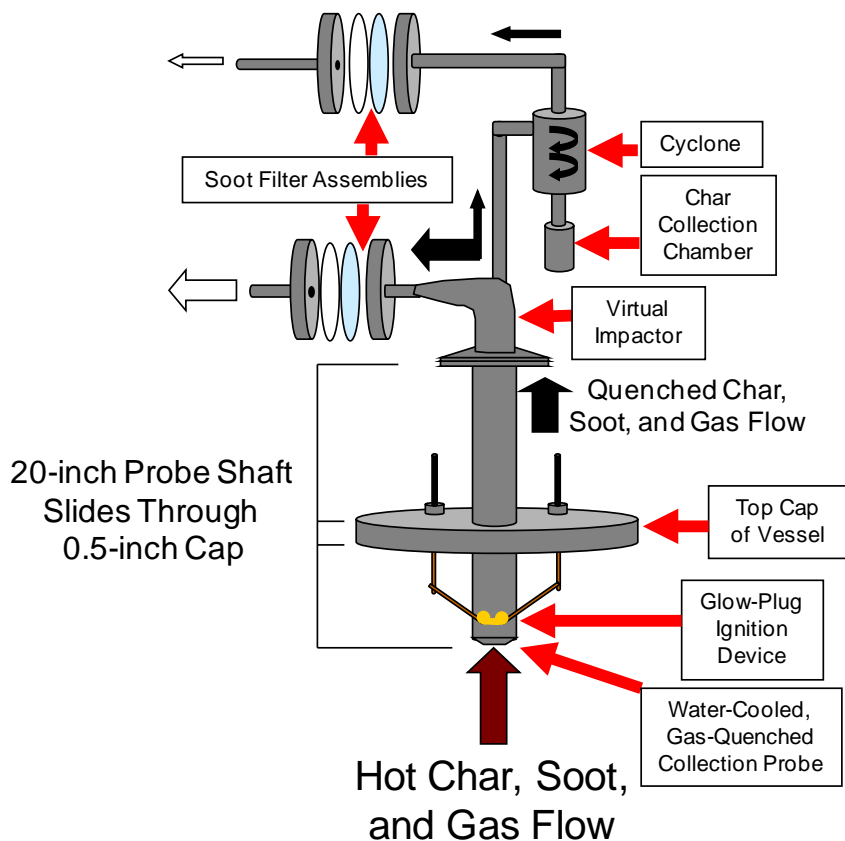


Figure 4.4. Collection probe with aerodynamic separation system for char and soot collection.

Tar/soot yields were determined by weighing the filters, which could then be scraped to recover the tar/soot samples. High static on the filters often prevented accurate weights from being measured. In these cases, the tar/soot was weighed after scraping. The collection system was designed so that the filtered gases could be collected and analyzed for composition. Char

and soot were analyzed separately. The average change in particle mass was determined by a direct mass balance and also by ash and/or elemental tracer techniques for regression of gasification kinetic parameters. The average change in particle size was calculated from the measured changes in mass and bulk density, with the assumption that the particle shape did not change enough to alter the packing factor.

4.1.1 Coal Feeding System

Calculations of settling velocity revealed that a gas velocity of 0.18-0.26 m/s was required to entrain the coal particles with diameters of 100 μm at pressures of 2.5 to 15 atm (Appendix C). Since the gas density was proportional to the pressure, a higher mass flow rate of N_2 was needed at higher pressures to maintain this velocity. Using excess N_2 was considered undesirable because it reduced the heating rate and maximum temperature of the coal particles.

In the upgraded HPFFB with the 1-inch burner the coal entrainment tube was removable and had an internal diameter of 0.041 inch and an outer diameter of 0.0625 inch. This tube size was selected because it was large enough to prevent frequent clogging and was small enough to allow a low flow of N_2 to be used for entrainment. At the bottom of the burner system, the coal entrainment tube was encased in a protective outer sheath of 0.125-inch OD stainless steel tubing, as illustrated in Figure 4.5. This sheath extended back to the coal feeder and was sealed to the feeder tube at both ends with epoxy resin to direct flow into the coal entrainment channel rather than the sheath annulus. Compression fittings on the outer sheath provided a secure pressure seal to the coal feeder and the burner. The use of a double-walled entrainment tube protected the smaller tube from accidental bending and also prevented constriction of the flow path by the compression fittings.

The new pressurized coal feeder shown in Figure 4.5 was based on the one used in the BYU atmospheric flat-flame burner (Ma, 1996). This syringe-type coal feeder was designed and built in collaboration with Aaron Lewis, who described it in detail (Lewis, 2011). Software was written in Visual Basic to allow a desktop computer to drive the stepper motor using a parallel port connection (see Appendix D). The particle feeder from the previous facility (Monson, 1992) caused frequent clogging of the coal entrainment tube when used with the new HPFFB; the reliability of particle feeding was significantly enhanced through the use of the new particle feeder. Experiments that used to take several days with the old particle feeder could be accomplished in a few hours with the new feeder. This new feed system made it possible to perform multiple experiments and obtain several hundred milligrams of char in a single day. Feeding efficiency was increased by adding an extra o-ring to the plunger slightly behind the particle bed to prevent char or coal from falling into the annular space around the plunger. This change made reinjection of char practical.

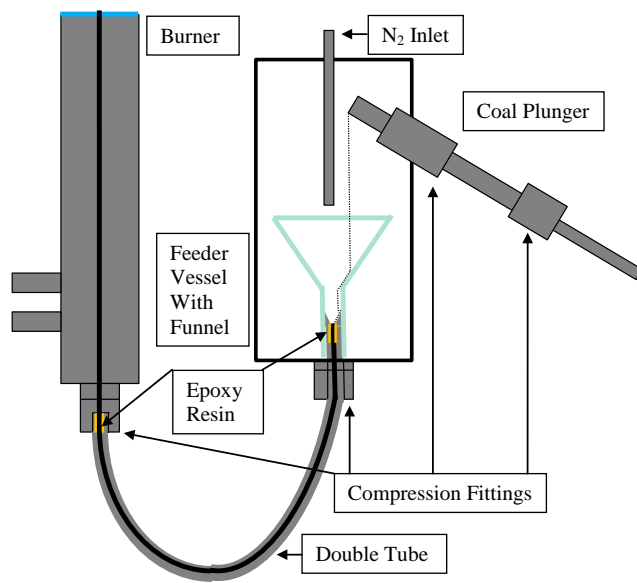


Figure 4.5. Illustration of HPFFB coal feeder system, excluding vibrators on coal plunger and feeder tube.

4.1.2 Nichrome Wire Heaters

The HPFFB used supplemental heaters to maintain high gas temperatures for longer residence times (Figure 4.1). Without the use of heaters, the centerline gas temperature was found to peak at slightly less than 1 inch above the burner and then decay several hundred degrees in just a few inches.

The heaters installed initially used Nichrome wire heating elements, with a maximum operating temperature of 1200°C. These heaters had the advantage of being very robust; they were subjected to frequent rapid thermal cycling with no signs of damage due to thermal shock. The insulators associated with these heaters were not very effective at high pressures. At 5 atm the temperature in the reaction zone decreased by 300-400 K to a nearly constant value over a distance of 3-4 inches after the peak. At 15 atm the magnitude of the decrease in temperature over the first few inches was at least 100 K greater. According to corresponding states theory, the thermal conductivities of the gas species present were not strong functions of pressure in the range of the HPFFB operating pressures (Bird et al., 2002). The enhanced heat loss at high pressures may have been caused by enhanced free convection within the vessel, and perhaps even through the fibrous insulators.

4.1.3 Molybdenum Disilicide Heaters

Molybdenum disilicide heating elements were acquired to replace the original heaters in some of the final studies associated with this work. These high-temperature heaters allowed gas temperatures to be maintained at levels of up to 1700°C. Heat losses observed using these heaters and insulators at high pressures were much lower than with the Nichrome wire heaters. Heater set points higher than 1350°C at elevated pressures caused temperatures in excess of 540°C on the inner surface of the vessel wall at pressures of up to 15 atm. Higher pressure vessel wall

temperatures were considered dangerous, and hence, heater set points above 1350°C were not attempted. It was also found that the power leads must be cooled using a small stream of N₂ to avoid damage.

The high-temperature heating units had a total length of 8 inches, compared to 18 inches for the original low-temperature heaters. There was room for a second unit in the vessel if longer residence times were desired. The existing power supply was sufficient for two heaters of either type, but the manufacturers were unsure whether the heater control system would be able to control two high-temperature units effectively. Due to the high cost and safety concerns, only one molybdenum disilicide heater was installed.

The control thermocouples were placed carefully so that the control algorithms were based on the maximum heater temperatures. The molybdenum disilicide heaters were controlled using B-type thermocouples. The thermocouple wires and heater power supply leads penetrated the lower vessel wall by means of pressure-tight insulating fittings. Temperatures in locations other than the surfaces of the high-temperature heaters were measured using K-type thermocouple probes inserted through compression fittings.

The molybdenum disilicide heating elements were vulnerable to thermal shock. Thermal shock to the heating elements was avoided by using temperature ramp-up rates of 30°C/min or less and ramp-down rates of 20°C or less. The heater control system also included an automatic current limiting feature (set to a maximum of 75 amps) to reduce the risk of thermal shock. The manufacturer of the heating elements recommended that they be regenerated periodically by heating to 1450-1600°C in an oxidizing atmosphere for 1 hour. This would cause a protective layer of silica to form on the surface of the elements. It was recommended that this be done near atmospheric pressure, since the vessel shell became very hot at high pressures. However, the first

set of high-temperature heaters used did not last long enough to be treated in this manner due in part to damage that occurred during the initial installation and testing, before a means was devised to cool the power leads.

4.1.4 Quartz Tubing

Thermal shock to the quartz occurred as the water-cooled probe was lowered or raised within the quartz tube, especially when the heaters were turned on. Introducing a flow of ~15 SLPM of N₂ in the lower chamber of the vessel while moving the probe prevented the quartz from breaking. This flow took a tortuous path along the outside and then the inside surfaces of the quartz, which reduced the thermal gradients.

Fused quartz tubing formed a layer of cristobalite when used with heater temperatures above 1200°C. This made the tubes very fragile; the outer tube could not be disturbed without breaking once it was treated in this manner. Slow initial heating of the quartz helped the cristobalite to form more evenly so that it acted as a protective layer. The outer quartz tube (ID of 42 mm, OD of 45 mm and length of 21 inches) provided a layer of electrical insulation between the heating elements and the metal probe. The outer quartz tube also served as a barrier to prevent soot from depositing on the heating elements. The inner quartz tube (ID of 26 mm, OD of 30 mm) had a length that was chosen to correspond to the desired residence time. To avoid crushing the inner quartz tube, the length was chosen to leave a gap of ~0.125 inch between the quartz and the collection probe inlet.

4.1.5 Ignition System

The HPFFB system was pressurized with N₂ before each experiment to allow a leak test to be conducted at the desired operating pressure in the absence of fuels (including toxic CO) and

oxidizers. After the leak test, the desired pressure was maintained while inert flows through the burner were changed to include oxidizers and fuels. The burner gases were then ignited near the top of the vessel, after which the flame dropped to the burner surface. Finally, the probe was lowered to the desired position using a hand crank system.

Several gas ignition systems for the HPFFB were tested. A custom glow-plug system powered by a variable transformer was found to be superior to spark-ignition systems, especially at high pressure (Figure 4.6). Ignition was achieved consistently with the glow plug at pressures of up to 15 atm. Ignition was also achieved using heaters at temperatures above 800°C.

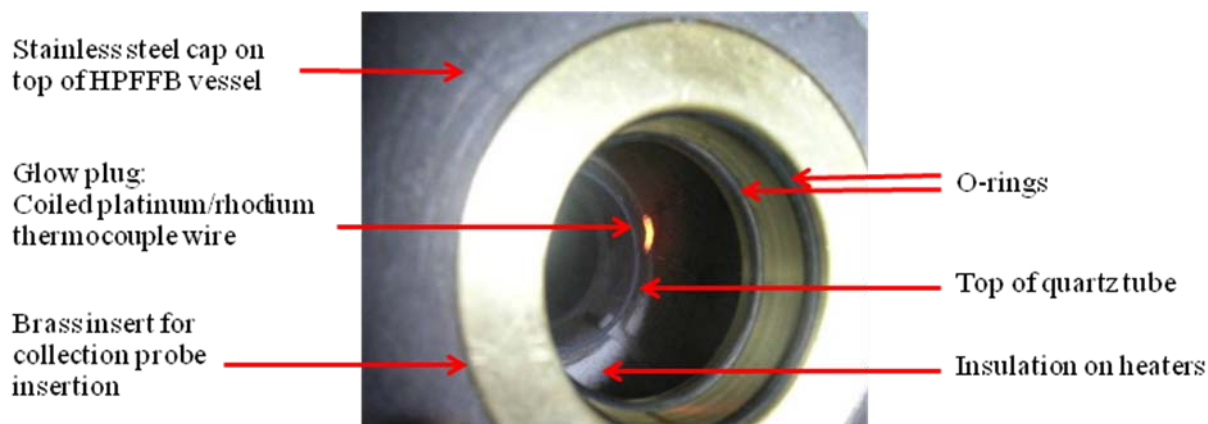


Figure 4.6. Glow plug ignition system and brass insert in top cap of pressure vessel.

Careful management of flame speed (through gas composition and total flow rate) during ignition was found to be very important, especially at high pressures. If the flame speed was too high compared to the gas flow rate then the whole column of gas contained by the quartz tube combusted nearly instantaneously. This event was observed through viewports near the top and bottom of the vessel and caused an audible surge in pressure (~10 psi) that pushed combusted gases upstream into the burner, extinguishing the flame. If the flame speed was too low, then the

flame either extinguished or hovered near the top of the vessel instead of dropping to the burner surface. The ignition event was also sensitive to the initial temperature of the quartz tubing; starting cold was more difficult than restarting a recently extinguished flame.

4.1.6 Quench Probe

The moveable collection probe developed deep scratches that compromised the seal provided by the o-ring in the vessel cap. This was due to similar metals rubbing on each other; the stainless steel surfaces formed and broke bonds as the probe was moved. A brass insert for the cap with double o-rings was built to correct this problem (Figure 4.6). The outer surface of the probe was replaced to remove the scratches. The scratches did not reappear and leaks were no longer detected from the probe during pressure tests. The brass insert contained 2 o-rings that the probe was designed to slide through. The water cooling in the probe itself protected these o-rings from the high temperatures in the vessel. A similar brass insert with its own water cooling system was used to create a pressure seal between the burner and the bottom cap (Figure 4.2).

The inner layer of the collection probe was a porous sintered steel tube, similar to the design used for the BYU atmospheric flat-flame burner (Ma, 1996). N_2 penetrated the walls through the pores and prevented soot from sticking to the shaft. N_2 also entered through jets at the bottom tip to quench reactions in the hot gases and particles entering the probe, as illustrated in Figure 4.1. The first probe design attempted did not quench the hot gases effectively. Design modifications to the HPFFB quench system are documented in Appendix B. In the final version, about 75% of the N_2 supplied to the collection probe passed through the quench jets. When the quench flow rate was set to twice the burner volumetric flow rate, the gas temperature dropped ~500 K within 0.25 inch of the probe entrance.

4.2 Product Separation and Collection System

The initial configuration of the piping associated with the product collection system of the new HPFFB was not ideal. Extra valves were installed to allow individual filters to be isolated and replaced without shutting down the system. The char was not separating from the soot because the flow distribution in the virtual impactor was not optimized; flow meters and valves were installed to monitor and control these flows. Ideally, about 25% of the outlet flow would pass through the cyclone, but in practice it was difficult to set the flow so precisely. Cyclone flow rates equivalent to 15% to 35% of the total flow were used.

4.2.1 Char Fragmentation

The virtual impactor and cyclone used in the current HPFFB were taken from the previous version of the facility (Daines, 1990; Monson, 1992; Zeng, 2005). It was found that the char collected in the horizontal cyclone rather than the collection chamber or char trap. Pumping the char into the collection chamber worked well for subbituminous coals, but cenospheres from bituminous coals often shattered, especially at pressures above 10 atm (Figure 4.7).

This fragmentation phenomenon was attributed in part to the accumulation of char in the cyclone; at sufficiently high number densities the particles collided with each other at high velocities. However, most of the shattering was probably due to the high velocities induced by opening a valve between the pressurized cyclone and the atmospheric pressure char trap, where the particles collided with the chamber wall. This fragmentation made it very difficult to determine the original char particle sizes. Moderate improvements in performance were achieved using a design with an elbow between the cyclone and the char trap.

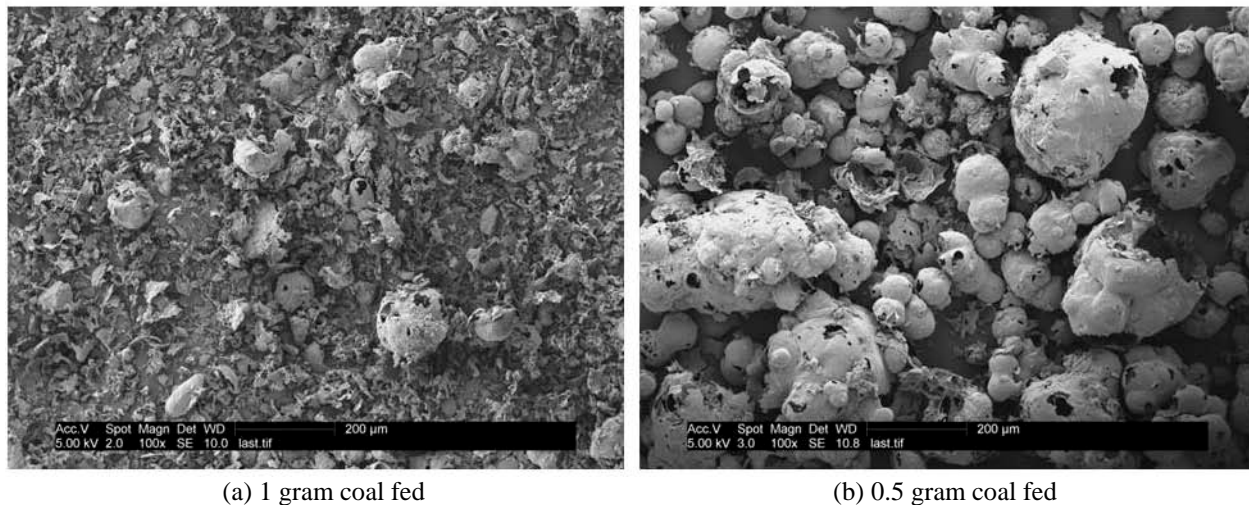


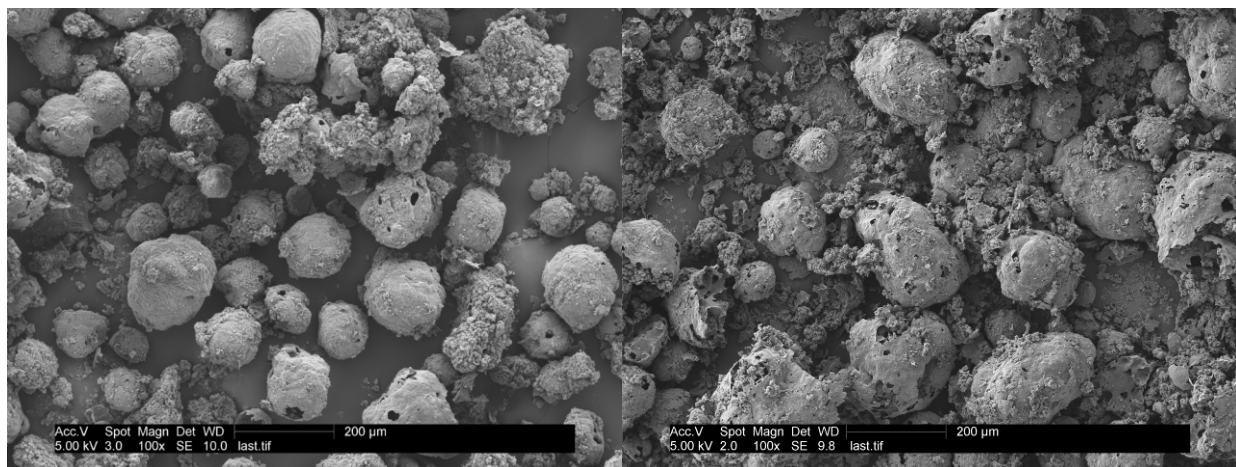
Figure 4.7. SEM images of fragmented EBB char produced at 10 atm, 1722 K, 42 ms.

Two features were added to increase char collection efficiency without breaking the particles. The first was a staged vent system consisting of two valves with a length of pipe and a pressure gauge in between. The staged vent allowed the char trap to be partially depressurized in a controlled manner rather than vented all at once. This feature allowed the char to be pumped from the cyclone to the collection chamber at lower particle velocities. The second was a custom elbow fitting that allowed the cyclone to be mounted in a vertical position with a straight drop into the char trap (Figure 4.4). These upgrades eliminated the char fragmentation problem.

4.2.2 Soot Contamination

Many of the char samples collected were contaminated with large soot particles. SEM images showed that the collection system was unable to separate the very large soot agglomerates from the char (see Figure 4.8). The aerodynamic separation system was designed with a 5 μm diameter cut point, which explained why large soot agglomerates would be collected with char particles. The soot needed to be removed from the char to accurately quantify mass

change via elemental or ash tracer techniques. Also, accurate determination of swelling by the tap density technique was hindered by the presence of large, low density soot agglomerates. Soot contamination increased with increasing temperature and residence time, and was much more pronounced at the highest pressures.



(a) 5 atm, 1867 K, 662 ms

(b) 15 atm, 1918 K, 660 ms

Figure 4.8. SEM images of EBB char. Note that soot (with a fuzzy/clumpy texture compared to char) occurred in very large soot agglomerates and sometimes as a coating on the char particles or as an adhesive that bound char fragments together in clumps.

The primary cause of the increased yield of soot and especially of large soot agglomerates with increasing pressure was the increased molar concentration of tar at elevated pressures. Higher concentrations promoted polymerization of the tar into soot particles. The formation of more primary soot particles at lower residence times promoted the development of larger soot agglomerates.

The very large soot agglomerates collected with the char samples have interesting implications for gasifier design. Because of its high surface area, radiation heat transfer from soot can lower local gas temperatures by up to 300 K (Brown and Fletcher, 1998). In the vicinity of char particles, this would significantly decrease initial gasification rates, increasing the

required reactor size. Thermal radiation from soot may shorten the useful life of coal injectors and other components of gasifiers. Soot is much less reactive than tar. In addition, the agglomeration of primary soot particles into large structures may inhibit gasification by increasing the magnitude of mass transfer limitations. It is convenient in gasification modeling to represent char geometry as spherical, but soot agglomerates can be highly non-spherical and irregular compared to char. Hence, modeling gasification of soot in this form may be more difficult than modeling gasification of char, even considering the complex structures that have been observed in char.

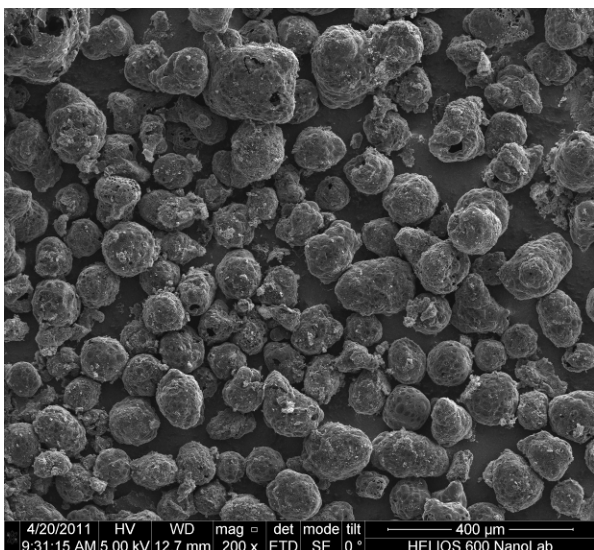
Attempts to improve the separation of char and soot by changing the operating conditions of the aerodynamic separation system were not successful. A liquid-phase density separation technique was also attempted (Appendix E). Char was immersed in a mixture of ethanol and water and subjected to vibration. Although this technique appeared to be effective in removing soot agglomerates, it also caused the char to partition into two density fractions. This had the effect of increasing the experimental noise in the extents of reaction that were measured using the ash tracer technique. The char separation technique was eventually abandoned because of the extra experimental noise and because it was very time consuming.

The original goal of this research was to conduct in-situ pyrolysis followed by gasification. This strategy would have provided the most realistic thermal history of the char and hence the best gasification kinetics. However, the soot contamination added enough noise to the experimental data to obscure the trends in the low extents of gasification that were measured. Hence, in-situ pyrolysis followed by gasification was abandoned in favor of a char reinjection technique, as used previously by others (Hurt et al., 1998).

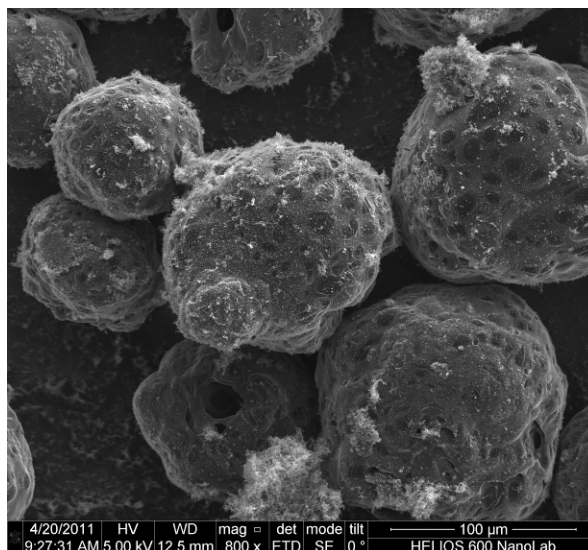
Reinjection of char was the strategy used for the last experiments pursued in this work. Coal was pyrolyzed in the HPFFB at short residence times in gas environments with ~2 mole % O₂ to inhibit the formation of soot from tar without causing significant oxidization of the char. The O₂ concentrations of these flames measured with an Alpha-Omega Instruments (Series 2000) O₂ analyzer (Pickett, 2008) exceeded the values predicted using the NASA-CEA code by only 0.4-0.6 absolute mole % (McBride et al., 2002). This good agreement suggests that equilibrium calculations yielded reasonable estimates of the gas composition for the HPFFB system when the 1-inch burner was used with a CO flame. Several grams of char were produced at pressures of 10 and 15 atm in this 2 mole % environment to generate char for gasification experiments. Soot contamination under these conditions was minimal and fragmentation was eliminated by the changes implemented in the collection system (Figure 4.9).

The raw char was used to determine the volatiles yield through a direct mass balance verified with an ash tracer. Swelling was determined using the mass balance and the tap density technique. The raw char was then sieved to obtain a narrower size distribution to reduce the uncertainty associated with particle size in the kinetic analysis. About 50% of the char ended up in the size fraction of 75-106 μm, which was selected for reinjection in CO₂ gasification environments (Figure 4.9).

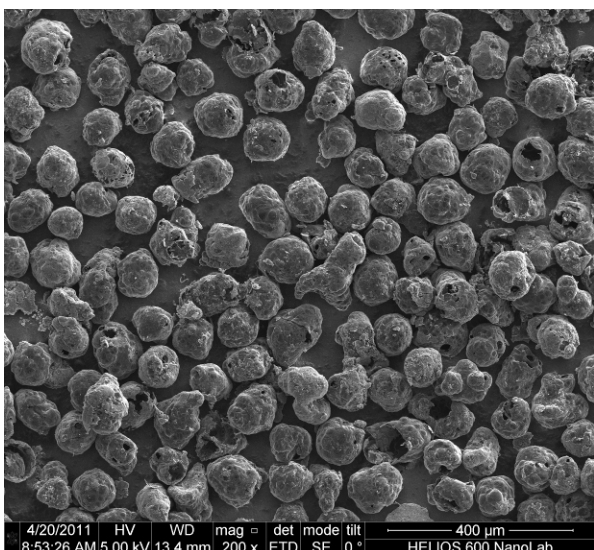
The sieved char was reinjected in the HPFFB at the same total pressure at which it was formed (initially 10 atm). Two levels of CO₂ concentration were used at each pressure (40% and 90%), and the heater temperature was set to two different levels (1250°C and 1350°C). Similar experiments at 15 atm were planned, but the molybdenum disilicide heaters broke before the additional experiments could be completed. Additional reinjection experiments were carried out at 10 atm and 15 atm without heaters to investigate gasification at lower conversion levels.



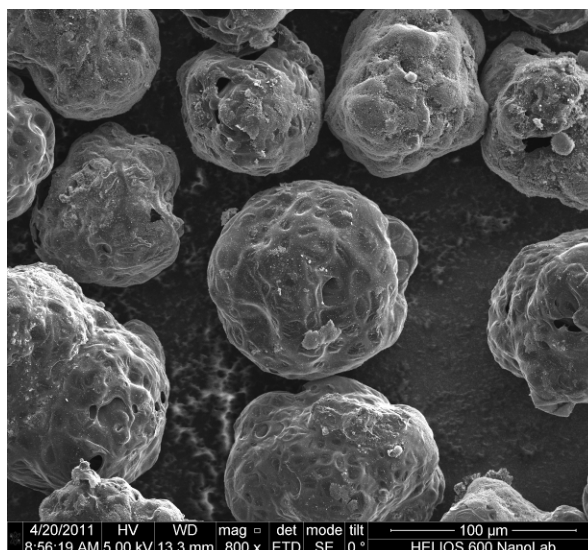
(a) 15 atm pyrolysis (raw sample)



(b) 15 atm pyrolysis (raw sample)



(c) 10 atm pyrolysis (sieved to 75-106 μm)



(d) 10 atm pyrolysis (sieved to 75-106 μm)

Figure 4.9. Illinois 6 char pyrolyzed with 2% O₂ at a collection height of 1.5 inches.

The collection efficiency was high using the updated design for char particles of 75-106 μm and apparent densities of ~0.15 g/cm³. In 6 of 8 cases where Illinois #6 char was reinjected at 10 atm, the mass balance determined by direct weight differed by less than 3% from the value determined by ash tracer. In the remaining 2 cases, less than 200 mg of char was fed and only

~100 mg of char was collected, which accounts for the higher errors of 10-20%. For reinjection, 300-400 mg of feedstock char was found to yield reliable results at a reasonable cost.

For pyrolysis cases the collection efficiency in the cyclone was lower, probably due to the presence of particles with aerodynamic properties that were not optimal for the char collection system. For Wyodak and Kentucky #9 coals the mass release from direct weight exceeded the value determined by ash tracer by 15-20 absolute mass %. Cenospheres with very high surface areas and low densities were observed to collect on the filter attached to the cyclone outlet when the cyclone was used in a horizontal position. Non-ideal aerodynamic properties of char also caused some of the char particles to spread from the centerline and impact the exterior of the probe.

4.3 Development of Viable Fuel Mixtures

In flat-flame burners, flow rates of fuel and oxidizer are varied to adjust the post-flame temperature and species concentrations (i.e. O₂, CO₂, and/or H₂O). A fuel-rich CH₄ flame produced soot that contaminated the char samples, even at low pressures of 2.5 atm. A CO flame was chosen to produce conditions suitable for pyrolysis and CO₂ gasification studies in the HPFFB. A trace amount of H₂ was always used to stabilize the flame. The CO flame had the advantage of not forming soot under any conditions. The existence of both CO and CO₂ in the coal reaction zone allowed investigation of gasification under the influence of CO inhibition, which is an industrially realistic scenario. In future studies H₂ or steam may be added to the CO flame in moderate amounts to conduct studies on combined CO₂/H₂O gasification kinetics. It was found that excessive concentrations of H₂ caused burner damage (see Appendix B).

Safety upgrades to use CO as a fuel included a new gas detection system with automatic shutoff valves on flammable and toxic gas sources. Ventilated gas cabinets for CO, H₂, and/or

CH₄ were installed. The outlet of the reactor was plumbed into the outlet of the gas cabinets to avoid the risks associated with venting high concentrations of CO directly out the window.

It was found that a 1:1 ratio of oxidizer flow to fuel flow did not produce steady flat flames suitable for experiments with coal. Fuel tubes occupied 25% of the burner surface area. Therefore, the ideal oxidizer to fuel flow ratio was 3:1 on a volumetric basis, but ratios as low as 2:1 were used successfully. The proper flow or velocity ratio was achieved under fuel-rich conditions by adding a diluent (N₂) or a gasification reactant (CO₂) to the oxidizer (Air or O₂) line. For oxidizer-rich pyrolysis conditions, air was used in the oxidizer line and N₂ was added to the fuel line to achieve the proper flow ratio.

High pressure increased the density of the gas in the vessel, which decreased the velocity for a fixed mass flow rate. The gas velocities required to maintain particle entrainment were maintained at high pressures by increasing the total flow rate through the burner. These higher flow rates also caused the flame to generate more heat, which partially compensated for the higher heat loss experienced with increasing pressure.

Wyodak coal was also gasified under H₂O-rich conditions at 2.5 atm during the early stages of this work (see Appendix J). These experiments used a mixture of H₂ with 16% CH₄ as fuel (to prevent soot formation) and were very costly in terms of time and damage to the burner. Since little useful data was obtained from these early experiments, the decision was made to focus on the simpler CO₂ gasification studies until the HPFFB operating procedures could be standardized and simplified.

4.4 Temperature Measurement

Centerline gas temperatures were measured for much of this work by inserting a thermocouple through an o-ring attachment at the top of the probe (Lewis, 2011). These

measurements were corrected for radiation effects using the methods described in Appendix F. The corrected gas temperature profiles and compositions are tabulated in Appendix G. The temperature measurements were difficult and hazardous to make due to the high pressure and the fragility of the ceramic sheath that protected the thermocouple wires. Frequent thermocouple repairs and replacements were required.

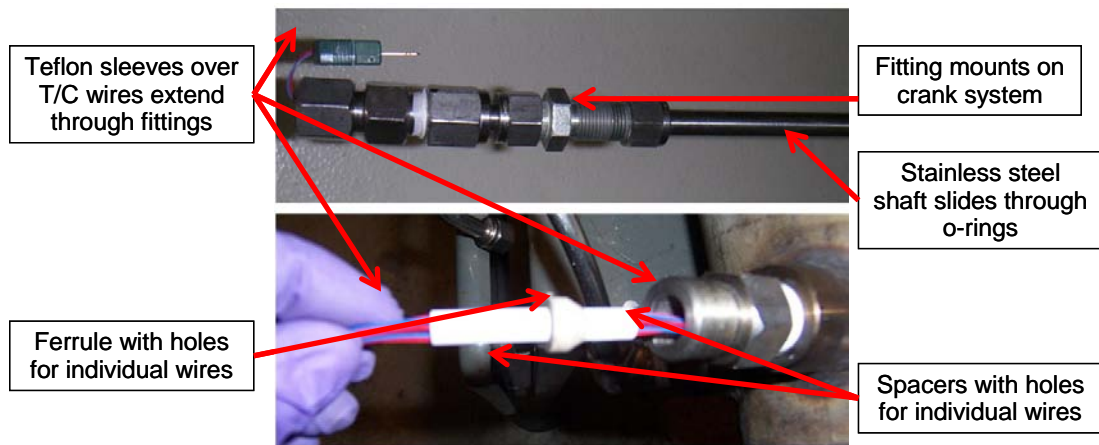


Figure 4.10. New centerline thermocouple fitting (top) and assembly of a similar fitting in the vessel wall (bottom).

Upgrades were implemented during the last year of this work to make gas temperature measurement safer and easier. The top section of the ceramic sheath was encased in a metal tube and the wires were fed through a pressure-tight fitting obtained from Conax[®] Technologies (Figure 4.10). The metal tube was attached to a crank system to move it through o-rings at the top of the probe. This modification secured the thermocouple and prevented the release of toxic CO gas. The metal tube around the thermocouple was about 20 inches long. This length was sufficient to allow the thermocouple to be moved all the way down through the collection probe to the burner surface while keeping the metal portion of the protective sheath above the location where cold nitrogen quenched the burner gases.

Most of the temperature profiles with collection heights above ~6 inches had to be measured in a piecewise fashion because of the imperfect alignment of the long thermocouple shaft with respect to the small quartz tube surrounding the burner. It was found that unreasonably low temperatures were sometimes measured at locations near the burner when the collection height was high. The thermocouple as seen through the view port appeared to be touching the quartz tube for these cases. The thermocouple was centered with respect to the probe at its tip, so the centerline temperatures near the probe were most likely of higher quality, assuming that the alignment of the burner and the quartz tube around it were not far from the centerline of the vessel.

4.5 Determination of Residence Times

A high-speed video camera was used previously to measure particle velocities in the luminous zone of the atmospheric flat-flame burner (FFB) (Ma, 1996). The same technique was applied on a more limited basis in the HPFFB using a window located near the burner (below the heaters, see Figures 4.1 and 4.3). Magnification effects of the windows and the layers of quartz tubing in the HPFFB were measured and taken into account.

In the HPFFB particle velocities were measured at two locations for each flame condition (Figure 4.11). The higher location was either 0.75 inch or 1 inch above the burner and the lower location was close to the beginning of the luminous zone, usually less than $\frac{1}{2}$ inch. For comparison, theoretical particle velocities were calculated for a non-reacting spherical particle based on an average gas velocity calculated at the local temperature from the gas flow rates (Appendix C). A momentum balance was performed on the particle using a drag coefficient. The theoretical particle velocity rapidly approached the average theoretical gas velocity.

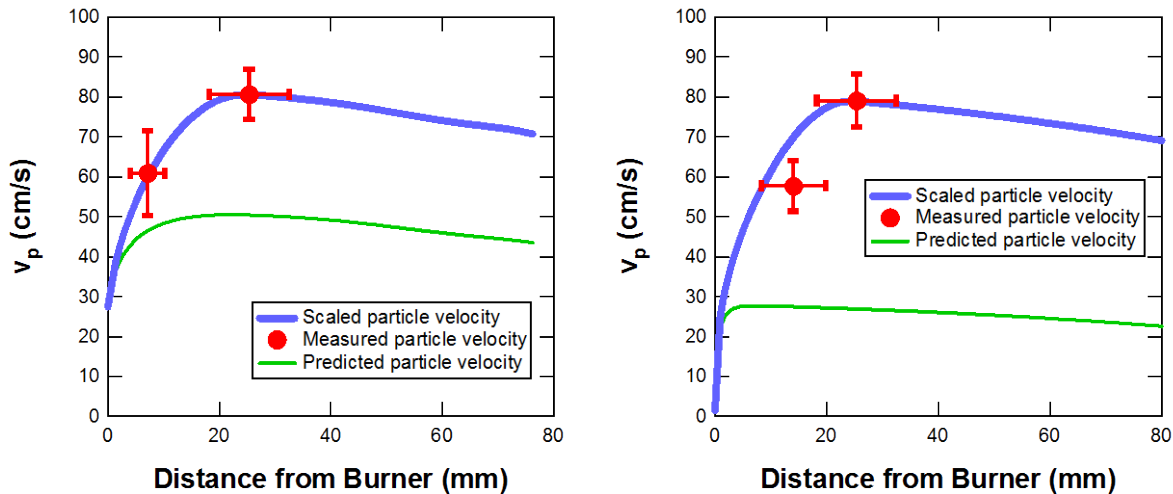


Figure 4.11. Velocity profiles at 2.5 atm (left) and 10 atm (right), both at ~1700 K peak temperature.

The difference between the particle and gas theoretical velocities was ~30% at 10 ms and ~10% at 30 ms. However, the optical particle velocity exceeded the theoretical velocity by a factor of 1.4 to 3.1 at the 1 inch location (Figure 4.11). The theoretical particle velocity was predicted by assuming the gas velocity was uniform in the radial direction. The high observed centerline velocity was attributed to rapid development of a parabolic velocity profile with respect to the radius of the cylindrical flow path, and perhaps some non-uniform flow through the burner. The vertical error bars in Figure 4.11 represent the 95% confidence intervals based on at least 5 replicate velocity measurements. The horizontal error bars are from the window size and the height of initial luminescence.

A scaling scheme was applied to reconcile the theoretical trends with the measured velocities. The 1-inch location was close to the maximum flame temperature, and the theoretical particle velocity was nearly flat from about 0.75 inch to 3 inches above the burner. Therefore, it was assumed that the optical velocity at the 1-inch location represented a maximum velocity. The ratio of the maximum optical particle velocity at 1-inch above the burner to the theoretical

velocity at the same location was denoted as m . The particle velocity at the burner surface was determined by calculating the terminal particle velocity in the coal feeder tube (0.042 inch ID) at room temperature using N_2 gas properties. A linear scaling factor between the surface theoretical velocity and the 1-inch optical velocity was attempted, but this approach resulted in a velocity profile with an artificial sharp corner at 1 inch and underestimated velocities closer to the burner surface. A closed-form quadratic scaling scheme was adopted. The theoretical velocity at locations up to 1 inch above the burner was multiplied by the following scaling factor:

$$SF(z) = az^2 + bz + c \quad (4.1)$$

where SF is the scaling factor and z is the distance above the burner. To be consistent with theory at the surface, $SF(0) = 1.0$, which means $c=1.0$. To be consistent with the optical velocity, $SF(l) = m$, where l is the height where the maximum optical velocity was measured (usually 1 inch). The derivative of SF at $x = l$ was set to zero to prevent an artificial sharp corner and other physically nonrealistic shapes in the velocity profile. These last two conditions resulted in:

$$a = \frac{1-m}{l^2} \text{ and } b = -2al \quad (4.2)$$

Thus, the quadratic scaling factor required no optimization of parameters and used a single measurement to yield a smooth velocity profile that was consistent with the theoretical velocity at the burner surface and the maximum measured velocity. When the 95% confidence intervals of both measured points were taken into account, the scaled velocity profile was found to be consistent with the point that was not used for scaling in all cases, as shown in Figure 4.11. In most cases, the agreement with the measurement closer to the burner surface was still excellent even without taking into account the statistical error of the measurements.

Measurements at longer residence times in the FFB were used to validate the technique of scaling the particle velocities with the temperature and the scaling factor m . The residence times derived with the scaling technique using Euler's method agreed within 15% of the measurements at 100 ms. The accuracy of this method was probably better for the HPFFB because the HPFFB appeared to have fully developed flow at the 1-inch scaling point, but the FFB did not ($m \approx 1.5$). Residence times between 40 ms and 690 ms were calculated for conditions used in the HPFFB.

The gas temperature was used to scale the measured velocity at residence times corresponding to heights above the measured optical velocity. This approximation was based on the ideal gas law and the close agreement between the predicted gas and particle velocity profiles (~8% difference at 100 ms or longer). Since the momentum balance on the particle assumed constant particle mass, the real particle velocity was probably even closer to the gas velocity because the particles lost mass through pyrolysis and gasification reactions.

4.6 Sample Characterization

The proximate analysis was carried out in accordance with ASTM standards. Coal samples were dried in crucibles in a furnace at 107°C for 1 hour. The fraction of the original coal sample that was lost is defined as the moisture content.

The dried sample was returned to the oven, which was ramped to 500°C in 1 hour. A small flow of air was introduced into the back of the furnace to maintain oxidizing conditions. The sample was then ramped to 750°C in 1 hour, where it remained for at least 12 hours before returning to room temperature. The remaining ash was weighed to determine the ash fraction.

The standard sample size for ASTM proximate analyses of 1 gram was used for analysis of coal, but less was used for char samples. A sensitivity study of the scale used in the laboratory showed that coal samples of 100 mg or more consistently yielded results comparable to a 1-gram

sample. Independent tests of this scale showed that results were repeatable if the total ash content in the sample exceeded ~8 mg (Lewis, 2011).

A freshly dried sample of coal in a crucible was covered with a loose-fitting lid and inserted into a furnace at 950°C for exactly 7 minutes. The crucible was placed inside a larger crucible to allow easier handling with tongs. The difference in weight was used to calculate the fraction of volatiles. Alternatively, an as-received coal sample was subjected to the same test and the fraction of moisture from a separate test was subtracted off to obtain the moisture-free volatiles.

The ultimate analyses (CHNS elemental composition) for coal, char, and soot samples were conducted at Huffman Labs in Golden, CO. Attempts were made to use a LECO TruSpec Micro Instrument at BYU, but the carbon readings for coal were found to be inaccurate (Sowa, 2009). Tests with model compounds with 2-3 aromatic rings yielded good results, and the polycyclic aromatic hydrocarbons (PAHs) produced from coals and model compounds at low residence times and temperatures had reasonable compositions.

For coals, chars, and soot produced at higher temperatures the LECO instrument yielded carbon percentages that were 10% to 30% too low. It appeared that the furnace in the BYU LECO machine did not reach temperatures that were sufficiently high to burn out all the carbon in the sample for highly aromatic substances, which prevented accurate measurements of elemental composition. Due to cost and sample size limitations, many of the char and soot samples produced later in this work were not subjected to ultimate analysis.

Depending on the contract provider and the purpose of the experiment, different sizes of particles were used. Some coals were sieved in-house to produce a 45-75 μm size cut. Others were supplied in different size cuts, most commonly 53-63 μm . Particle size distributions for the coals used in this study were measured using a Coulter Counter LS series machine (see

Appendix G). Unsuccessful attempts were made to measure the size distributions of chars using this device. The Coulter Counter entrained the solid particles in water and measured the obscuration of a laser beam. Bituminous chars produced at high pressures were sufficiently swollen that they did not stay entrained due to a large buoyant force. The Coulter Counter was not used for subbituminous chars because most of the available char was used for other analyses.

The properties of the coals studied in this work are listed in Table 4.1. The full names and the sulfur and oxygen compositions of Eastern Bituminous A (EBA) and Eastern Bituminous B (EBB) were withheld to comply with research funding contracts. The NMR parameters in Table 4.1 are defined in Table 2.1 and were predicted using correlations with the ultimate and proximate analyses (Genetti et al., 1999), which are reproduced in Appendix L. The correlated parameter c_0 is used in the CPD model (Fletcher et al., 1992) to represent stable bi-aryl linkages in very high rank coals and low-temperature cross-linking in low rank coals.

Table 4.1. Properties of coals studied in this work

Coal	*EBA	*EBA	*EBA	*EBB
Particle size (μm , from mesh)	149 to 177	88 to 105	53 to 66	53 to 66
Mass mean size (μm)	160	115	65	55
C (mass % daf)	79.08	78.68	79.00	83.04
H (mass % daf)	5.84	5.79	5.73	5.62
N (mass % daf)	1.49	1.51	1.53	1.57
*S+O (mass % daf, by diff.)	13.59	14.02	13.74	9.77
VM (mass % daf)	47.87	46.98	48.75	43.22
Ash (mass % dry)	7.36	6.88	6.90	5.74
Moisture (mass % as rec'd)	4.65	5.1	4.43	0.42
Apparent particle density (g/cc)	1.31	1.28	1.22	1.14
M_δ	37.7	38.0	37.1	31.0
MW	435.8	432.7	422.3	384.5
p_0	0.410	0.413	0.421	0.462
$\sigma+I$	5.24	5.26	5.28	5.15
c_0	0	0	0	0
*Full names and elemental analysis withheld by contract with the provider of research funds				

Table 4.1 (continued)

Coal	Wyodak 2010	Wyodak 2011*	Kentucky #9	
Particle size (μm , from mesh)	45-75	45-75	45-75	
Mass mean size (μm)	77	67	58	
C (mass % daf)	71.90	68.83	77.01	
H (mass % daf)	5.10	5.59	5.61	
N (mass % daf)	1.00	0.94	1.69	
S (mass % daf)	0.55	0.53	4.00	
O (mass % daf, by diff.)	21.45	24.12	11.69	
VM (mass % daf)	50.75	53.61	46.27	
Ash (mass % dry)	5.63	5.03	8.07	
Moisture (mass % as rec'd)	11.14	Dried to 5.7	1.84	
Apparent particle density (g/cc)	1.35	1.23	1.21	
M_{δ}	43.8	49.7	40.1	
MW	343.3	398.9	416.1	
p_0	0.582	0.547	0.445	
$\sigma+I$	4.82	4.38	5.18	
c_0	0.125	0.150	0	
*Wyodak 2011 came from a bottle labeled >75 μm , which was then reground and sieved				
Coal	Illinois #6	Dietz	Pittsburgh #8	Lower Kittanning
Particle size (μm , from mesh)	53 to 66	63-75	*45-75	63-75
Mass mean size (μm)	68	74	*37	74
C (mass % daf)	76.68	68.48	82.19	86.38
H (mass % daf)	5.54	5.37	5.42	4.84
N (mass % daf)	1.45	0.86	1.58	1.59
S (mass % daf)	3.60	0.48	2.23	2.53
O (mass % daf, by diff.)	12.73	24.81	8.58	4.66
VM (mass % daf)	42.27	44.64	38.80	21.64
Ash (mass % dry)	8.46	4.83	6.57	17.56
Moisture (mass % as rec'd)	7.53	17.71	1.21	0.71
Apparent particle density (g/cc)	1.21	1.25	1.28	1.39
M_{δ}	40.5	49.7	31.9	21.3
MW	408.8	388.6	360.7	297.7
P_0	0.471	0.591	0.508	0.662
$\sigma+I$	5.12	4.38	5.08	4.88
C_0	0.003	0.150	0	0.059
*The mesh size was listed on the bottle, but the Coulter Counter results show a lot of material < 45 microns.				

4.6.1 Swelling Ratio Measurement

The tap technique was used to determine bulk densities of all coals and chars (Tsai and Scaroni, 1987; Fletcher, 1993; Gale et al., 1995). The swelling ratio was determined using the following relationship:

$$\frac{d}{d_0} = \left(\frac{m/m_0}{\rho/\rho_0} \right)^{1/3} = \left(\frac{\left[\frac{m}{m_0} \right]}{\left[\frac{\rho_b}{1 - \varepsilon_b} \right] \cdot \left[\frac{1 - \varepsilon_{b0}}{\rho_{b0}} \right]} \right)^{1/3} \quad (4.3)$$

where the terms with the subscript “0” refer to the parent coal and the other terms refer to the char. The residual mass ratio m/m_0 in this equation is expressed on an as-received basis. The density ratio ρ/ρ_0 refers to the ratio of apparent densities, where apparent density is defined as the mass of a particle divided by the total volume enclosed by the outer surface of the particle (assumed to be spherical). The bulk or bed density (ρ_b for the char and ρ_{b0} for the coal) was measured using the tap technique, and it includes the volume in between particles.

The apparent density was obtained from the bulk density by using a packing factor or inter-particle void fraction (ε_b for char and ε_{b0} for coal), which typically has a value of 0.45 for particles of nearly spherical geometry (Tsai and Scaroni, 1987; Gale et al., 1995). In this work the coal and the char particles were assumed to have approximately the same average shape and hence the same packing factor. With this assumption the packing factors canceled out and the bulk densities were used directly to determine the swelling ratio. The error associated with this method has been estimated to be 10% (Tsai and Scaroni, 1987).

4.6.2 Measurement of Mass Release

Whenever possible, the change in mass during pyrolysis or gasification was measured directly. The collected char (typically a few hundred milligrams) was weighed after each

experiment and the plunger loaded with coal was weighed before and after each experiment. This allowed the residual mass ratio m/m_0 to be calculated on an as-received basis. The filters were also weighed before and after to determine the yield of tar and soot. When excessive static charge or loss of filter material prevented accurate measurements of filter weights, the tar/soot was scraped from the polycarbonate filters and weighed in a bottle of known mass. Some black material came out of the collection system with blowing after shutdown.

A test with Pittsburgh #8 coal was conducted at ~1900 K with a residence time of ~100 ms to quantify soot accumulation in the collection system. 36% of the 377 mg coal fed was deposited on the soot filters. 34% of the soot found in the filter assemblies was stuck to the filter itself. The rest was sitting in the bottom of the filter assembly. Some of the soot that collected in this manner was prone to blow or drop away if the flange was not opened with sufficient care. The mass of material that came out of the collection system with further blowing was negligible. Insignificant amounts of tar/soot were found to accumulate in the collection system at the high temperatures used for full pyrolysis and gasification experiments. It appears that a normal depressurization of the HPFFB caused nearly all of the mature soot formed from coals at these conditions to be swept onto the filters. The observed soot yields may have been lowered slightly in cases when the filters were changed without shutting down.

The change in mass from direct measurements was subject to several sources of error. First, leaks sometimes occurred between the funnel and the coal feeder tube in the new coal feeder system (Figure 4.5). This sometimes resulted in a small amount of coal accumulation at the bottom of the coal feeder. This type of leakage was minimized by wrapping the coal feeder tube in a layer of Teflon tape to allow a better fit with the glass funnel. Second, the feeder tube was prone to clog, especially when pressure swings in the HPFFB caused temporary back-flow

in the feeder tube and contamination of its inner surface with moisture. The feeder tube was cleaned daily with a wire and compressed air to minimize this problem. More consistent pressure control also helped prevent clogs and damage to the feeder tube.

Anything that interfered with the collection efficiency of the char would decrease m/m_0 . Causes of low collection efficiency included poor alignment between the burner and the collection probe and improper flow distributions in the virtual impactor and cyclone. Cenospheres with very low densities and large external surface areas were observed to collect on the filter at the outlet to the cyclone when the cyclone operated in a horizontal orientation. Improper flow distributions and/or very large soot agglomerates sometimes caused soot to collect with the char, especially in the earlier stages of this work.

Tracer techniques were used to verify the accuracy of a direct mass balance or to replace mass measurements that had obvious errors. The dry, ash-free (daf) fractional mass release is defined as:

$$MR_{daf} = 1 - \left(\frac{m}{m_0} \right)_{daf} = \frac{m_{coal} - m_{char}}{m_{coal} - m_{ash}} \quad (4.4)$$

where m_{coal} , m_{char} , and m_{ash} are the masses of coal, char, and ash on a dry basis. The simplest and least expensive tracer is the ash tracer. By assuming that the mass of ash remained constant, a comparison of the ash content in the coal and the char allowed the mass release to be determined. The expression for mass release in terms of the ash fraction is (Zeng, 2005):

$$MR_{daf} = \frac{1 - x_{ash,coal}}{1 - x_{ash,char}} \quad (4.5)$$

where $x_{ash,char}$ and $x_{ash,coal}$ are the dry-basis mass fractions of ash in the char and the coal, respectively. The ash tracer technique was used throughout this work. For char reinjection

experiments, $x_{a,0}$ became the ash fraction in the reinjected char. In the most recent cases where the coal or char was fed very carefully and char was collected using the vertical cyclone, the agreement of the direct mass balance with the ash tracer was very good (Section 4.2.2). In most of the previous work this level of agreement was not achieved due to soot contamination and char loss through misalignment of the collection system with respect to the burner.

Some of the ash may have vaporized during rapid heating, depending on the temperatures achieved and the mineral composition in the ash. Elements occurring in mineral forms that do not vaporize at the experimental operating temperatures are the most accurate tracers available. Si, Ti, and Al tracers as measured by inductively coupled plasma-atomic emission spectroscopy (ICP-AES) are commonly used to close the mass balance for combustion experiments (Fletcher, 1989b). The expressions for any of these tracers are analogous; the expression for the Ti tracer is:

$$MR_{def} = \frac{1 - \frac{x_{Ti,coal}}{x_{Ti,char}}}{1 - \frac{x_{Ti,coal}}{x_{Ti,ash}}} = \frac{1 - \frac{x_{Ti,coal}}{x_{Ti,char}}}{1 - x_{ash,coal}} \quad (4.6)$$

where x_{Ti} represents the mass fraction of titanium in the coal, char, or ash, denoted by the remainder of the subscript.

The assumption that an element is conserved in the char is also subject to error. It has been shown that stable elements that are present in dispersed form can be removed from coal particles by convective processes during pyrolysis (Baxter et al., 1997). Early experiments in this work showed that the Ti tracer often yielded mass release that was 5% - 20% lower than the Al and Si tracers for both subbituminous and bituminous coals. This could have been due to preferential loss of titanium or a low signal-to-noise ratio for this element.

The difficulty of conducting ICP-AES on small samples of coal ash (~10 mg) in a repeatable and quantitative manner made the in-house application of this technique impractical. All ICP measurements used in this study were outsourced to Huffman Laboratories in Golden, Colorado. The Si, Ti, and Al tracers were used for a limited number of early experiments, but were discontinued for later experiments due to the high expense of outsourcing this analysis.

Direct mass balances were used whenever possible as a basis of comparison in this work. The ash tracer technique was used to verify the direct mass balance. The ash tracer was used in place of the direct mass balance for gasification experiments when the direct mass balance trends did not make sense, especially when such anomalies could be attributed to spills, clogged coal feeder lines, or similar events that were documented in the laboratory notebooks. Deposits observed on the exterior of the collection probe after pyrolysis experiments probably account for the excessively high measured volatiles yields that were measured for some coals. The ash tracer was used almost exclusively for pyrolysis experiments due to the better agreement with experiments conducted in other facilities as well as the ASTM volatiles yield. When the horizontal cyclone was in use, large cenospheres with very low densities were observed on the filters at the outlet to the cyclone. Separation inefficiencies such as these may also have contributed to the high pyrolysis yields that were observed for some bituminous coals.

4.6.3 Surface Area Measurements

A Micromeritics Tristar 3000 was used to measure adsorption isotherms with N₂ to determine macropore surface area and CO₂ for micropore surface area. The procedures were identical to those used in previous char studies (Zeng, 2005). Macropore and mesopore surface areas were measured at the boiling point of N₂ (77 K) and the Micromeritics software used the BET equation to calculate surface area from the adsorption isotherm (Brunauer et al., 1938).

Micropore surface area was measured at 273 K, which allows for greater penetration of the CO₂ adsorbate in the smallest pores. The Micromeritics software used the Dubinin-Polyani equation to calculate surface area from the isotherms (Marsh and Siemieniowska, 1967). Sample sizes of ~150 mg were measured for the chars used in HPFFB reinjection experiments and also Wyodak 2011 chars from low residence time gasification experiments.

CHAPTER 5. PARTICLE SWELLING DURING COAL PYROLYSIS

Changes in the physical structure of coal particles during pyrolysis strongly influence subsequent Zone II heterogeneous reaction rates. Knowledge of the particle size is critical to modeling transport processes and hence char reaction rates. The particle size change is most often expressed as the swelling ratio d/d_0 . Knowledge of the particle size and the pyrolysis yield can be used to estimate the wall thickness for cenospheres, which is another critical parameter for calculating transport rates. Thermal swelling of coal varies strongly with coal rank, maximum particle heating rate, and total pressure (Lee et al., 1991; Fletcher, 1993).

A simple example of the effect of particle size on gasification rates is shown in Figure 5.1. These conversion profiles were estimated using 1st-order Illinois #6 rate parameters from the literature (Goetz et al., 1982). Coal particles with diameters of 60 μm and 7% dry ash content were assumed. A constant gas temperature of 1700 K was specified at 15 atm with surroundings at 1000 K and 20 mole % CO_2 in the bulk gas. A more sophisticated model would predict decreasing rates rather than constant rates due to changes in particle size during gasification (which were neglected in Figure 5.1), non-isothermal conditions, and thermal deactivation. The relationship between the predicted rate and particle diameter is more complex when effectiveness factors are used. Figure 5.1 shows that gasification rates and conversion times are highly sensitive to the swelling ratio, particularly when the swelling ratio is less than 2. This 1st-order model predicts faster reaction rates for highly swollen particles because the particle has increased

external surface area, even though the mass flux in the particle boundary layer is lower. The effects of initial particle size on apparent kinetic parameters are discussed in Chapter 6.

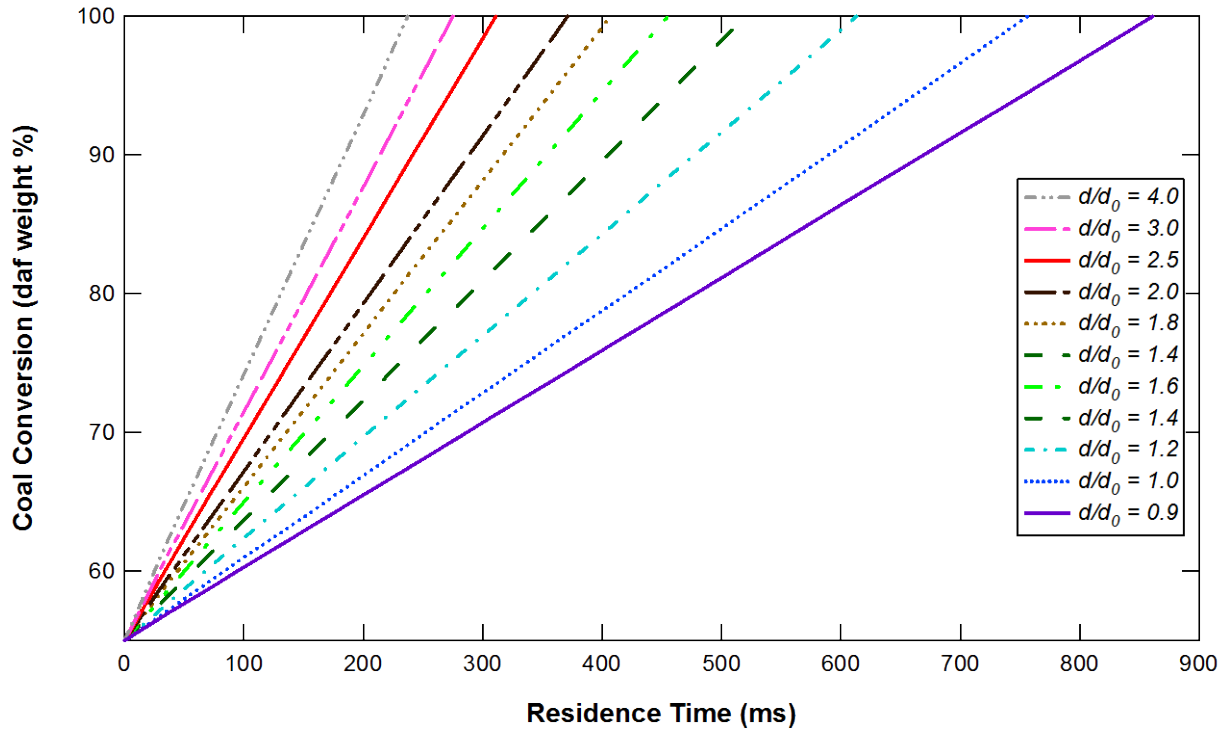


Figure 5.1. Illinois #6 conversion profiles for different swelling ratios at $T_g = 1700$ K, $P = 15$ atm, 20% CO_2 .

The ability to make improved estimates of the swelling ratio at industrial conditions is of great practical interest in combustion and gasification modeling. In this study, new swelling data are presented that illustrate the effect of particle heating rate and pressure. Also, a new coal-dependent swelling correlation with heating rate dependence is developed. The performance of the new swelling correlation is evaluated through comparisons to published experimental data as well as recently acquired data.

5.1 Experimental Investigation of the Effect of Heating Rate at Atmospheric Pressure

A U.S. coal designated as “Eastern Bituminous A” (due to industrial funding) was studied at atmospheric pressure in the FFB as a function of particle heating rate. Maximum particle heating rates near 10^5 K/s are typical for this facility, and the local ambient pressure is 0.84 atm. Experiments with three different particle sizes (see Table 4.1) were conducted to vary the heating rate. A fuel-rich CO flame with a peak centerline gas temperature of 1546 K was used for these experiments. Residence times corresponding to full pyrolysis were chosen based on calculations using the CPD model (Fletcher et al., 1992; Genetti et al., 1999).

In collaboration with this work, pyrolysis experiments were performed elsewhere on the same coal using a bench-scale gasifier (BSG), which was similar to an atmospheric drop-tube reactor (Eiteneer et al., 2009). The particle heating rate of the BSG exceeded 10^4 K/s at temperatures of up to 1400°C at atmospheric pressure. The BSG provided particle residence times of up to 2-3 s. The BSG had a gas-quenched collection probe with an aerodynamic separation system for separating char from soot that was similar in design to the BYU FFB.

The experiments were performed using these two facilities to investigate a greater range of particle heating rates than would be possible with a single facility. The BSG achieved particle heating rates between 9.2×10^3 K/s and 1.4×10^4 K/s. The highest particle heating rates in the BSG were attained by adding oxygen to the gas stream to burn some of the volatiles. The FFB was chosen to complement the BSG experiments because the heating rates of 2.4×10^4 K/s to 1.5×10^5 K/s in the FFB are closer to those found in utility boilers and gasifiers.

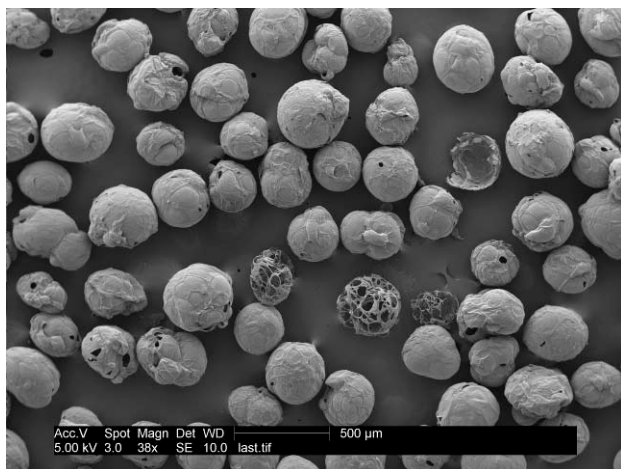
The experimental volatiles yield determined from samples collected in the BYU FFB using the ash tracer technique was 61-63 daf wt % for all three coal sizes, as shown in Table 5.1. Al and Si elemental tracers were also used on the two larger size cuts. The volatiles yield using

elemental tracers was 67-70 daf wt % for all three coal sizes. The ash tracer technique was used to determine mass release in the BSG, so the ash tracer was also used for analysis of the FFB swelling results for consistency in the modeling work. The use of the ash tracer led to swelling ratios 2-8% larger than those calculated using the more accurate Al and Si tracers.

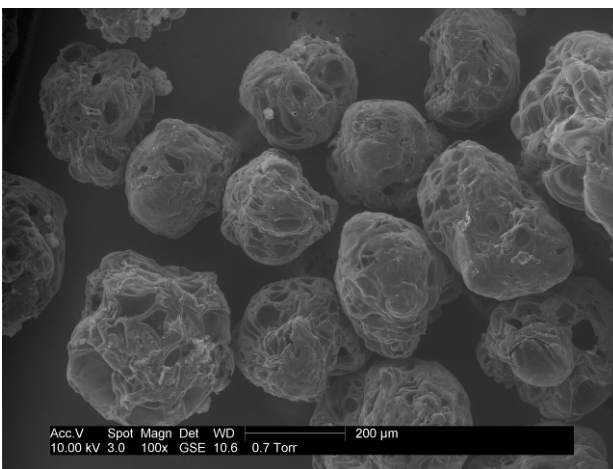
Table 5.1. Experimental conditions for Eastern Bituminous A at 0.84 atm

Particle size (μm)	149 to 177	88 to 105	53 to 66
Swelling ratio d/d_0 (ash tracer)	1.21	1.00	0.93
Density ratio ρ/ρ_0 (tap technique)	0.24	0.39	0.51
Volatiles yield (% daf, ash tracer)	61.2	63.4	61.4
Volatiles yield (% daf, average of Si, Al)	69.4	67.7	N/A
Heating rate (K/s)	2.4×10^4	6.5×10^4	1.5×10^5
Collection height (inches)	6	3.5	2
Residence time (ms)	90	48	25

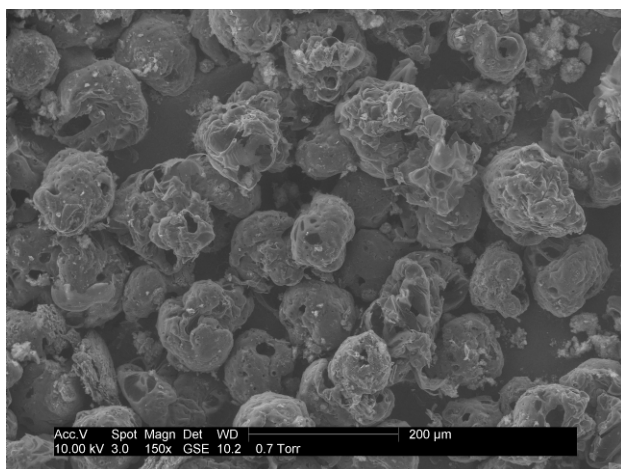
When the experiments from the FFB and the BSG are plotted together, as in Figure 5.2, it becomes clear that swelling decreased rapidly at heating rates from slightly below 10^4 K/s until nearly 10^5 K/s. The consistency of the data from the two facilities was very good; i.e. there was no significant discontinuity in the trend. It appears that the swelling ratio had an asymptote of ~ 0.9 as the heating rate increased beyond 10^5 K/s. These new data confirm and clarify trends observed previously using a different facility and a different bituminous coal (Pittsburgh #8, Figure 5.2) (Gale et al., 1995). The consistency of these results with the previous measurements implies that it is common for bituminous coals suitable for steam production in utility boilers (steam coals) to exhibit large decreases in swelling at heating rates between 10^4 K/s and 10^5 K/s. The effect of heating rate on swelling would be expected to be smaller for coals with ranks that are higher or lower than those typically classified as steam coals due to lower volatiles yield and higher viscosities in the metaplast (the viscous coal melt that exists during pyrolysis).



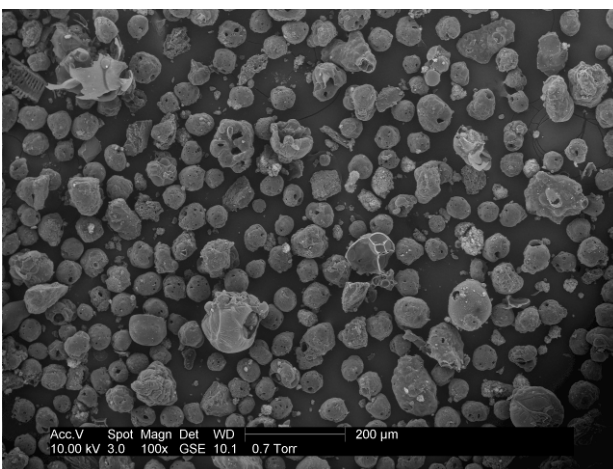
(a) BSG char from 105 to 149 μm coal, $\sim 9.2 \times 10^3$ K/s



(b) FFB Char from 149 to 177 μm coal, 2.4×10^4 K/s.



(c) FFB Char from 88 to 105 μm coal, 6.4×10^4 K/s.

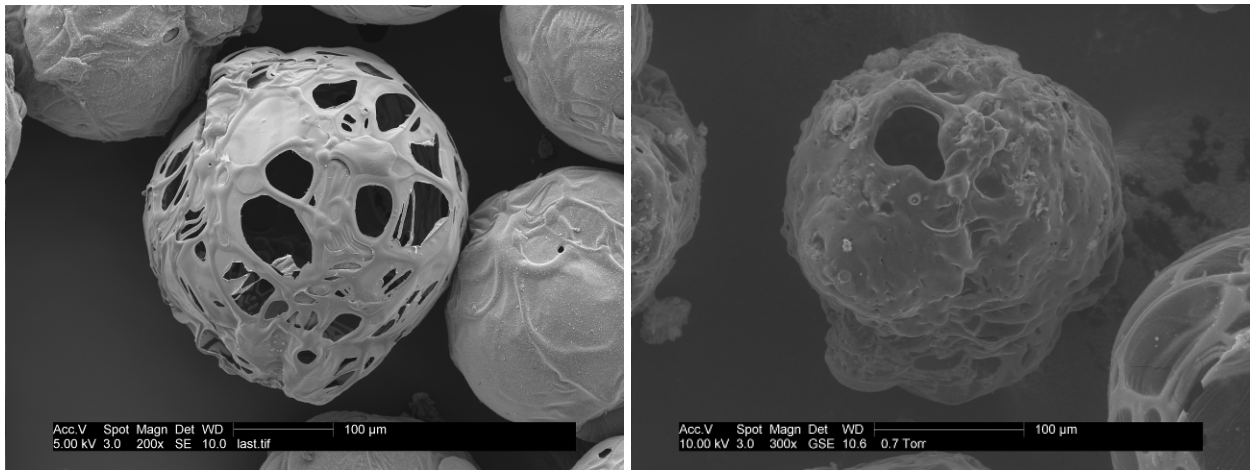


(d) FFB Char from 53 to 66 μm coal, 1.5×10^5 K/s.

Figure 5.3. SEM images of Eastern Bituminous A chars produced at different heating rates (scales differ).

The observed swelling behavior can be conveniently viewed in terms of two regimes of heating rate (Figure 5.2). Electrically heated reactors with stationary particles (thermogravimetric analyzers and wire-mesh reactors) usually operate at heating rates below 10^3 K/s, designated in this study as Regime 1. Electrically heated entrained-flow reactors (e.g. drop-tube furnaces) typically operate near 10^4 K/s, which is slightly above the lower boundary of Regime 2. Flat-flame burners typically operate closer to 10^5 K/s for particles smaller than ~ 100 μm . The details

of swelling behavior at the transition between these two regimes is very difficult to characterize experimentally because of equipment limitations and uncertainties in the calculated particle heating rate. Both mechanistic and empirical models have failed to quantitatively predict the decrease in swelling with increasing heating rate observed for bituminous coals in Regime 2. This nomenclature for the regimes of swelling behavior with changes in heating rate is introduced as a convenience for comparison of experimental data and model development.



(a) BSG char, 1 atm, $\sim 9.2 \times 10^3$ K/s

(b) FFB char, 0.84 atm, 2.4×10^4 K/s

(c) FFB char, 0.84 atm, 6.5×10^4 K/s

(d) FFB char, 0.84 atm, 1.5×10^5 K/s

Figure 5.4. SEM images of Eastern Bituminous A chars produced at different heating rates (scales differ).

5.2 Experimental Investigation of the Effect of Pressure at High Heating Rates

Pressurized pyrolysis experiments were conducted in fuel-rich CO flames in the high pressure flat-flame burner (HPFFB) to provide information needed for gasification studies, especially char particle size. Unfortunately, fragmentation of the char and contamination of the char with large soot agglomerates were prevalent when these experiments were conducted (see Section 4.2). A density separation procedure in an ethanol-water mixture was developed in an attempt to fix these problems (Appendix E). Due to the lower tar yield and lack of swelling behavior, the Wyodak subbituminous coal studied was not strongly influenced by soot contamination and fragmentation, so it was not subjected to the separation procedure.

More recent pyrolysis experiments with 2 mole % O₂ and a vertical cyclone yielded intact char particles with little soot (see Section 4.2.2). The swelling ratios were evaluated on a raw basis, without the use of the density separation technique in a liquid. The quality of the char density measurements was checked by vibrating the chars in argon overnight. The stratified char sample was checked for the presence of a dark, sooty layer, and the char bed was then remixed to remove the stratification effects. If there were large differences in the bulk density of the char before and after vibration, it was taken as an indicator of soot in the raw char. SEM images were used to verify the presence or lack of soot in each char sample and to determine whether the pre-vibration or post-vibration densities were most suitable for swelling ratio calculations.

The soot layer that was sometimes present in the vibrated char was very thin and occurred at the bottom of the glass vial. This differed from previous observations of atmospheric chars with shorter vibration times (Zhang, 2001). It is thought that the prolonged vibration time caused the soot agglomerates to become denser. Very dense soot agglomerates were observed by SEM in some of the vibrated chars.

5.2.1 Fuel-Rich Pyrolysis Conditions

Wyodak subbituminous coal (2010 sample), Kentucky #9 bituminous coal, and Eastern Bituminous A and B (see Table 4.1) were initially subjected to fuel-rich pyrolysis experiments in the HPFFB at peak gas temperatures of ~1700 K, residence times of 33-46 ms, and pressures of 2.5, 5, 10, and 15 atm. The swelling ratios obtained in these experiments are shown in Figure 5.5. The size fraction used was 45-75 μm for the Wyodak and Kentucky #9 coals. Particles of 53-66 μm were used for the other coals. According to CPD model predictions (Fletcher et al., 1992; Genetti et al., 1999), all of these coals were fully pyrolyzed at 25-35 ms. The volatiles yield and density data are tabulated in Appendix I.

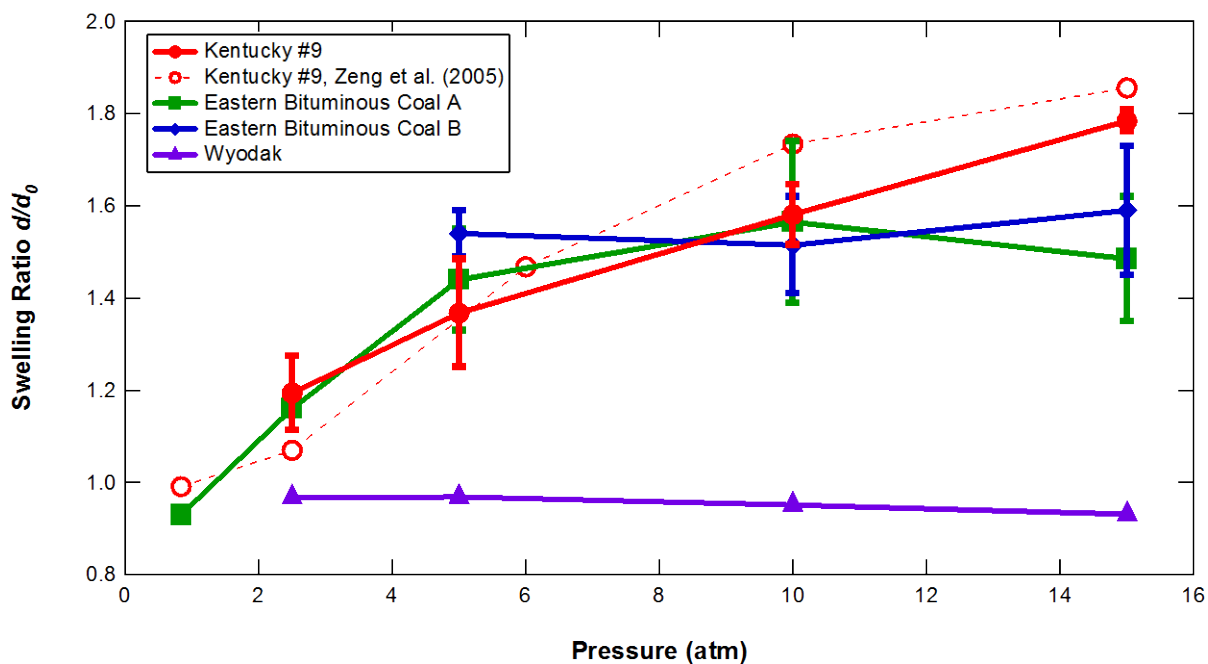


Figure 5.5. HPFFB swelling ratios at peak gas temperatures of ~1700 K and residence times of ~40 ms.

The error bars in Figure 5.5 correspond to limiting behavior derived from the bulk densities and ash content of the density-separated char samples (Appendix E). The points

correspond to the arithmetic mean of the limits. Points without error bars correspond to whole samples that were analyzed before the char separation scheme was put into effect. Char fragmentation was a common problem for the bituminous coals in these pyrolysis experiments. Soot agglomerates also interfered with the measurements of mass release and density needed to calculate the swelling ratio, but this problem was not as severe as it was for the early gasification experiments due to the low experimental residence times.

The swelling ratio for the Kentucky #9 coal under fuel-rich conditions increased monotonically with increasing pressure (Figure 5.5). This trend is consistent with swelling measurements made using the previous version of the HPFFB with slightly oxidizing conditions and the same Kentucky #9 coal (Zeng et al., 2005). The swelling ratios from the experiments in this work were slightly lower at 10 atm and 15 atm. The values of the d/d_0 error bars from this work agreed within 0.09 of the previous Kentucky #9 measurements, and the nominal values agreed within 0.15 of the previous measurements (Figure 5.5).

The other two bituminous coals in Figure 5.5 exhibited an initial increase in the swelling ratio, followed by a nearly constant swelling ratio with further increases in pressure. The large uncertainty associated with these measurements prevented conclusive identification of a pressure corresponding to peak swelling for any of the coals.

The high extent of overlap for the bituminous coal swelling measurements may be an artifact of the data collection procedure. The largest cenospheres with the thinnest walls were either fragmented during collection or else they passed through the cyclone and were collected on the soot filter. After the separation procedure was implemented, more reliance was placed on the densities measured from the top fraction, since that fraction was known to be free of fragmentation. However, the top fraction contained particles with sizes and densities that were

artificially more uniform than would be observed in a hypothetical raw sample without soot or fragments. The insights gained from the analysis of these data provided some of the rationale for abandoning the char separation technique that involved vibration in a liquid.

The Wyodak subbituminous coal showed no significant increase in swelling with increasing pressure (Figure 5.5). There might be a slight decrease in swelling at pressures above 5 atm, but the trend is well within the 10% uncertainty expected for swelling measurements using this technique (Tsai and Scaroni, 1987). SEM images of the Wyodak chars confirm that many of the irregularities in shape found in raw coal have been preserved (Figure 5.6). However, the edges of the particles are more rounded than the parent coal, suggesting that some softening occurred.

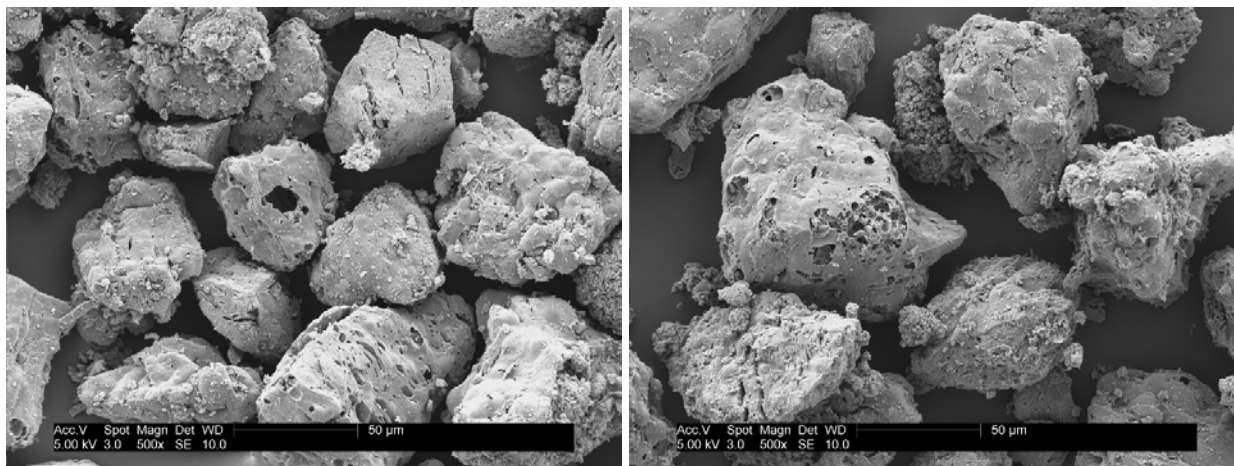


Figure 5.6. Wyodak chars produced at 2.5 atm, 33 ms (left) and 15 atm, 44 ms (right).

The smooth surface textures and what is visible of the porous structure in the interior of some Wyodak char particles suggest that there may have been some limited bubble formation in the metaplast during pyrolysis. Bubble formation and growth do not proceed to any great extent

in subbituminous coals because the high oxygen content promotes rapid cross-linking before significant pyrolysis can occur. The CPD model captures this effect of early cross-linking on devolatilization rates for low-rank coals when the c_0 factor is used to represent the fraction of stable bridges that are present initially or formed at low temperatures (Genetti et al., 1999).

The particle heating rates corresponding to the experiments in Figure 5.5 varied slightly from 8.3×10^4 K/s to 1.0×10^5 K/s for the bituminous coals, assuming particle diameters of 60 μm . The Wyodak coal was dried to promote better entrainment, which resulted in slightly lower heating rates of 6.3×10^4 K/s to 7.4×10^4 K/s. The particle heating rates increased as pressure increased from 2.5 atm to 5 atm, and then decreased as the pressure increased to 15 atm.

5.2.2 Oxidizer-Rich Pyrolysis Conditions

Lower Kittanning, Pittsburgh #8, Kentucky #9, Illinois #6, and Dietz coals (see Table 4.1) were pyrolyzed in 2% O_2 in the HPFFB at pressures of 5, 10, and 15 atm to provide swelling data with little or no soot contamination (see Figure 4.9). Larger quantities of char were produced from the Kentucky #9 and Illinois #6 coals at 10 atm and 15 atm for use in gasification studies (see Section 4.2). These oxidizer-rich pyrolysis experiments were conducted with the cyclone in a vertical orientation to allow collection of unfragmented char. These coals were also pyrolyzed in the atmospheric FFB at the ambient pressure of 0.84 atm.

It was found by examination of the volatiles yield data for these oxidizer-rich experiments that the ash tracer technique yielded more reasonable numbers compared to the direct mass balance in the HPFFB. Volatiles yields at high experimental heating rates normally exceed the ASTM values, but this effect diminishes with increasing pressure. For example, the volatiles yield for Pittsburgh #8 at 15 atm exceeded the ASTM volatiles by 20% (absolute) when

the direct mass balance was used, compared to 5% when the ash tracer was used. The direct mass balance was found to yield better volatiles yield data when using the atmospheric FFB. The lower Kittanning in particular tended to yield chars with lower ash concentrations than the parent coal when used in the FFB. The atmospheric FFB had maximum particle heating rates 50% higher than those occurring in the HPFFB, which could lead to enhanced vaporization of some ash constituents, especially during pyrolysis (Baxter et al., 1997). The atmospheric FFB had a slightly larger probe diameter and a virtual impactor and cyclone that were optimized at atmospheric pressure for a narrow range of gas flow rates and particle sizes, which made particle collection and separation in the FFB more efficient compared to the HPFFB.

These O₂-rich experiments were conducted at higher temperatures compared to the fuel-rich experiments. The maximum particle heating rates were in the range of 9×10^4 K/s to 1.6×10^5 K/s in the HPFFB, with an average of 1.2×10^5 K/s. Heating rates in the atmospheric FFB were typically $\sim 1.5 \times 10^5$ K/s, but the low-moisture Lower Kittanning had a heating rate of 1.0×10^5 K/s and the Pittsburgh #8 with very small particle sizes had a heating rate of 2.2×10^5 K/s. The higher average particle heating rates in the atmospheric FFB were probably caused by particle velocities that were more than twice as high as those measured in the HPFFB. Oxidation of pyrolysis products near the particles may also have enhanced the heating rates slightly, but this effect was probably small due to the high mass transfer rates away from the particle (the blowing effect).

The oxidizer-rich pyrolysis swelling data are presented in Figure 5.7 and tabulated in Appendix H. The Dietz subbituminous coal exhibited little if any swelling enhancement attributable to pressure, similar to the Wyodak swelling measurements under fuel-rich conditions. The bituminous coals exhibited very similar swelling ratios of ~ 1.8 at 10 and 15 atm. In this data set, the Kentucky #9 exhibited a maximum near 10 atm instead of increasing

monotonically as in Figure 5.5. It is possible that the different trend was caused by variations in the heating rate, but further experiments at more pressures would be required to answer this question definitively. Better characterization of the particle temperatures through optical measurements would also help to determine whether the difference in the Kentucky #9 trend is attributable to the heating rate. Pittsburgh #8 exhibited a slight increase in swelling between 10 atm and 15 atm, contrary to the other bituminous coals (Figure 5.7) and previously observed trends (see Figure 2.4).

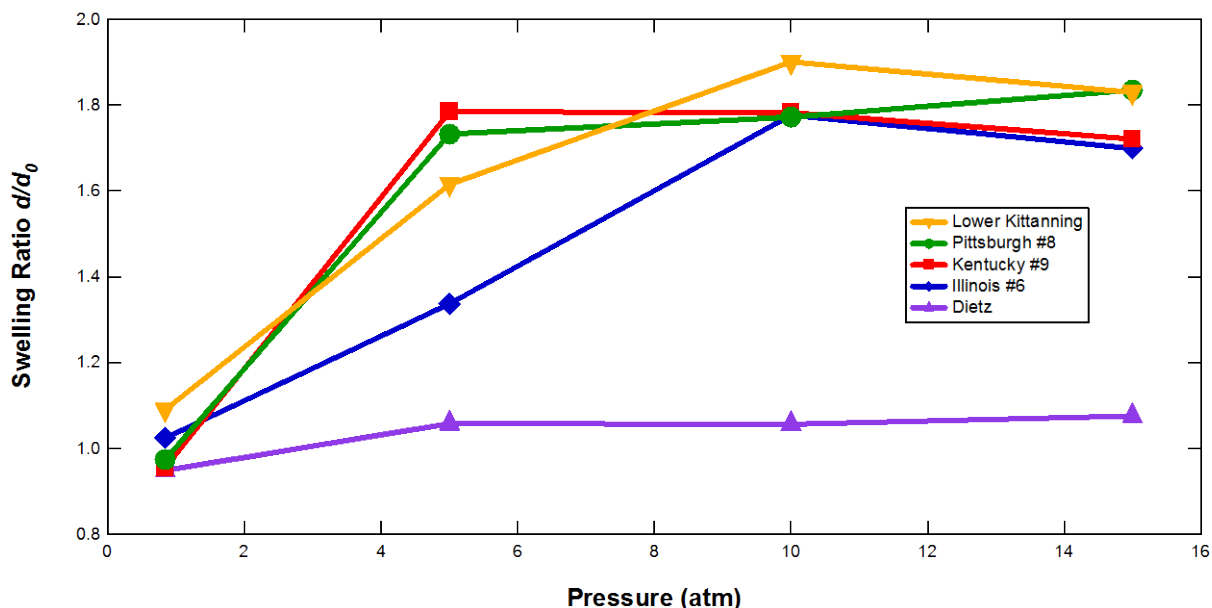


Figure 5.7. Swelling ratios in 2% O₂ with peak gas temperatures of 1700-1900 K and residence times of ~60 ms.

Some soot was observed with the chars produced at 5 atm, which may explain the larger variations in the swelling ratio observed at this pressure (Figure 5.7). Future experiments should probably use a fixed partial pressure of O₂ to inhibit soot formation rather than a fixed mole fraction of O₂. This would require that gas flames used at lower pressures be more O₂-rich.

5.3 Calculation of Particle Heating Rates

The heating rate that seemed to correlate best with swelling behavior was the maximum derivative of particle temperature with respect to residence time, assuming lumped capacitance (see Section 2.2.3):

$$\dot{T} = \left(\frac{dT_p}{dt} \right)_{\max} \quad (5.1)$$

The heating rate was calculated for a given set of entrained-flow experimental conditions using an energy balance on the particle which includes transient, convection, radiation, and reaction/vaporization terms (Fletcher, 1989a):

$$m_p c_p \frac{dT_p}{dt} = \theta h A_p (T_g - T_p) - \sigma \varepsilon_p A_p (T_p^4 - T_{surr}^4) - \frac{dm}{dt} \Delta H \quad (5.2)$$

where

$$\theta = \frac{B}{e^B - 1} \quad (5.3)$$

is the blowing parameter, which accounts for the effects of high mass transfer. The parameter m_p is the particle mass, c_p is the specific heat of the reacting coal, h is the convection heat transfer coefficient, A_p is the external surface area of the particle, T_g is the local gas temperature, T_p is the particle temperature, σ is the Stefan-Boltzmann constant, ε_p is the particle emissivity, and T_w is the wall temperature of the surroundings. The final term contains dm/dt , which is the rate of mass loss due to water vaporization and devolatilization. ΔH is the enthalpy of reaction and phase change associated with these processes. The mass flux term B in the blowing parameter is calculated from the expression (Spalding, 1955; Fletcher, 1989a; Bird et al., 2002):

$$B = \frac{\sum_{i=1}^m N_i \tilde{c}_{pgi}}{h_{loc}} \approx \frac{-\frac{dm}{dt} \hat{c}_{pg}}{2\pi d_p k_g} \quad (5.4)$$

The final expression for the B term includes the assumption of a Nusselt number of 2 and all species fluxes being directed outward from the particle. The latter assumption is appropriate for devolatilization, but should not be applied when heterogeneous reactions dominate. The term with the summation includes the molar heat capacity of each gas species leaving the particle with molar flux N_i , divided by the local convection heat transfer coefficient. The simplified version on the right includes the mass devolatilization rate and the heat capacity of the gas mixture leaving the particle in mass units. The denominator of the simplified expression includes the particle diameter and the thermal conductivity of the gas. The gas properties used to calculate B are evaluated at the film temperature. In the absence of more detailed information, the mixture heat capacity is usually approximated as the heat capacity of a single gas species, such as N_2 .

Correction factors have sometimes been used to reconcile calculated temperatures with optical measurements (Fletcher, 1989a). In the analysis of the atmospheric swelling experiments using Eastern Bituminous A in the FFB, calculations that did not include a correction factor yielded modest errors in devolatilization times for particles with diameters near 50 μm , but more significant errors for particles larger than 150 μm . In this study, a correction factor was applied to the energy balance by using the Merrick heat capacity (Merrick, 1983) evaluated at 300 K, as used by Maloney et al. (Maloney et al., 1999). This approach was tested by comparison to previous experiments that included particle temperature measurements (Fletcher, 1989a; Fletcher and Hardesty, 1992). The use of the room-temperature heat capacity yielded calculated particle temperatures that were consistent with previous measurements and calculations (Figure 5.8).

This correction method was simple and seemed to work well for a wider variety of operating conditions compared to the previous method of adjusting the particle density. It also has a theoretical basis; the degrees of freedom that cause increased heat capacity at high

temperatures are initially “frozen” at high heating rates (Van Krevelen and Hoftyzer, 1976; Maloney et al., 1999). This method is not recommended for heating rates below $\sim 10^4$ K/s.

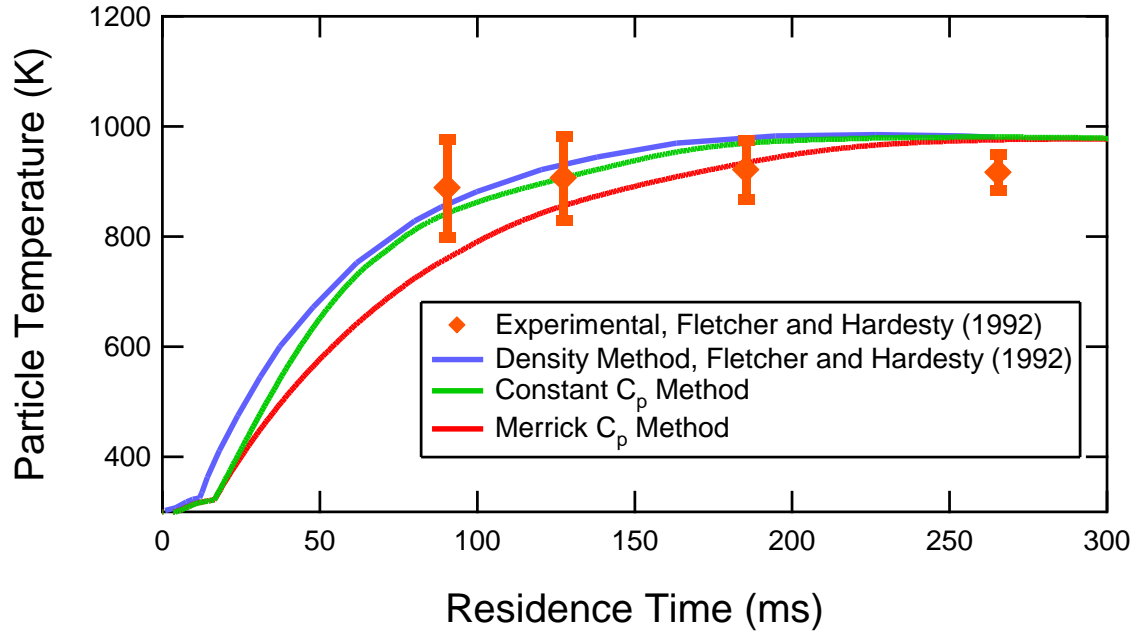


Figure 5.8. Illinois #6 temperature measurements and predictions in Sandia CDL drop-tube furnace at 1050 K.

Figure 5.8 shows a delay in the onset of heating followed by a steeper rise in temperature using the constant heat capacity method compared to the method with the adjusted density. This difference is due to the higher initial mass of water to be vaporized when the particle density is not artificially lowered. Coal particles with high moisture content will stay cool long enough to penetrate to a hotter gas region; thus high moisture content enhances the maximum particle heating rate.

For the laminar, dispersed entrained-flow reactors considered in this work, a 1-D code (Fletcher, 2011) using the CPD model (Fletcher et al., 1992; Genetti et al., 1999) was used to solve the particle energy balance (Equation 5.2). Gas temperatures in the region of the coal

injector have high uncertainty and large gradients; slight deviations in the paths of particles lead to a distribution of particle temperature histories. Throughout this work, gas temperatures measurements were used for distances greater than ~ 1 cm from the location where coal was injected into the hot reactor (Fletcher and Hardesty, 1992). The temperature at the injector was assigned the value of 300 K. The code used to calculate the energy balance interpolates in a linear fashion between temperatures at specified locations. This procedure should be followed to make comparisons to the heating rates used in this work.

5.4 High Heating Rate Swelling Model Development

Two major regimes of bituminous coal swelling behavior have been observed (Figure 5.2). Regime 2, corresponding to heating rates greater than $\sim 10^4$ K/s, is of primary interest for applications utilizing pulverized coal. In this regime, swelling initially decreases rapidly with increasing heating rate up to $\sim 10^5$ K/s. It appears that the swelling ratio approaches an asymptotic minimum of ~ 0.9 at higher heating rates. This swelling model is primarily intended to represent behavior in Regime 2. The model is intended to represent coal swelling in dispersed entrained flow, primarily using laminar-flow experimental data. Fluid dynamics should not affect swelling except through the heating rate, which is explicitly included in the model.

The starting point for the development of the swelling correlation was a compilation of Sandia combustion and pyrolysis data (Fletcher and Hardesty, 1992; Mitchell et al., 1992). The wide range of coal ranks in the data set allowed many of the effects of coal rank on swelling to be captured. The correlation matched observed shrinkage for lignites and subbituminous coals. Maximum swelling occurs at ranks slightly higher than hva bituminous, with decreased swelling for even higher rank coals. The resulting model is simple enough for CFD applications and can be used as a guide for future experiments.

During model development, different coal properties and functional forms were tried to allow a good fit of the Sandia bituminous coal data. A correlation for the swelling ratio that has the capability to match observed swelling behavior at high heating rates (above $\sim 10^4$ K/s, denoted by subscript “HHR”) is:

$$\left(\frac{d}{d_0}\right)_{HHR} = s_{var} \left(\frac{\dot{T}_{Base}}{\dot{T}}\right)^{c_{HR}} f(P) + s_{min} \quad (5.5)$$

$$s_{min} = (FC_{ASTM} + A_{ASTM})^{1/3} \quad (5.6)$$

where FC_{ASTM} is the ASTM fixed carbon fraction and A_{ASTM} is the ASTM ash fraction on a dry basis. The parameter s_{min} represents the theoretical lower limit of swelling at infinitely high heating rates, assuming that the apparent particle density is constant and the trends in the volatiles yield with coal rank are well-represented by the ASTM volatiles content.

The parameter s_{var} can be determined from experimental data at an arbitrary standard heating rate (denoted by the subscript “Base”), where the heating rate ratio reduces to unity and the heating rate exponent c_{HR} can be ignored. The standard heating rate of 5.8×10^4 K/s was selected to correspond with the average of the heating rates calculated for the Sandia combustion data, which had a range of 5.3×10^4 K/s to 6.1×10^4 K/s.

The pressure function $f(P)$ was assigned a value of unity at 1 atm, which allowed atmospheric pressure data to be used in the development of the heating rate dependence. This approach assumed that the effect of heating rate on swelling is similar at all pressures.

The CPD network devolatilization model makes use of chemical structural parameters that can be obtained from ^{13}C NMR spectroscopy (Fletcher et al., 1992), as listed earlier in Table 2.1. It seems logical that these same chemical structure properties would also affect coal swelling through the extent and rate of volatiles release and through their effect on viscoelastic properties

of the pyrolyzing coal. Because NMR parameters are only available for a few coals, correlations for these parameters were developed (Genetti et al., 1999), based on the coal proximate and ultimate analyses. The chemical structure parameters used in the current swelling model were therefore obtained from Genetti's correlations, since the proximate and ultimate analyses of coals are generally available. Genetti's correlations are reproduced in Appendix L.

After many attempts at correlating model parameters, the ratio $(\sigma+I)/M_\delta$ was selected to correlate the s_{var} term from the Sandia combustion data (shown in Table 5.2). This ratio represents the average number of attachments per aromatic cluster ($\sigma+I$) divided by the average molecular weight of a side chain (M_δ). The ratio $(\sigma+I)/M_\delta$ serves as a coal rank index; coals tend to have more cross links, shorter chains, and less oxygen as rank and aromaticity increase. Some coals do not appear in their traditional rank orders when this index system is used, but the overall swelling trends made more sense using this system compared to other rank indices attempted, including attempts to use combinations of other NMR parameters, elemental composition, and volatile matter.

The ratio $(\sigma+I)/M_\delta$ is closely related to the initial extent of cross-linking in the coal. At heating rates in Regime 2 the characteristic relaxation time of the metaplast is longer than the characteristic time of devolatilization. Viscosity is very high for highly cross-linked polymers, which may explain why swelling correlates well with this index at these high heating rates. An index that is more closely related to aromaticity may be more appropriate for correlating swelling at heating rates in Regime 1.

Table 5.2. Coal properties for correlation of s_{var} with rank

Coal	Beulah Zap	Lower Wilcox	Smith-Roland	Dietz	Blue #1
PSOC #	1507D	1443D	1520D	1488D	1445D
Source State	North Dakota	Texas	Wyoming	Montana	New Mexico
Rank	Lignite A	Lignite A	Sub. C	Sub. B	HVC Bit.
Size (μm)	106-125	106-125	106-125	106-125	106-125
Reactor, O₂ %	CCL, 6% O ₂	CCL, 6% O ₂	CCL, 6% O ₂	CCL, 6% O ₂	CCL, 6% O ₂
Collection Height	64 mm	64 mm	64 mm	64 mm	64 mm
C daf %	62.97	67.95	66.39	86.81	77.93
H daf %	4.42	5.33	5.22	5.81	5.49
N daf %	0.94	1.36	0.98	1.16	1.42
S daf %	2.00	1.36	1.76	0.40	0.71
O daf %, by diff.	29.67	24.00	25.65	5.81	14.44
Volatiles daf %	49.29	52.78	48.17	41.87	46.77
Ash %, dry	13.41	19.29	9.13	4.90	3.56
$(\sigma+I)/M_{\delta}$	0.068	0.084	0.077	0.156	0.131
Experimental d/d₀	0.92	0.93	0.87	1.07	1.16
Heating Rate (K/s)	6.07×10^4	5.93×10^4	6.19×10^4	5.34×10^4	5.90×10^4
Free Swelling Index	0	0	0	0	0
Coal	Hiawatha	Pittsburgh #8	Lower Kittanning	Pocahontas #3	
PSOC #	1502D	1451D	1516D	1508D	
Source State	Utah	Pennsylvania	Pennsylvania	West Virginia	
Rank	HVC Bit.	HVA Bit.	LV Bit.	LV Bit.	
Size (μm)	106-125	106-125	106-125	106-125	
Reactor, O₂ %	CCL, 6% O ₂	CCL, 6% O ₂	CCL, 6% O ₂	CCL, 6% O ₂	
Collection Height	64 mm	64 mm	64 mm	64 mm	
C daf %	79.69	82.62	82.76	89.01	
H daf %	5.27	5.33	4.70	4.34	
N daf %	1.22	1.77	1.41	1.03	
S daf %	0.44	2.13	3.79	0.59	
O daf % (diff.)	13.38	8.14	7.34	5.03	
Volatiles daf %	37.24	39.83	21.18	17.18	
Ash %, dry	7.17	9.95	28.48	17.04	
$(\sigma+I)/M_{\delta}$	0.143	0.164	0.208	0.246	
Experimental d/d₀	1.08	1.11	1.26	1.14	
Heating Rate (K/s)	5.29×10^4	5.76×10^4	6.12×10^4	6.03×10^4	
Free Swelling Index	0.5	7.5	8.5	6.5	
Data from (Mitchell et al., 1992)					
NMR structural parameters predicted (Genetti et al., 1999)					

The resulting correlation of s_{var} with $(\sigma+I)/M_{\delta}$ is shown in Figure 5.9 for the coals in Table 5.2. Data from two coals were omitted from the regression as non-representative (Figure 5.9). It seemed unreasonable that the Blue #1 coal (which is sometimes reported as subbituminous) would exhibit the highest swelling potential. It also seemed reasonable that

lignites would exhibit more shrinkage than subbituminous coal, so the Smith-Roland coal was also omitted. This may indicate errors in the experimental data, errors in the calculated heating rate, limitations in the accuracy of the correlations for NMR parameters, or other limitations of the model. The presence of outliers is to be expected and indicates that other factors besides the properties in the selected rank index may be influential in swelling/shrinkage for some coals, especially under oxidizing conditions.

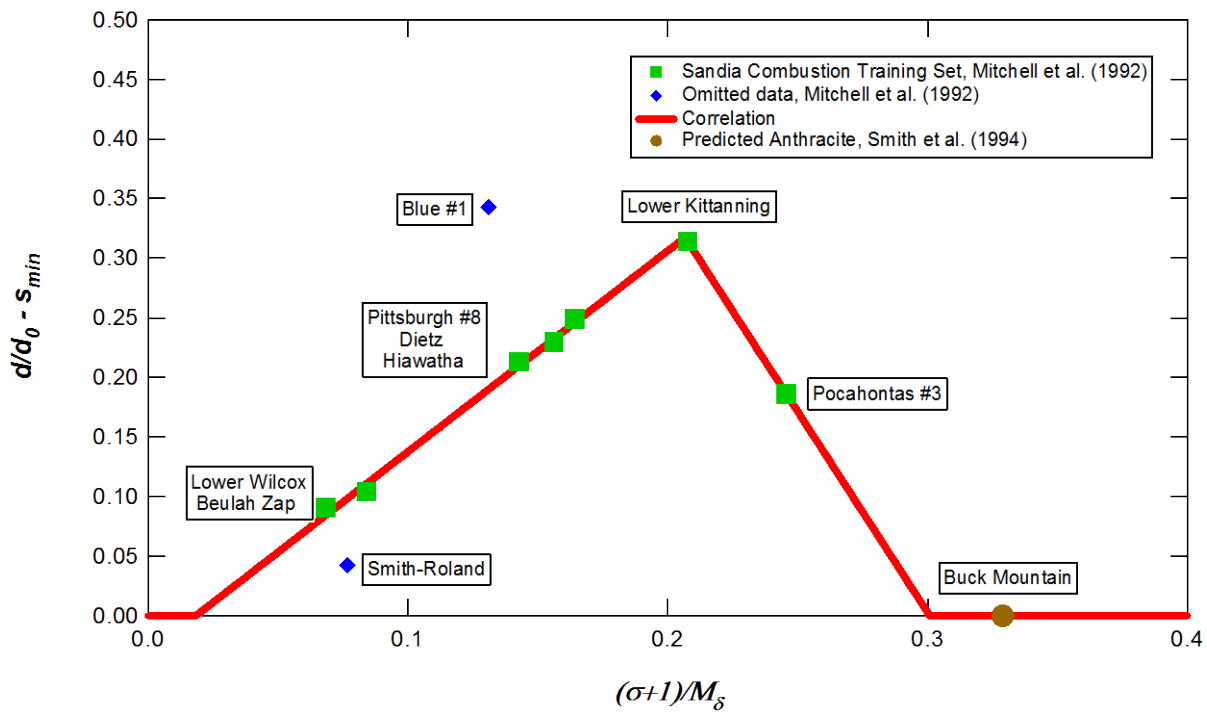


Figure 5.9. Correlation of s_{var} with NMR-based rank index using Sandia combustion data.

The free swelling index has traditionally been used as a qualitative measure of the swelling or caking characteristics of a coal, especially when large particles are used (Speight, 2005). Comparison of the parameters in Table 5.2 and Figure 5.9 shows that the four non-zero free swelling indices have a trend that is somewhat consistent with the trends in the measured

swelling ratios. However, the current model provides a more quantitative relationship between the coal rank and the swelling ratio than the free swelling index, especially for small coal particles at high heating rates.

It seems reasonable that variations in chemical structure with coal rank would cause the heating-rate dependence of swelling (c_{HR}) to first increase and then decrease with increasing rank in a manner similar to s_{var} . Therefore, the same rank index was used for both s_{var} and c_{HR} . The heating rate exponent c_{HR} was determined by rearranging Equation 5.5, provided that s_{var} had already been determined for the coal of interest or that pyrolysis swelling data were available at several heating rates. The parameter s_{var} is dependent on the choice of the standard heating rate, but c_{HR} is independent of the standard heating rate.

Linear and quadratic fits of c_{HR} from the Sandia pyrolysis data set (Fletcher and Hardesty, 1992) (see Table 5.3) are presented in Figure 5.10. The piecewise linear fit assumes that maximum sensitivity to swelling occurs at the same rank index as maximum swelling and is shown to illustrate the coal ranks where there is high uncertainty in the swelling ratio. In the absence of more extensive data, the quadratic fit was recommended because it yielded more conservative estimates, especially for low-rank coals. Coals with optimal viscoelastic properties for swelling would be expected to have shorter characteristic relaxation times compared to coals of lower ranks at the same heating rate. Therefore, swelling of coals with maximum s_{var} may not be inhibited by the high heating rates as much as coals of slightly lower ranks. This argument supports behavior of c_{HR} with changing coal rank that is close to the quadratic fit shown in Figure 5.10.

Table 5.3. Coal properties for correlation of c_{HR} with rank

Coal	Illinois #6	Blue #1	Pittsburgh #8	Pittsburgh #8	Pocahontas #3
PSOC #	1493D	1445D	1451D	1451D	1508D
Source State	Illinois	New Mexico	Pennsylvania	Pennsylvania	West Virginia
Rank	HVC Bit.	HVC Bit.	HVA Bit.	HVA Bit.	LV Bit.
Size (μm)	106-125	106-125	106-125	63-75	106-125
Reactor	CDL	CDL	CDL	CDL	CDL
Collection Height	250 mm	250 mm	250 mm	250 mm	250 mm
C daf %	74.12	75.60	81.92	84.23	88.83
H daf %	4.96	5.26	6.45	5.54	4.37
N daf %	1.45	1.32	1.65	1.65	1.06
S daf %	6.29	0.49	1.26	1.01	0.60
O daf % (diff.)	13.18	17.33	8.72	7.56	5.14
Volatiles daf %	43.37	46.77	39.83	38.69	17.18
Ash %, dry	11.3	3.48	11.2	3.73	16.72
$(\sigma+I)/M_{\delta}$	0.123	0.124	0.131	0.161	0.244
Experimental d/d_0	1.13	1.12	1.31	1.37	1.22
Heating Rate (K/s)	1.69×10^4	1.95×10^4	1.38×10^4	2.66×10^4	1.49×10^4
Free Swelling Index	3.0	0	7.5	7.5	6.5
Data from (Fletcher and Hardesty, 1992) NMR structural parameters predicted (Genetti et al., 1999)					

It is interesting to note that the value of c_{HR} calculated from the correlated value of s_{var} for Blue #1 coal fits the c_{HR} trend very well (Figure 5.10), even though this coal was omitted from the regression of s_{var} (Figure 5.9). This result suggests that there may have been some inaccuracy associated with the characterization of the Blue #1 swelling ratio shown in Figure 5.9 or the corresponding coal properties and/or heating rate listed in Table 5.2, which would justify the omission of this coal's swelling data from the development of the s_{var} correlation.

The recommended correlations for s_{var} and c_{HR} are presented in Table 5.4. The swelling measurements from the two Sandia reports (Fletcher and Hardesty, 1992; Mitchell et al., 1992) used to develop the correlations for s_{var} and c_{HR} constitute the “training set” for the swelling correlation. All other data sets that are compared to the results of the correlations in Table 5.4 are designated as “evaluation sets.”

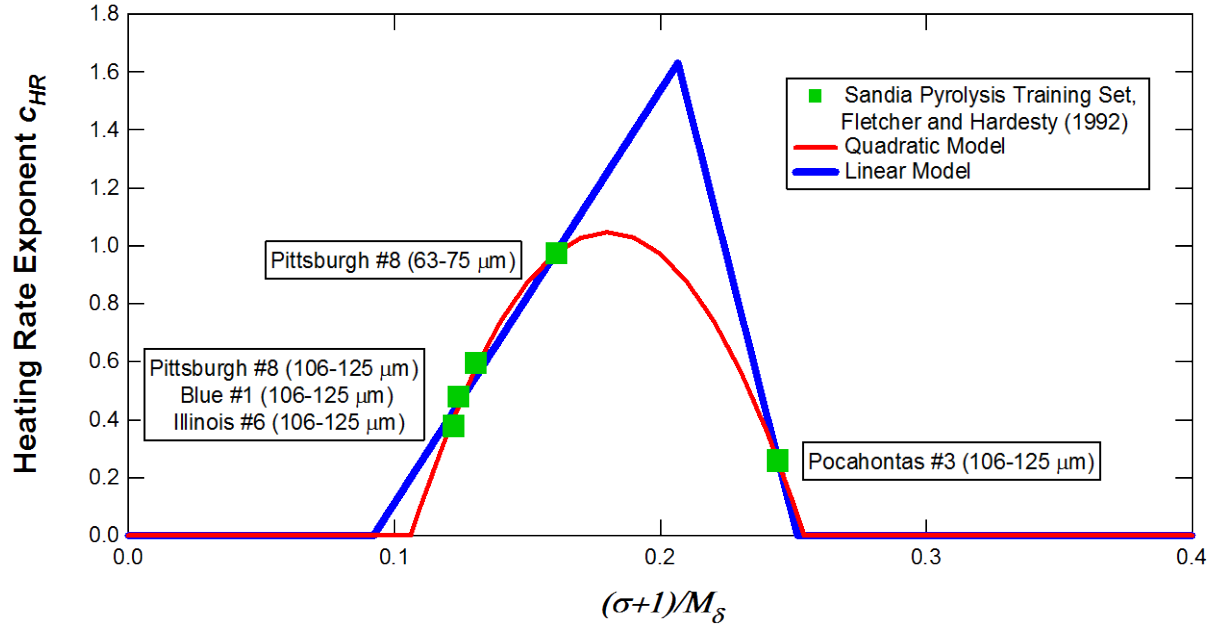


Figure 5.10. Heating rate exponent fitted to Sandia pyrolysis data.

Table 5.4. Correlations for s_{var} and c_{HR} with NMR-based rank index $(\sigma+1)/M_{\delta}$

Correlation	Range of Applicability
$s_{var} = 1.69 \frac{\sigma+1}{M_{\delta}} - 0.0309$	$0.018 \leq \frac{\sigma+1}{M_{\delta}} < 0.207$
$s_{var} = -3.37 \frac{\sigma+1}{M_{\delta}} + 1.01$	$0.207 \leq \frac{\sigma+1}{M_{\delta}} \leq 0.301$
$s_{var} = 0$	$\frac{\sigma+1}{M_{\delta}} < 0.018$ or $\frac{\sigma+1}{M_{\delta}} > 0.301$
$c_{HR} = -191 \left(\frac{\sigma+1}{M_{\delta}} \right)^2 + 68.9 \frac{\sigma+1}{M_{\delta}} - 5.16$	$0.106 < \frac{\sigma+1}{M_{\delta}} < 0.254$
$c_{HR} = 0$	$\frac{\sigma+1}{M_{\delta}} < 0.106$ or $\frac{\sigma+1}{M_{\delta}} > 0.254$

5.4.1 Comparison to Additional Data at Atmospheric Pressure

Although much swelling data are available in the literature, such data are often unsuitable for comparison to this swelling model. The required ultimate and proximate analyses are usually

provided, but there are exceptions (Zygourakis, 1993). However, the particle heating rates for the experiments are often not reported (Fermoso et al., 2010). When the particle heating rate is reported, different definitions and/or calculation procedures are often used, rendering the heating rate unsuitable for use in this model (Yoshizawa et al., 2006; Kiden et al., 2007). This model may yield very unrealistic swelling ratios if time-averaged particle heating rates are substituted for maximum instantaneous particle heating rates. Often only the order of magnitude is reported (or cited) for the heating rate, typically 10^4 K/s for a drop-tube reactor (Lee et al., 1991), which is insufficient to characterize swelling of bituminous coals for the range of 10^4 K/s to 10^5 K/s. The operating conditions are rarely reported in enough detail to allow calculation of the particle temperature history. The heating rate is somewhat sensitive to the moisture content of the coal; drying the coal before pyrolysis experiments at heating rates in Regime 2 may enhance swelling by decreasing the heating rate (Fletcher and Hardesty, 1992).

Two data sets were initially chosen to evaluate the atmospheric swelling model (see Figure 5.11), each having a broad range of well-characterized heating rates. The first set consisted of the Eastern Bituminous A data presented in this work and the accompanying BSG experiments (Eiteneer et al., 2009). The predicted rank index for this coal was 0.142. The second set consisted of data from Pittsburgh #8 coal in a helium-enhanced drop-tube reactor (Gale et al., 1995). The predicted rank index for this Pittsburgh #8 coal was 0.154. The quadratic fit of the heating rate exponent yielded very satisfactory results for both sets of bituminous coal data over the whole range of heating rates without further adjustment of model parameters (Figure 5.11). Only 2 calculated swelling ratios out of 17 deviated from the corresponding experimental values by more than 0.1. This result is a significant improvement over previous attempts to fit the two data sets directly with a universal heating rate exponent.

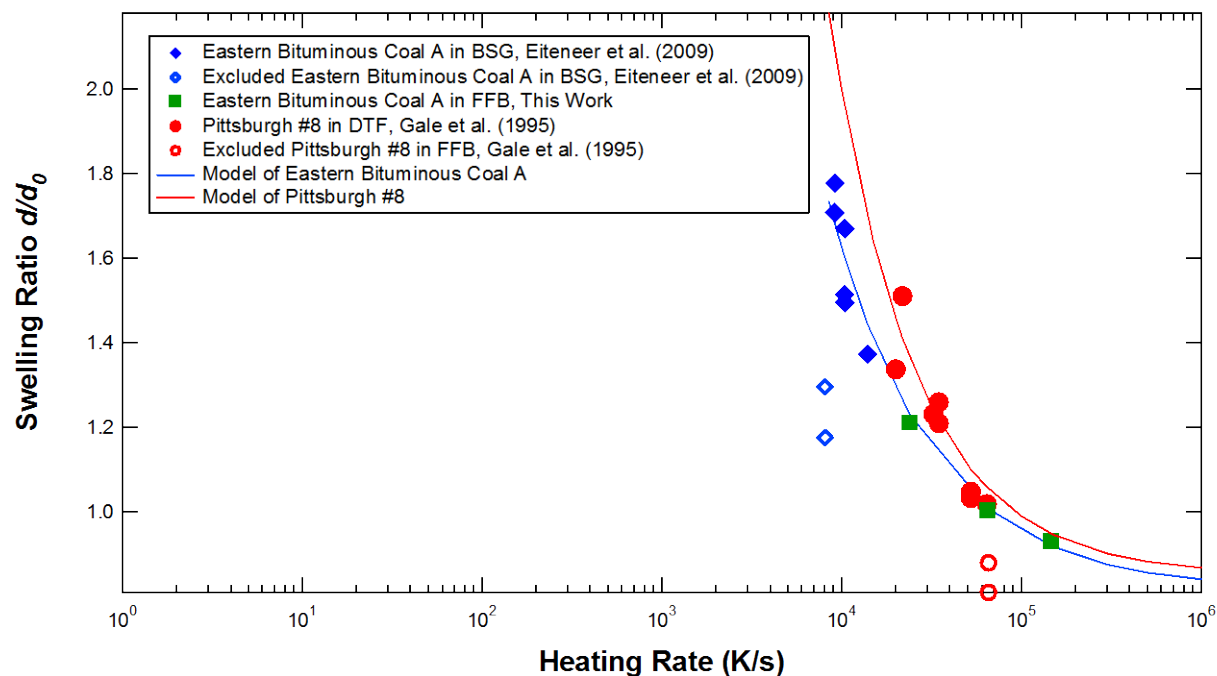


Figure 5.11. Bituminous coal validation data sets compared to model.

Four data points were excluded from the analysis in Figure 5.11 and from all other figures in this work. The Eastern Bituminous A data from the BSG included two points that did not line up with the trend (Eiteneer et al., 2009). It seems unreasonable that maximum swelling would occur in the form of such a narrow spike with respect to heating rate. It seems more likely that fragmentation would be favored in the vicinity of maximum swelling due to cenospheres with extremely thin walls. This result may be a function of the experimental apparatus, especially the char collection system.

The data of Gale et al. (1995) included two points from a flat-flame burner. This burner preceded the FFB used in the current study, and the descriptions of the experimental system indicate that the char collection system was different from the current FFB and that there were visible irregularities in the flame that lowered the particle heating rate (Gale, 1994).

Fragmentation and inaccurate characterization of the heating rate are possible causes for the very low swelling ratios observed.

The fit of the training data sets and the evaluation data sets at heating rates above $\sim 10^4$ K/s are presented in Figure 5.12. The CBK swelling correlation (Niksa et al., 2003) is also shown for the Sandia combustion data (\square in Figure 5.12). The CBK swelling model (which lacks heating rate dependence) was developed from the same Sandia combustion data used to develop the current model (Hurt et al., 1998; Niksa et al., 2003; Hurt, 2010) The current model yields a superior fit of the Sandia combustion data when compared to the CBK swelling correlation (Figure 5.12).

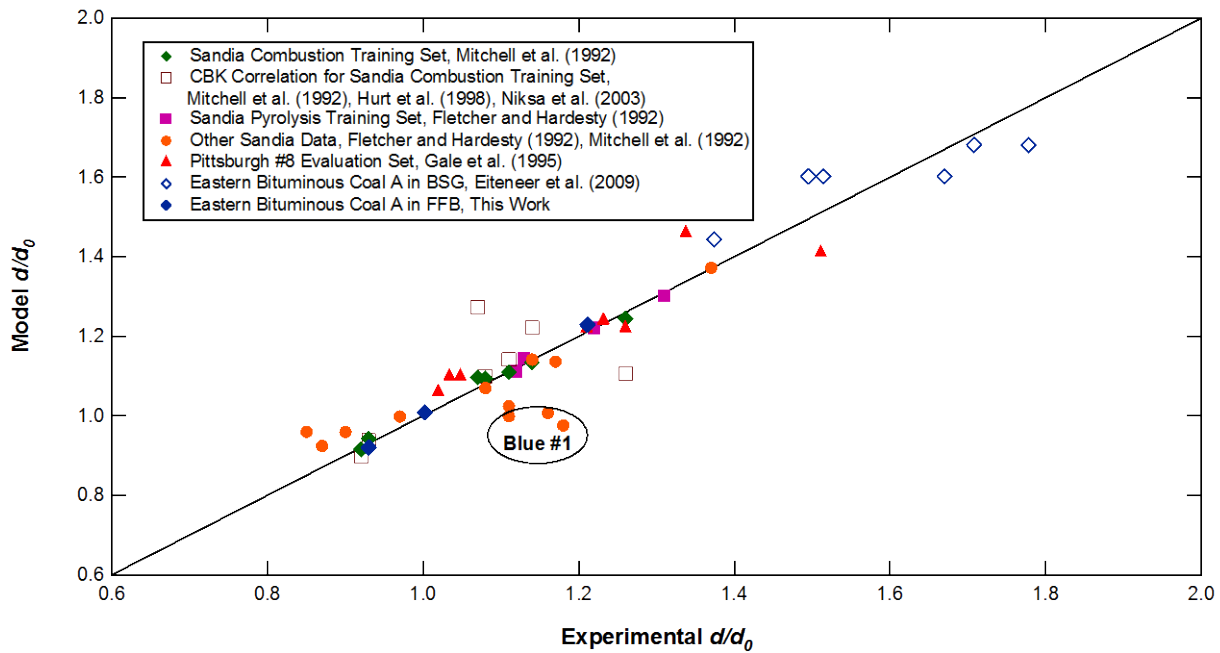


Figure 5.12. Swelling parity plot at heating rates above $\sim 10^4$ K/s. CBK swelling model also shown.

The other Sandia data presented in Figure 5.12 include 8 coals that serve as a third data set to evaluate the swelling model. These data include combustion data from three coals of

smaller size fractions (with higher heating rates) and also the two coals rejected from the s_{var} correlation (Figure 5.9) (Mitchell et al., 1992). Also included are data from seven Sandia pyrolysis experiments that were either from coals of smaller size fractions or were conducted in a flat-flame burner rather than a drop-tube furnace (Fletcher and Hardesty, 1992). The fit of the other Sandia data is generally excellent; all calculated swelling ratios deviated from the experimental values by less than 0.2, and only 4 of the 12 calculated swelling ratios deviated from experimental values by more than 0.1. Of those 4, 3 are Blue #1 (Figure 5.12), which was omitted from the s_{var} correlation (Figure 5.9). The other coal with higher deviation was Beulah Zap lignite under pyrolysis conditions. A total of 5 of the 12 calculated swelling ratios from the other Sandia data deviated from experimental values by 0.03 or less.

These three sets of data and the Sandia training sets include 11 types of coal from a wide range of ranks. Most of these coals were investigated at multiple heating rates through the use of different particle sizes, experimental facilities, and operating conditions. Together these data show that the effect of heating rate on coal swelling should not be ignored, especially for bituminous coals. The basic form of the swelling model as represented in Equation 5.5 appears to be appropriate to represent the effects of heating rate and coal rank at atmospheric pressure in Regime 2. The approach of assigning most of the rank dependence to the s_{var} term appears to be robust, but some modest rank dependence in c_{HR} is required if the model is to be applied to coals from a wide range of ranks. The correlations for these two terms may need to be updated as appropriate data from more coals become available. Figures 5.9 and 5.10 should serve as guides to determine whether a coal of interest is likely to be well-represented by this swelling model, or whether such a coal is suitable for experiments intended for use in the development of revised correlations.

5.5 Low Heating Rate Correlation

For swelling at low heating rates (Regime 1 of Figure 5.2), the data available were less suitable for direct regression of parameters. Thermogravimetric analyzers (TGA) and wire mesh reactors (WMR) operate at heating rates from below 1 K/s up to 10^3 K/s, and sometimes higher. Determination of swelling is difficult for these reactors because particles in a bed often fuse together and particles may also melt into the matrix of a heated grid (Hamilton, 1980). Experiments are often performed with coal particles larger than 200 μm (Khan and Jenkins, 1986; Zygourakis, 1993) where internal mass transfer limitations begin to be influential (Solomon and Fletcher, 1994).

Inspection of the heated grid data of Zygourakis (1993) shows that swelling in Regime 1 increases approximately linearly with the logarithm of heating rate for Illinois #6 coal (Figure 5.2). Also, the swelling ratio at 1 K/s is greater than unity for this bituminous coal. The swelling ratio appears to be relatively constant below 1 K/s. However, in another heated grid study with 100 μm vitrinite particles, very few signs of plasticity were observed at 0.1 K/s (Hamilton, 1980). This contradicted trends observed in coking applications; the authors attributed the difference to the small, dispersed particles used in their study. It was proposed that at 0.1 K/s, resistance to mass transfer in larger particles inhibits the release of tar, which plasticizes the coal melt and increases swelling. The influence of heat and mass transfer limitations on swelling may have a complex dependence on heating rate (Section 2.2.3).

The trends of the available experimental data were used in the current study to define a method to transfer the predicted composition dependence of the high heating rate model from Regime 2 to Regime 1 (Zygourakis, 1993). The approach chosen for the low heating rate (Regime 1) model is very simple compared to the high heating rate (Regime 2) model. The

Regime 1 correlation is presented mostly as a reminder not to extrapolate the Regime 2 model to heating rates much below 10^4 K/s. It is expected that the Regime 2 model will be more useful for realistic pulverized coal applications.

Several assumptions were needed to use the trends of the Zygourakis data. First, it was assumed that all major transitions in swelling behavior happen near the same heating rates for all coals. Second, the heating rate corresponding to maximum swelling was assumed to be 8.5×10^3 K/s. This value of the heating rate was chosen to allow coverage of the available Regime 2 data without excessive extrapolation of the Regime 2 model. This assumption can be adjusted when data become available to more precisely identify the location of peak swelling with respect to heating rate or the magnitude of maximum swelling. Third, the Illinois #6 coal used by Zygourakis is assumed to have ultimate and proximate analyses similar to the corresponding Argonne premium coal sample (Winans, 2010) with only small transport limitations attributable to the large particles (250-300 μm), especially at the highest heating rates. The form chosen for the low heating rate correlation is:

$$\left(\frac{d}{d_0} \right)_{LHR} = m \log(\dot{T}) + b \quad (5.7)$$

Heating rates that yield Regime 2 swelling ratios (Equation 5.5) equivalent to those measured by Zygourakis in Regime 1 were identified (Table 5.5, Figure 5.13). The low heating rate model (Equation 5.7) uses the composition dependence from the high heating rate model (Equation 5.5) by transferring swelling ratios predicted in Regime 2 to Regime 1 and interpolating between them. This approach assumes a highly consistent shape for the swelling ratio versus heating rate curve for coals of different ranks.

Table 5.5. Heating rates in Regimes 1 and 2 with equivalent model swelling ratios

Regime 1 Heating Rate	Regime 2 Heating Rate
$\dot{T}_{Peak} = 8.5 \times 10^3$ K/s	$\dot{T}_{Peak} = 8.5 \times 10^3$ K/s
1000 K/s	$\dot{T}_{Mid} = 1.63 \times 10^4$ K/s
1 K/s	$\dot{T}_{Low} = 3.37 \times 10^4$ K/s

Figure 5.13 shows two piecewise methods to implement Equation 5.7 for bituminous coals. A two-piece interpolation scheme (evenly dashed line) yields no swelling at ~ 0.1 K/s and no major transitions in behavior from that point up to the regime change. A three-piece interpolation scheme (chain-dashed line) provides a better fit of the Zygourakis data and features accelerated swelling above 10^3 K/s. Much more data in Regime 1 would be needed to determine whether either of these methods will yield more accurate swelling ratios.

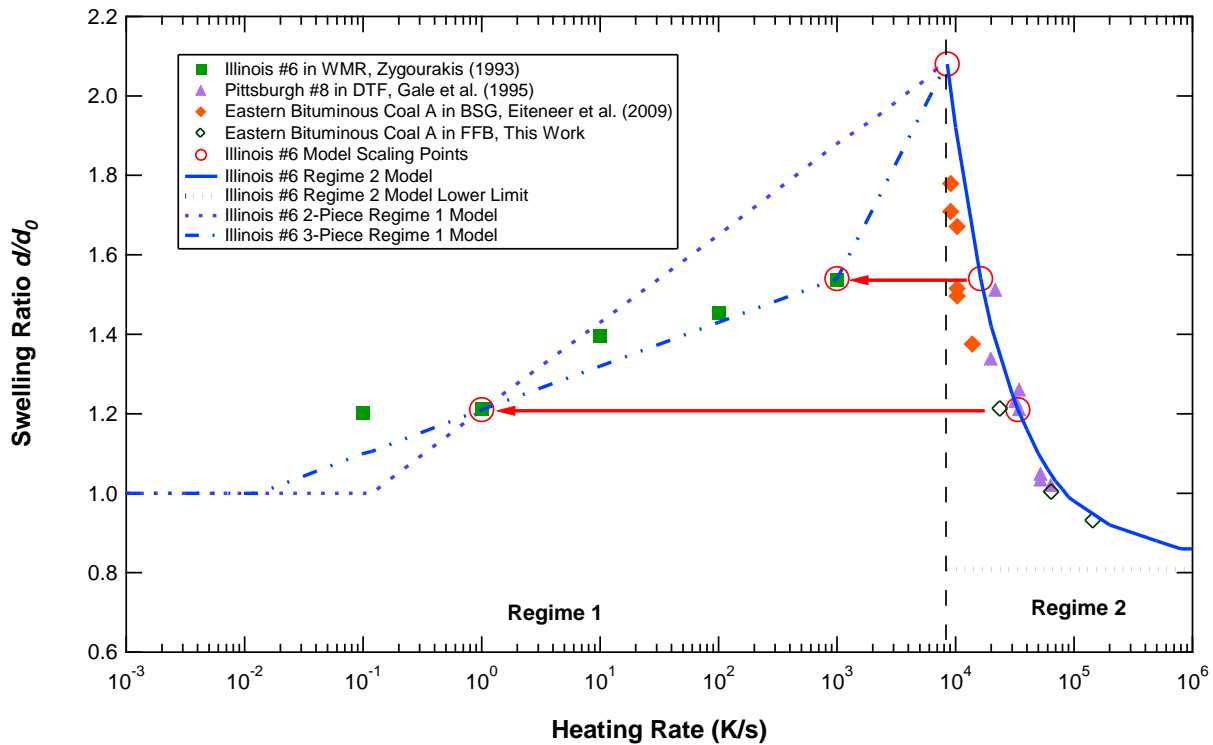


Figure 5.13. Complete swelling model (Regimes 1 and 2) for Illinois #6 data of Zygourakis.

In summary, when Regime 1 swelling ratios are needed for coals smaller than $\sim 200 \mu\text{m}$ and no data are available, the swelling ratio may be estimated using the following procedure:

1. Use the ultimate and proximate analysis with the correlation of Genetti et al. (1999) to calculate $(\sigma+1)/M_\delta$
2. Calculate s_{var} and c_{HR} using the correlations in Table 5.4
3. Use Equation 5.5 with a standard heating rate of $5.8 \times 10^4 \text{ K/s}$ to calculate d/d_0 at the Regime 2 heating rates listed in the right-hand column of Table 5.5, treating the second heating rate in the table as optional
4. Assume the swelling ratios calculated in step 3 also correspond to the Regime 1 heating rates listed in the left-hand column of Table 5.5 to fit the parameters m and b of Equation 5.7 in a piecewise manner
5. Use Equation 5.7 to interpolate the swelling ratio to the Regime 1 heating rate of interest, with unity as a lower bound for d/d_0 at the lowest heating rates

For subbituminous coals and lignites, the use of Equation 5.7 to interpolate between the maximum swelling ratio at $8.5 \times 10^3 \text{ K/s}$ and a swelling ratio of unity at 1 K/s should also yield reasonable behavior. This approach appears to yield physically realistic Regime 1 behavior (with the exception of the unrealistically sudden transitions in the slope of swelling ratio vs. heating rate) without requiring that additional parameters be fit to the insufficient data currently available.

5.6 Pressurized Swelling Model Development

Equation 5.5 contains a pressure function that should have a value of unity at atmospheric pressure. The Regime 2 model can be extended to higher pressures by specifying the form of this pressure function and fitting parameters to pressurized pyrolysis data with well-defined heating rates in Regime 2. The placement of the pressure dependence in this equation is critical, as can be seen by comparison to other swelling models. The most recent version of the CBK swelling correlation accounted for pressure effects by raising the atmospheric swelling ratio to a power that is a piecewise linear function of pressure (Niksa et al., 2003). The atmospheric swelling experiments in this work show that bituminous coals can have swelling ratios with values below 1.0 at sufficiently high heating rates (see Section 5.1). If a formulation of pressure dependence similar to the CBK swelling model were to be used in this work, it would cause a physically unrealistic reduction in swelling with increasing pressure at high heating rates.

Extension of this swelling model to elevated pressures at heating rates in Regime 1 is beyond the scope of this work. Extension of the model to sub-atmospheric pressures is also beyond the scope of this work. For application of this model, all ambient pressures can be assigned the value of 1 atm, regardless of the local value of absolute pressure. The consistency in the fit of the data obtained in laboratories at elevations within 500 feet of sea level compared to the BYU data (0.84 atm at 4700 feet above sea level) in Figure 5.12 support this approximation.

Equation 5.5 can be used to back-calculate the pressure factor $f(P)$ from experimental data if the heating rate is characterized carefully. This approach allows most of the effects of heating rate and some of the effects of coal type to be removed from the data so that the effects of pressure on swelling can be compared more directly between different coals and experimental conditions. The pressure factors obtained in this manner are sensitive to errors in the swelling

ratio, the coal ultimate and proximate analyses, predicted NMR parameters, heating rates, and the correlations for s_{var} and c_{HR} .

When pressurized swelling data are reported, associated heating rates are often reported as identical (at least to 1 significant figure) for all pressures. If such reports are accurate (which in some cases is debatable) and one of the swelling ratios in the data set was obtained at atmospheric pressure the pressure factor can be calculated from Equation 5.5 as:

$$f(P) = \frac{\left(\frac{d}{d_0}\right)_{P_2}^{-s_{\min}}}{\left(\frac{d}{d_0}\right)_{P_1}^{-s_{\min}}} \quad (5.8)$$

where the subscript P_2 indicates a char produced at high pressure and P_1 indicates a char produced at atmospheric pressure. This approach allows the effect of pressure on swelling to be determined even if the correlations for s_{var} and c_{HR} are inaccurate for the coal in question. Equation 5.8 provides a convenient analysis approach in cases where the heating rates are believed to be nearly identical at all pressures investigated, but the numerical value of the heating rate is not available or calculated in a manner that is inconsistent with this work (Section 5.3). If the coal of interest is well-represented by the model at atmospheric pressure, then the pressure factor can be calculated from Equation 5.8 with the denominator (P_1) swelling ratio calculated from Equation 5.5 at 1 atm.

When pressure factors are calculated for the data from previous studies presented in the literature review (see Figure 2.4) several trends become apparent (see Figure 5.14). Most significantly, the Illinois #6 data of Lee et al. (1991) at 10^4 K/s no longer exceed the data with higher heating rates by a factor of two to three. Rather, Lee's data are in good agreement with the Illinois #6 data of Zeng et al. (2005). This result clearly demonstrates that the effect of heating

rate is very important at elevated pressures. It appears that the relationship between heating rate and pressure dependence used in this model formulation is a useful approximation.

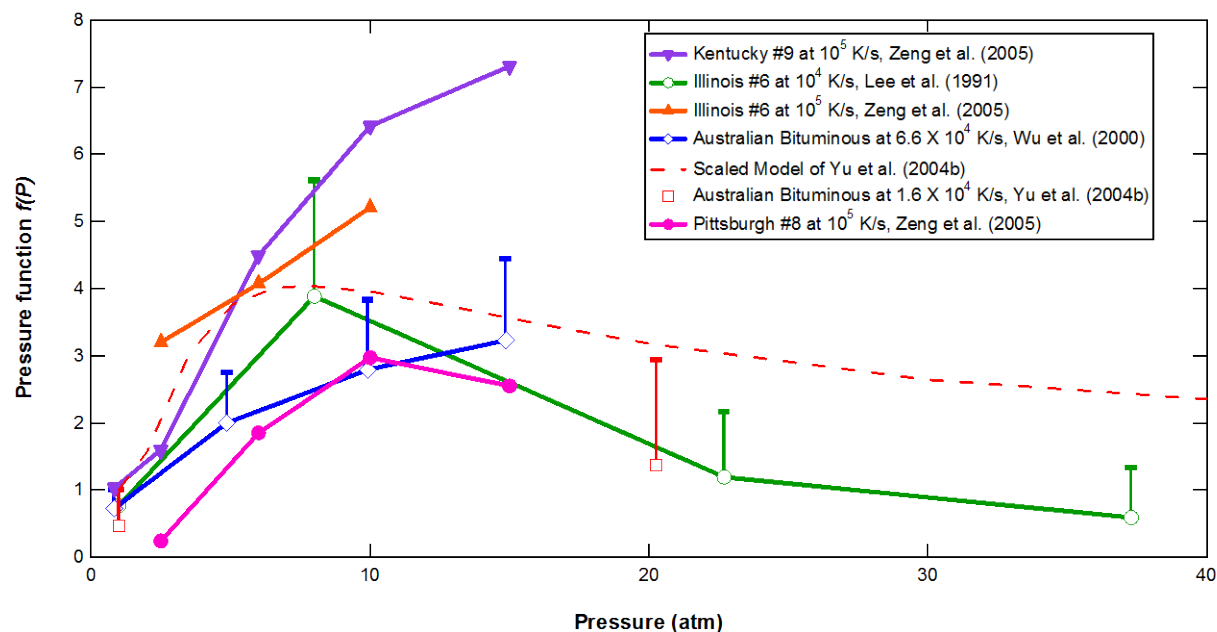


Figure 5.14. Effect of pressure on swelling for bituminous coals in previous studies.

The pressure factors in Figure 5.14 were calculated using the reported heating rates. The error bars were obtained by adjusting the heating rate to force the atmospheric pressure factor to have a value of 1. This scaling method is equivalent to using Equation 5.8, and yields a reasonable estimate of a corrected heating rate when the coals are known to be well-represented by the atmospheric pressure model. The scaled heating rates and chemical structure information are listed in Table 5.6. It appears that the mechanistic model of Yu et al. (2004b) yields behavior that is qualitatively in good agreement with the available data. This model has a maximum effect of pressure at about 8 atm, which could be considered a lower limit in consideration of other data that exhibit continued increases in swelling up to at least 15 atm (Figure 5.14). However, it is

possible that these apparent monotonic increases are caused by maximum particle heating rates that decrease as the pressure increases. In both this study and the data of Lee et al. (1991), high heat loss at elevated pressures often resulted in decreasing heating rates with increasing pressure.

Table 5.6. Heating rates and chemical structure information for coals in Figure 5.14

Coal	Source	<i>C/O</i>	$(\sigma+1)$	M_δ	<i>MW</i>	Reported HR	Scaled HR (Error Bar)
Kentucky #9	(Zeng et al., 2005)	6.15	5.20	39.3	382.3	10^5 K/s	N/A
Illinois #6	(Lee et al., 1991)	6.28	5.22	38.2	374.2	$\sim 10^4$ K/s	1.46×10^4 K/s
Illinois #6	(Zeng et al., 2005)	7.37	5.27	37.0	380.4	10^5 K/s	N/A
Australian Bituminous	(Wu et al., 2000)	9.44	4.84	28.6	308.5	6.6×10^4 K/s	9×10^4 K/s
Australian Bituminous	(Yu et al., 2004b)	9.73	4.84	30.4	344.5	1.6×10^4 K/s	3.52×10^4 K/s
Pittsburgh #8	(Zeng et al., 2005)	11.4	4.80	29.0	344.9	10^5 K/s	N/A

Heating rates of 10^4 K/s at 0.1 MPa and 7×10^3 K/s at 1.7 MPa were reported in the work of Lee et al. (1991). The pressure factors (Figure 5.14) for this data set were obtained by assuming that the heating rate was linear with the logarithm of pressure. The heating rates at 22.7 atm and 37.3 atm have extrapolated values of 6.1×10^3 K/s and 4.4×10^3 K/s, respectively. It is likely that these two measurements correspond to Regime 1 behavior, even if there was some error in this extrapolation method and/or the choice of the regime transition used in this work (8.5×10^3 K/s). If Lee's highest pressure data are in Regime 1, the extrapolated Regime 2 model (Equation 5.5) would over-estimate the effect of heating rate on swelling at these conditions. An over-estimate of the effect of heating rate would result in pressure factors that are underestimated for the Illinois #6 data of Lee et al. (1991) at pressures above 8 atm (Figure 5.14).

The remaining data in the Figure 5.14 have a few anomalies, but there is also support for the formulation of this model. The Kentucky #9 data of Zeng et al. (2005) include a swelling measurement at atmospheric pressure that is in excellent agreement with the model. However,

the Pittsburgh #8 data from the same publication appear to be too low at 2.5 atm; the pressure factor should not be less than 1. This could be due to some error in the measured coal properties, the swelling ratio, the calculated heating rate, or the correlations for s_{var} and c_{HR} . Errors in the correlations seem unlikely, since Pittsburgh #8 was in the model training set and has been shown to be well-represented by this model at atmospheric pressure (Section 5.4.1).

Scaling bars were not included for the Pittsburgh #8 series in Figure 5.14 because no atmospheric data were included in the publication (Zeng et al., 2005). The pressure factors for the Pittsburgh #8 series could be scaled up until $f(2.5atm) > 1$ by adding a uniform offset or multiplying by some correction factor. Doing so would result in maximum pressure factors between 4 and 15 for Pittsburgh #8, which would yield a more reasonable trend for this highly swelling coal.

The high extent of overlap in the pressure factor error bars in Figure 5.14 makes it difficult to identify rank-dependence for swelling trends. However, the low effect of pressure on swelling for the Australian Bituminous coal of Wu et al. (2000) compared to the other coals may be related to the low values of $(\sigma+I)$, M_δ and/or MW . This trend is particularly evident when this coal is compared to the Kentucky #9 data of Zeng et al. (2005) (see Figure 5.14 and Table 5.6).

A mathematical form for the pressure function that can fit the observed behavior is:

$$f(P) = 1 + \frac{c_{scale} [\ln(P)]^{c_{visc}}}{P^{c_{ext}}} \quad (5.9)$$

where the parameter c_{scale} determines the maximum magnitude of the effect of pressure. The parameter c_{visc} represents changes in viscoelastic properties of the metaplast that allow increased swelling with increasing pressure. The parameter c_{ext} represents the extent to which the external pressure force restrains swelling. This function has a derivative of zero at P [atm] = 1 and at P_{peak} [atm] = $\exp(c_{visc}/c_{ext})$. If c_{visc} is not an integer, this function is undefined below P [atm] = 1

because $\ln(P)$ is negative. Therefore, any ambient atmospheric pressure should be assigned the numerical value of 1 atm for application in this model.

The Wyodak swelling data from Figure 5.5 and the O₂-rich swelling data from Figure 5.7 are presented in terms of their pressure factors in Figure 5.15. The other coals from Figure 5.7 were omitted from the analysis due to the larger variation associated with the measurements. The Lower Kittanning coal exhibits the smallest effect of pressure on swelling compared to the bituminous coals of lower ranks, even though the swelling ratios are very similar. This may indicate that the vapor pressure effect tends to optimize the metaplast viscosity of bituminous coals to similar values. The subbituminous coals exhibit pressure factors close to 1. The clustering of the pressure factors at values near unity at 0.84 atm indicates that these coals are represented reasonably well by the atmospheric portion of this model. The curve fits using Equation 5.9 extrapolate to reasonable values (Figure 5.15), considering the very limited data available above 20 atm (see Figure 5.14). The predicted magnitudes of 2 to 4 for bituminous pressure functions at 40 to 60 atm in Figure 5.15 are also consistent with trends predicted by mechanistic bubble models (Yu et al., 2004b).

The curve-fits of the pressure factor shown in Figure 5.15 capture the trends of the data very well and were derived in a stepwise fashion. The steam coals Pittsburgh #8, Kentucky #9, and Illinois #6 have very similar pressure factors and are well-represented by the atmospheric model. The pressurized data from these three coals were fit to Equation 5.9 with a single set of coefficients. Values of $c_{visc} = 7.77$ and $c_{ext} = 3.47$ were obtained, yielding $P_{peak} = 9.4$ atm, which is close to the lower limit of 8 atm suggested by previous data and models (Lee et al., 1991; Yu et al., 2004b). These values for c_{visc} and c_{ext} were applied to all coals. This is equivalent to assuming that all coals exhibit peak swelling at the same pressure.

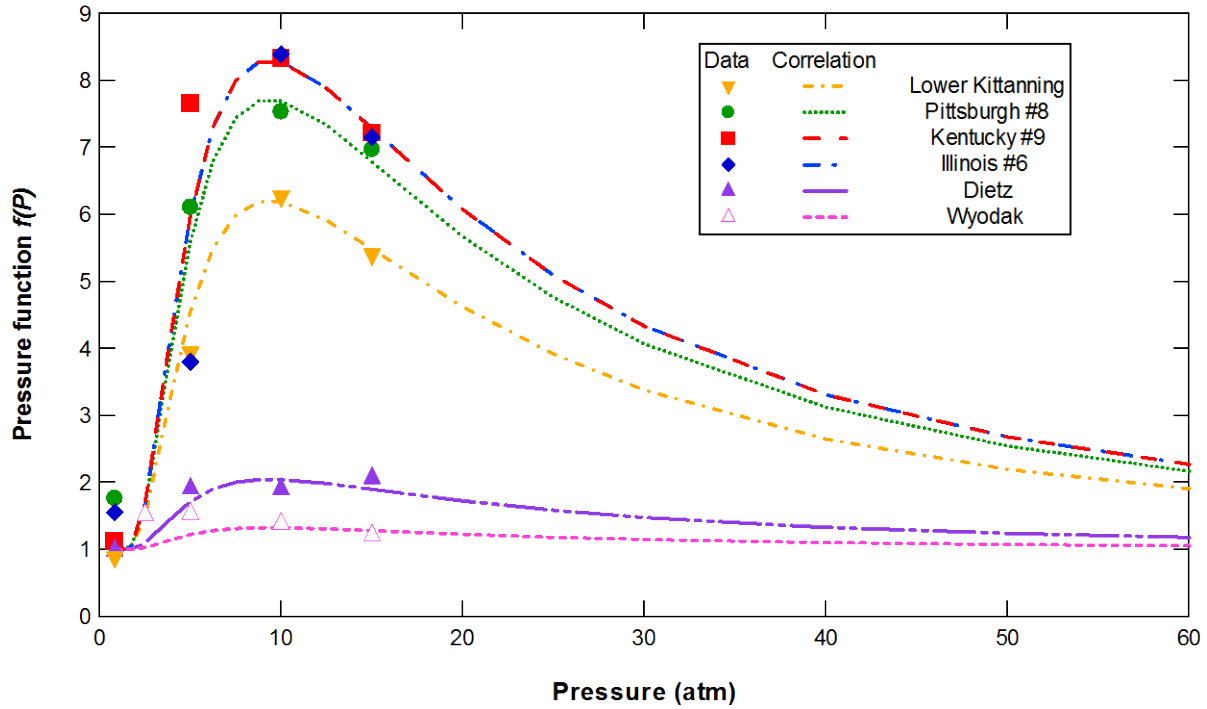


Figure 5.15. Pressure factors from HPFFB and FFB data, including curve-fits extrapolated to 60 atm.

The values of c_{scale} used in Figure 5.15 were fit for each coal using only the data from 10 atm and 15 atm. The fitted c_{scale} values are shown in Table 5.7. Only the highest pressures were used to produce the curves shown in Figure 5.15 because the atmospheric data were irrelevant to the fit and the 5 atm data exhibited more scatter. This approach seemed reasonable because practical systems that include pressurized pyrolysis of particles smaller than 200 μm at heating rates above 10^4 K/s usually operate at pressures above 10 atm. It appears that maximum pressure factors occurring near 10 atm with values of 7.5 to 8.5 are common for bituminous steam coals (see Figure 5.15), which corresponds to c_{scale} values of 30 to 33 (see Table 5.7).

Table 5.7. Scaling factors for pressure function assuming $c_{visc} = 7.77$ and $c_{ext} = 3.47$

Coal	Wyodak 2010	Wyodak 2011	Dietz	Illinois #6	Kentucky #9	Pittsburgh #8	Lower Kittanning
c_{scale}	0	1.48	4.72	33.0	32.9	30.3	23.5

The values of the scaling factor c_{scale} were compared to various measures of coal chemical structure (see Table 4.1). The simplest fit of the parameter c_{scale} was linear with respect to $(\sigma+1)$ (see Figure 5.16), which initially increased with coal rank and then began to decrease at coal ranks slightly below high-volatile bituminous. Figure 5.16 and Table 5.7 include 2 Wyodak points. The actual swelling measurements shown in Figure 5.5 were made using the coal designated as Wyodak 2010 in Table 4.1. When the Wyodak 2010 properties were used to calculate the pressure factors, a c_{scale} value of zero was derived along with a higher $(\sigma+1)$ value (see Figure 5.16). The Wyodak 2011 properties were chosen for the regression because they yielded a fit that was more consistent with the Dietz coal, which has a very similar subbituminous rank.

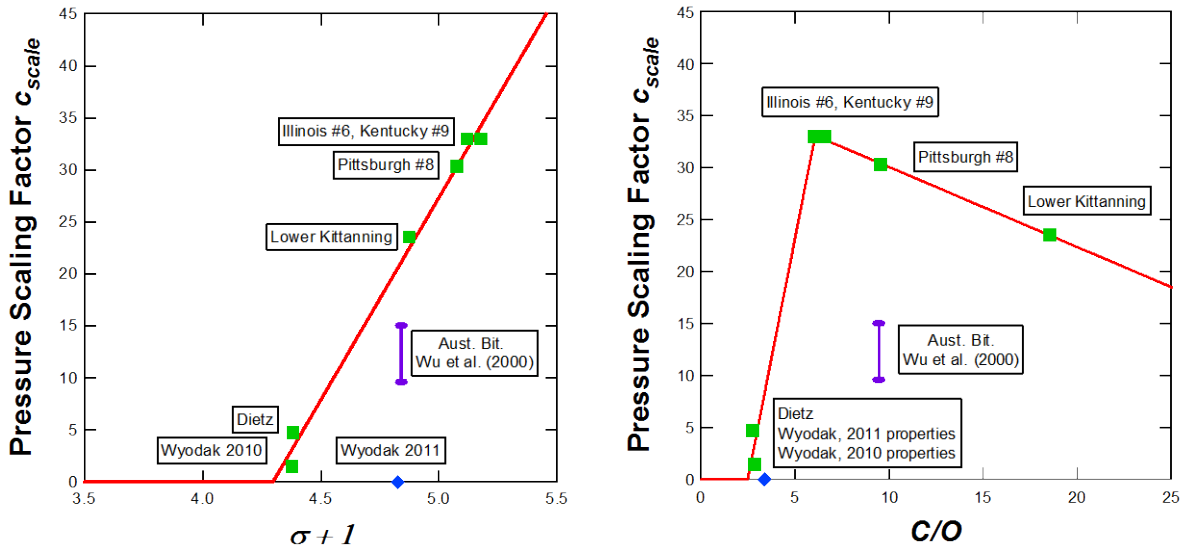


Figure 5.16. Correlations of c_{scale} versus coal rank.

More experimental data would be required to confidently evaluate the performance of the c_{scale} correlations for the highest and lowest ranks of bituminous coals. In Table 5.8, the Wyodak 2010 properties and the Pocahontas #3 properties from Table 5.2 were used to estimate c_{scale} with both correlations. It appears that the fit of c_{scale} versus C/O is less likely to be affected by small variations in the elemental analysis for very low-rank coals. The c_{scale} versus C/O correlation yields a pressure effect for Pocahontas #3 that is practically identical to the Lower Kittanning coal, which cannot be verified without experimental data. Estimates of c_{scale} for an Australian bituminous coal (see Figure 5.14) are shown in Figure 5.16 (Wu et al., 2000). These estimated c_{scale} values for the Australian bituminous coal depend on the reported heating rate and the other parameters in this swelling model, which means that the range of values shown in Figure 5.16 could be larger for this coal. The Australian c_{scale} values of Wu et al. (2000) were more consistent with the $(\sigma+I)$ correlation compared to the C/O correlation. The trends of the other pressure factors derived from literature data (see Table 5.6 and Figure 5.14) mostly increase with increasing $(\sigma+I)$, but the trend is not as good for C/O . This suggests that the $(\sigma+I)$ correlation predicts more reasonable values for a greater variety of bituminous coals. The $(\sigma+I)$ correlation is therefore recommended, especially for bituminous coals, due to its simplicity and apparent robustness.

The final pressure factors resulting from the $(\sigma+I)$ and C/O correlations (see Table 5.8) are compared to the experimental values in Figure 5.17. The scatter in the pressure factors at 5 atm appear to result from the high slope of $f(P)$ at pyrolysis pressures below ~8 atm and the uncertainties in the calculated heating rate. Because of the structure of Equation 5.5, moderate variations in the pressure factor do not have large effects on the swelling ratio, especially at heating rates $>10^5$ K/s. If a value of 0.9 is assumed for s_{min} with $d/d_{0-s_{min}} = 0.25$ at 1 atm, and the

pressure factor has a range of 4 to 12 (typical for bituminous coal), changing the pressure factor by 1 unit changes the swelling ratio by 7-13%. Variations of 8-9% are obtained using a value of $d/d_{0-s_{min}} = 0.1$ with a pressure factor range of 1 to 4 (typical values for subbituminous coal). These variations in the swelling ratio are comparable to the reported experimental error of 10% for the swelling ratio as determined by the tap density technique (Tsai and Scaroni, 1987).

Table 5.8. Correlations of c_{scale} for use in the pressure function $f(P)$ (Correlation 1 recommended)

	Correlation	Range of Applicability	R ²	Wyodak 2010 c_{scale}	Pocahontas #3 c_{scale}
1.	$c_{scale} = 38.89(\sigma + 1) - 167.1$	$\sigma + 1 \geq 4.297$	0.991	20.5	1.70
2a.	$c_{scale} = -0.7704\left(\frac{C}{O}\right) + 37.77$	$6.04 \leq \frac{C}{O} \leq 49.0$	0.998	N/A	24.1
2b.	$c_{scale} = 9.213\left(\frac{C}{O}\right) - 22.73$	$2.47 \leq \frac{C}{O} \leq 6.04$	0.986	8.15	N/A

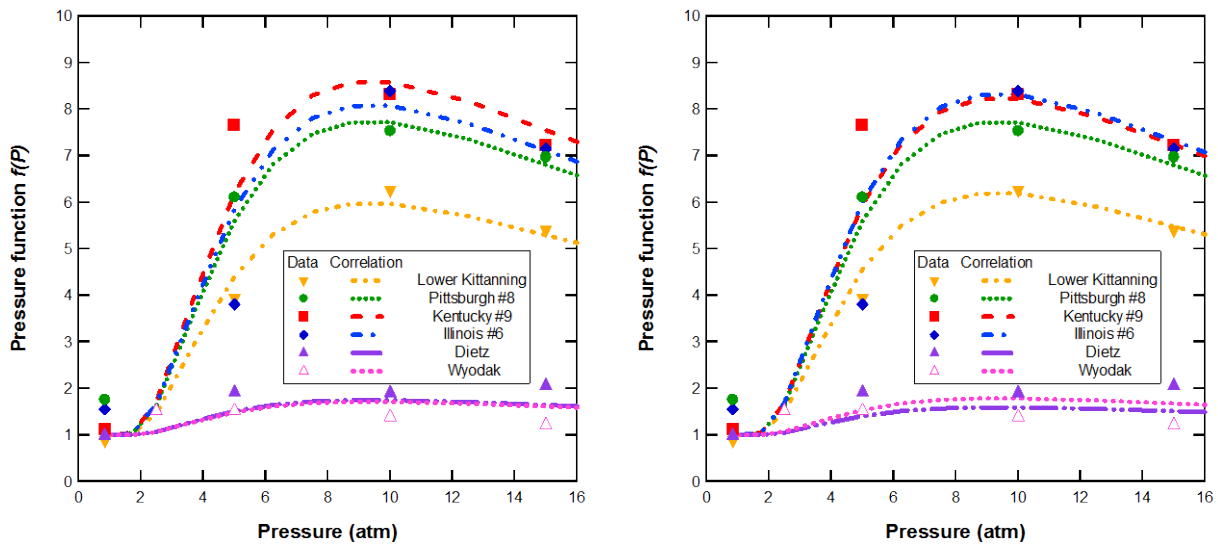


Figure 5.17. Pressure factor from fits of c_{scale} versus $(\sigma + 1)$ (left) and C/O (right) compared to experimental values.

The Australian bituminous data of Wu et al. (2000) had an effect of pressure on swelling that was smaller than most other bituminous coals in the literature (see Figure 5.14). Southern hemisphere coals are petrographically different from northern hemisphere coals, with higher concentrations of inertinite compared to vitrinite. For this reason, studies that include southern hemisphere coals often correlate pyrolysis and combustion properties with vitrinite and inertinite concentrations rather than the more convenient ultimate and proximate analyses (Benfell et al., 2000; Yu et al., 2007). Heating rates would need to be calculated with methods identical to this work to determine how well this swelling model performs for southern hemisphere coals. However, it appears that the NMR parameters predicted from correlations (Genetti et al., 1999) with the ultimate and proximate analyses yield reasonable swelling trends for the data of Wu et al. (2000) (see Figure 5.16).

5.7 Discussion of Model Application

In cases where the heating rate has been calculated properly and experimental swelling ratios in Regime 2 are not in good agreement with the model, the experimental data can be used to modify one or more terms of this correlation. Any deviations of calculated swelling ratios from measurements will probably be most pronounced at heating rates slightly below 10^4 K/s, near the transition between Regimes 1 and 2. For some coals, fragmentation may be favored at the regime transition due to very thin cenosphere walls. Fragmentation reduces swelling ratios observed using either density measurements or image analysis.

A potential difficulty arises in implementing this swelling correlation into large codes. The maximum particle heating rate must be calculated from an energy balance on the particle before the correlation can be used. However, the maximum heating rate often occurs before the extent of devolatilization becomes significant (Fletcher, 1989b). In such cases, the swelling

correlation may be applied after the time-step when a maximum heating rate is found, thereby eliminating the need for an iterative solution. A small initial peak in the heating rate typically occurs immediately before water begins to vaporize, followed by a true maximum heating rate after water vaporization is complete (illustrated in Figure 5.18). The moisture content should be checked at the time corresponding to each local maximum in heating rate to ensure that the correct heating rate is used for this swelling model.

As a simple alternative, an order-of-magnitude estimate for the heating rate may be assumed based on the experimental or industrial device being modeled. Due to the asymptotic behavior of the swelling correlation⁶, a utility boiler heating rate of 10^6 K/s may be used to calculate swelling ratios with very small error attributable to the uncertainty in the heating rate. An order-of magnitude estimate of 10^4 K/s for a conventional drop-tube reactor may produce large errors in the calculated swelling ratio for bituminous coals due to the high sensitivity of the model to heating rate at this order of magnitude, especially at elevated pressures.

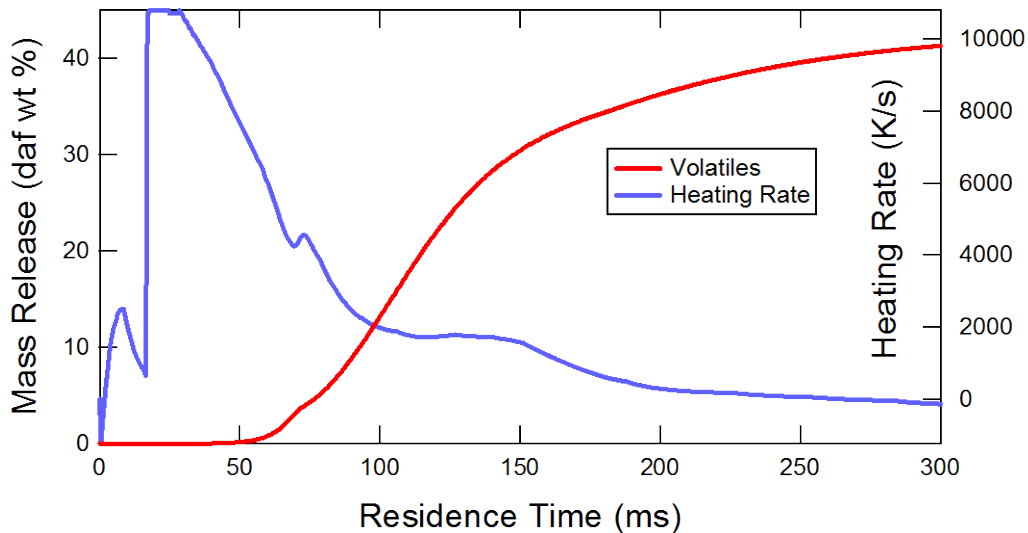


Figure 5.18. Heating rate and volatiles yield predicted for Illinois #6 coal with 3.3% moisture in a drop-tube furnace at ~ 1050 K peak centerline gas temperature (Fletcher and Hardesty, 1992).

In real systems, swelling does not occur instantaneously. A common modeling approach is to apply the swelling or shrinkage in a linear fashion proportional to the release of volatiles (Smoot and Pratt, 1979). This approach is sufficient for most models of utility boilers and gasifiers because swelling is low and devolatilization is fast at $\sim 10^6$ K/s. In the CPD model, there is a parameter \mathcal{L} which represents the labile bridge fraction in the polymer network (Fletcher et al., 1992). During devolatilization calculations, the labile bridges are converted to reactive intermediates \mathcal{L}^* that can either cleave into two side chains or react to form stabilized char bridges and light gases. As the labile bridge fraction decreases from its initial value \mathcal{L}_0 to zero, the polymer network of the coal is converted to a highly cross-linked char structure, which would tend to limit swelling. Therefore, in the 1-D CPD-based code used in this work (Fletcher, 2011), the labile bridge fraction was treated as a measure of the extent of pyrolysis. The particle diameter was varied using the following equation:

$$d_p = d_{p0} (1 + \text{swell} [1 - \mathcal{L} / \mathcal{L}_0]) \quad (5.10)$$

where *swell* is the fractional swelling that is related to the experimental or model swelling ratio by $\text{swell} = (d - d_0) / d_0 = d / d_0 - 1$.

If sufficient transient swelling data are available then a nonlinear relationship could be devised to relate transient swelling to the extent of pyrolysis. Measurements of partially pyrolyzed coals indicate that the transient swelling ratio may exceed the final swelling ratio by 3-20% (Fletcher and Hardesty, 1992). This can be explained in terms of bubbles collapsing as they burst, before cross-linking has advanced sufficiently to cause the metaplast to stiffen. The swelling model in its current form is only intended to estimate the swelling ratio of the fully pyrolyzed char.

The early occurrence of the maximum heating rate with respect to the characteristic time of devolatilization in Figure 5.18 is very typical for the atmospheric drop-tube furnaces and flat-flame burners examined in this study. This early maximum heating rate suggests that coal swelling should not strongly affect the heating rate used in this model at atmospheric pressure. However, pyrolysis calculations for conditions in the HPFFB indicated that the global maximum heating rate occurred at high extents of devolatilization at elevated pressures (see Figure 5.19). When calculations were performed for Illinois #6 coal, swelling caused an increase in convective heat transfer, which caused a slight increase in the maximum particle heating rate. The particle temperature and devolatilization rate consequently increased compared to the non-swelling case (see Figure 5.19).

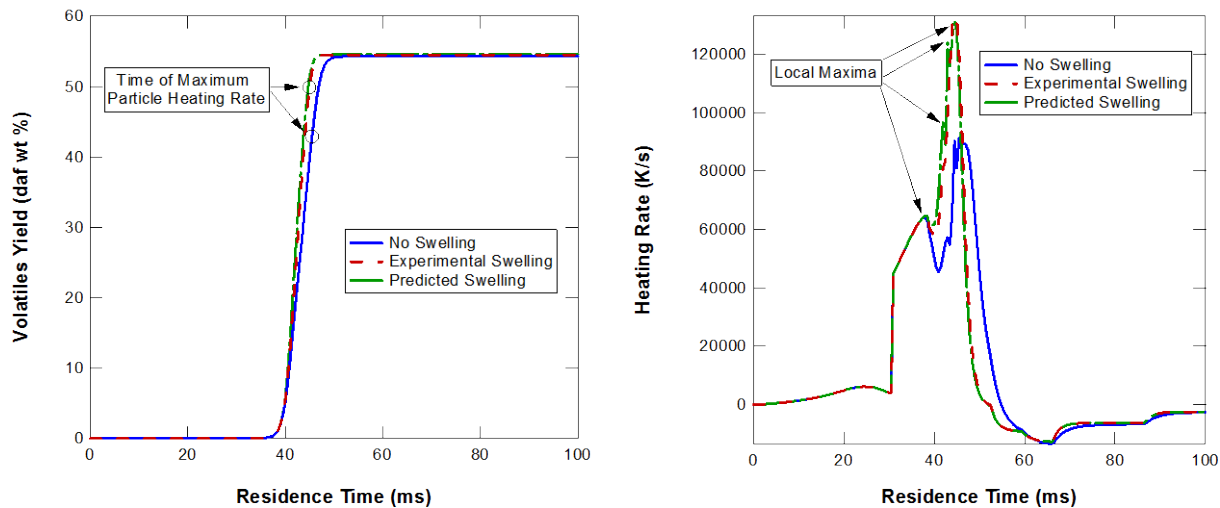


Figure 5.19. CPD predictions of volatiles yield and heating rate for Illinois #6 pyrolysis at 15 atm in the HPFFB.

When there are interactions between the heating rate and particle swelling, iteration is normally required to calculate pyrolysis behavior that is coupled to an energy balance and a particle swelling model. However, this would not necessarily increase the computational cost in

a large scale code, since iterative solution techniques are generally used in discrete phase CFD calculations. It is recommended that the swelling ratio from this model be implemented in conjunction with CPD (Fletcher et al., 1992) calculations using Equation 5.10. The use of different measures of the extent of pyrolysis other than $\mathcal{L}/\mathcal{L}_0$ with different pyrolysis models may yield differences in the predicted particle heating rate and swelling ratio if the maximum particle heating rate occurs after the onset of devolatilization. The effects of the chosen extent of pyrolysis should be evaluated for this swelling model to be used with other pyrolysis models.

An example iterative calculation was performed using the 1-D CPD-based code (Fletcher, 2011) with the 15 atm Illinois #6 pyrolysis conditions with ~2% O₂. First, the heating rate was computed for a non-swelling case, and the swelling ratio was computed manually with the $(\sigma+1)$ pressure factor correlation (see Correlation 1 in Table 5.8). This new swelling ratio was used in a new pyrolysis calculation that yielded a new heating rate, and the process was repeated. The model swelling ratio had an initial value of 1.9 at a heating rate of 9.3×10^4 K/s. The calculated heating rate changed to 1.37×10^5 K/s in a single iteration and did not change significantly with further iterations, as the swelling ratio approached the experimental value of 1.7. The solutions with the experimental swelling ratio and the iterative technique were consistent because the pressurized swelling model was developed using the maximum heating rate predicted with the experimental swelling ratio.

An alternative to iteration that was found to work well is presented in Figure 5.19. The swelling correlation developed in this work was incorporated into the 1-D CPD-based code (Fletcher, 2011). The swelling ratio was recalculated each time a local maximum heating rate greater than the previous maximum particle heating rate was found, as shown in Figure 5.19. This technique resulted in a final swelling ratio, maximum heating rate, and volatiles yield that

were consistent with the values obtained with the experimental swelling ratio (see Figure 5.19) and also with the values obtained by iterating.

Fitting experimental data to Equations 5.5 and 5.9 requires very careful characterization of the heating rate because moderate errors in the effect of heating rate are magnified in the pressure factor. It appears that swelling behavior changes most rapidly at pressures between 1 atm and 25 atm, so experiments conducted at small pressure increments within this range are very useful for model development. Pulverized coal gasifiers typically operate at 30 to 60 atm, and the limited data that have been reported above 20 atm do not include heating rates that are characterized sufficiently for application in this model (Lee et al., 1991). Therefore, measurements with well-characterized heating rates at any pressure above 20 atm would also have high value.

5.8 Summary and Conclusions

Coal pyrolysis experiments with Eastern Bituminous A at atmospheric pressure and heating rates of 10^4 K/s- 10^5 K/s confirmed the strong dependence of swelling on heating rate observed previously for Pittsburgh #8. It appears that maximum swelling occurs for bituminous coals at heating rates slightly less than 10^4 K/s. Swelling seems to approach an asymptotic minimum with a value of d/d_0 slightly less than 1.0 as the particle heating rate increases above 10^5 K/s.

Pressurized coal pyrolysis experiments confirmed that the maximum magnitude of the swelling ratio is usually less than 2 at heating rates of $\sim 10^5$ K/s. Swelling initially increased rapidly with increasing pressure for bituminous coals. Very similar swelling ratios were observed for several different bituminous coals. Little or no swelling occurred for subbituminous coals, even at elevated pressures. It was found that O₂-rich pyrolysis yielded cleaner swelling data by

inhibiting formation of large soot agglomerates that tended to increase the apparent swelling ratio by decreasing the bulk density. These data expand and clarify knowledge of swelling trends with pressure and coal rank. Maximum swelling appears to occur for most coals in the vicinity of 10 atm, and most of the increase in swelling appears to occur below 5 atm. Some of the data suggest that swelling continues to increase for some coals at pressures of at least 15 atm. However, other data show little change from 5 atm to 15 atm, suggesting that moderate decreases in the particle heating rate with increasing pressure could cause the apparent monotonic increase in swelling.

A correlation for coal swelling during pyrolysis that is suitable for CFD applications was developed. The form of the model allows the observed swelling trends at atmospheric pressure to be correctly calculated. Atmospheric model parameters were correlated with literature data using a rank index based on NMR structural parameters. This correlation was used to accurately predict swelling during pyrolysis at atmospheric pressure for Eastern Bituminous A and Pittsburgh #8 bituminous coals at several heating rates in the range of 10^4 K/s- 10^5 K/s. Comparison of the model to additional swelling data from coals that were used in the model training set also shows that the model is capable of predicting differences in swelling with varying heating rate. This implies that the basic form of the model is robust and appropriate for modeling coal swelling at heating rates greater than $\sim 10^4$ K/s. A form has also been proposed to extrapolate the composition dependence of the high heating rate model to heating rates below 10^4 K/s while maintaining expected trends.

The new swelling model includes a term that allows the effects of pressure on coal swelling to be separated from the effects of heating rate. This pressure factor approach was used to largely eliminate the differences observed in the effect of pressure on swelling ratios measured

in drop-tube furnaces and flat-flame burners. The new pressurized swelling data were used to correlate the effect of pressure with the chemical structure of the coal. It was found that some of the most commonly used bituminous steam coals have very similar pressure factors.

CHAPTER 6. GASIFICATION EXPERIMENTS AND MODELING

Gasification experiments were initially conducted with Wyodak, Eastern Bituminous A, Eastern Bituminous B, and Kentucky #9 coals, which were also used in associated pyrolysis studies (see Section 5.2.1). Pressures of 5, 10 and 15 atm were used for these initial experiments with ~20 mole % CO₂. Gas temperatures peaked at 1700 K to 2000 K at 40 ms or less and then decreased. Extended residence times were used for the gasification experiments (hundreds of milliseconds) compared to the pyrolysis experiments (tens of milliseconds). Initially, the low extents of gasification resulting from low operating temperatures were difficult to measure accurately, especially with in-situ pyrolysis. Massive soot contamination further hindered accurate determination of the extent of gasification, as described in Section 4.2. A reinjection strategy and upgrades to the collection system helped solve these problems. In these reinjection experiments the extent of gasification was increased through the use of molybdenum disilicide heaters along with higher concentrations of CO₂ in the reaction zone (see Section 4.1.3).

The final version of the HPFFB facility with improved gasification conditions was used to study Illinois #6 with the reinjection strategy at pressures of 10 and 15 atm with 40 and 90 mol % CO₂. The molybdenum disilicide heaters broke down soon after they were put in service, so the final gasification studies of Illinois #6 and Kentucky #9 chars were conducted without supplemental electric heat. Wyodak coal was subjected to the new gasification conditions without reinjection, since soot contamination and char fragmentation were not severe for this

subbituminous coal. The high reactivity of the subbituminous Wyodak made rate measurements with in-situ pyrolysis practical.

6.1 First-Order Gasification Model

A simple gasification model was coded in spreadsheet format. This model is based on a char oxidation model developed previously at BYU (Sowa, 2009). The model assumes a first-order reaction of carbon with CO₂ and an effectiveness factor of unity. The reaction rate expression for this model is:

$$\frac{1}{A_p} \frac{dm}{dt} = -k_{rxn} P_{CO_2,S} \quad (6.1)$$

where A_p is the external surface area of the particle (assumed spherical), k_{rxn} is the Arrhenius surface reaction rate constant for heterogeneous carbon gasification by CO₂, and $P_{CO_2,S}$ is the partial pressure of CO₂ at the particle surface.

The particle temperature was calculated using a simplified energy balance:

$$0 = hA_p (T_g - T_p) + \varepsilon_p \sigma A_p (T_{surr,avg}^4 - T_p^4) + \frac{dm}{dt} \Delta H_{rxn} \quad (6.2)$$

The zero on the left-hand side of the energy balance is a result of the assumption that the particle temperature is at steady state with its surroundings at each time step. The first term on the right is convective heat transfer and the second term is radiation heat transfer. The last term is heat generated in the particle or on its surface due to reaction. The parameter h is the heat transfer coefficient calculated by assuming $Nu = 2$, T_p is the particle temperature (assumed spatially uniform), and T_g is the gas temperature in the vicinity of the particle. $T_{surr,avg}$ is the temperature of the surrounding surfaces averaged over space (with view factors) and gasification residence time using the methods described in Appendix F. $\varepsilon_p = 0.8$ is the emissivity of the char particle

(Fletcher, 1989a) and σ is the Stefan-Boltzmann constant. The parameter dm/dt is the rate of change of particle mass (negative because the particle is being consumed, calculated from the reaction rate and particle external surface area), and ΔH_{rxn} is the enthalpy of reaction (positive for endothermic CO₂ gasification).

The particle temperature was calculated from Equation 6.2 using an iterative method at each time step with an under-relaxation factor; the particle temperature from the previous time step was used in the radiation term, gas properties, and the reaction rate to solve for T_p in the convective term. An under-relaxed secant method was implemented to solve for the particle temperature in cases where the successive substitution approach led to numerical instabilities. Linear correlations of the experimental swelling ratios versus particle location were used to specify the change in particle size during gasification.

The 1st-order kinetic rate expression for CO₂ gasification was set equal to the film mass transfer rate to calculate the surface partial pressure of CO₂, as follows:

$$\frac{1}{A_p} \frac{dm}{dt} = k_{rxn} P_{CO_2,S} = \frac{h_m}{\nu_{CO_2}} (C_{CO_2,\infty} - C_{CO_2,S}) \quad (6.3)$$

where h_m is the mass transfer coefficient calculated from a Sherwood number $Sh = 2$, and $C_{CO_2,S}$ and $C_{CO_2,\infty}$ are the concentrations of CO₂ at the external particle surface and in the bulk, respectively. The parameter ν is a stoichiometric coefficient; for CO₂ gasification it has a value of $\nu_{CO_2} = 0.0833$ [moles CO₂ consumed per gram carbon reacted]. Using the ideal gas law to convert concentrations to partial pressures and solving for $P_{CO_2,S}$ yields:

$$P_{CO_2,S} = \frac{h_m P_{CO_2,\infty}}{\nu_{CO_2} R_g T_g \left(k_{rxn} + \frac{h_m}{\nu_{CO_2} R_g T_p} \right)} \quad (6.4)$$

where R_g is the universal gas constant and $P_{CO_2,\infty}$ is the partial pressure of CO_2 in the bulk. Equation 6.4 was inserted into Equation 6.3 or 6.1 to calculate the gasification rate dm/dt .

The Arrhenius kinetic parameters were optimized in the spreadsheet. The MS Excel Solver was used to minimize the sum of squared errors SSE , defined as:

$$SSE = \sum_{i=1}^n (X_i^P - X_i^E)^2 \quad (6.5)$$

where X_i is the dry, ash-free percent conversion for data point i , n is the total number of data points, and the superscripts P and E refer to the predicted and experimental values, respectively. Two other statistical measures of fitness were calculated. The relative error was also calculated to indicate the average percent deviation of the model from the experimental values. The relative error RE is defined as:

$$RE = \frac{\sqrt{\sum_{i=1}^n \left(\frac{X_i^P - X_i^E}{X_i^E} \right)^2}}{n} \quad (6.6)$$

6.2 Advanced CBK-Based Gasification Models

A new gasification code named the Char Conversion Kinetics (CCK) model was developed. CCK is intended to be a combination of CBK/E (Niksa et al., 2003) and CBK/G (Liu and Niksa, 2004), and utilizes the same reaction mechanism (see Section 2.4.4). The CBK/E source code was used as a starting point (Niksa et al., 2003). Kinetics, gas transport equations, and effectiveness factors for gasification were added. CCK calculates transport of O_2 , CO_2 , H_2O , H_2 , and CO , with the assumption that any excess mole fraction not accounted for by these species is inert and has the properties of N_2 . It appears that CBK/G did not include the oxidation kinetics of CBK/E in the same code; CCK includes the full 8-step mechanism for both oxidation and gasification (see Section 2.4.4).

6.2.1 Physical Properties

Transport properties were taken from curve-fits of Chapman-Enskog theory developed at Sandia National Laboratories (Mitchell, 1980), with the exception of water. As a polar species, water is not well represented by Chapman-Enskog theory. The thermal conductivity of water from the DIPPR database (Rowley et al., 2010) was refit to an equation of the same form used for the other species in the CCK model. For the diffusivity of water, a corresponding-states formulation with a higher temperature dependence was chosen (Bird et al., 2002). The mixture thermal conductivity was approximated by weighting the thermal conductivities of individual species by their mole fractions, as in previous versions of CBK. For simplicity the transport properties of the mixture in the vicinity of the particle were assumed to be adequately represented as calculated from the bulk mole fractions and the film temperature.

Diffusivities of individual species in the gas mixture were calculated as follows (Fairbanks and Wilke, 1950; Bird et al., 1960; Mitchell, 1980):

$$D_{i,mix} = \frac{1 - y_i}{\sum_{\substack{j=1 \\ j \neq i}}^{Species} \frac{y_j}{D_{i,j}}} \quad (6.7)$$

where $D_{i,mix}$ is the effective binary diffusivity of species i in the mixture, $D_{i,j}$ is a binary diffusivity, and y_i and y_j are mole fractions. This definition of the mixture diffusivity uses a mole fraction in the numerator term. In other formulations a mass fraction has been used in the numerator (Kee et al., 1986; Paul, 1997). The different formulations result from different combinations of conventions used for velocities and driving forces (mass or molar based) (Kee et al., 2003). Equation 6.7 assumes mole fraction driving forces are used to calculate a molar flux with respect to the molar average velocity. This mixture diffusivity approach is less rigorous than the Maxwell-Stefan approach (Kee et al., 2003). However, it resulted in simpler equations, which

reduced the computational burden and simplified implementation in the existing structure of CBK.

The effective diffusivity $D_{eff,i}$ of species i in the porous char is calculated from the expression:

$$D_{eff,i} = \frac{D_{i,comb} \varepsilon_{core}}{\tau / f} \approx \frac{D_{i,mix} \varepsilon_{core}}{\tau / f} \quad (6.8)$$

where ε_s is the porosity of the carbonaceous core of the particle (Hurt et al., 1998). The parameter τ/f is the tortuosity divided by the fraction of the total porosity in the macropores (Sun and Hurt, 2000; Liu and Niksa, 2004). The combined diffusivity $D_{i,comb}$ should properly be calculated from Equation 2.10. However, in most of the CBK codes and CCK, Knudsen diffusion is neglected, which means that any experimentally observed effects of Knudsen diffusion (including changes in pressure effects) are lumped into τ/f and/or the rate parameters.

Thermodynamic properties (heat capacities and heats of reaction) in CCK were calculated using coefficients from the Gordon-McBride database (McBride et al., 2002). A simplified linear fit is used below 1000 K. As in CBK, coal char was assumed to have the properties of graphite. This assumption was checked by comparing heats of combustion calculated using the Dulong formula to the heat of combustion of graphite (Green and Perry, 1984). Three chars derived from bituminous coals and a subbituminous char (Fletcher and Hardesty, 1992) were found to have Dulong heats of combustion within 5% of the graphite value. For Beulah Zap lignite char the deviation was 13%. Results were similar using a more recent formula for the heat of combustion, with a 12% deviation for Beulah Zap (Green and Perry, 2008).

6.2.2 Calculation Methods

The particle temperature and reactant surface partial pressures in CCK were determined at each time step using a method expanded from the one used in CBK (see Figure 6.1). An energy balance was used to solve for the particle temperature in an outer loop. The reactant partial pressures at the external surface of the particle were optimized in an inner loop. An under-relaxation factor was used when the number of iterations was high in the inner loop.

CCK uses the same expression as CBK for mass transfer of O₂ in the boundary layer. Equation 2.9 was rearranged to solve for the partial pressure of oxygen at the particle surface:

$$P_{O_2,S} = \frac{P}{\gamma_{O_2}} \left[1 - \left(1 - \gamma_{O_2} \frac{P_{O_2,\infty}}{P} \right) \exp \left(\frac{\gamma_{O_2} q_{O_2}}{k_{D,O_2} P} \right) \right] \quad (6.9)$$

CBK/G used a simpler expression to calculate the surface partial pressure of reacting species (Liu and Niksa, 2004):

$$P_{i,S} = P_{i,\infty} - \frac{q_i}{k_{D,i}} \quad (6.10)$$

where P_i is the partial pressure of species i at the surface (S) or in the bulk (∞), q_i is the net depletion flux (due to reaction) of species i , and $k_{D,i}$ is the mass transfer coefficient of species i as defined in Equation 2.8. This expression was used in CCK for species other than O₂. The species H₂, CO, and CO₂ can be both reactants and products of heterogeneous reactions. For this reason, Equation 6.10 uses the *net* depletion flux q_i for each species, which is obtained from the sum of all reactions that include species i . The mass transfer rate of CH₄ was not calculated in CCK because it is a product of an irreversible reaction; the flux of CH₄ away from the particle was assumed to be equal to its production rate.

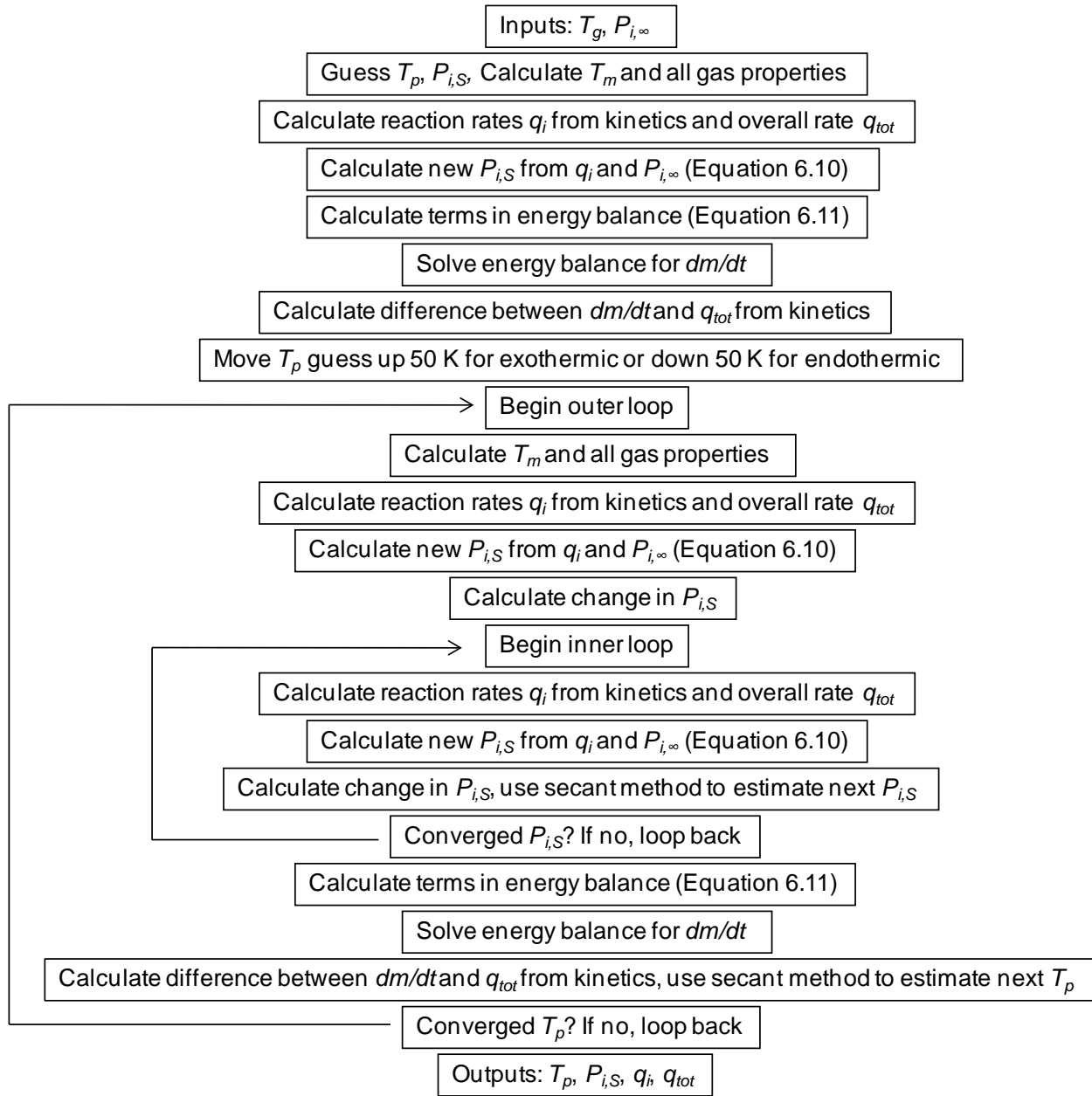


Figure 6.1. Algorithm for determining T_p and $P_{i,S}$ at each time step in CCK.

An energy balance similar to Equation 5.2 was used in the CCK code to determine the particle temperature T_p (Sun and Hurt, 2000):

$$m_p c_p \frac{dT}{dt} = \theta U A_p (T_g - T_p) - \sigma \varepsilon_p A_p (T_p^4 - T_{surr}^4) - \frac{dm}{dt} \Delta H \quad (6.11)$$

where U is the overall heat transfer coefficient that accounts for effects of the boundary layer and an ash film (if present). The effective temperature of the surrounding surfaces T_{surr} at each residence time is a required input for CCK and was calculated using the methods described in Appendix F. The final approximate expression for the B term in the blowing parameter θ was included in previous versions of CBK (see right-hand side of Equation 5.4). This expression depends on the assumption of a Nusselt number of 2 and all species fluxes having the same direction, i.e. away from the particle. The latter assumption is reasonable for devolatilization, but does not hold for heterogeneous reactions. For this reason, the more rigorous formulation for the B term from Equation 5.4 (Bird et al., 2002) was used for the CCK blowing parameter. The blowing parameter is typically close to unity under gasification conditions because the reaction rates are slow. The gas properties used to calculate the mass transfer coefficient and the blowing parameter were evaluated at the film temperature T_m .

6.2.3 Effectiveness Factors and Kinetic Mechanism

Typographical errors in the relationship between the effectiveness factors and the Thiele Moduli were found in the publication associated with CBK/G and were corrected in CCK (Liu and Niksa, 2004). The correct relationship is of the form (Sun and Hurt, 2000):

$$\eta_j = \frac{1}{\phi_j} \left[\coth(3\phi_j) - \frac{1}{3\phi_j} \right] \quad (6.12)$$

where “ j ” refers to reactant species O_2 , CO_2 , and H_2O ; the effectiveness factor for H_2 is assumed to be unity.

The Thiele Moduli for gasification and oxidation reactants in CCK were calculated using the following expression:

$$\phi_j = \frac{d_p}{2} \sqrt{\frac{\rho_C v_j (n_j + 1) R_{j,S}}{2 D_{eff,j} C_{j,S}}} \quad (6.13)$$

where d_p is the particle diameter and ρ_C is the apparent density of the carbonaceous core. $R_{j,S}$ is the reaction rate of species j at the surface of the carbonaceous core and n_j is the effective or observed reaction order with respect to the partial pressure of species j . $C_{j,S}$ is the concentration of species j at the surface of the carbonaceous core. $R_{j,S}$ was calculated for CO₂ and H₂O using the expressions:

$$R_{CO_2,S} = \frac{K_{1a} P_{CO_2,S}}{1 + K_2 P_{CO_2,S} + K_3 P_{H_2O,S}} \quad (6.14)$$

$$R_{H_2O,S} = \frac{K_{1b} P_{H_2O,S}}{1 + K_2 P_{CO_2,S} + K_3 P_{H_2O,S}} \quad (6.15)$$

where

$$K_{1a} = \frac{k_7 k_4}{\omega} \quad (6.16)$$

$$K_{1b} = \frac{k_7 k_6}{\omega} \quad (6.17)$$

$$K_2 = \frac{\gamma k_4 - 2\gamma k_4' \left(\frac{D_{eff,CO_2}}{D_{eff,CO}} \right)}{\omega} \quad (6.18)$$

$$K_3 = \frac{k_6 - k_6' \left(\frac{D_{eff,H_2O}}{D_{eff,H_2}} \right) - \gamma k_4' \left(\frac{D_{eff,H_2O}}{D_{eff,CO}} \right)}{\omega} \quad (6.19)$$

$$\begin{aligned} \omega = & k_7 + \gamma k_4' \left(P_{CO,S} + 2P_{CO_2,S} \left[\frac{D_{eff,CO_2}}{D_{eff,CO}} \right] + P_{H_2O,S} \left[\frac{D_{eff,H_2O}}{D_{eff,CO}} \right] \right) \\ & + k_6' \left(P_{H_2,S} + P_{H_2O,S} \left[\frac{D_{eff,H_2O}}{D_{eff,H_2}} \right] \right) \end{aligned} \quad (6.20)$$

$$\gamma = \frac{k_7}{k_5} \quad (6.21)$$

The forward rate constants k_i ($i = 1$ to 8) and the reverse rate constants k'_i are of Arrhenius form and correspond to the steps in the CBK/G reaction mechanism as listed in Section 2.4.4. The effective gasification reaction orders in Equation 6.13 were calculated using the expressions:

$$n_{CO_2} = 1 - \frac{K_2 P_{CO_2,S}}{1 + K_2 P_{CO_2,S} + K_3 P_{H_2O,S}} \quad (6.22)$$

$$n_{H_2O} = 1 - \frac{K_3 P_{H_2O,S}}{1 + K_2 P_{CO_2,S} + K_3 P_{H_2O,S}} \quad (6.23)$$

The partial pressures in Equations 6.22 and 6.23 should properly be mean partial pressures within the porous char particle. In CCK they were approximated as the partial pressures at the surface of the carbonaceous core, as in CBK/G.

The oxidation rates in CCK were calculated as in CBK/E (Niksa et al., 2003). The char gasification rates were calculated in a similar manner using the following expressions:

$$R_{C-CO_2} = \frac{d_p}{6} \eta_{CO_2} \rho_C R_{CO_2,S} \quad (6.24)$$

$$R_{C-H_2O} = \frac{d_p}{6} \eta_{H_2O} \rho_C R_{H_2O,S} \quad (6.25)$$

$$R_{C-H_2} = \frac{d_p}{6} \rho_C k_8 P_{H_2,S} \quad (6.26)$$

The hydrogasification rate (Equation 6.26) was assumed to be 1st-order with no internal transport limitations. The q_i used in Equations 6.9 and 6.10 are defined by:

$$q_{CO_2} = R_{C-CO_2} - R_{C-O_2} f_{CO_2} \quad (6.27)$$

$$q_{H_2O} = R_{C-H_2O} \quad (6.28)$$

$$q_{H_2} = R_{C-H_2} - R_{C-H_2O} \frac{V_{H_2O}}{V_{H_2}} \quad (6.29)$$

$$q_{CO} = -[2R_{C-CO_2} + R_{C-O_2}(1 - f_{CO_2}) + R_{C-H_2O}] \quad (6.30)$$

where f_{CO_2} is the fraction of carbon converted to CO_2 through oxidation (some carbon is converted to CO). The parameter q_{tot} that is compared to dm/dt from Equation 6.11 to solve for the particle temperature (see Figure 6.1) is defined as:

$$q_{tot} = R_{C-O_2} + R_{C-CO_2} + R_{C-H_2O} + R_{C-H_2} \quad (6.31)$$

6.2.4 Kinetic Parameters

Care was taken in the development of CCK to follow the procedures reported for CBK/G (Liu and Niksa, 2004) as closely as possible so that the same correlations for rate parameters could be used. The rate parameters in CCK have the Arrhenius form:

$$k_i = A_i \exp\left(\frac{-E_i}{R_g T_p}\right) \quad (6.32)$$

where A_i is the pre-exponential or frequency factor, E_i is the activation energy, R_g is the universal gas constant, and T_p is the particle temperature. The pre-exponential factor was calculated by applying the annealing and random pore models to the initial value, denoted by $A_{i,0}$. Ratios of rate constants were used to apply the adjustments made to the rate-limiting reactions 3 and 7 to the other reactions. Table 6.1 contains the rate parameter correlations used in CCK.

A maximum temperature of 1573 K was used in Equation 6.39 at particle temperatures above 1573 K, and a minimum temperature of 1073 K was used at particle temperatures below 1073 K, as in CBK/G (Liu and Niksa, 2004). All other rate equations in Table 6.1 used the particle temperature without limitations.

Table 6.1. Rate parameter correlations used in the CCK and CBK/G models (Liu and Niksa, 2004)

$$\frac{A_{4,0}}{A_{7,0}} = 1.84 \times 10^3 \exp(C_{daf}) \quad (6.33)$$

$$\frac{A'_{4,0}}{A_{7,0}} = 3.57 \times 10^{-5} C_{daf} - 1.73 \times 10^{-3} \quad (6.34)$$

$$\frac{A_{6,0}}{A_{7,0}} = 0.5 \quad (C_{daf} \leq 90.6) \quad (6.35)$$

$$\frac{A_{6,0}}{A_{7,0}} = 0.021 C_{daf} - 1.86 \quad (C_{daf} > 90.6) \quad (6.36)$$

$$\frac{A'_{6,0}}{A_{7,0}} = -3.68 \times 10^{-8} C_{daf} + 3.2 \times 10^{-6} \quad (6.37)$$

$$\frac{A_{8,0}}{A_{7,0}} = 7.9 \times 10^{-5} \quad (6.38)$$

$$\gamma = \frac{k_7}{k_5} = 6.92 \times 10^2 \exp\left(\frac{-1.19 \times 10^4 \frac{\text{cal}}{\text{mol} \cdot \text{K}}}{R_g T_p}\right), \quad (1073\text{K} \leq T_p \leq 1573\text{K}) \quad (6.39)$$

$$E_7 = (8.41 \times 10^2 C_{daf} - 3.13 \times 10^4) \frac{\text{cal}}{\text{mol} \cdot \text{K}} \quad (6.40)$$

$$E_4 - E_7 = 1.29 \times 10^4 \frac{\text{cal}}{\text{mol} \cdot \text{K}} \quad (6.41)$$

$$E'_4 - E_7 = -1.29 \times 10^4 \frac{\text{cal}}{\text{mol} \cdot \text{K}} \quad (6.42)$$

$$E_6 - E_7 = -3.82 \times 10^3 \frac{\text{cal}}{\text{mol} \cdot \text{K}} \quad (6.43)$$

$$E'_6 - E_7 = -3.73 \times 10^4 \frac{\text{cal}}{\text{mol} \cdot \text{K}} \quad (6.44)$$

$$E_8 - E_7 = -6.21 \times 10^3 \frac{\text{cal}}{\text{mol} \cdot \text{K}} \quad (6.45)$$

6.2.5 Options and Outputs Included in CCK

As in CBK/G, a random pore model was included in CCK to account for effects of changing surface area during reaction (see Equation 2.11). The CBK/G default value of 4.6 for the structural parameter ψ_0 was also used in CCK. The surface area reduction factor f_{RPM} from Equation 2.11 was multiplied by the same oxidation and gasification pre-exponential factors used to implement the annealing mechanism. This method was used because the pre-exponential factors used in CBK and CCK include internal surface area (Sun and Hurt, 2000).

By default, the mode-of-burning parameter α was assigned an average experimental value of 0.2 in oxidation versions of CBK (Hurt et al., 1998; Sun and Hurt, 2000; Niksa et al., 2003). CBK/G used a theoretically-based value of 0.95 for gasification (Essenhigh, 1994; Liu and Niksa, 2004). When conversion vs. density data are not available, the user of CCK should determine whether oxidation or gasification is likely to dominate the overall conversion process and specify the corresponding α value of 0.2 or 0.95, respectively. This practice allows the kinetic parameters from CBK/E and CBK/G to be used. Examination of the Wyodak CO₂ gasification data using the 1st-order model confirmed that α values greater than 0.5 were more consistent with the density and diameter data.

Unlike CBK/G, no option to equilibrate the gas composition was included in CCK. However, the outputs for CCK include molar production/consumption rates for each gaseous species, which would facilitate species equilibration if CCK is integrated into larger codes. The output of CCK also includes a η factor and two χ factors for each gasification reactant (with and without the ash layer). The effective orders for each reactant species were also included (see Equations 6.22 and 6.23).

6.2.6 Nth-Order Gasification Model

A variant of CCK was developed that uses a simplified n^{th} -order chemistry model. This code, designated CCK^N, was developed to be similar to CBK8 (Sun and Hurt, 2000), which is the most widely used CBK oxidation code. The optional random pore model found in CCK was omitted in CCK^N. In CCK^N, the species O₂, H₂O, and CO₂ each react with carbon via a single step with the global rate expression:

$$R_{j,S} = k_j \left(\frac{P_{j,S}}{R_g T_p} \right)^{n_j} \quad (6.46)$$

where n_j is the reaction order for O₂, H₂O, and CO₂. This form is consistent with CBK8. The term in parentheses is the molar concentration of the gaseous reactant. H₂ gasification is calculated using the same expression as CCK (see Equation 6.26), with the partial pressure rather than the concentration raised to a power.

The effective diffusivity expression in CBK, CCK and CCK^N (see Equation 6.8) requires the user to supply a pore structure parameter τ/f , which has been assigned different values in different versions of the code. This parameter represents the tortuosity divided by the fraction of the total porosity in the feeder pores (macropores), but also absorbs neglected factors, such as contributions from Knudsen diffusion. The effect of Knudsen diffusion on the overall reaction rate was found to be negligible for char oxidation (Hong et al., 2000a), but may be more important for the slower gasification reactions (Roberts et al., 2010).

The n^{th} -order CBK8 code has successfully modeled combustion behavior for a wide variety of coals using a value of 6 for τ/f (Sun and Hurt, 2000). Codes with more sophisticated chemical mechanisms (CBK/E) have used a value of 12 for τ/f (Niksa et al., 2003; Hurt, 2010). The value of τ/f was changed in the development of CBK/E to allow the correct initial rate to be

predicted. The practice used to specify τ/f in CBK/G was not specified in detail, although the authors imply that experimental data was used to specify or scale τ/f (Liu and Niksa, 2004). However, specifying τ/f with data seems rather impractical in consideration of the number of extra measurements required, the number of adjustable kinetic parameters in the CCK models, and the number of physical phenomena that are lumped into τ/f . Additionally, the HPFFB chars were collected in small quantities that limited the practicality of surface area measurements. To be consistent with the previous CBK oxidation models, a value of 6 for τ/f was used when fitting data with CCK^N and a value of 12 was used for CCK.

6.3 CO₂ Gasification Data with 1st-Order Model

The CO₂ gasification data from the HPFFB are presented with the 1st-order model in Figure 6.2. The experimental data are also tabulated in Appendix I, and the experimental conditions are presented in Appendix G. Wyodak and early bituminous coal data with in-situ pyrolysis are included. The more recent Illinois #6 bituminous coal gasification data and some of the Kentucky #9 data were obtained using the char reinjection strategy and CO₂ partial pressures higher than 4 atm. In the latter experiments, greater time and care was taken to measure the extents of reaction directly and compare them to the values obtained using the ash tracer technique. The char reinjection technique allowed higher extents of reaction to be measured for the two experiments with Kentucky #9 bituminous coal compared to the previous experiments with this coal using in-situ pyrolysis (Figure 6.2).

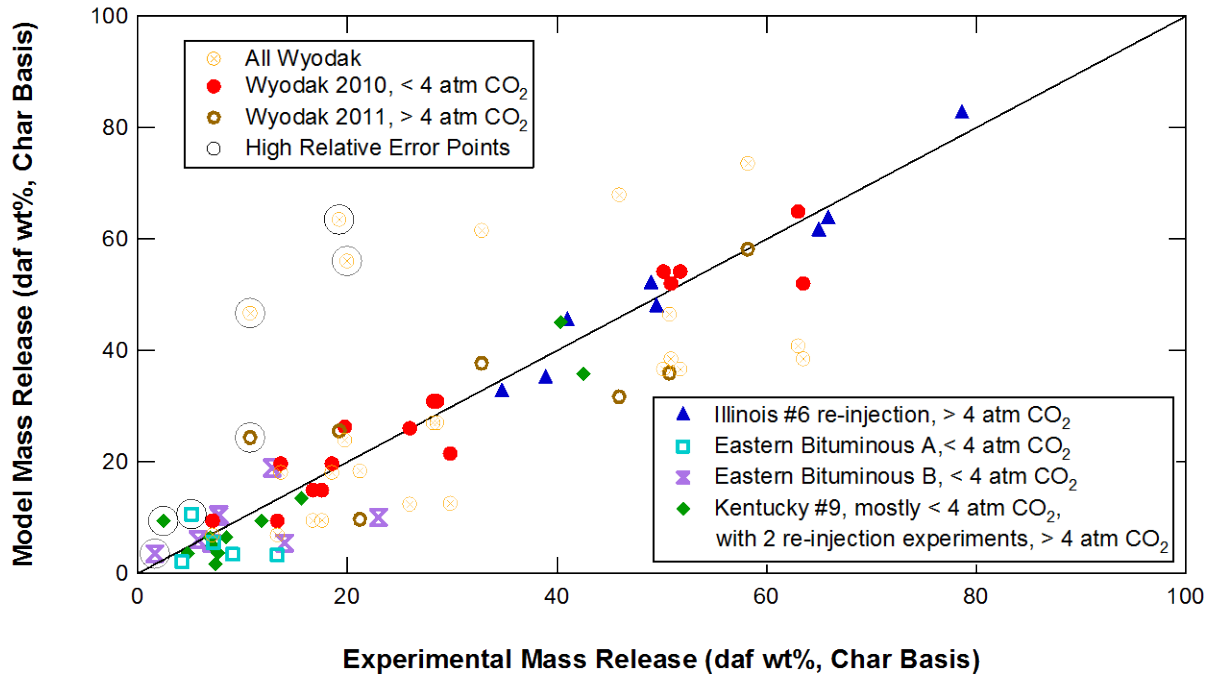


Figure 6.2. Parity plot of HPFFB gasification data with 1st-order model.

The Illinois #6 gasification data included only reinjection experiments, and some of these were conducted using the molybdenum disilicide heaters to maintain high gas temperatures for longer residence times. The effects of heaters on gas and particle temperatures are shown in Figure 6.3 for a 10 atm gas condition with 41 mole % post-flame CO₂ with reinjected Illinois #6 char. The higher apparent initial gas temperature for the case without heaters in Figure 6.3 is attributable to radial variations in the thermocouple position near the burner surface. The energy balance with a transient term used in CCK (Equation 6.11) would predict a more gradual rise in particle temperature. Another typical gas temperature profile with Nichrome wire heaters is shown in Appendix F. The Illinois #6 data in Figure 6.2 clearly show that the reinjection strategy facilitated collection of high-temperature gasification data with a wider range of conversion while reducing the experimental noise attributable to variations in volatiles yield and

contamination by soot. Reinjection was not attempted with Eastern Bituminous A and B because the available supplies were used up in the earlier pyrolysis and gasification studies.

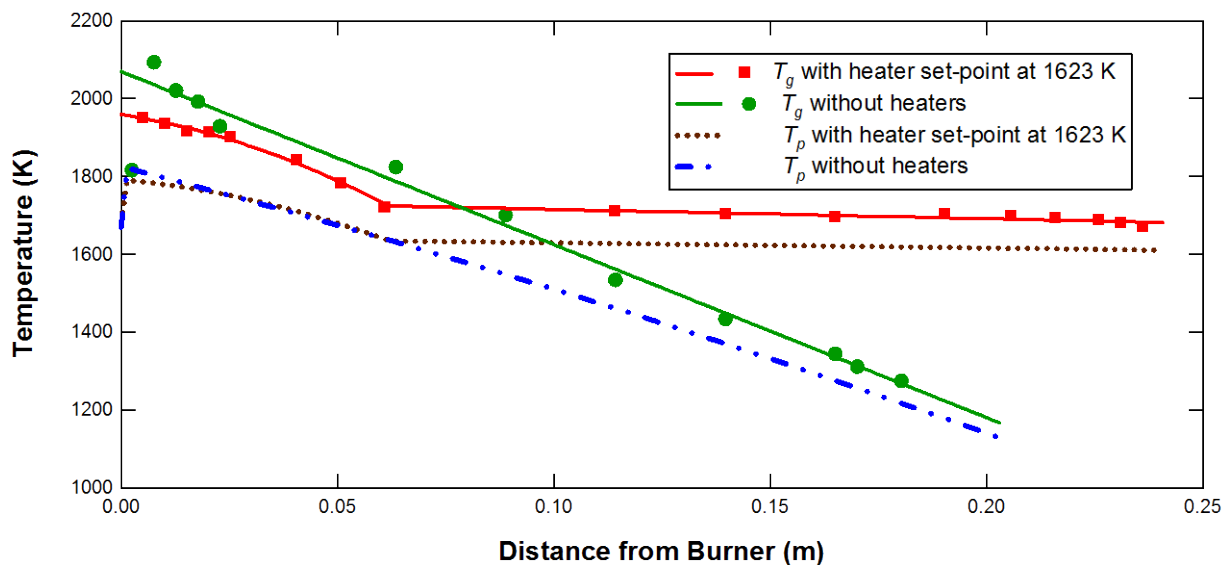


Figure 6.3. Comparison of gas and particle temperature profiles for Illinois #6 char gasification conditions.

Two groups of Wyodak gasification data are presented in Figure 6.2. The solid circles are from earlier experiments with less than 4 atm CO₂ in the HPFFB. After these first experiments, insufficient Wyodak coal remained in the 45-75 μm size range to continue experiments. Additional Wyodak coal was available from a larger size fraction, which was reground and sieved to produce more of the 45-75 μm size range. The mass mean diameter for this resized Wyodak was 10 μm smaller than the size measured with the original supply of Wyodak coal, and the density was lower (see Table 4.1). The size distributions measured in 2010 and 2011 for the Wyodak had odd shapes that suggested the coal particles clumped together in the Coulter Counter. The portions of the two size distributions with more reasonable shapes were spliced and rescaled to produce a single distribution with a mass mean diameter of 64 μm.

The open circles in Figure 6.2 correspond to experiments conducted at a later period with the resized Wyodak coal using more than 4 atm CO₂. These experiments were conducted during a transitional period when the HPFFB did not have operational heaters. Due to rapid decreases in gas temperature with increasing residence time (see Figure 6.3) and the high centerline particle velocities (see Figure 4.11), the 2011 Wyodak experiments may have had more random variation in particle residence times compared to experiments that used heaters. The crossed circles represent a fit of all the Wyodak data together. The 1st-order model converged faster and yielded a much better fit when the Wyodak gasification data were optimized as two separate series.

A representative fit of Wyodak 2010 data from two gas conditions is shown in Figure 6.4. Gasification rates were quantified by collecting chars at low residence times (corresponding to distances of 0.02 to 0.05 m above the burner in Figure 6.3) and also at higher residence times. The low-residence time data were used as the initial conditions and the activation energy and pre-exponential factors were adjusted until the best fit of the high-residence time data were obtained. This approach allowed the full pyrolysis yield to be measured and prevented uncertainties in the low-residence time particle temperature histories from influencing the model predictions.

The experimentally measured extents of gasification in Figure 6.4 represent integrated gasification rates. The best possible kinetic parameters can be obtained from this experimental technique when the temperatures are close to isothermal for a given experiment. However, the temperature was not isothermal in the HPFFB (see Figure 6.3), which made traditional statistical analysis of the joint confidence region of the derived rate parameters (Draper and Smith, 1998; Seber and Wild, 2003) difficult to implement in a meaningful way. When excessively long residence times are used with a decaying temperature profile, the temperature where gasification

rates cease to be significant becomes ambiguous and the number of combinations of Arrhenius parameters that can fit the data within a given confidence interval becomes very large. To help compensate for the drawbacks inherent in this experimental technique, care was taken to avoid using excessively long residence times at low temperatures in the HPFFB experiments so that the measurements of integrated gasification rates did not include long periods of insignificant rates (see nonzero slopes of lines in Figure 6.4).

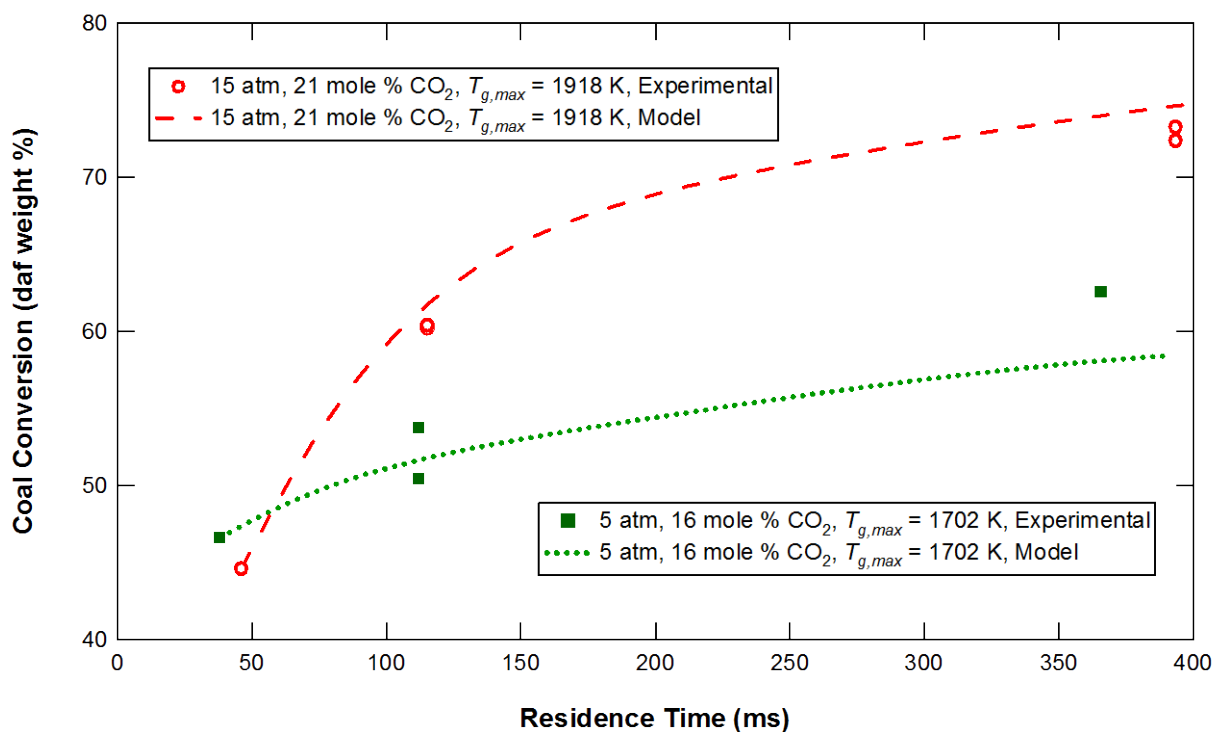


Figure 6.4. 1st-order fit of CO₂ gasification data with Wyodak 2010 subjected to different gas conditions.

The cost of doing replicates for every condition with every coal was prohibitive. Due to its high reactivity and ease of feeding, more replicates were carried out with the Wyodak 2010 coal than with any other coal in this study. A total of 6 experiments were carried out in duplicate for the Wyodak 2010 coal, and 3 of these conditions are shown in Figure 6.4. The coal

conversion varied by 0.3% to 8.7% for the 6 replicated cases. The average experimental repeatability for the Wyodak 2010 data was 3.7% of the measured dry, ash-free coal conversion. Variation of the same magnitude should be representative of the entire suite of coals.

The CPD model (Fletcher et al., 1992; Genetti et al., 1999) was used to estimate residence times required for full pyrolysis. The gas-quenched probe was set to a minimum collection height that exceeded the theoretical distance needed for full pyrolysis by at least 10%, and often more than 50%. The experimental volatiles yield at the low residence time and was sometimes lower than the ASTM volatiles yield by up to ~4% (absolute, daf), but lower volatiles yields are to be expected at elevated pressures. Additionally, the ash tracer technique used for most of the early work has the tendency to underestimate the mass release due to vaporization of the ash. For example, the Kentucky #9 had 46% (daf) ASTM volatile matter, and typically had a dry, ash-free volatiles yield of 42% in the HPFFB at 5 atm and 15 atm with collection heights of 0.75 inches and peak gas temperatures above 1700 K. When chars were made for reinjection in an environment with similar temperatures and 2 mole % O₂, with a collection height of 1.5 inches, the dry, ash-free volatiles yield only increased to 45% for the Kentucky #9 coal. These results and similar results for the other coals in this study suggest that the minimum collection heights chosen were sufficient to allow the pyrolysis reactions to run to completion.

The 1st-order model fit most of the gasification data fairly well, especially for the coals for which higher levels of conversion were measured (see Figures 6.2 and 6.4). This observation is consistent with the three-zone theory (Figure 2.6) and with previous intrinsic gasification studies (Turkdogan and Vinters, 1970). Under Zone I conditions, Turkdogan and Vinters observed 1st-order behavior for CO₂ gasification with a fixed partial pressure of CO, but a reaction order of 0.5 was observed in the absence of CO. At temperatures corresponding to Zone

II, apparent reaction orders of $n = (m+1)/2$ are typically observed, where n is the observed order and m is the intrinsic order that would be observed at temperatures in Zone I (see Figure 2.6). The variation of the CO₂ partial pressure in these experiments was large compared to the variation of the CO partial pressure, which was present in concentrations of ~10% (Appendix G). Under ideal Zone II conditions where the observation of Turkdogan and Vinters regarding the effect of CO holds true, 1st-order behavior would be expected.

The best-fit kinetic parameters obtained for different particle sizes and coals are shown in Table 6.2. The mass mean particle size was used in the fitting procedure. The rate parameters were also optimized using the maximum and minimum particle sizes from the size distribution to show the magnitude of the effect of uncertainty in particle size on apparent kinetics. The particle diameter influenced the rates through transport effects (see Figure 5.1). Additionally, the particle diameter determined the total mass available for reaction in the model. The kinetics optimized with the mass mean particle sizes in Table 6.2 are appropriate for use in models of gasification systems where the initial coal particle size and the swelling ratio are well characterized. The limiting cases of particle size in Table 6.2 were calculated for illustrative purposes and were not intended for use in modeling.

In some cases the relative error was strongly influenced by just a few data points, especially when a char basis was used and the experimental conversion was very low. Table 6.2 lists the relative error and the sum of squared errors on the experimental basis (usually a coal basis) and on a char basis. The relative error and the sum of squared errors were recalculated on a char basis without the possible outlier points. No attempt was made to refit the model to the remaining data. The points that made the largest contributions to relative error are circled in Figure 6.2. These points all correspond to conversions below 20% on a char basis, which means

the measurements were sensitive to experimental noise. The Kentucky #9 and Wyodak 2011 series had the largest decreases in the relative error when 1 point was omitted (Table 6.2). The very high sum of squared error for the combined Wyodak series and the large change in the squared error with the omission of just a few points indicates that it is more appropriate to fit the Wyodak as two independent series.

There are multiple reasons that could explain why the attempt to fit the Wyodak data with a single set of kinetic parameters was unsuccessful. First, it is possible that the two Wyodak samples had enough chemical dissimilarity to produce differences in the measured reactivities. It seems likely that the two samples of Wyodak experienced different extents of low-temperature oxidation over a storage period of ~10 years. Unfortunately, it was not possible to verify the difference using techniques more advanced than the ultimate and proximate analyses (see Table 4.1) because the supply of Wyodak 2010 was used up by the time the difference in reactivities was observed. Second, the extended range of partial pressures used may have been too large to be accurately modeled with 1st-order kinetics. This may be an indication of the onset of CO₂ saturation on the char surface, similar to the effect shown in Figure 2.7. If this is the case, a more sophisticated kinetic mechanism would be required to model the data over the whole range of partial pressures. Third, if the gas flow in the reaction zone had large temperature gradients in the radial direction, the true distribution of particle residence times could have a mean value that differed significantly from estimates based on a single optical velocity and the centerline temperature. This would be more likely when heaters were not in use, which was the case for the 2011 data.

Table 6.2. 1st-order CO₂ gasification kinetic parameters

Coal	Wyodak 2010	Wyodak 2011	All Wyodak	
Pyrolysis	In-situ	In-situ	In-situ	
Min/Mass Mean/Max Size (µm)	45/64/77	45/64/77	45/64/77	
Points fitted	16	7	24	
Mass Mean Size Fit				
A (g/cm ² /s/atm)	67.86	1.509	17044	
E (kJ/mol)	137.0	110.8	213.7	
Relative Error (experimental basis)	0.99%	2.65%	2.63%	
Relative Error (char basis)	5.14%	21.3%	19.9%	
Relative Error (char basis, w/o largest contributors to Relative Error)	N/A	13.0% (-1 point)	14.8%, 8.22% (-1, -3 points from 2011)	
SSE (experimental basis)	103.3	145.1	1774.0	
SSE (char basis)	352.2	802.0	8488.8	
SSE (char basis, w/o largest contributors to Relative Error)	N/A	615.4 (-1 point)	7194.0, 3926.5 (-1, -3 points from 2011)	
Minimum Size Fit				
A (g/cm ² /s/atm)	4.581	0.551	8.662	
E (kJ/mol)	112.7	106.4	132.2	
SSE (experimental basis)	279.8	143.9	2682.1	
Maximum Size Fit				
A (g/cm ² /s/atm)	138.2	3.259	1354000	
E (kJ/mol)	139.5	115.0	256.8	
SSE (experimental basis)	76.9	146.5	1188.4	
Coal	EBA*	EBB*	Illinois #6	Kentucky #9
Pyrolysis	In-situ	In-situ	Reinjection	In-situ and reinjection
Min/Nominal/Max Size (µm)	53/60/65	53/60/65	75/90.5/106	45/58/75 (coal), 90.5 (char)
Points fitted	5	8	8	9 coal + 2 char
Mass Mean Size Fit				
A (g/cm ² /s/atm)	0.6665	0.02941	0.8876	0.003578
E (kJ/mol)	124.4	73.46	121.3	58.94
Relative Error (experimental basis)	2.41%	2.49%	2.40%	2.11%
Relative Error (char basis)	31.0%	20.4%	2.40%	27.9%
Relative Error (char basis, w/o largest contributors to Relative Error)	28.0 (-1 point)	15.8 (-1 point)	N/A	10.8% (-1 coal point)
SSE (experimental basis)	42.3	104.2	83.4	101.5
SSE (char basis)	169.2	297.4	83.4	184.2
SSE (char basis, w/o largest contributors to Relative Error)	138.8 (-1 point)	293.6 (-1 point)	N/A	135.0 (-1 coal point)
Minimum Size Fit				
A (g/cm ² /s/atm)	0.4047	0.02404	0.7781	0.0003261
E (kJ/mol)	120.5	72.95	123.2	33.02
SSE (experimental basis)	42.4	102.4	105.9	102.2
Maximum Size Fit				
A (g/cm ² /s/atm)	0.9750	0.03351	0.9525	0.02923
E (kJ/mol)	127.6	73.75	119.0	82.23
SSE (experimental basis)	42.2	105.4	70.0	115.8
*Eastern Bituminous A and B				

A test of the Wyodak 2011 coal at a 2010 experimental condition with a CO₂ partial pressure of 3.15 atm yielded 20% char conversion. The 2011 model parameters were used to predict 22% char conversion for the Wyodak 2011 coal at this condition, which is much closer than the 65% char conversion predicted with the model parameters that were fit to the 2010 data. The 2010 model prediction deviated 226% from the test point compared to an average deviation of 16% for all of the 2010 data. The 2011 prediction of the test condition deviated 8% from the experimental value compared to an average deviation of 41% for all of the 2011 data. When the same experiment was performed previously with the 2010 coal, a char conversion of 28% was measured, which deviated from the 2010 model by 10%. The better agreement of the test condition with the 2011 model suggests that the different coal sample was primarily responsible for the different observed rate parameters. However, the higher overall deviation of the 1st-order model from the 2011 experiments with more than 4 atm CO₂ suggests that surface saturation effects may be important.

Figure 6.5 shows χ factors (as defined in Equation 2.4) for the CO₂ gasification data. A logarithmic scale was used to allow the different coals to be distinguished. Steam gasification data are also presented in Figure 6.5, corresponding to early attempts to gasify Wyodak coal (see Appendix J). The χ factors all had values below 0.3, which indicates that the HPFFB did not produce gasification behavior near the film-diffusion limit (Zone III). The χ factors increased slightly with increasing pressure. The small χ factors in Figure 6.5 suggest that Zone I behavior may have prevailed for bituminous coals at the particle temperatures in the HPFFB. The Wyodak coal exhibited decreases in both particle size and apparent density (see Appendix I), which is indicative of Zone II behavior. The size and density data for the bituminous coals were too sparse and noisy to give a strong indication of Zone I or Zone II behavior due to the low

experimental conversions and the very low densities of the cenospherical particles. The effectiveness factors in CCK and CCK^N would be better indicators of whether the CO_2 gasification data from the HPFFB correspond to Zone II or Zone I conditions.

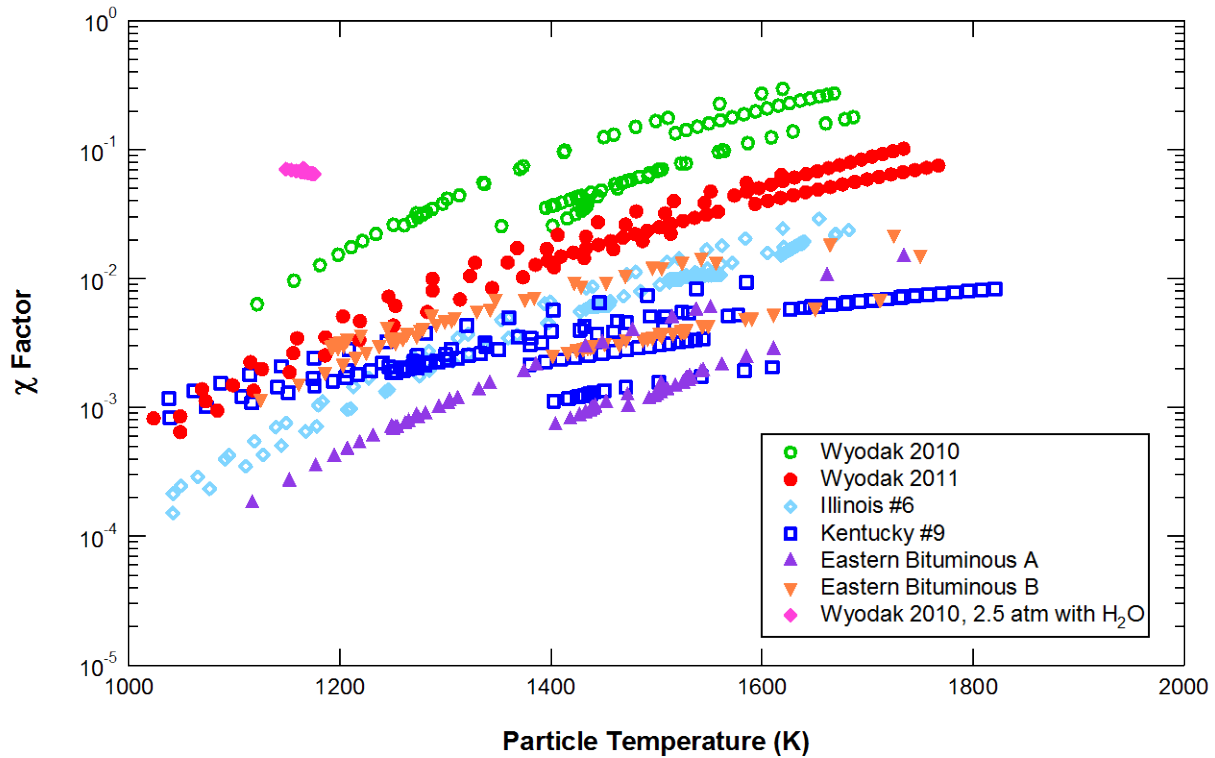


Figure 6.5. CO_2 and H_2O gasification χ -factors versus particle temperature from 1st-order model of HPFFB data.

6.3.1 Comparison of 1st-Order Rate Parameters to Literature

Figure 6.6 shows a comparison of the 1st-order CO_2 rate parameters from Table 6.2 (mass mean size) to rate parameters obtained using an atmospheric drop-tube furnace (Goetz et al., 1982). The range of gas temperatures used by Goetz is indicated with vertical lines on the plot. The Goetz particle temperatures were probably slightly lower than the gas temperatures due to endothermic gasification reactions and radiation to cold surfaces such as the collection probe.

The transitions from dashed to solid lines in Figure 6.6 indicate the particle temperature limits predicted by the 1st-order model for the HPFFB data. These particle temperature limits are averages over the temperature range where the optimized 1st-order model predicted the occurrence of the initial and final 1% daf char conversion. As such, they are somewhat conservative compared to the maximum and minimum particle temperatures. The complete temperature range of 1000 to 1800 K is shown in Figure 6.5. For the lower temperature limit, differences of up to 200 K for the last 1% conversion were not uncommon. The first 1% conversion at the highest particle temperatures occurred over a much narrower temperature difference of 1 to 30 K.

The temperature limits of the HPFFB data in Figure 6.6 indicate that the maximum particle temperatures were similar to the maximum gas temperatures of Goetz et al. (1982), and the minimum particle temperatures where gasification was measured were 100 K to 250 K lower than the lowest Goetz gas temperature. It is noteworthy that the maximum particle temperatures in the HPFFB were similar to the maximum Goetz gas temperatures, because heat loss is so pronounced in facilities operating at elevated pressures (Monson, 1992; Zeng, 2005). The higher partial pressures of CO₂ used in the HPFFB allowed conversion to be measured at low temperatures compared to the atmospheric data of Goetz. It is important to measure gasification at low temperatures as well as high temperatures to obtain the best possible activation energies and to determine at what temperatures gasification rates become insignificant.

The slopes of the lines in Figure 6.6 represent the apparent activation energies in Zone II. The Goetz activation energies range from 165 kJ/mol (39.5 kcal/mol) for Texas lignite to 236 kJ/mol (56.4 kcal/mol) for Illinois #6. The HPFFB activation energies are all lower than those of Goetz et al. (1982) for coals of similar ranks (see Table 6.2). The low activation energies may be

due to the combined effects of the high particle heating rates and elevated pyrolysis pressures on the physical and chemical structures of the char. In terms of the three-zone theory (see Figure 2.6), the low activation energies may be indicative of Zone II behavior, where the activation energy is typically $\sim 1/2$ the value measured under intrinsic kinetic conditions (Zone I).

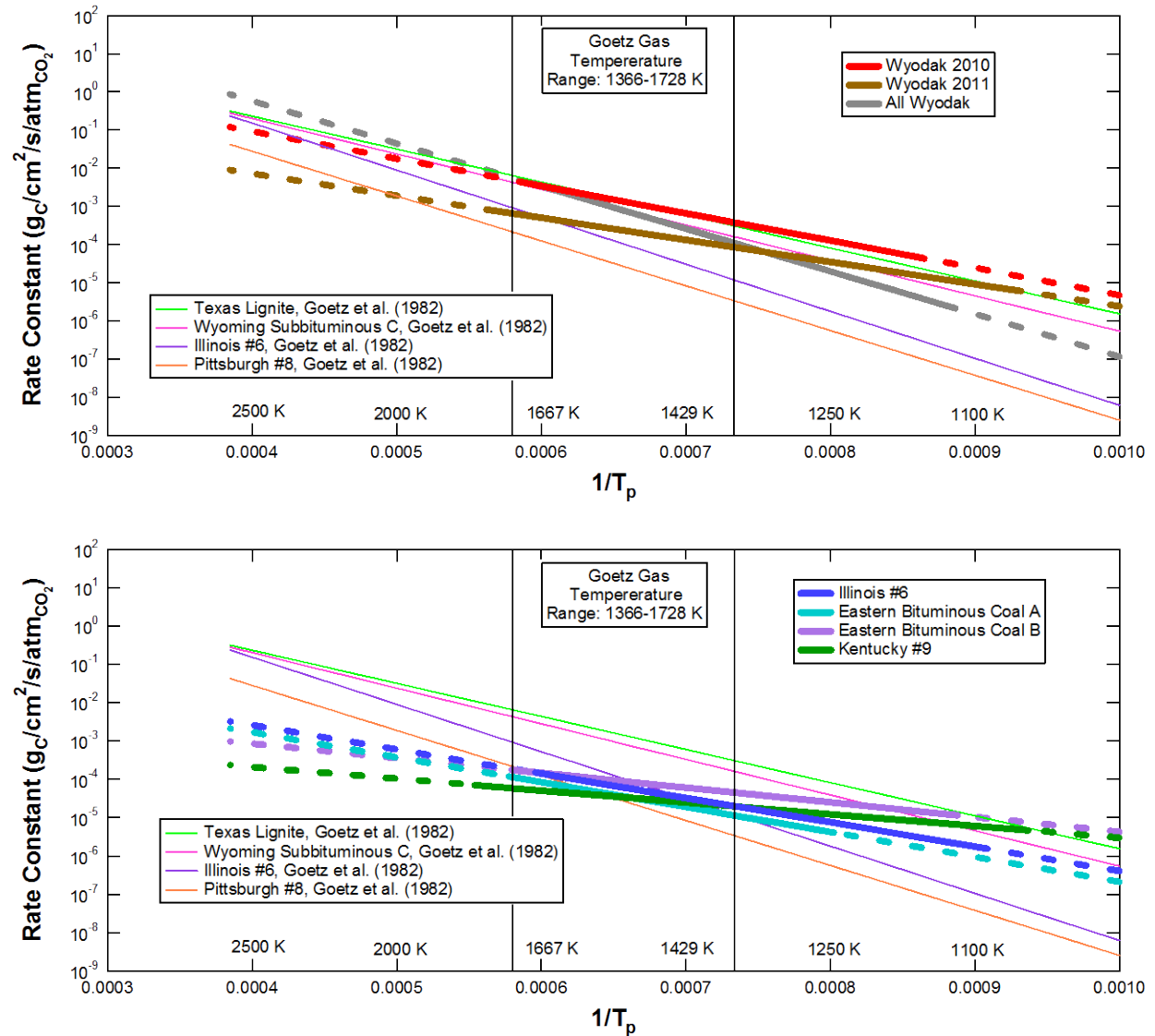


Figure 6.6. HPFFB 1st-order CO₂ gasification rate parameters for Wyodak subbituminous coal (top) and 4 bituminous coals (bottom) compared to rates of Goetz et al. (1982).

The Wyodak rate parameters from Figure 6.6 are shown again with particle size error bars in Figure 6.7. These are not statistical error bars; the bars are shown to indicate the influence of errors in the measured particle size distribution on the optimal kinetic parameters. The particle size error bars represent the optimized rate parameters that result from assuming that the particle size corresponds to the maximum and minimum sieve sizes (see Table 6.2). If the measured mass mean diameter is within a few μm of the true value, the kinetic parameters represented by the solid lines in Figure 6.7 should adequately represent CO_2 gasification behavior for any pulverized coal particles of the same type at similar particle temperatures. However, as particles increase in size beyond 150 - 200 μm , intra-particle temperature gradients become important and models that assume a spatially uniform particle temperature cease to be applicable.

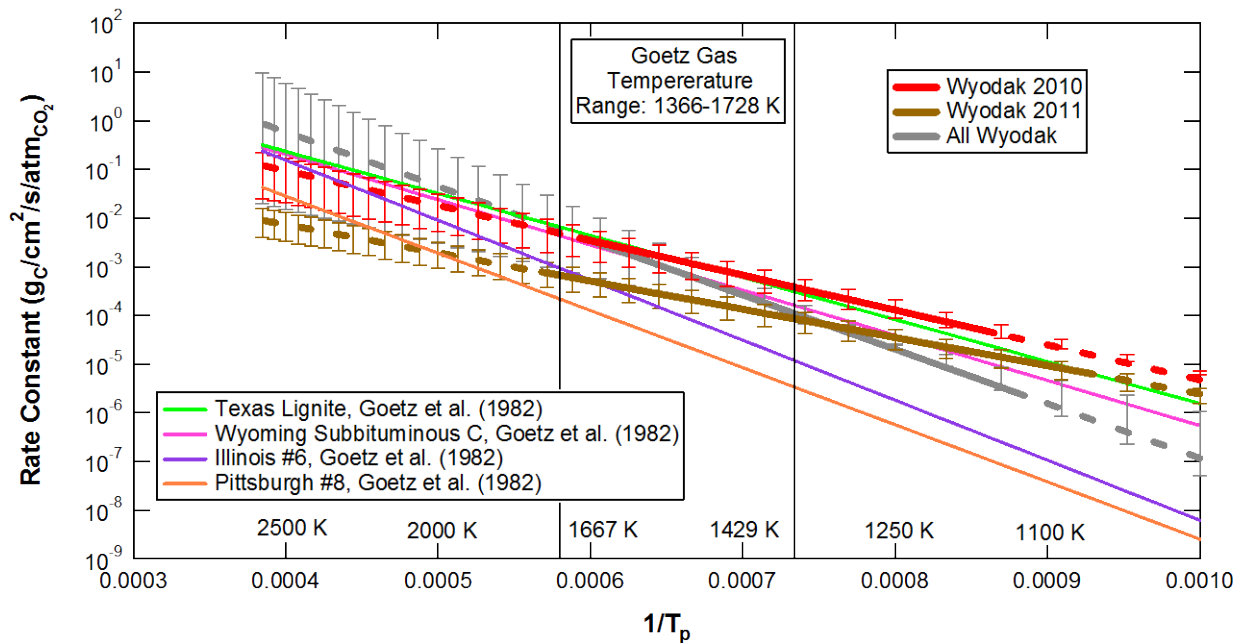


Figure 6.7. CO_2 gasification rates for Wyodak with particle size error bars and comparison to literature.

The particle size error bars for the fit of all of the Wyodak data together are very large compared to the separated series, especially at high temperatures. This is consistent with the different fits of the data shown in Figure 6.2 and provides further evidence in favor of fitting the data as two series. The fit of all the Wyodak data agrees with the 2010 rates at the high end of the experimental temperature range and matches the 2011 rates near 1300 K. This means that more of the conversion occurred at high temperatures for the 2010 data. The high conversions at higher average temperatures were achieved in 2010 through the use of Nichrome wire heaters, which helped limit heat loss in a manner similar to the more powerful molybdenum disilicide heaters shown in Figure 6.3. High conversions were achieved at lower temperatures in 2011 through the use of higher partial pressures of CO₂.

Since the 2010 parameters include a better fit of more total measurements and more gasification at high temperatures, the Wyodak 2010 kinetics are more likely to be representative of subbituminous coals. The 2010 parameters also predict rate constants that are very consistent with the subbituminous rates of Goetz et al. (1982) and do not intersect the bituminous rates of Goetz at realistic gasification temperatures. It is thought that differences in the physical structure of chars produce most observed differences in high-temperature reactivity through complex transport effects (Roberts et al., 2003). Since the physical structures of subbituminous chars are unlikely to change much when the heating rate and pyrolysis pressure are changed, it makes sense that the observed rates for subbituminous coal in the HPFFB would be similar to those in the atmospheric drop-tube furnace of Goetz et al. (1982). Greater differences would be expected for bituminous coal gasification rates obtained from atmospheric drop-tube furnaces and pressurized flat-flame burners because of the effects of particle heating rate and pressure on the particle size and physical structure of char after pyrolysis. The comparison of the bituminous

CO₂ gasification rates in the HPFFB to those of Goetz et al. (1982) shows that the differences in activation energy can be significant (see Figure 6.8). The bituminous gasification rates near 1700 K yield the most reasonable trends of reactivity with coal rank since gasification is easier to measure accurately at higher temperatures (see Figures 6.4 and 6.8).

The Eastern Bituminous B (EBB) gasification rates in Figure 6.8 have almost negligible dependence on particle size and temperature compared to all the other coals. The small error bars are due in part to the narrow size cut used for the EBB coal (see Table 4.1). The high carbon content of this coal (83%, Table 4.1) indicates that it probably has the highest rank in this suite of coals, and the trends of the Goetz data suggest that it probably also has the lowest reactivity. It is likely that the sparse EBB data were corrupted by excessive soot contamination at long residence times (see Figure 4.8). It is also possible that the measured swelling ratios used in the model were influenced by soot and/or fragmentation in the char collection system (see Figure 4.7).

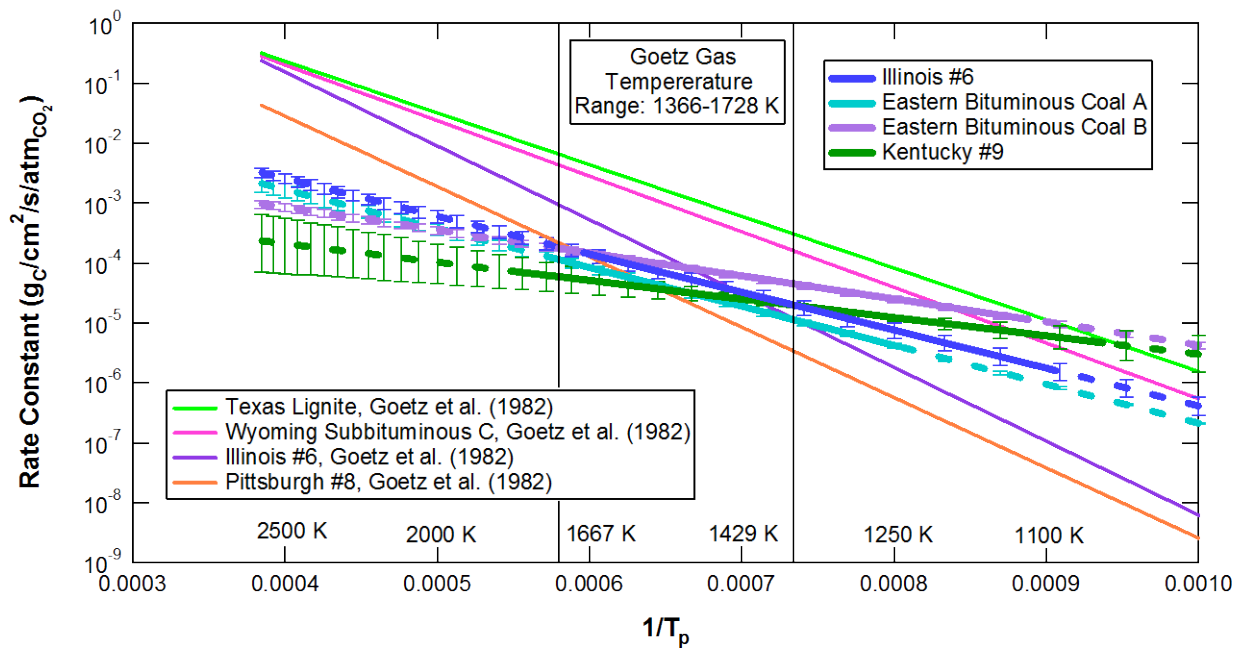


Figure 6.8. CO₂ gasification rates for bituminous coals with particle size error bars and comparison to literature.

The Kentucky #9 activation energy also appears to be suspiciously low (see Figure 6.8). However, the Kentucky #9 rate parameters determined from the low-CO₂ experiments changed very little when the 2 reinjection experiments with high CO₂ were added, and the fit was reasonable (Figure 6.2). The Kentucky #9 data include fewer measurements with heaters compared to the Wyodak and Illinois #6. For the reinjection experiments at 15 atm with ~90% CO₂, the model predicted that ~25% of the total gasification occurred below particle temperatures of 1250 K, and another 25% occurred from 1500 K to the maximum of 1580 K. At the 10 atm reinjection condition, ~33% of the gasification occurred below 1275 K, and another 33% occurred from 1400 K to the maximum of 1520 K. These results suggest that the Kentucky #9 rates should be quite reliable at temperatures of about 1250 K to 1450 K, which is about the middle third of the inverse temperature range in Figure 6.8.

It seems odd that so many bituminous coal gasification rates would be identical at ~1400 K (see Figure 6.8). However, the Kentucky #9, Illinois #6, and Eastern Bituminous A (EBA) all have carbon content of 77% to 79% (see Table 4.1); it appears that they are fairly similar in rank. The NMR parameters listed in Table 4.1 are also similar for these three coals. The similarity of the bituminous rates to each other and to the rates of Goetz et al. (1982) suggests high pressure and high heating rates affect CO₂ gasification rates most strongly through transport effects relating to the particle size developed during pyrolysis. Char particle size effects were accounted for in the 1st-order model and also in the work of Goetz through use of the experimental swelling ratios. It appears that differences in other morphological features and chemical characteristics of the chars weakly influenced gasification rates under the conditions of this study.

The 1st-order model produced a good fit to the Illinois #6 reinjection data over a wide range of conversions (see Figure 6.2). Sieving the Illinois #6 char to 75-106 μm before

reinjection had the desired effect of producing small error bars on the derived rates, especially at high temperatures. The reinjection strategy appears to be the best method for obtaining gasification kinetics from bituminous coals in the HPFFB. As the highest quality fit of bituminous data, the Illinois #6 probably has the most representative activation energy for bituminous coals. However, some of the variation in apparent activation energies for the bituminous coals may result from differences the physical particle structures that were produced during pyrolysis.

The maximum particle temperature for the Illinois #6 was slightly lower than the other coals due to differences in experimental procedures that were implemented when the reinjection strategy was used. In all of the experiments in this study, conversion was measured at high and low residence times, as shown in Figure 6.4. The consistency of particle entrainment was visually checked through the view port (see Figure 4.1) on a regular basis as a means of quality control. The absence of soot in the reinjection experiments resulted in a dimmer particle streak that was more difficult to observe. The burner was lowered by 1.25 inches to move the most luminous portion of the particle streak into a better position for viewing. This increased the collection height and resulted in a longer minimum residence time for the reinjection experiments compared to the experiments with in-situ pyrolysis. The highest temperatures occurred near the burner (see Figure 6.3) and the model was only used to fit the differences between the high and low residence times (see Figure 6.4). Therefore, increasing the minimum residence time for the reinjection experiments had the effect of excluding gasification at the highest experimental particle temperatures from the regression of kinetic parameters.

6.3.2 Correlation of 1st-Order Model with Coal Rank

Char reactivity was correlated with coal rank using the results of the 1st-order model. Various measures of coal rank, including elemental composition and NMR parameters, were compared to the Arrhenius rate parameters of all the coals at the two selected temperatures. No reasonable correlation of activation energy with coal rank was found. Since the Kentucky #9 and EBB coals had suspiciously low activation energies, they were omitted from the correlation. The combined Wyodak series was also omitted from the rank correlation. The pre-exponential factor was re-optimized for all of the coals using a mean activation energy of 123 kJ/mol.

Carbon and/or oxygen content in the parent coal are commonly used to correlate char combustion and gasification reactivities (Hurt and Mitchell, 1992; Hurt et al., 1998) because they are convenient to measure. However, char gasification reactivities should correlate better with char properties because of the changes in chemical and physical properties that occur during pyrolysis. For the remaining 4 coals (counting Wyodak as 2 coals), the best correlation of the pre-exponential factor with elemental composition of the coal was with C/O (daf mass ratio) and the best correlation with NMR parameters was with $MW-M_{\delta}(\sigma+1)$ (see Figure 6.9). This group of NMR parameters represents the average mass of an aromatic cluster without the aliphatic attachments that are present in the coal. As such, $MW-M_{\delta}(\sigma+1)$ can be thought of as an estimated char structural parameter, since aliphatic material is eliminated as light gases during pyrolysis and much of the aromatic material in the coal becomes integrated into the char. As in the coal swelling model developed in this work (see Section 5.4), the NMR parameters used to correlate CO_2 gasification rate parameters were estimated from correlations (Genetti et al., 1999) developed from ultimate and proximate analysis for the CPD model (Fletcher et al., 1992). In other words, readily available coal properties were used to estimate coal NMR parameters

(which are much more expensive to measure), and then the NMR parameters were combined to estimate a property of the char that correlates well with heterogeneous reaction behavior. The correlations used to estimate NMR parameters are reproduced in Appendix L.

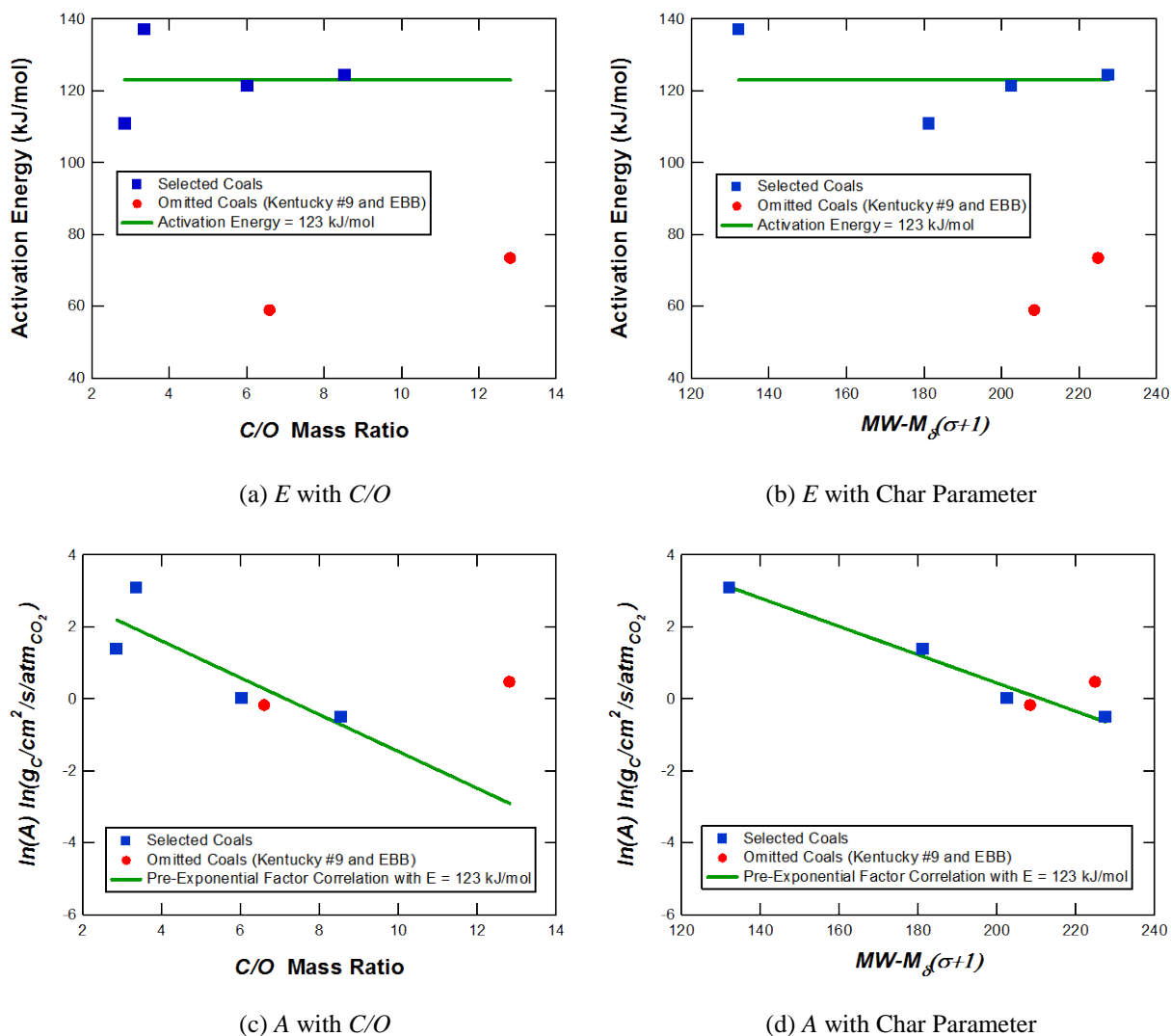


Figure 6.9. Correlations of kinetic parameters with coal rank for 1st-order CO₂ gasification model.

The parameter $MW-M_{\delta}(\sigma+1)$ is a measure of the average size of an aromatic cluster in the char without attachments. Small fractions of the total number of aromatic carbon atoms occur

on the cluster edges when the cluster size is large. The intrinsic reactivity and hence the apparent reactivity should correlate well with the fraction of carbon atoms found in these edge structures because they are most accessible to gaseous reactants. There is no comparable mechanistic link between the C/O ratio in the coal and the CO_2 reactivity of the char, although C/O is often used as a reasonable measure of coal rank.

The correlations for the 1st-order rate parameters are presented in Table 6.3. The symbol $Char_{Ar}$ in Table 6.3 is shorthand for $MW-M_{\delta}(\sigma+1)$, or the aromatic cluster mass of the char. The units for pre-exponential factors are listed in Table 6.2 and in the captions of Figure 6.9. The R^2 values in Table 6.3 correspond to the fits shown in Figure 6.9, and show that the $Char_{Ar}$ rank parameter yields a better fit of the rate parameters compared to C/O . The term $SSER$ in Table 6.3 is a percent change in SSE with respect to the optimum, averaged over all of the coals that were correlated. It is defined by:

$$SSER = \frac{\sum_{i=1}^{n_{Coals}} \frac{SSE_{fit} - SSE_{base}}{SSE_{base}}}{n_{Coals}} \quad (6.47)$$

where the n_{Coals} is the number of coals used in the correlation. The subscript “base” refers to the experimental basis SSE values from an unconstrained optimization of the kinetic parameters using the mass mean particle size. The subscript “fit” refers to SSE values obtained when the correlations in Table 6.3 were used in the 1st-order model.

The $SSER$ values in Table 6.3 for the activation energy E correspond to the incremental percent increases in SSE when a fixed E of 123 kJ/mol was used instead of the optimal parameters. The low $SSER$ values for E indicate that fixing the activation energy does not seriously hinder the 1st-order model from achieving a good fit of the HPFFB data, except for Kentucky #9 and EBB.

Table 6.3. Coal rank correlations for CO₂ gasification rate parameters in the 1st-order model

Correlation	R ²	SSER 4 Coals	SSER with Kentucky #9 (5 coals)	SSER with EBB (5 coals)	SSER 6 Coals
$E = 123 \frac{kJ}{mol}$	N/A	1.74%	9.46%	7.82%	13.23%
$\ln[A_{C/O}] = -0.51207(C/O) + 3.6505$	0.70	1649%	1364%	1369%	1178%
$\ln[A_{Char_{Ar}}] = -0.039337(Char_{Ar}) + 8.3031$	0.98	323%	279%	283%	253%

The *SSER* values in Table 6.3 for the 2 pre-exponential factor correlations indicate that the use of a correlation with the 1st-order model causes the fit to depart considerably from the optimum. However, the fit with $Char_{Ar} = MW-M_{\delta}(\sigma+1)$ is far better than with C/O . The correlations were only developed for the two Wyodak series, Illinois #6, and EBA, but the $Char_{Ar}$ correlation also performs well for Kentucky #9 and to a lesser extent EBB. The superior reactivity versus rank trend of $MW-M_{\delta}(\sigma+1)$ compared to C/O is confirmed by inspection of parts c and d of Figure 6.9.

The 1st-order model with the $Char_{Ar} = MW-M_{\delta}(\sigma+1)$ rank correlation is compared to the HPPFB data in Figure 6.10. While the fit of the omitted EBB coal in Figure 6.10 is far from ideal, the rest of the coals (including Kentucky #9) still tend to follow the 45-degree line. The Illinois #6 deviates the most from the optimal fit. The *SSER* value for just the two Wyodak coals and the EBA is only 7.7%, and *SSER* is only 31.2% for the same coals plus Kentucky #9. It appears the correlation with $Char_{Ar}$ in Table 6.3 can be used to make reasonable estimates of CO₂ gasification rates when data for a coal of interest are not available. The correlation performed best for lower coal ranks, but more data for the highest ranks of coals are probably needed to evaluate or improve the correlation. In any case, it appears that $MW-M_{\delta}(\sigma+1)$ is a very useful index of CO₂ gasification reactivity.

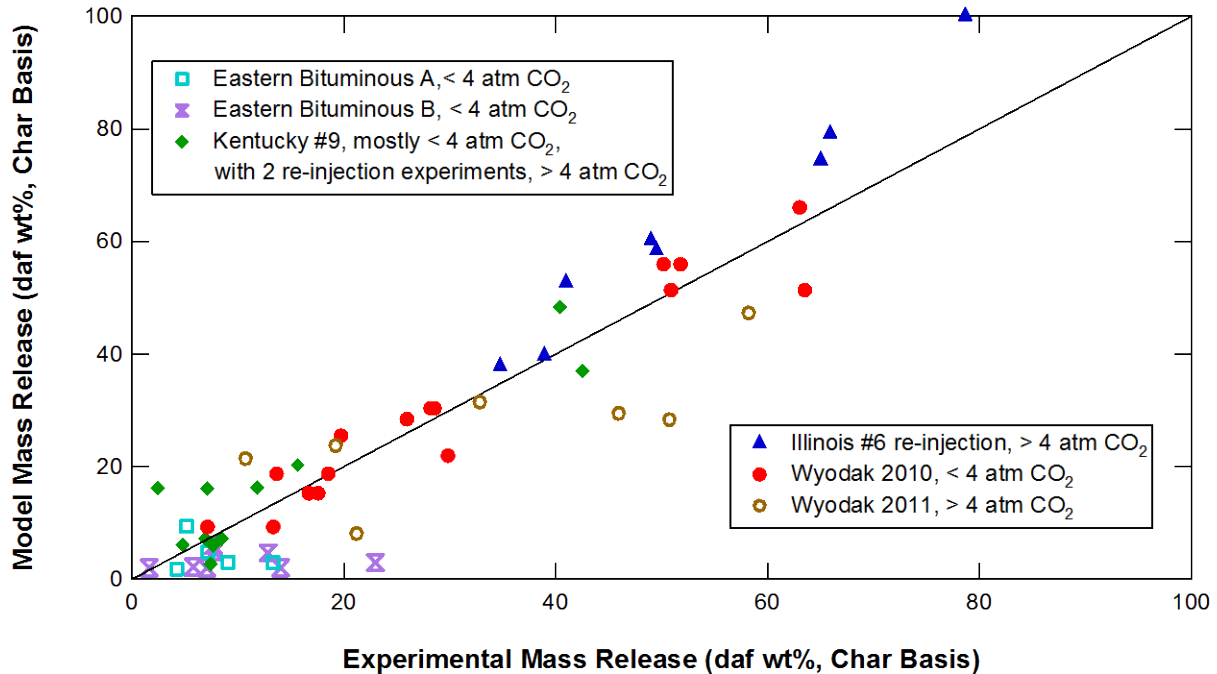


Figure 6.10. Fit of HPFFB data with 1st-order model using $E = 123$ kJ/mol and A from correlation with $Char_{Ar}$.

6.4 CO₂ Gasification Data with the CCK^N Model

The n^{th} -order Char Conversion Kinetics model (CCK^N) was used to fit the HPFFB gasification data. The CCK^N model was modified from the stand-alone version to interface with OptdesX, an optimization software package (Parkinson and Balling, 2002). The sum of squared errors SSE (Equation 6.1) was minimized using the generalized reduced gradient (GRG) algorithm, which is the same algorithm used in the MS Excel Solver with the 1st-order model.

The inputs for CCK^N included the particle size distributions measured in the Coulter Counter (see Appendix G), which typically included 15 size bins for 45-75 μm Wyodak coal. For the re-injected Illinois #6 and Kentucky #9 chars, the swelling ratio determined from the pyrolysis experiments was applied to the whole distribution of coal particle sizes. Because the re-injected chars were sieved after pyrolysis, this procedure resulted in 5 particle size bins for the

10 atm Illinois #6 reinjection experiments. The use of the full particle size distribution was found to be important to obtaining good results in previous versions of CBK (Maloney et al., 2005).

The partial pressures of CO, H₂O, and H₂ were neglected in the optimization of rate parameters because CCK^N has no CO inhibition mechanism and the concentrations of the other species were low. The pre-exponential factor, activation energy, and reaction order for CO₂ gasification were varied to obtain the best fit of the data. The resulting kinetic parameters and statistics are presented in Table 6.4. Features of the CCK^N model such as the thermal annealing sub-model strongly influence the optimal rate parameters. Therefore, the rate parameters in Table 6.4 are only suitable for application in models that include all of the features of CCK^N. A parametric study of some of these specialized features that CCK and CCK^N have in common is presented in Section 6.5.

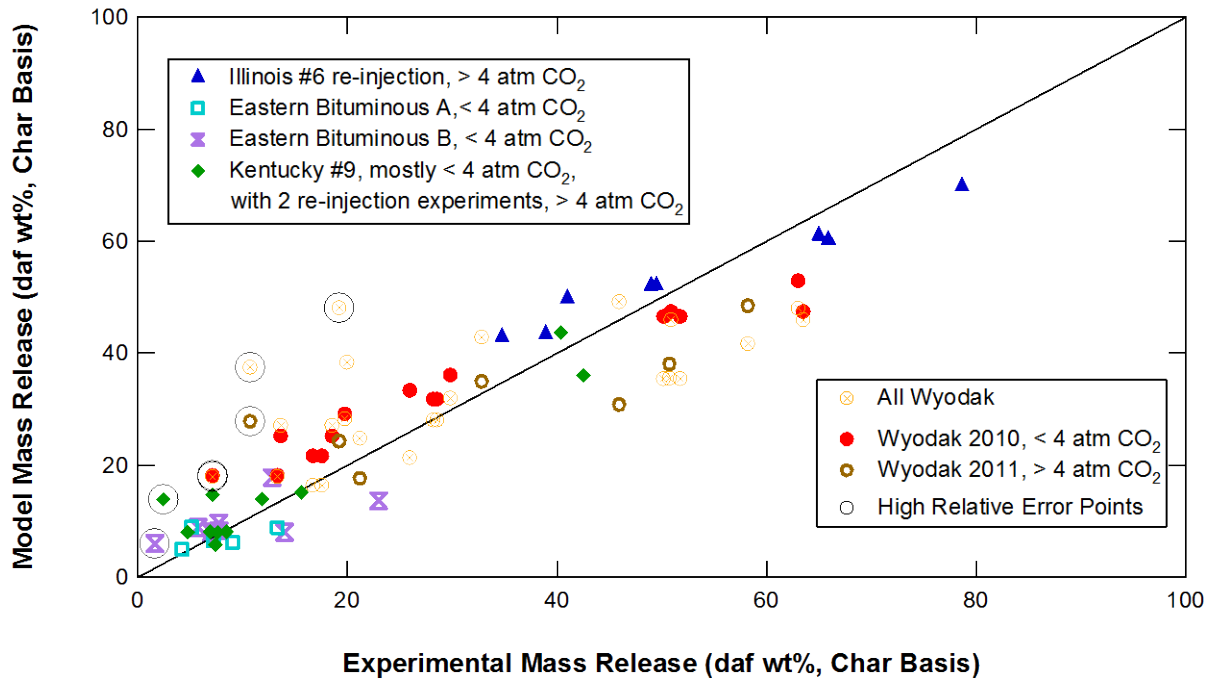
Table 6.4. CO₂ gasification kinetic parameters for the CCK^N model

Coal	Wyodak 2010	Wyodak 2011	All Wyodak
Pyrolysis	In-situ	In-situ	In-situ
Points fitted	16	7	24
<i>A [s⁻¹ (mol/m³)⁻ⁿ]</i>	6.497×10 ⁶	7.490×10 ⁶	1.670×10 ⁶
<i>E [kcal/mol]</i>	33.54	30.01	42.56
Reaction order <i>n</i>	0.4960	0.7466	0.1448
Relative Error (experimental basis)	1.72%	2.61%	1.90%
Relative Error (char basis)	12.6%	24.2%	15.6%
Relative Error (char basis, w/o largest contributors to Relative Error)	8.53% (-1 point)	9.12% (-1 point)	12.0%, 8.29% (-1, -3 points, 2/3 from 2011)
SSE (experimental basis)	287.8	139.5	866.5
SSE (char basis)	987.7	817.8	4053.8
SSE (char basis, w/o largest contributors to Relative Error)	864.5 (-1 point)	522.8 (-1 point)	3333.7, 2379.7 (-1, -3 points, 2/3 from 2011)
Parameters with fixed reaction order of <i>n</i> = 0.5			
<i>A [s⁻¹ (mol/m³)⁻ⁿ], n=0.5</i>	6.616×10 ⁶	4.327×10 ⁶	4.646×10 ⁶
<i>E [kcal/mol], n=0.5</i>	33.45	36.11	33.57
Relative Error (experimental basis)	1.72%	2.74%	2.08%
Relative Error (char basis)	12.6%	24.8%	16.6%
SSE (experimental basis)	287.9	166.2	1102.1
SSE (char basis)	988.2	1363.5	4641.4

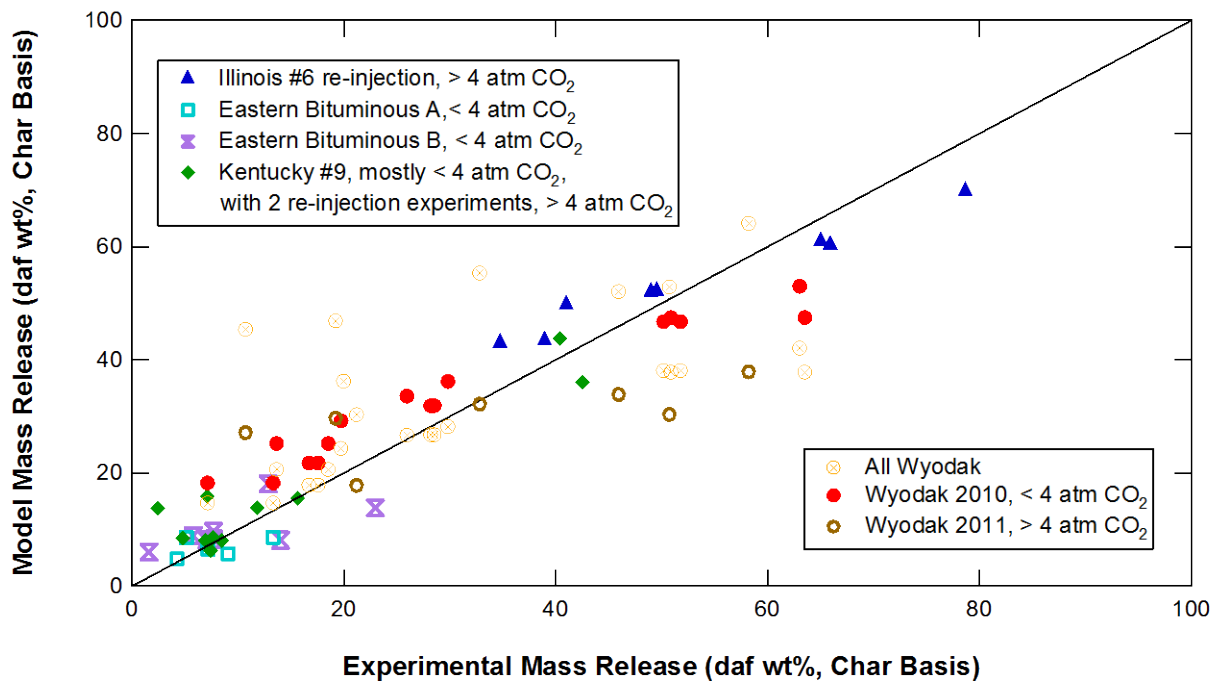
Table 6.4 (continued)

Coal	Kentucky #9	Illinois #6	EBA*	EBB*
Pyrolysis	In-situ and reinjection	Reinjection	In-situ	In-situ
Points fitted	9 coal + 2 char	8	5	8
$A [s^{-1} (mol/m^3)^{-n}]$	6.300×10^5	7.378×10^6	1.118×10^5	8.150×10^2
$E [kcal/mol]$	32.72	37.58	30.12	12.99
Reaction order n	0.5188	0.5016	0.4767	0.4997
Relative Error (experimental basis)	2.29%	4.77%	1.28%	2.03%
Relative Error (char basis)	44.6%	4.77%	18.06%	36.5%
Relative Error (char basis, w/o largest contributors to Relative Error)	13.3%, 8.7% (-1, -2 coal points)	N/A	N/A	13.4% (-1 point)
SSE (experimental basis)	121.0	307.3	11.3	63.9
SSE (char basis)	263.3	307.3	43.2	181.0
SSE (char basis, w/o largest contributors to Relative Error)	130.9, 72.6 (-1, -2 coal points)	N/A	N/A	161.0 (-1 point)
Parameters with fixed reaction order of $n = 0.5$				
$A [s^{-1} (mol/m^3)^{-n}], n=0.5$	6.350×10^5	7.145×10^6	2.968×10^5	8.163×10^2
$E [kcal/mol], n=0.5$	33.27	37.53	32.52	12.97
Relative Error (experimental basis)	2.33%	4.78%	1.30%	2.03%
Relative Error (char basis)	44.6%	4.78%	17.2%	36.1%
SSE (experimental basis)	126.5	308.0	11.8	64.0
SSE (char basis)	281.1	308.0	45.65	181.5
*Eastern Bituminous A and B				

The fit of the HPFFB data with CCK^N shown in Figure 6.11 was better for the EBB coal, the EBA coal, and the combined Wyodak series than it was in the simple 1st-order model (see Figure 6.2). The fit was also very good for the other coals. The EBB activation energy was lower than the other coals (see Table 6.4), as in the 1st-order model (see Table 6.2). The unrealistic activation energies in both models suggest that the EBB data set was not extensive enough in terms of temperature and perhaps CO₂ partial pressure for kinetic modeling, and the conversions obtained were low enough to be strongly influenced by experimental noise. It is likely that the kinetic parameters obtained for EBB were biased towards excessively low rates because soot agglomerates collected with the char became larger and more numerous with increasing residence time. Soot contamination was a more severe problem for this high-rank bituminous coal with in-situ pyrolysis than for any other coal in this study.



(a) CCK^N fit with variable CO₂ reaction order



(b) CCK^N fit with fixed CO₂ reaction order of $n = 0.5$

Figure 6.11. Parity plot of HPFFB gasification data with optimized CCK^N model predictions.

The points that made the largest contributions to the relative error values listed in Table 6.4 occurred at experimental char conversions below 20% (see circled points in top half of Figure 6.11). This means that the conversion on a coal basis was on the order of 10% or less beyond full pyrolysis, where experimental noise makes accurate measurement of mass release difficult.

The reaction order for the combined Wyodak series was 0.14. CO₂-char reaction orders near 0.5 are more typical of the coals in this study and previous studies, although reaction orders between 0.1 and 1.0 have been reported (Roberts et al., 2010). The very low combined Wyodak reaction order suggests that the two Wyodak series should be treated as different coals. Similar fits were obtained for most of the HPFFB data when the reaction order was fixed at a value of 0.5 (see Figure 6.11 and Table 6.4). The largest increases in *SSE* occurring for Wyodak 2011 and the combined Wyodak series, which had reaction orders that deviated the most from 0.5.

The effectiveness factors that were predicted by CCK^N indicate that the HPFFB experimental conditions used in this study corresponded to the transition between Zone II and Zone I gasification behavior. The Wyodak 2010 had effectiveness factors below 0.9 at temperatures as low as 1350 K, indicating Zone II behavior. The effectiveness factors for the bituminous coals were very close to 1 at particle temperatures below 1500 K, indicating Zone I behavior. However, the bituminous coal effectiveness factors decreased at higher temperatures, indicating the onset of Zone II behavior (see Appendix K for effectiveness factor graphs).

Overall, it appears that the fit with the CCK^N model is slightly skewed. CCK^N over-predicted the low conversions and under-predict the high conversions, with the best fit occurring near the midpoint of the experimental conversion for each coal. Some of this skewed behavior may be due to outlier data points, but it seems odd that it would occur for nearly every coal.

Outliers do not seem as likely for the Wyodak 2010 and Illinois #6 series, especially in consideration of the lack of skew in the fit with the 1st-order model (see Figure 6.2). The effect of non-kinetic CCK and CCK^N model parameters on predicted rates are discussed in Section 6.5, including possible sources of the slight skew observed in Figure 6.11.

6.4.1 Correlation of CCK^N Model with Coal Rank

The CCK^N rate parameters with a fixed CO₂ reaction order of 0.5 (see Table 6.4) were correlated with coal rank in a manner similar to the 1st-order model (See Section 6.3.2). Arrhenius parameters are difficult to correlate independent of each other. Statistically small changes in activation energy require large compensating changes in the pre-exponential factor when fitting a given set of measured reaction rates. An autocorrelation approach used in previous combustion kinetics studies (Essenhig and Misra, 1990; Hurt and Mitchell, 1992) was applied to fit the CO₂ gasification data from coals in the HPFFB.

Of the two Arrhenius parameters, the apparent temperature dependence expressed as the activation energy has the most physical meaning; it is a combination of the temperature dependence of the intrinsic reaction kinetics and the various transport processes that contribute to the overall rate. Therefore, in the autocorrelation approach, the activation energy is first fit to some measure of coal rank or char properties. Next, new pre-exponential factors must be optimized from the available experimental data using the correlated values of the pre-exponential factor. This is necessary to insure that the correlated parameters yield reasonable fits of the data (though often not the best possible fit). Finally, the pre-exponential factor is correlated with both the correlated activation energy and coal rank, using the following form:

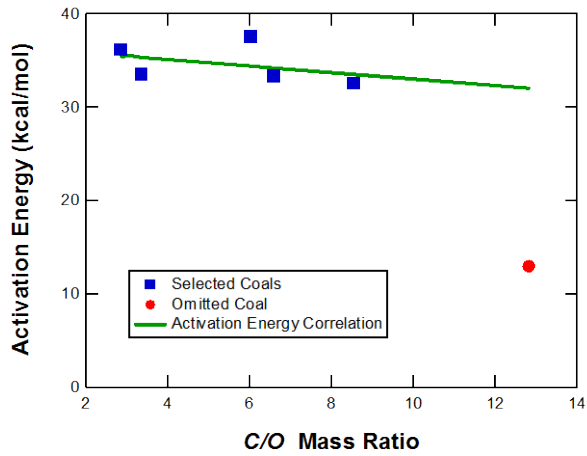
$$E = f_1(rank) \quad (6.48)$$

$$\ln(A) = f_2(rank) + \frac{E}{R_g T_{ref}} \quad (6.49)$$

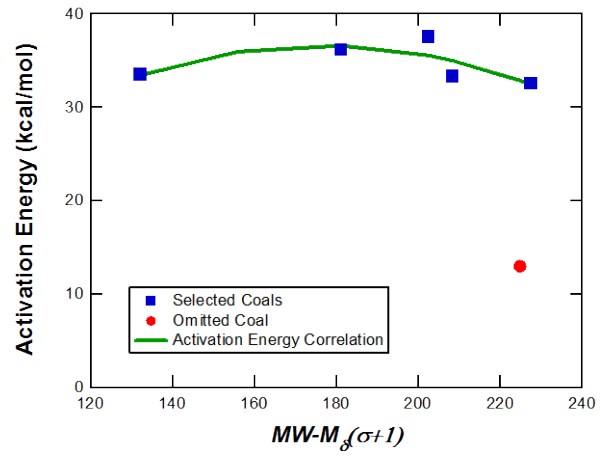
where E is the correlated activation energy, A is the correlated pre-exponential factor, R_g is the universal gas constant, and T_{ref} is a reference temperature, typically at or near the midpoint of the experimental particle temperature range (Essenhig and Misra, 1990; Hurt and Mitchell, 1992). For this study, a temperature of 1450 K was selected for T_{ref} . The functions f_1 and f_2 are functions of a selected measure of coal rank. The observed reactivity is related to the chemical structure of the char as well as char morphology, including size, internal voids, and pore structure, which all vary with coal rank.

As in the 1st-order rank correlation, EBB and the combined Wyodak series were omitted from the CCK^N rank correlations. However, Kentucky #9 was included because it exhibited better trends in the CCK^N model (see Figure 6.12). The CCK^N Arrhenius parameters were compared to many measures of coal rank. As with the 1st-order model, the best correlations were found with C/O and $Char_{Ar} = MW \cdot M_{\delta}(\sigma+1)$. A linear form was used for C/O and a quadratic form was chosen for $MW \cdot M_{\delta}(\sigma+1)$, as shown in Figure 6.12.

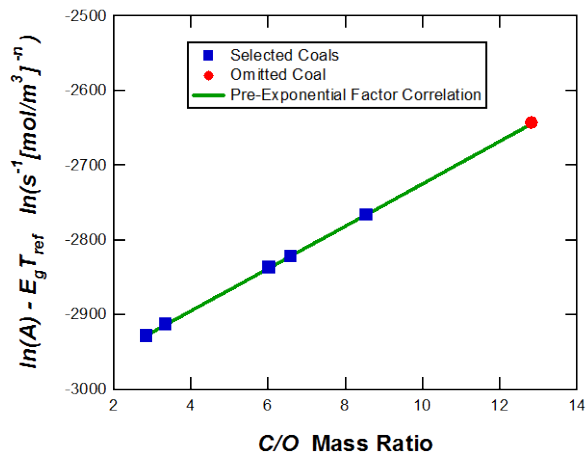
The correlations that correspond to Figure 6.12 are presented in Table 6.5. The R^2 values for the activation energy indicate that the quadratic fit with $Char_{Ar} = MW \cdot M_{\delta}(\sigma+1)$ in part b of Figure 6.12 is much better than the linear C/O fit shown in part a of Figure 6.12. It appears that the parameter $Char_{Ar} = MW \cdot M_{\delta}(\sigma+1)$ yields a more meaningful rank order for gasification reactivity. The R^2 values for the pre-exponential factor correlations in Table 6.5 are essentially unity for both measures of coal rank (compare to parts c and d of Figure 6.12). This result indicates the success of the autocorrelation approach.



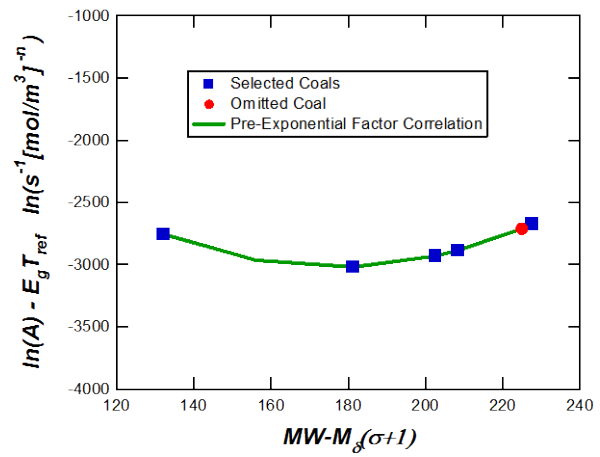
(a) E with C/O



(b) E with Char Parameter



(c) A with C/O



(d) A with Char Parameter

Figure 6.12. Correlations of kinetic parameters with coal rank for CCK^N gasification model.

The partial $SSER$ values for E in Table 6.5 were calculated using Equation 6.47 with SSE_{base} obtained from the optimal E and A values (from Table 6.4, see also the (■) points for E in parts a and b of Figure 6.12). The partial $SSER$ values for E used SSE_{fit} from the correlated E values (green lines in parts a and b of Figure 6.12) and the corresponding re-optimized A values (shown as (■) points in parts c and d of Figure 6.12).

Table 6.5. Coal rank correlations for CO₂ gasification parameters in the CCK^N model with $T_{ref} = 1450$ K

Correlation	R ²	Partial SSER	Full SSER
$E_{C/O} = -348.3(C/O) + 36482 \frac{cal}{mol}$	0.15	10.9%	146%
$\ln[A_{C/O}] = 95.776(C/O) - 3221.0 + \frac{E_{C/O}}{R_g T_{ref}}$	1.00	128%	
$E_{Char_{Ar}} = -1.622Char_{Ar}^2 + 573.0Char_{Ar} - 13988 \frac{cal}{mol}$	0.61	9%	115%
$\ln[A_{Char_{Ar}}] = 0.21101Char_{Ar}^2 - 70.876Char_{Ar} + 2924.0 + \frac{E_{Char_{Ar}}}{R_g T_{ref}}$	1.00	99%	

The partial *SSER* values for *A* in Table 6.5 were calculated with SSE_{base} obtained from the best fit with correlated *E* values (green lines in parts a and b of Figure 6.12) and SSE_{fit} was obtained from correlated values of both *A* and *E* (all green lines in Figure 6.12). The full *SSER* is the percent change in *SSE* with respect to the best-fit SSE_{base} values listed in Table 6.4. SSE_{fit} was calculated using the correlated values of both *A* and *E* (green lines in Figure 6.9).

The large partial *SSER* values for *A* compared to the partial *SSER* values for *E* indicate that the correlations for the pre-exponential factor made the largest contributions to the deviation of model predictions from experimental values. The full *SSER* values in Table 6.5 show that the fit of the experimental data with the $Char_{Ar}$ correlation is better compared to the *C/O* correlation. The magnitudes of the full *SSER* values indicate that the *C/O* correlation performed considerably better for CCK^N compared to the 1st-order model (compare Table 6.5 to Table 6.3). The CCK^N fit with the $Char_{Ar}$ correlation is shown in Figure 6.13. Figure 6.13 shows that the correlation increased the predicted conversion for most of the coals with respect to the optimal $n = 0.5$ fit shown in part b of Figure 6.12. The $Char_{Ar}$ correlation yielded lower conversion for Illinois #6 and EBB (which was excluded from the correlation). The overall fit using the $Char_{Ar}$ correlation is very good, and the fit of the Illinois #6 data in particular is much better than the best

correlation with the 1st-order model (see Figure 6.10). It appears that the use of a model with a reaction order of 0.5 and advanced features such as effectiveness factors made better correlations with coal rank possible compared to the 1st-order model.

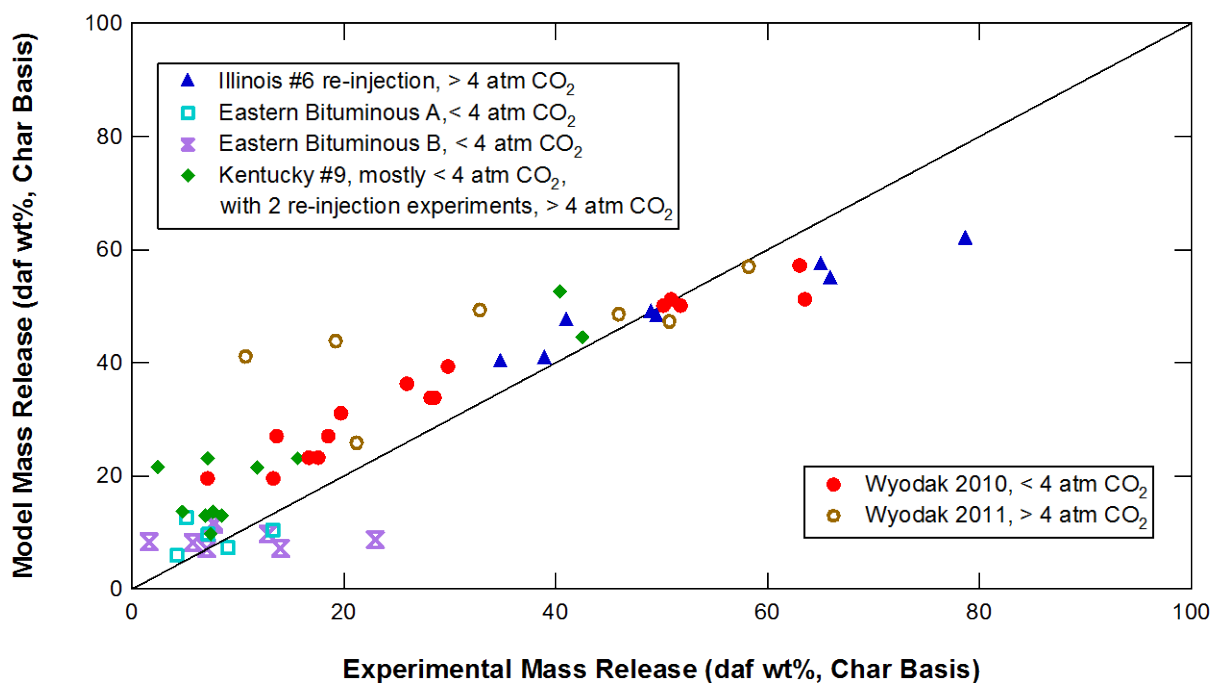


Figure 6.13. Parity plot of HPFFB CO₂ gasification data with CCK^N predictions using $Char_{Ar}$ kinetic correlation.

6.5 CCK Parametric Studies

In the attempts to fit the HPFFB data using the CCK model, a slight skew similar to the CCK^N fit was observed. This indicates that the skew observed in Figure 6.11 was probably caused by features of the models other than the kinetic mechanism. Therefore, a series of calculations were performed to establish the effect of different parameters on CCK predictions.

A 15 atm gas condition was used with the Wyodak 2010 properties and kinetic parameters. For simplicity, a single particle size of 64 microns was used. The pre-exponential

factor $A_{7,0}$ was assigned an initial value of $7.833 \times 10^8 \text{ s}^{-1}$, the activation energy E_7 was set to 35 kcal/mol, and the built-in correlations were used to predict the other parameters from the coal composition (see Section 6.2.4). The gas temperature was set to a constant value of 1700 K and the temperature of the surroundings was set to a constant value of 1000 K. Residence times of up to 240 ms were calculated because this was typical for many of the experiments in this study. Figure 6.14 shows the predicted conversion profile with changes in the gas composition. As expected, the trace amount of H_2 had no significant effect on the gasification rate. CO at the base concentration of 1.13 atm partial pressure had little effect on conversion. H_2O at 0.1 atm increased the conversion at 150 ms slightly more than 2.26 atm CO decreased the conversion at the same residence time.

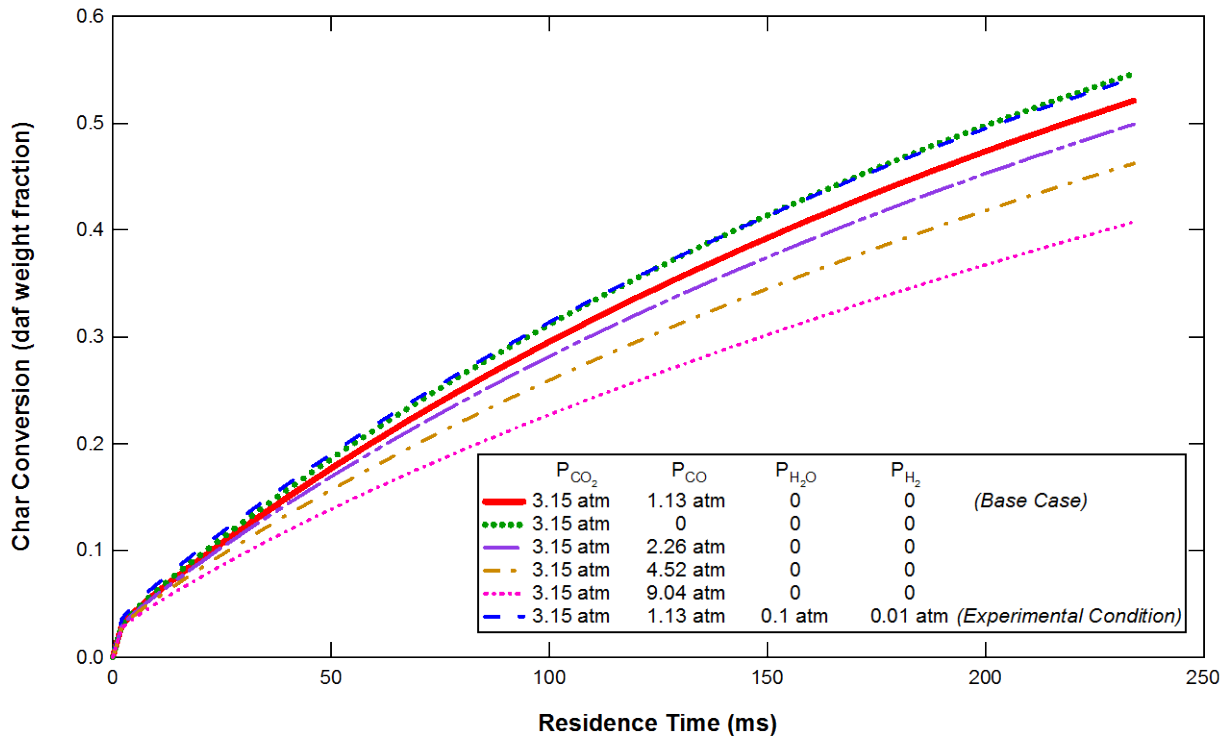


Figure 6.14. Effect of gas composition on conversion of Wyodak char at $T_g = 1500 \text{ K}$, $P = 15 \text{ atm}$, $T_{surr} = 1000 \text{ K}$.

The effects of the random pore model, the mode of conversion, and the tortuosity parameter are shown in Figure 6.15. The base cases for Figures 6.12 and 6.13 are identical. The parameters ψ_0 , τ/f , and α affect the shape of the conversion profile in similar ways. It appears that a higher value of τ/f or a lower value of ψ_0 or α in combination with a higher value of $A_{7,0}$ could be used to remove the slight skew from the fit shown in Figure 6.19. A higher value of τ/f corresponds to macropores with higher tortuosity or a lower fraction of the total porosity in the macropores. It may also correspond to conditions where Knudsen diffusion has a strong influence on the rate. A lower value of α would be consistent with experimental combustion measurements that were used in CBK8 and CBK/E, but more conversion probably happens on the interior of the particle for slow gasification reactions compared to fast oxidation reactions.

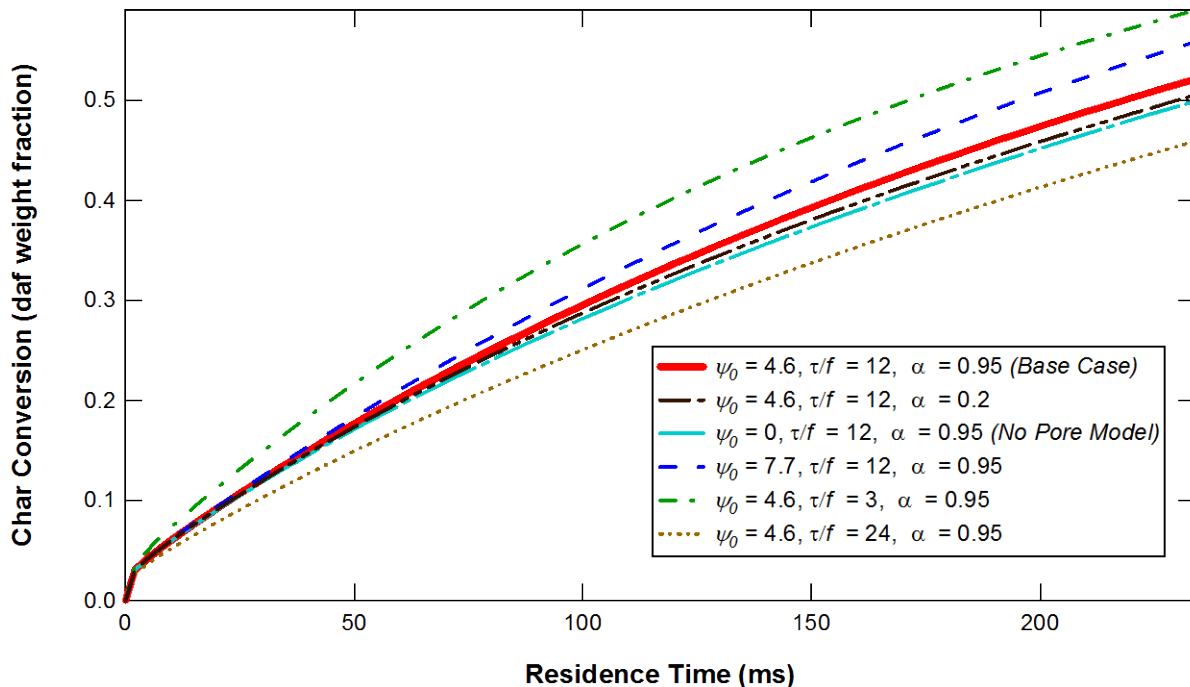


Figure 6.15. Effect of ψ_0 , τ/f , and α on Wyodak 2010 char conversion at $T_g = 1500$ K, $P = 15$ atm, $T_{surr} = 1000$ K.

A lower value of ψ_0 would indicate that the influence of gasification-induced changes in the pore structure on the observed rate is small. It seems that the most straightforward way to improve the fit of high-temperature pulverized coal gasification data would be to turn the random pore model off ($\psi_0 = 0$), choose an appropriate value for α , and use both $A_{7,0}$ and τf as fitting parameters. If needed, the kinetic parameter E_7 could also be adjusted (Liu and Niksa, 2004). Ideally, universal values of τf and α should be determined for CCK as has been done in previous versions of CBK (Sun and Hurt, 2000).

There is evidence that Knudsen diffusion may be more important for gasification (Roberts et al., 2010) compared to combustion (Hong et al., 2000a) because the reactions are slower, which ought to allow reactants to penetrate deeper into the micropores. Since CCK does not include Knudsen diffusion or explicit pore structural information, any effects of these phenomena are lumped into the parameter τf (Sun and Hurt, 2000). If more detailed models of mass transport behavior in porous chars are desired, future versions of CCK could be modified to be consistent with the more explicit formulation for effective diffusivity used in HP-CBK (Hong et al., 2000a) (see Section 2.4.4).

The Wyodak 2010 and the Illinois #6 gasification data were fit by varying $A_{7,0}$ and E_7 , with τf at its CBK/E default value of 12 (see ▲ and ⊕ series in Figure 6.16). The random pore model was disabled and α was set to the CBK default value of 0.2. Then the data were refit while varying τf as well (▼ and ● series in Figure 6.16). A base case with a fixed E_7 of 35 kcal/mol (open upright triangle and open circle series in Figure 6.16) and another case with no annealing (open sideways triangles in Figure 6.16) were also optimized.

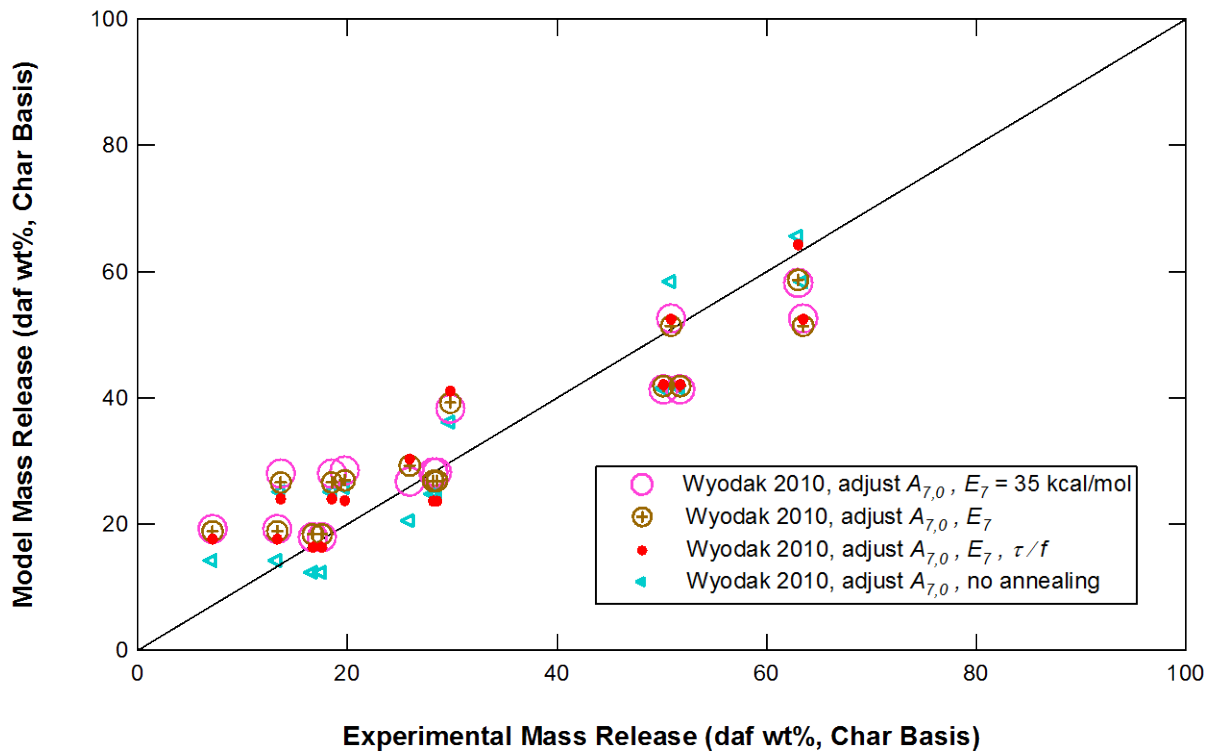
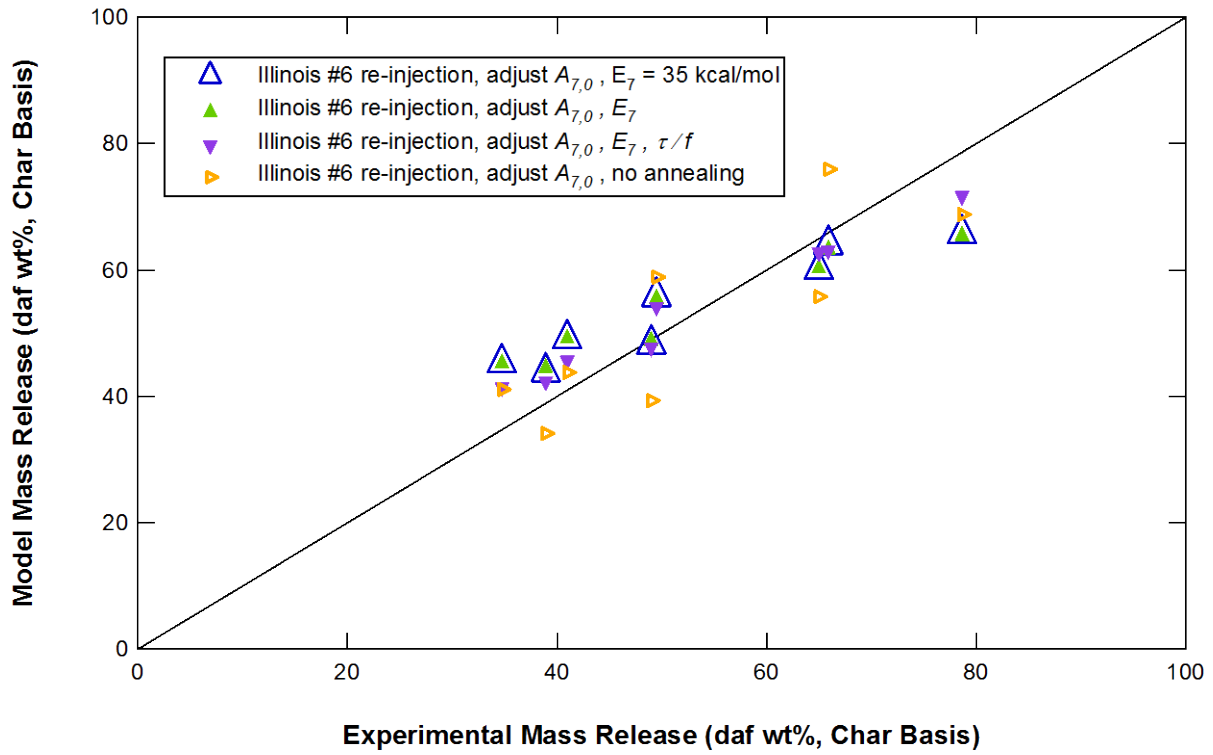


Figure 6.16. CO₂ gasification for Illinois #6 (top) and Wyodak (bottom) with different variable parameters.

The comparison of the fits is shown in Figure 6.16. Alternate fits with α assigned a value of 0.95 yielded insignificant differences and are not shown. The fits with a single adjustable parameter are quite comparable to the fit with 2 adjustable parameters for both coals. This suggests that enough rank dependence is already built into the activation energies other than E_7 to render the use of more than one adjustable kinetic parameter superfluous, especially with respect to the limited size of this data set. The model with no annealing had a more accurate fit without skew. However, the spread of the model predictions at similar levels of conversion increased on average, suggesting that the annealing model helps increase precision. The *SSE* for Wyodak decreased when annealing was removed, but *SSE* for Illinois #6 increased. It seems likely that annealing of the char occurred in the HPFFB gasification experiments, but the CBK annealing model used in this study over-predicted the rate of thermal deactivation.

Optimization with variable τ/f in Figure 6.16 resulted in a fit with reduced skew and τ/f values of 161 for Wyodak and 908 for Illinois #6 (▼ and ●). These τ/f values exceed the combustion default value by about 1 order of magnitude for the subbituminous coal and 2 orders of magnitude for the bituminous coal. It seems unreasonable that the values of tortuosity and macroporosity would differ much from the flat-flame burner coal chars used to develop the CBK kinetic correlations (Hurt et al., 1998; Sun and Hurt, 2000). This suggests that Knudsen diffusion reduced the combined diffusivity $D_{i,comb}$ in Equation 2.10 to ~10% of the molecular diffusivity for the subbituminous coal and ~1% for bituminous coal.

The combined diffusivity of CO₂ in N₂ as a function of pressure and pore diameter at 1500 K is plotted in Figure 6.17. The Knudsen diffusivities were calculated from:

$$D_K = 4850d_{pore} \sqrt{\frac{T}{M_{gas}}} \quad (6.50)$$

where D_K is in cm^2/s , d_{pore} is the pore diameter in cm, T is the temperature in K, and M_{gas} is the molecular weight of the diffusing gas molecules in g/mol. The combined diffusivities in Figure 6.17 were calculated using Equation 2.10 and were then normalized by the molecular diffusivity. At pressures of 10 atm to 15 atm used in HPFFB, the combined diffusivity reaches a value equal to 10% of the molecular diffusivity in pores having diameters of ~ 10 nm. The combined diffusivities would be equal to 1% of the molecular diffusivity in pores with diameters of ~ 5 nm.

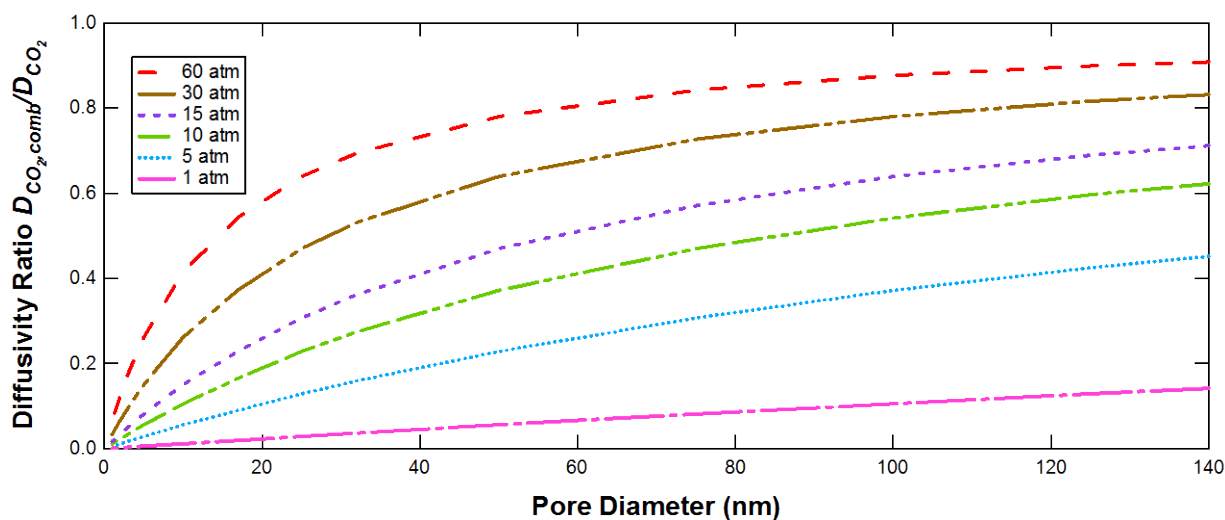


Figure 6.17. Combined diffusivity compared to molecular diffusivity as a function of pore diameter and pressure.

Surface areas were measured for some of the Wyodak 2011 chars and the Illinois #6 and Kentucky #9 chars that were used for the final reinjection gasification studies (see Section 4.6.3). The surface areas and pore diameters weighted by volume are presented in Table 6.6 for these freshly pyrolyzed chars. The bituminous chars used for reinjection were sieved prior to analysis. The average micropore diameters are all about 1.15 nm, which is easily small enough to account for the large size of the fitted τ/f parameters. These pore sizes for chars formed at $\sim 10^5$ K/s and 10 and 15 atm are slightly smaller than the sizes of 1.5 nm to 3.0 nm reported for Australian

bituminous chars formed in a pressurized entrained-flow reactor at $\sim 2 \times 10^4$ K/s and 10 to 20 atm (Roberts et al., 2010).

Table 6.6. Surface areas and pore diameters from adsorption measurements of HPFFB chars

Char	BET N ₂ Surface Area (m ² /g)	Mesopore Diameter (nm)	CO ₂ Surface Area (m ² /g)	Micropore Diameter (nm)
Wyodak 2011 10 atm	370.6 +/- 8.9	116.8 +/- 4.5 41.6% BET Volume	396.1	1.13
Wyodak 2011 15 atm	393.3 +/- 9.6	111.7 +/- 4.3 40.4% BET Volume	414.6	1.13
Illinois #6 10 atm, 75-106 μm	89.3 +/- 2.2	81.3 +/- 3.1 86.2% BET Volume	272.8	1.16
Illinois #6 15 atm, 75-106 μm	106.2 +/- 2.5	89.3 +/- 3.4 74.3% BET Volume	281.9	1.16
Kentucky #9 10 atm, 75-106 μm	79.8 +/- 1.8	84.9 +/- 3.3 78.8 % BET Volume	260.3	1.15
Kentucky #9 15 atm, 75-106 μm	55.9 +/- 1.2	106.1 +/- 3.7 84.7% BET Volume	246.2	1.16

The Wyodak chars had BET surface areas that were about 4 times the values obtained for bituminous coals. Similar high values of surface area were measured for Blue #1 char (which is borderline in rank between subbituminous and hvc bituminous) produced at atmospheric pressure, 1250 K, and a heating rate of 2×10^4 K/s (Fletcher and Hardesty, 1992). The BET surface areas of the bituminous coals ranged from 55 to 106 m²/g, which is similar to values obtained for bituminous coals at atmospheric pressure and heating rates of $\sim 5.8 \times 10^4$ K/s (Mitchell et al., 1992) and also for bituminous coals in the previous version of the HPFFB at $\sim 10^5$ K/s (Zeng, 2005).

The high subbituminous surface areas were caused by the fact that the Wyodak did not develop a highly fluid metaplast during pyrolysis as bituminous coals do. Rather, the original pore structure of the Wyodak coal was retained and expanded during pyrolysis. This resulted in a very broad distribution of pore sizes compared to the bituminous chars. The lower volume

percent in the mean pore size for the Wyodak indicates that the N₂ adsorption measurement included considerable surface area in pores smaller than the mean. The extra mesopore (BET) surface area available for reaction in the Wyodak helps explain why the fitted τ/f parameter was nearly an order of magnitude smaller for Wyodak compared to Illinois #6. In other words, a larger fraction of the CO₂ reacted on mesopore surfaces in the Wyodak before it could reach the micropores compared to the bituminous coals. The bituminous coals filled in their original pore structure as the metaplast became fluid during pyrolysis. Entirely new structures were formed in the bituminous chars, including very large internal voids. The formation of cenospherical shells limited the length of macropores and mesopores that could form.

The slightly skewed fit with the CCK codes could be explained if the annealing mechanism over-predicts the decrease in rate for gasification conditions, as shown in Figure 6.16. The effect of the CCK annealing mechanism on the rate and particle temperature is shown in Figure 6.18 along with a comparison to an alternate annealing mechanism (Zolin et al., 2001). Aside from the rapid decrease in the first 1 or 2 times steps, the CCK annealing mechanism probably does not change the annealing factor enough to cause much of the skew observed in the fits of the HPFFB data. The calculation conditions in Figure 6.18 correspond to the base case in Figure 6.14, but the pre-exponential factor $A_{7,0}$ was reduced to 5.5×10^7 (s⁻¹) with the Zolin case to obtain a reasonable match of the rates and particle temperatures at residence times greater than 100 ms. The mechanism of Zolin et al. (2001) does not decrease as much on the first time step, but thereafter yields lower predicted particle temperatures and faster decreases in reactivity. This implies that the Zolin mechanism would make the skewed fit of the gasification data worse. No attempt was made to alter or replace the annealing mechanism in these initial versions of CCK because it was considered desirable to maintain similarity with the CBK codes so that the

previously published correlations for oxidation and gasification kinetic parameters could be used (Niksa et al., 2003; Liu and Niksa, 2004).

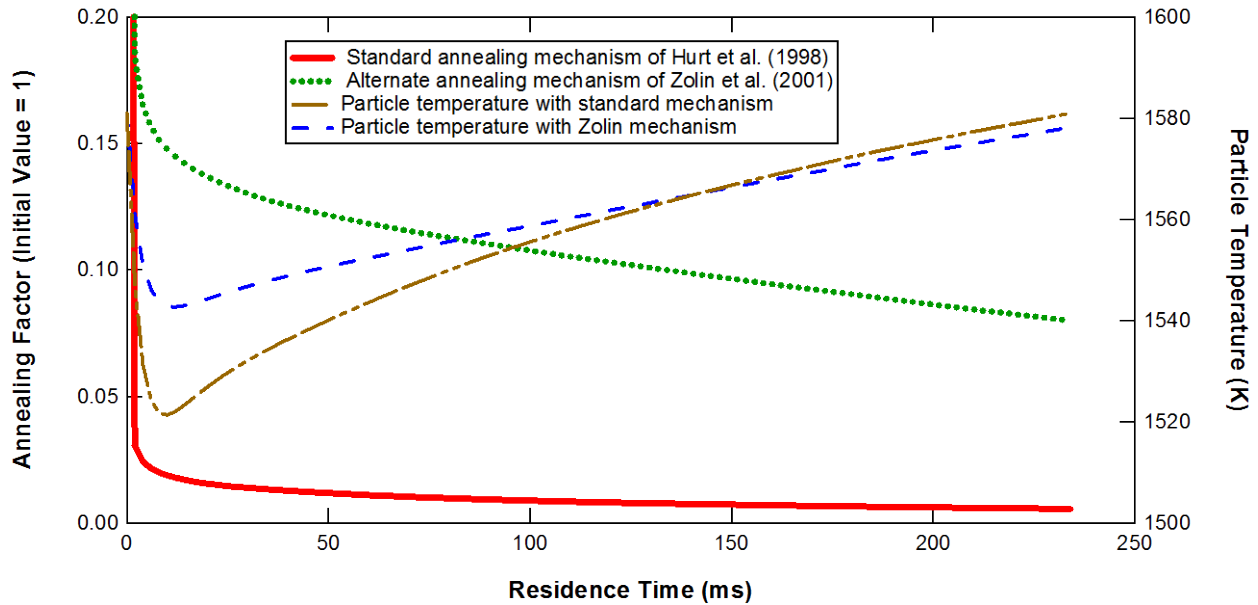


Figure 6.18. Effect of annealing mechanisms on rate and temperature at $T_g = 1500$ K, $P = 15$ atm, $T_{surr} = 1000$ K.

Other investigators have suggested that the CBK ash inhibition mechanism initially over-predicts the magnitude of ash inhibition (Cloke et al., 2003). Although occasional mineral grains were observed as bright spots in SEM images of the coal chars in this study, nothing resembling a coherent ash film was observed on any of the particles at the levels of conversion in this study. The ash inhibition mechanism in CBK and CCK does not have user-adjustable parameters and is not found in a subroutine that could be easily isolated, so the magnitude of this effect in the model was not quantified in this study.

6.6 CO₂ Gasification Data with the CCK Model

CCK was used to fit the HPFFB gasification data using the same procedures that were used with CCK^N. The partial pressures of CO, H₂O, and H₂ from the reaction zone in HPFFB were included in the CCK inputs for each case. Since it was found that adjusting the activation energy and the pre-exponential factor together did not significantly improve the fit of the two best data sets, only the pre-exponential factor $A_{7,0}$, was adjusted. The activation energy was assigned a value of 35 kcal/mol for all coals.

CBK/G included a rough correlation for $A_{7,0}$ (Liu and Niksa, 2004):

$$\log_{10}(A_{7,0}) = 0.1C_{daf} - 0.64 \quad (6.51)$$

Attempts to fit $A_{7,0}$ to the HPFFB data while using the default correlation for E_7 (see Equation 6.40) yielded values of $A_{7,0}$ that were 1 to 2 orders of magnitude higher than the values obtained from Equation 6.51. This indicates that there are differences between the CCK and CBK/G models or the parameters they use. The nature of the difference could not be determined with certainty because the CBK/G source code is not available, and the description of the code was limited (Liu and Niksa, 2004). Another possibility is that the HPFFB produced chars with physical structures that were significantly different from those used to fit Equation 6.51.

The kinetic parameters obtained from the optimization procedure are listed in Table 6.7. It is important to remember that the CBK and CCK codes have annealing and ash inhibition models that also strongly influence the predicted rates. This means that the parameters in Table 6.7 are unsuitable for use in other gasification codes, even if the basic kinetic mechanism is the same as the one used in CCK.

Table 6.7. Optimized CO₂ gasification $A_{7,0}$ with the CCK model using $E_7 = 35$ kcal/mol, $\psi_0 = 0$, and $\tau f = 12$

Coal	Wyodak 2010	Wyodak 2011	All Wyodak	
Pyrolysis	In-situ	In-situ	In-situ	
Points fitted	16	7	24	
Fitted $A_{7,0}$ (s^{-1})	8.659×10^8	3.462×10^8	6.461×10^8	
Relative Error (experimental basis)	1.77%	2.85%	1.80%	
Relative Error (char basis)	13.8%	25.2%	14.7%	
Relative Error (char basis, w/o largest contributors to Relative Error)	9.36% (-1 point)	15.9% (-1 point)	10.6%, 7.22% (-1, -3 points, 2/3 from 2011)	
SSE (experimental basis)	281.8	184.4	783.4	
SSE (char basis)	961.5	1547.1	3369.3	
SSE (char basis, w/o largest contributors to Relative Error)	814.6 (-1 point)	1294.3 (-1 point)	2622.1, 1852.2 (-1, -3 points, 2/3 from 2011)	
Coal	EBA*	EBB*	Illinois #6	Kentucky #9
Pyrolysis	In-situ	In-situ	Reinjection	In-situ and reinjection
Points fitted	5	8	8	9 coal + 2 char
Fitted $A_{7,0}$ (s^{-1})	6.488×10^7	6.914×10^7	3.943×10^8	1.200×10^8
Relative Error (experimental basis)	1.47%	3.57%	5.53%	3.12%
Relative Error (char basis)	20.5%	69.2%	5.53%	54.1%
Relative Error (char basis, w/o largest contributors to Relative Error)	N/A	21.3% (-1 point)	N/A	21.9%, 8.67% (-1, -3 coal points)
SSE (experimental basis)	13.7	198.8	435.4	229.1
SSE (char basis)	48.0	563.2	435.4	491.1
SSE (char basis, w/o largest contributors to Relative Error)	N/A	489.0 (-1 point)	N/A	309.4, 144.8 (-1, -3 coal points)
*Eastern Bituminous A and B				

The CCK fit of the HPFFB gasification data shown in Figure 6.19 exhibits a slight skew similar to that found for CCK in Figure 6.11. The fit with CCK^N appears to be slightly better than CCK, especially for Kentucky #9 and Eastern Bituminous B (EBB), which were the two least reactive coals. This is most likely due to the fact that 3 rate parameters were adjusted in an empirical nth-order mechanism compared to 1 parameter in CCK. The points that contributed most to the high relative errors for CCK in Table 6.7 are circled in Figure 6.19, and are mostly the same low-conversion points that caused high relative errors in the other two models.

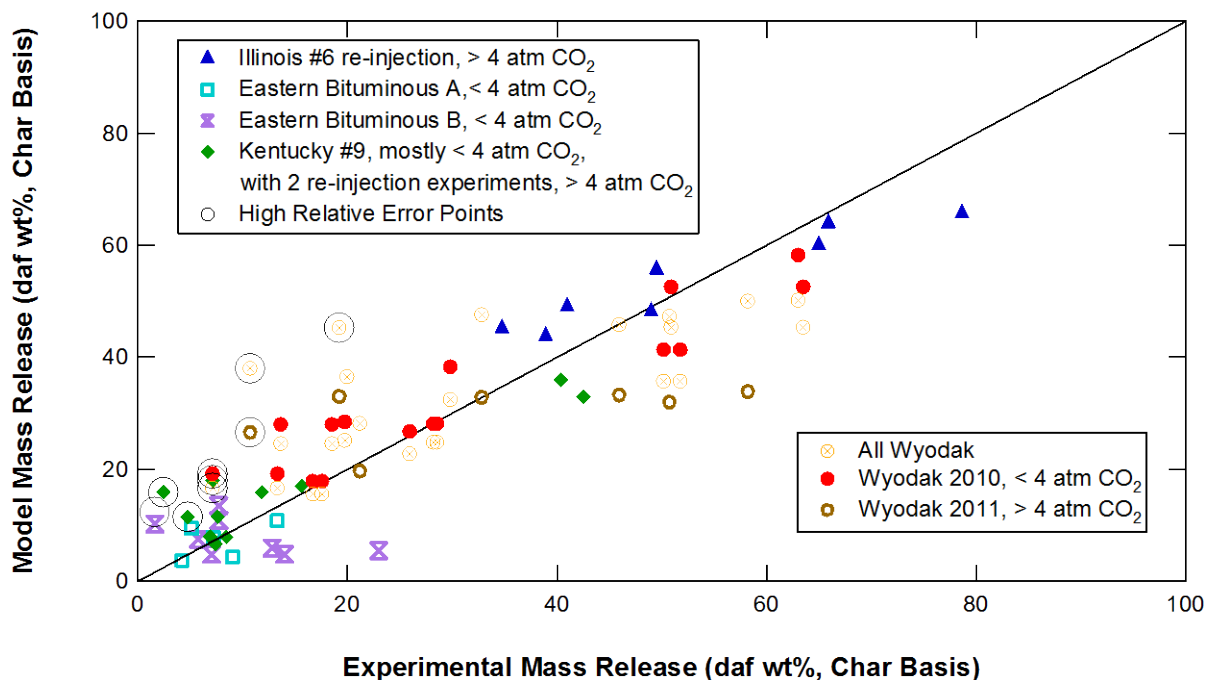


Figure 6.19. Parity plot of HPFFB gasification data with optimized CCK model predictions.

The CCK model fit the Wyodak 2010 series slightly better than CCK^N (compare Figures 6.17 and 6.19 and also Tables 6.4 and 6.7). The CCK model fit the combined Wyodak series better than both CCK^N and the first order model (see Figures 6.2 and 6.11). These results are encouraging, especially considering that the number of adjusted parameters decreased from 3 to 1. The fit of the Wyodak 2010 data was still better as an independent series at char conversions below 20% compared to the combined Wyodak series (Figure 6.19). However, the CCK model predicted conversions for three of the Wyodak 2011 experiments that were closer to the experimental values (above 40% experimental char conversion) using the parameters from the fit of all the Wyodak data compared to the parameters from the 2011 series alone.

The CCK model produced a poor fit of the Eastern Bituminous B coal (Figure 6.19, Table 6.7). This result with the most mechanistically advanced model used in this study provides

further evidence for the lower quality of the EBB data, which had low conversions and soot contamination, in addition to the unrealistically low activation energies of 13 to 17 kcal/mol derived for EBB with the other two models.

6.6.1 Correlation of CCK Model with Coal Rank

The kinetic parameter $A_{7,0}$ was compared to various measures of chemical structure for the same coals that were correlated with CCK^N (see Section 6.4.1). As with the 1st-order model and CCK^N , the best correlation for CCK was found with C/O and the char structural parameter $MW-M_{\delta}(\sigma+1)$ (see Figure 6.20 and Section 6.3.2). A quadratic correlation with $Char_{Ar} = MW-M_{\delta}(\sigma+1)$ was found to yield a fit that was more consistent with the higher-quality Illinois #6 data (compare parts b and c of Figure 6.20).

The correlations for the rate parameter $A_{7,0}$ are presented in Table 6.8. The magnitudes of the SSE values for correlations 1 and 3 in Table 6.8 are lower than those in Table 6.3, indicating that the more advanced mechanism and the single adjusted parameter used in CCK allowed for a better correlation with rank. Part of this improved fit may be due to the fact that the activation energies in the CCK model are scaled with E_7 , which was previously correlated with the carbon content of the coal (Liu and Niksa, 2004). The right-hand column of Table 6.8 indicates that the quadratic correlation with $Char_{Ar} = MW-M_{\delta}(\sigma+1)$ produces the best fit of the higher quality Illinois #6 data, and the C/O correlation predict conversion for Illinois #6 better than the linear $Char_{Ar} = MW-M_{\delta}(\sigma+1)$ correlation. Both of the $Char_{Ar}$ correlations produce better fits of the Wyodak series than the C/O correlation. Therefore, the quadratic $Char_{Ar} = MW-M_{\delta}(\sigma+1)$ is recommended because it produces the best fit of the highest quality data in this study (Illinois #6 and Wyodak 2010). The fit with this correlation is shown in (Figure 6.21).

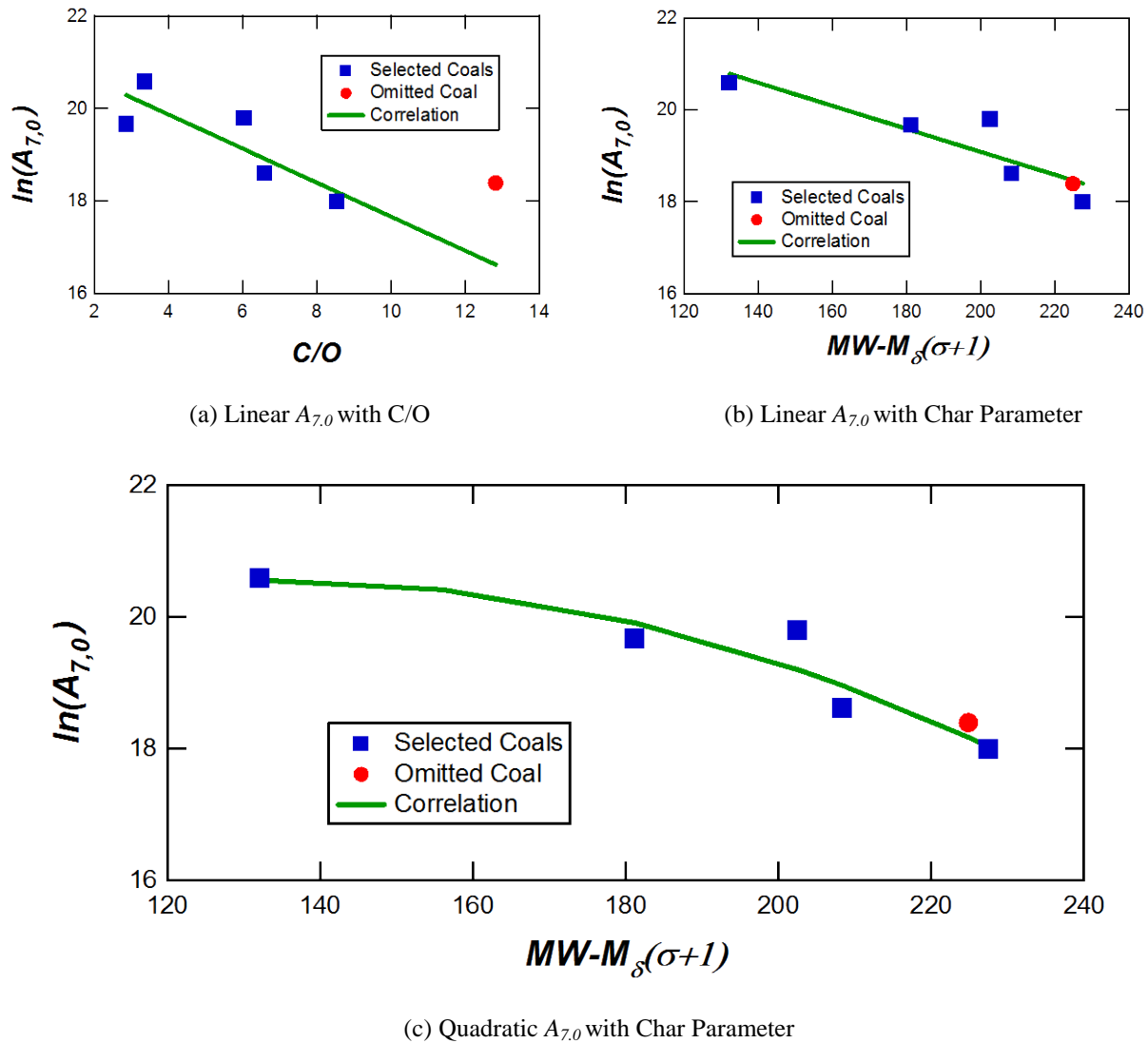


Figure 6.20. Correlations of kinetic parameter $A_{7,0}$ with coal composition and NMR parameters.

Table 6.8. Correlations for $A_{7,0}$ with coal rank for CO_2 gasification with the CCK model

	Correlation	R^2	SSER	SSER Illinois #6 only
1.	$\ln[A_{7,0}] = -3672(C/O) + 21.33$	0.71	102%	283%
2.	$\ln[A_{7,0}] = -0.02500Char_{Ar} + 24.08$	0.79	90%	360%
3.	$\ln[A_{7,0}] = -0.0002863Char_{Ar}^2 + 0.07652Char_{Ar} + 15.44$	0.87	54%	235%

Of the three models, the CCK^N rank correlations with the $Char_{Ar} = MW - M_{\delta}(\sigma + 1)$ parameter appear to yield the best overall predictions of CO₂-char reactivities when compared to the HPFFB data (compare Figures 6.10, 6.13, and 6.21). Revision of the rank correlations from CBK/G (Liu and Niksa, 2004) listed in Table 6.1 through optimization with highly detailed gasification data would probably allow CCK to yield rank correlations superior to CCK^N. However, it is also possible that the chars produced at $\sim 10^5$ K/s in the HPFFB have different reactivities compared to the chars used to produce the correlations in Table 6.1 for CBK/G.

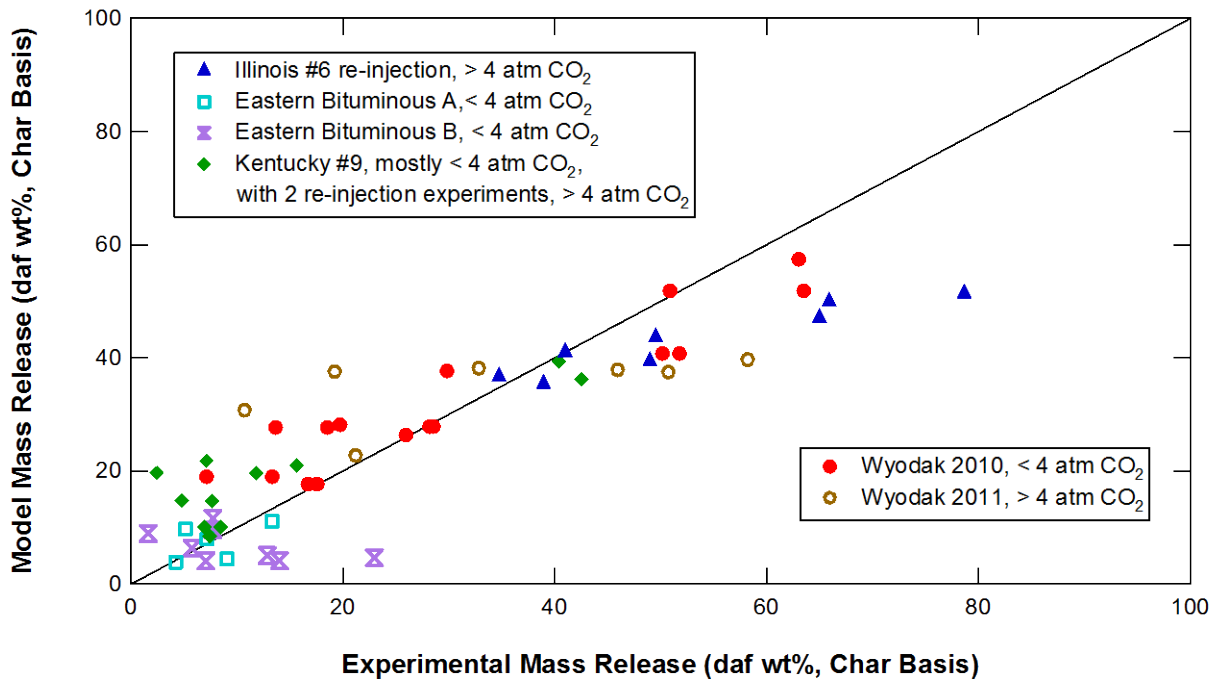


Figure 6.21. Parity plot of HPFFB gasification data with CCK predictions from quadratic $Char_{Ar}$ kinetic correlation.

6.7 Summary and Conclusions

CO₂ gasification was measured for 4 bituminous coals and a subbituminous coal (in two experimental series) at pressures of up to 15 atm with maximum particle heating rates of $\sim 10^5$

K/s. In-situ pyrolysis was found to be successful for subbituminous coals, but a reinjection strategy was found to be the most effective way to obtain good bituminous coal gasification kinetics at high temperatures without the influence of soot contamination. The reinjected chars were sieved to reduce the effects of the particle size distribution on the apparent kinetics. This reinjection strategy was implemented for the Illinois #6 experiments, yielding higher quality gasification data compared to the other bituminous coals that had few if any reinjection measurements.

Three models were developed and implemented to help interpret the data. A simple 1st-order model was used to obtain a reasonable fit of most of the data. The two series of Wyodak coal were difficult to fit together, probably due to the different sources of the coal. Better fits of the combined Wyodak series were obtained with the other two models (CCK and CCK^N), which suggests that surface saturation effects may have caused deviations from 1st-order behavior. The Wyodak 2010 series gave the most reasonable fit for all three of the models.

The 1st-order activation energies were lower than previously reported values. The lower activation energies suggest Zone II behavior prevailed in the HPFFB. This may indicate that the observed reaction rates were influenced by the physical structure of the chars that were developed during pyrolysis at high heating rates and elevated pressures. The optimal kinetic parameters were sensitive to the measured particle size. The high extent of overlap in the 1st-order rate constants from this study with previously reported rate constants suggests that the strongest effect of high pressures and heating rates on gasification rates occurs as a result of the particle diameter developed during pyrolysis, at least for the particle temperatures that occurred in this study.

Eastern Bituminous B (EBB) had a very low activation energy in the 1st-order model compared to the other coals. The fit of this coal was very poor in the most mechanistic model (CCK). The best-fit activation energy in CCK^N was also unrealistically low for EBB. These results suggest that either this high-rank coal did not reach high enough temperatures and residence times to yield data appropriate for kinetic analysis, or else the soot contamination was severe enough to interfere with mass release measurements. The Kentucky #9 also had a low activation energy in the 1st-order model, but the rate parameters were reasonable in the other two models.

The two advanced gasification models were based on the CBK oxidation models. The fit of the CO₂ gasification data with these models (CCK and CCK^N) showed some skew. This skew suggests that some of the non-kinetic model parameters ought to be adjusted so that the rate does not decrease as fast with increasing conversion. Parametric studies of model parameters indicate that the rates of thermal deactivation were probably over-predicted. The parametric studies also suggest that Knudsen diffusion is probably more important for gasification compared to combustion. Notwithstanding the slight skew, the fit of the data with the advanced models was generally quite good. Fits of the data with CCK and CCK^N were mostly comparable to each other. Differences in the fit for some of the coals were attributable to the quality of the data, the number of adjustable parameters, and the balance between theoretical and empirical forms in the kinetic mechanisms.

The HPFFB gasification data were found to yield rates far below the film-diffusion limit. There were indications of the influence of both intrinsic kinetics and diffusion through pores on the overall rate. It appears that Knudsen diffusion may make significant contributions to the observed rate. A random pore model was found to have little effect on the rates predicted by

CCK. CCK predicted that the concentrations of CO present in the HPFFB should have little impact on the observed rates at the temperatures and residence times typical in this study.

Correlations of kinetic parameters with coal rank were made for all three models. Reactivities generally decreased with increasing rank. C/O in the coal and the NMR parameter group $MW-M_{\delta}(\sigma+1)$ were used as indices of rank. $MW-M_{\delta}(\sigma+1)$ represents an estimate of the aromatic cluster mass in the char, and yielded better reactivity correlations than the more traditional C/O in all cases. The performance of C/O as a reactivity rank index was least comparable to $MW-M_{\delta}(\sigma+1)$ with the simple 1st-order model. Rank correlations for the CCK^N kinetic parameters yielded the best overall fits of the HPFFB data. However, the CCK rank correlations yielded predicted gasification rates that were more consistent with the optimal fit for the same model. Therefore, optimization of additional parameters in CCK would likely yield rank correlations superior to CCK^N.

CHAPTER 7. SUMMARY AND CONCLUSIONS

Coal pyrolysis and CO₂ gasification studies were conducted at maximum particle heating rates of $\sim 10^5$ K/s, pressures of up to 15 atm, and gas temperatures of up to 2000 K. Particle temperatures as high as 1800 K occurred in the CO₂ gasification experiments. CO₂ concentrations of 20 to 90 mole % were used with residence times of up to 690 ms. The High Pressure Flat-Flame Burner (HPFFB) was completely redesigned and rebuilt to enable these studies to occur. The new design included a smaller burner (1-inch diameter compared to 2 inches previously) in an up-flow configuration with a CO flame. The modular design enabled residence times of up to 800 ms with one vessel section and possibly up to 1600 ms if the extension section was used. Residence times were determined using optical particle velocities that were measured through a view port located ~ 1 inch above the burner. Gas temperature measurements were used to scale the particle velocity at locations downstream from the measured velocity and a momentum balance was used to estimate the particle velocity profile closer to the burner.

Very large soot agglomerates were formed from coal tar at the high gas temperatures and elevated pressures used in this study. These large soot agglomerates made accurate measurement of gasification rates more difficult for bituminous coals, because aerodynamic methods did not effectively separate the soot agglomerates from the char. Soot agglomerates of such large sizes are expected to strongly affect radiation heat transfer and carbon conversion in gasifiers. The

best gasification data for bituminous coals were obtained by pyrolyzing the coals in an oxidizer-rich flame at short residence times. The recovered char was then reinjected in fuel-rich flames with high CO₂ content to measure gasification rates.

7.1 Coal Swelling During Pyrolysis at High Heating Rates

Pyrolysis experiments conducted in two atmospheric pressure facilities using Eastern Bituminous A confirmed the strong dependence of swelling on heating rate at heating rates of 10⁴ K/s to 10⁵ K/s that had previously been observed with another bituminous coal in a different facility. These data clearly show that swelling ratios measured in drop-tube furnaces at heating rates of ~10⁴ K/s should not be applied to utility boilers and gasifiers that operate at heating rates of ~10⁶ K/s. A new nomenclature for heating rate regimes with increasing and decreasing swelling behavior was introduced.

Pyrolysis experiments were conducted in the HPFFB to measure swelling ratios as a function of pressure (up to 15 atm) and coal type at heating rates of ~10⁵ K/s. The swelling ratios from these experiments were much lower than swelling ratios measured for similar coals at heating rates of ~10⁴ K/s. This demonstrated that the effect of heating rate on swelling is also very important at elevated pressures. The maximum swelling ratios were observed at pressures near 10 atm. There are some indications that continued increases in swelling that have been observed at higher pressures may be attributable to decreases in the heating rates at increasing pressures.

Existing empirical and mechanistic swelling models did not accurately describe the observed changes in particle size as a function of heating rate, pressure and coal rank. Therefore, a new empirical swelling model was developed. A simple form was specified for the new swelling model that explicitly accounts for heating rate, pressure and coal rank. The swelling

model requires inputs of the coal ultimate and proximate analyses, the pyrolysis pressure, and the maximum derivative of particle temperature with respect to time, which can be calculated from a transient energy balance that includes convection, reaction, and radiation terms. Parameters in the swelling model were optimized using atmospheric pyrolysis data from Sandia National Laboratories. Rank effects were correlated using NMR structural parameters that were estimated from correlations that were previously developed for use with the CPD devolatilization model. At atmospheric pressure the new swelling model accurately predicted the swelling ratio for a wide variety of coals for which accurate estimates of the maximum particle heating rates were available.

The HPFFB pyrolysis data were used to optimize parameters related to the effect of pressure on swelling. Although the effect of pressure was only calibrated at pressures of 15 atm and below, the model predictions seemed reasonable when compared to mechanistic models and the limited data that were available at higher pressures. The complete swelling model was found to be capable of predicting the observed differences between swelling ratios measured in pressurized facilities that operated at heating rates of 10^4 K/s and 10^5 K/s.

7.2 Experimental Studies and Modeling of CO₂-Char Gasification

Char gasification by CO₂ was investigated for a subbituminous coal and 4 bituminous coals at pressures of up to 15 atm in the HPFFB. The quality of the bituminous coal gasification data improved as the research progressed and changes were made to eliminate soot contamination and fragmentation of char particles in the aerodynamic char collection system. The two highest quality series of data were Wyodak 2010 with in-situ pyrolysis and Illinois #6 with reinjection of char.

The gasification data were interpreted through the use of three models with different levels of sophistication. The data were found to yield rates that were far below the film-diffusion limit, indicating that the optimized rate parameters yield predictions of chemical reaction behavior with some influence from diffusion through pores. A simple model with 1st-order kinetics yielded a good fit of the most of the data. It was necessary to fit the subbituminous Wyodak data as two series to obtain a good fit. The evidence suggests that the difference was caused by a change in the supply of coal, but improved fits with the more advanced models suggests that surface saturation may also have caused deviation from 1st-order behavior. The good agreement of the rate constants from the HPFFB data with previously reported data from an atmospheric drop-tube furnace suggests that high pressures and heating rates may influence CO₂-char gasification rates most strongly through their effect on the particle size developed during pyrolysis, at least for particle temperatures of up to ~1700 K. However, lower activation energies were derived from the HPFFB data compared to previously reported values.

Two advanced gasification models were developed from the published CBK combustion models. CCK^N used n^{th} -order oxidation and gasification kinetics and was designed to predict oxidation rates that were essentially identical to CBK8. CCK used the 5-step Langmuir-Hinshelwood semi-global mechanism from CBK/G along with the 3-step oxidation mechanism from CBK/E. The fits of the HPFFB data were comparable with the two models, and both were better than the simple 1st-order model.

Parametric studies with CCK showed that the random pore model had little effect on gasification at temperatures and particle sizes typical of the HPFFB. The skew in the fit of the HPFFB data was reduced by increasing the empirical tortuosity factor by 1 to 2 orders of magnitude from its default value from combustion studies. This suggests that Knudsen diffusion

had a significant effect on the measured gasification rates. The skew of the fit was also reduced by removing the annealing model, suggesting that thermal deactivation was over-predicted. One of the reaction steps in CCK was used to scale the rate parameters in the other reactions. Very similar fits were obtained when the activation energy for the scaling reaction was fixed and when it was varied. Therefore, only the pre-exponential factor for the scaling reaction was varied for CCK in this study.

The kinetic parameters for all three models were correlated with coal rank. The CCK kinetic correlations yielded model predictions that were most consistent with the optimal fit of the HPFFB data for the same model. The robustness of the CCK kinetic correlations was probably due to the more advanced kinetic mechanism and the fact that only one parameter was correlated in this study to fit the data. The CCK^N kinetic correlations yielded the best overall fit of the HPFFB data because the CCK^N model had a slightly better optimal fit of the data. The kinetic correlations for the 1st-order model appear to work reasonably well, although they yielded the poorer predictions of gasification rates compared to the other two models. Two types of coal rank correlations were developed for each gasification model. The carbon and oxygen composition of the coal were used to correlate rank effects in one version. The other type of correlation used a group of NMR parameters as a rank index. The NMR parameters were predicted from previously published correlations with the coal ultimate and proximate analyses. The combination of NMR parameters used was $MW-M_{\delta}(\sigma+1)$, which served as an estimate of the aromatic cluster mass in the char. The correlations with this char structural parameter were used to make better predictions of the optimal rate parameters and extents of gasification compared to correlations with C/O in all three gasification models.

7.3 Experimental Recommendations

The HPFFB was used successfully with two types of heaters. It also has an extension section to allow extended residence times that was not used due to the large decreases in temperature seen in a single vessel section. The primary vessel that was used in these studies should be fitted with the more robust Nichrome wire heaters and used for pyrolysis studies and also gasification studies of reactive materials such as subbituminous coals and biomass. The slightly shorter vessel extension should be modified for use as an interchangeable stand-alone vessel with a molybdenum disilicide heater for gasification studies of solid fuels with low reactivities, such as bituminous coals. With these changes, switching between the two types of heaters will be easier and the molybdenum disilicide heaters will experience less thermal cycling.

Heater temperatures above 1350°C are not recommended in the HPFFB because temperatures above 540°C on the inner surface of the pressure vessel were observed at this condition, and it is likely that higher temperatures would be quite dangerous in a pressure vessel. If pressures above 15 atm are desired in the HPFFB, the pressure control valve would need to be upgraded. Other components of the HPFFB such as the coal feeder and the mass flow controllers would need to be inspected to determine whether they are suitable for pressures of up to 30 atm. The crank system used for the burner would probably need to be upgraded for higher pressures. The crank systems on the burner and the probe would most likely need motors to operate effectively at higher pressures.

Steam gasification studies were attempted in the early stages of this work. The simplest way to create a steam gasification environment without soot in the HPFFB is to add H₂ to the CO flame. However, this results in a higher flame speed that can damage the burner. There is a burner with a non-ideal flame that was built in the course of the HPFFB upgrades. This old

burner should be used to evaluate flame conditions for steam gasification. Once an appropriate condition has been found that does not corrode the burner surface, the newer burner that was used in these studies can be reinstalled to conduct the gasification experiments.

Gasification studies of bituminous coals in the HPFFB with various combinations of H₂O and CO₂ should be conducted using the char reinjection technique described in this work to avoid soot contamination of the char. A large supply of sieved char should be produced at high heating rates and pressures to allow all planned experiments to be conducted on a fuel that is as uniform as possible. Having a larger supply of char would also allow better characterization of the char via adsorption and other techniques. Subbituminous coals should be studied with in-situ pyrolysis and also with reinjection in similar environments to determine how much the difference in thermal histories affects the derived kinetic parameters.

The HPFFB could be modified to have a drop-tube furnace mode, wherein the electric heaters would replace the burner as the primary source of heat to the coal. This would enable other types of pressurized studies to be conducted. Experiments with simple gas compositions in drop-tube mode could be compared to results with the complex gas compositions produced from the burner. This technique should be used to quantify CO and CO₂ inhibition effects in gasification studies. A drop-tube furnace mode would operate at $\sim 10^4$ K/s, compared to 10^5 K/s for the HPFFB used in this study. Studies of the effects of heating rate on coal swelling at elevated pyrolysis pressures should be conducted on a common suite of coals with these two types of facilities.

Studies should be conducted on the effects of different char sizes and structures developed during pyrolysis on gasification behavior. Chars from the same coal should be pyrolyzed in different facilities, such as drop-tube furnaces and flat-flame burners operating at

atmospheric pressure and elevated pressures. Some of these chars should be sieved, and all of the chars would then be studied under the same gasification conditions. This approach may permit the effects of particle size to be separated from the effects of chemical structure and particle morphology, including pore structure. The effects of heating rate and pressure during pyrolysis on the subsequent gasification behavior could then be determined in more detail.

7.4 Modeling Recommendations

The swelling model developed in this study should continue to be evaluated through comparison to additional experimental data. Pressurized pyrolysis experiments with large differences in heating rates would be particularly helpful in evaluating the basic form of the swelling model. Pyrolysis experiments at pressures above 20 atm would be particularly useful for evaluating how well the model extrapolates to higher pressures. The performance of the swelling model should be characterized with different devolatilization models and different measures of the extent of pyrolysis used to scale the particle diameter. This can be accomplished by integrating the swelling correlation into codes with different pyrolysis models and comparing the resulting pyrolysis calculations to experimental measurements and the 1-D CPD-based code that was used in this work.

The CCK and CCK^N models should be compared to more experimental data to determine how they perform under a wider variety of conditions and for more coals. Distribution of the models to other researchers would facilitate this process. Since some of the CBK/G rate parameter correlations were found to be inapplicable to the HPFFB data, the other CBK/G correlations should be verified, or new ones should be developed. Ideally, the CCK model should be compared to the same data sets that were used to develop the CBK/G correlations so that the performance of CCK can be compared to CBK/G. Both CCK and CCK^N should be used to fit

steam gasification data. A good fit of steam gasification data with the same CCK rate parameters that were developed in this study for CO₂ gasification would help validate the CBK/G mechanism that was used in CCK.

One or both of the CCK models should be combined with the swelling model developed in this study and the CPD model to make a complete 1-D combustion and gasification code. Such a code would have the advantage of using the energy balance and mass transport calculations to determine how much overlap there is between pyrolysis heterogeneous reactions. The time and particle temperature where heterogeneous reactions become significant would be easier to calculate in such a model. This kind of combined model would be highly useful for analyzing laboratory scale data, and would serve as a pattern for applying the individual models in CFD codes.

Some features of merit that were once included in various versions of the CBK model have since been discarded to simplify the code. It may be worthwhile to have a version of CCK that includes all of the advanced features for highly detailed studies of heterogeneous reaction behavior of chars. CCK should be modified to include the random pore model that was used to calculate the effective diffusivity in the HP-CBK model. The reintroduction of this sub-model would require experimental pore structural information, but it would allow the roles of molecular and Knudsen diffusion in gasification to be evaluated explicitly. The original CBK6 model included preferential consumption of the most reactive material at early residence times via a statistical kinetics sub-model. This model was quite cumbersome to implement previously, but it has a good theoretical basis. A sequential strategy rather than a parallel strategy could be used to speed up the distributed activation energy component of the statistical kinetics sub-model. A sequential strategy of this type has already been implemented with success in the CPD model.

Other advanced combustion and gasification models are beginning to use char morphology models. One or both of the CCK models should be upgraded with different effectiveness factors or some other morphology model and compared to gasification data with very detailed char structural characterization. This would allow the value of char morphology models to be evaluated. Any features that are added to the CCK models should be implemented in such a way that the user can specify which models are to be turned on or off, so that the value of different advanced features can be evaluated.

REFERENCES

- "FLUENT User's Guide," Lebanon, NH, FLUENT, Inc. (2007).
- Ahn, D. H., B. M. Gibbs, K. H. Ko and J. J. Kim, "Gasification kinetics of an Indonesian sub-bituminous coal-char with CO₂ at elevated pressure," *Fuel*, **80**(11), 1651-1658 (2001).
- Bahlawane, N., U. Struckmeier, K. T. S. and P. Oßwald, "Noncatalytic Thermocouple Coatings Produced with Chemical Vapor Deposition For Flame Measurements," *Review of Scientific Instruments*, **78**(1), 013905 (2007).
- Baxter, L. L., R. E. Mitchell and T. H. Fletcher, "Release of Inorganic Material during Coal Devolatilization," *Combustion and Flame*, **108**(4), 494-502 (1997).
- Benfell, K. E., G. S. Liu, D. G. Roberts, D. J. Harris, J. A. Lucas, J. G. Bailey and T. F. Wall, "Modeling Char Combustion: The Influence of Parent Coal Petrography and Pyrolysis Pressure on the Structure and Intrinsic Reactivity of its Char," *Proceedings of the Combustion Institute*, **28**, 2233-2241 (2000).
- Benfell, K. E., "Assessment of Char Morphology in High Pressure Pyrolysis and Combustion," PhD Thesis, Geology, University of Newcastle (2001).
- Bhatia, S. K. and D. D. Perlmutter, "A Random Pore Model for Fluid-Solid Interactions, Kinetic Control," *Aiche Journal*, **26**(3), 379-386 (1980).
- Bhatia, S. K. and D. D. Perlmutter, "A Random Pore Model for Fluid-Solid Interactions II: Diffusion and Transport Effects," *Aiche Journal*, **27**(2), 247-254 (1981).
- Bird, R. B., W. E. Stewart and E. N. Lightfoot, Transport Phenomena, New York, John Wiley & Sons (1960).
- Bird, R. B., W. E. Stewart and E. N. Lightfoot, Transport Phenomena, New York, John Wiley & Sons (2002).
- Bischoff, K. B., "Effectiveness Factors for General Reaction Rate Forms," *AICHE Journal*, **11**(2), 351-355 (1965).
- Brown, A. L. and T. H. Fletcher, "Modeling Soot Derived from Pulverized Coal," *Energy & Fuels*, **12**(4), 745-757 (1998).
- Brunauer, S., P. H. Emmett and E. Teller, "Adsorption of Gases in Multimolecular Layers," *J. Am. Chem. Soc.*, **60**, 309 (1938).

- Brunner, K. M., "Flatbed Telecine," <http://digireel.blogspot.com/2007/10/computer-io.html> (2007).
- Carberry, J. J., "The micro-macro effectiveness factor for the reversible catalytic reaction," *Aiche Journal*, **8**(4), 557-558 (1962).
- Chen, H., Z. Luo, H. Yang, F. Ju and S. Zhang, "Pressurized Pyrolysis and Gasification of Chinese Typical Coal Samples," *Energy & Fuels*, **22**(2), 1136-1141 (2008).
- Chen, J. C. Y., "Effects of Secondary Reactions on Product Distribution and Nitrogen Evolution from Rapid Coal Pyrolysis," Ph.D. Dissertation, Mechanical Engineering Department, Stanford University (1991).
- Cloke, M., T. Wu, R. Barranco and E. Lester, "Char characterisation and its application in a coal burnout model," *Fuel*, **82**(15-17), 1989-2000 (2003).
- Collis, D. C. and M. J. Williams, "Two-Dimensional Convection from Heated Wires at Low Reynolds Numbers," *Journal of Fluid Mechanics*, **6**, 357-384 (1959).
- Daines, R. L., "Collection and Characterization of Pyrolyzed Coal Char and Tar at High Pressure," M.S. Thesis, Mechanical Engineering, Brigham Young University (1990).
- Draper, N. R. and H. Smith, Applied Regression Analysis, New York, John Wiley & Sons (1998).
- Eiteneer, B. and M. Frenklach, "Experimental and modeling study of shock-tube oxidation of acetylene," *International Journal of Chemical Kinetics*, **35**(9), 391-414 (2003).
- Eiteneer, B., R. Subramanian, S. Maghzi, C. Zeng, X. Guo, Y. Long, L. Chen, R. JS, A. Raman, J. Jain, T. Fletcher and R. Shurtz, "Gasification Kinetics: Modeling Tools Development and Validation," 26th Annual International Pittsburgh Coal Conference, Pittsburgh, PA (2009).
- Ergun, S., "Kinetics of the Reaction of Carbon Dioxide with Carbon," *Journal of Physical Chemistry*, **60**, 480 (1956).
- Essenhigh, R. H. and M. K. Misra, "Autocorrelations of Kinetic Parameters in Coal and Char Reactions," *Energy & Fuels*, **4**(2), 171-177 (1990).
- Essenhigh, R. H., "Influence of Initial Particle Density on the Reaction Mode of Porous Carbon Particles," *Combustion and Flame*, **99**(2), 269-279 (1994).
- Fairbanks, D. F. and C. R. Wilke, "Diffusion Coefficients in Multicomponent Gas Mixtures," *Industrial & Engineering Chemistry*, **42**(3), 471-475 (1950).
- Fermoso, J., M. V. Gil, A. G. Borrego, C. Pevida, J. J. Pis and F. Rubiera, "Effect of the Pressure and Temperature of Devolatilization on the Morphology and Steam Gasification Reactivity of Coal Chars," *Energy and Fuels*, **24**, 5586-5595 (2010).

- Fletcher, T. H., "Time-Resolved Temperature Measurements of Individual Coal Particles during Devolatilization," *Combustion Science and Technology*, **63**(1-3), 89-105 (1989a).
- Fletcher, T. H., "Time-Resolved Particle Temperature and Mass Loss Measurements of a Bituminous Coal during Devolatilization," *Combustion and Flame*, **78**(2), 223-236 (1989b).
- Fletcher, T. H., A. R. Kerstein, R. J. Pugmire and D. M. Grant, "Chemical Percolation Model for Devolatilization. 2. Temperature and Heating Rate Effects on Product Yields," *Energy & Fuels*, **4**(1), 54-60 (1990).
- Fletcher, T. H. and D. R. Hardesty, "Compilation of Sandia Coal Devolatilization Data: Milestone Report," Livermore, CA, USA, Sandia National Laboratories, **SAND92-8209**: 346 pages (1992).
- Fletcher, T. H., A. R. Kerstein, R. J. Pugmire, M. S. Solum and D. M. Grant, "Chemical Percolation Model for Devolatilization. 3. Direct Use of ^{13}C NMR Data to Predict Effects of Coal Type," *Energy & Fuels*, **6**(4), 414-31 (1992).
- Fletcher, T. H., "Swelling Properties of Coal Chars during Rapid Pyrolysis and Combustion," *Fuel*, **72**(11), 1485-95 (1993).
- Fletcher, T. H., "CPDCP_NLG Code," <http://www.et.byu.edu/~tom/cpd/cpdcodes.html> (2011).
- Freihaut, J. D., W. M. Proscia and D. J. Seery, "Chemical Characteristics of Tars Produced in a Novel Low-Severity, Entrained-Flow Reactor," *Energy & Fuels*, **3**(6), 692-703 (1989).
- Frenklach, M. and H. Wang, "Detailed Modeling of Soot Particle Nucleation and Growth," *Symposium (International) on Combustion*, **23**, 1559-1566 (1991).
- Frenklach, M., "Reaction Mechanism of Soot Formation in Flames," *Phys. Chem. Chem. Phys.*, **4**(11), 2028-2037 (2002).
- Gadsby, J., F. J. Long, P. Sleightholm and K. W. Sykes, "The Mechanism of the Carbon Dioxide-Carbon Reaction," *Proceedings of the Royal Society of London. Series A, Mathematical and Physical Sciences*, **193**(1034), 357-376 (1948).
- Gale, T. K., "Effects of Pyrolysis Conditions on Coal Char Properties," Ph.D. Dissertation, Mechanical Engineering Department, Brigham Young University (1994).
- Gale, T. K., C. H. Bartholomew and T. H. Fletcher, "Decreases in the Swelling and Porosity of Bituminous Coals during Devolatilization at High Heating Rates," *Combustion and Flame*, **100**(1-2), 94-100 (1995).
- Gavalas, G. R., "A Random Capillary Model with Application to Char Gasification at Chemically Controlled Rates," *Aiche Journal*, **26**(4), 577-585 (1980).

- Genetti, D., T. H. Fletcher and R. J. Pugmire, "Development and Application of a Correlation of ^{13}C NMR Chemical Structural Analyses of Coal Based on Elemental Composition and Volatile Matter Content," *Energy & Fuels*, **13**(1), 60-68 (1999).
- Goetz, G. J., N. Y. Nsakala, R. L. Patel and T. C. Lao, "Combustion and Gasification Kinetics of Chars from Four Commercially Significant Coals of Varying Rank," Second Annual Contractors' Conference on Coal Gasification, Palo Alto, California (1982).
- Grant, D. M., R. J. Pugmire, T. H. Fletcher and A. R. Kerstein, "Chemical Model of Coal Devolatilization Using Percolation Lattice Statistics," *Energy & Fuels*, **3**(2), 175-86 (1989).
- Green, D. W. and R. H. Perry, Eds., Perry's Chemical Engineers' Handbook, 6th Edition (1984).
- Green, D. W. and R. H. Perry, Eds., Perry's Chemical Engineers' Handbook (8th Edition), McGraw-Hill (2008).
- Hamilton, L. H., "A Preliminary Account of Char Structures Produced From Liddell Vitrinite Pyrolysed at Various Heating Rates," *Fuel*, **59**(2), 112-116 (1980).
- Harris, D. J., D. G. Roberts and D. G. Henderson, "Gasification behaviour of Australian coals at high temperature and pressure," *Fuel*, **85**(2), 134-142 (2006).
- Hecker, W. C., P. M. Madsen, M. R. Sherman, J. W. Allen, R. J. Sawaya and T. H. Fletcher, "High-Pressure Intrinsic Oxidation Kinetics of Two Coal Chars," *Energy & Fuels*, **17**(2), 427-432 (2003).
- Hessler, J. P., S. Seifert, R. E. Winans and T. H. Fletcher, "Small-Angle X-Ray Studies of Soot Inception and Growth," *Faraday Discussions*, **119**(Combustion Chemistry: Elementary Reactions to Macroscopic Processes), 395-407 (2001).
- Hillier, J. L., "Pyrolysis Kinetics and Chemical Structure Considerations of a Green River Oil Shale and its Derivatives," Ph.D. Dissertation, Chemical Engineering, Brigham Young University (2011).
- Hodge, E. M., D. G. Roberts, D. J. Harris and J. F. Stubington, "The Significance of Char Morphology to the Analysis of High-Temperature Char-CO₂ Reaction Rates," *Energy & Fuels*, **24**, 100-107 (2010).
- Honeywell, "Microbridge Airflow Sensors: Gas Correction Factors Reference and Application Data," http://content.honeywell.com/sensing/prodinfo/massairflow/technical/c15_131.pdf (2011).
- Hong, J., W. C. Hecker and T. H. Fletcher, "Modeling high-pressure char oxidation using Langmuir kinetics with an effectiveness factor," *Proceedings of the Combustion Institute*, **28**(2), 2215-2223 (2000a).

- Hong, J., W. C. Hecker and T. H. Fletcher, "Improving the Accuracy of Predicting Effectiveness Factors for n th Order and Langmuir Rate Equations in Spherical Coordinates," *Energy & Fuels*, **14**(3), 663-670 (2000b).
- Hurt, R., J.-K. Sun and M. Lunden, "A Kinetic Model of Carbon Burnout in Pulverized Coal Combustion," *Combustion and Flame*, **113**(1-2), 181-197 (1998).
- Hurt, R. H. and R. E. Mitchell, "Unified high-temperature char combustion kinetics for a suite of coals of various rank," *Symposium (International) on Combustion*, **24**(1), 1243-1250 (1992).
- Hurt, R. H., M. M. Lunden, E. G. Brehob and D. J. Maloney, "Statistical kinetics for pulverized coal combustion," *Symposium (International) on Combustion*, **26**(2), 3169-3177 (1996).
- Hurt, R. H. and J. M. Calo, "Semi-global intrinsic kinetics for char combustion modeling," *Combustion and Flame*, **125**(3), 1138-1149 (2001).
- Hurt, R. H., "Personal Communication Regarding Details of CBK Codes," R. Shurtz (2010).
- Kajitani, S., S. Hara and H. Matsuda, "Gasification Rate Analysis of Coal Char with a Pressurized Drop Tube Furnace," *Fuel*, **81**(5), 539-546 (2002).
- Kajitani, S., N. Suzuki, M. Ashizawa and S. Hara, "CO₂ Gasification Rate Analysis of Coal Char in Entrained Flow Coal Gasifier," *Fuel*, **85**(2), 163-169 (2006).
- Kee, R. J., G. Dixon-Lewis, J. Warnatz, M. E. Coltrin and J. A. Miller, "A Fortran Computer Code Package for the Evaluation of Gas-Phase Multicomponent Transport Properties," Livermore, CA, USA, Sandia National Laboratories, **SAND86-8246** (1986).
- Kee, R. J., M. E. Coltrin and P. Glarborg, Chemically Reacting Flow: Theory and Practice, Hoboken, NJ, John Wiley & Sons (2003).
- Khan, M. R. and R. G. Jenkins, "Thermoplastic Properties of Coal at Elevated Pressures: 1. Evaluation of a High-Pressure Microdilatometer," *Fuel*, **63**(1), 109-115 (1984).
- Khan, M. R. and R. G. Jenkins, "Swelling and Plastic Properties of Coal Devolatilized at Elevated Pressures: An Examination of the Influences of Coal Type," *Fuel*, **65**(5), 725-731 (1986).
- Kidena, K., T. Yamashita and A. Akimoto, "Prediction of Thermal Swelling Behavior on Rapid Heating Using Basic Analytical Data," *Energy & Fuels*, **21**(2), 1038-1041 (2007).
- Laurendeau, N. M., "Heterogeneous Kinetics of Coal Char Gasification and Combustion," *Progress in Energy and Combustion Science*, **4**(4), 221-270 (1978).
- Ledesma, E. B., N. D. Marsh, A. K. Sandrowitz and M. J. Wornat, "An Experimental Study on the Thermal Decomposition of Catechol," *Proceedings of the Combustion Institute*, **29**, 2299-2306 (2002).

- Ledesma, E. B., M. J. Wornat, P. G. Felton and J. A. Sivo, "The Effects of Pressure on the Yields of Polycyclic Aromatic Hydrocarbons Produced during the Supercritical Pyrolysis of Toluene," *Proceedings of the Combustion Institute*, **30**(1), 1371-1379 (2005).
- Lee, C. W., A. W. Scaroni and R. G. Jenkins, "Effect of Pressure on the Devolatilization and Swelling Behavior of a Softening Coal During Rapid Heating," *Fuel*, **70**(8), 957-965 (1991).
- Leininger, J. P., F. Lorant, C. Minot and F. Behar, "Mechanisms of 1-Methylnaphthalene Pyrolysis in a Batch Reactor," *Energy & Fuels*, **20**(6), 2518-2530 (2006).
- Lewis, A. D., "Sawdust Pyrolysis and Petroleum Coke CO₂ Gasification at High Heating Rates," M.S. Thesis, Chemical Engineering, Brigham Young University (2011).
- Lim, J.-Y., I. N. Chatzakis, A. Megaritis, H.-Y. Cai, D. R. Dugwell and R. Kandiyoti, "Gasification and Char Combustion Reactivities of Daw Mill Coal in Wire-Mesh and 'Hot-Rod' Reactors," *Fuel*, **76**(13), 1327-1335 (1997).
- Liu, G.-S. and S. Niksa, "Coal Conversion Submodels for Design Applications at Elevated Pressures. Part II. Char Gasification," *Progress in Energy and Combustion Science*, **30**(6), 679-717 (2004).
- Liu, G., H. Wu, R. P. Gupta, J. A. Lucas, A. G. Tate and T. F. Wall, "Modeling the Fragmentation of Non-Uniform Porous Char Particles during Pulverized Coal Combustion," *Fuel*, **79**(6), 627-633 (2000).
- Liu, K., Z. Cui and T. H. Fletcher, "Coal Gasification," Hydrogen and Syngas Production and Purification Technologies, K. Liu, C. Song and V. Subramani, New York, John Wiley & Sons (2010).
- Logix4u, "Inpout32.dll for Windows 98/2000/NT/XP," <http://logix4u.net/> (2008).
- Lu, M. and J. A. Mulholland, "Aromatic hydrocarbon growth from indene," *Chemosphere*, **42**(5-7), 625-633 (2001).
- Lynch, B. and R. Durie, "Comparative Studies of Brown Coal and Lignin. II. The Action of Concentrated Alkali at Elevated Temperatures," *Australian Journal of Chemistry*, **13**(4), 567-581 (1960).
- Ma, J., "Soot Formation During Coal Pyrolysis," Ph.D. Dissertation, Chemical Engineering Department, Brigham Young University (1996).
- Ma, L. and R. E. Mitchell, "Modeling Char Oxidation Behavior under Zone II Burning Conditions at Elevated Pressures," *Combustion and Flame*, **156**(1), 37-50 (2009).
- Maloney, D. J., R. Sampath and J. W. Zondlo, "Heat Capacity and Thermal Conductivity Considerations for Coal Particles During Early Stages of Rapid Heating," *Combustion and Flame*, **116**, 94-104 (1999).

- Maloney, D. J., E. R. Monazam, K. H. Casleton and C. R. Shaddix, "Evaluation of char combustion models: measurement and analysis of variability in char particle size and density," *Proceedings of the Combustion Institute*, **30**, 2197-2204 (2005).
- Manton, N., J. Cor, G. Mul, D. Eckstrom and R. Malhotra, "Impact of Pressure Variations on Coal Devolatilization Products. 2. Detailed Product Distributions from 1.0 MPa," *Energy & Fuels*, **18**(2), 520-530 (2004).
- Marsh, H. and T. Siemieniewska, "The Surface Areas of Coals as Evaluated from the Adsorption Isotherms of Carbon Dioxide using the Dubinin-Polanyi Equation," *Fuel*, **44**, 355 (1967).
- Marsh, N. D., M. J. Wornat, L. T. Scott, A. Necula, A. L. Lafleur and E. F. Plummer, "The Identification of Cyclopenta-Fused and Ethynyl-Substituted Polycyclic Aromatic Hydrocarbons in Benzene Droplet Combustion Products," *Polycyclic Aromatic Compounds*, **13**(4), 379-402 (1999).
- Marsh, N. D., M. J. Wornat, L. T. Scott, A. Necula, A. L. Lafleur and E. F. Plummer, "The Identification of Cyclopenta-Fused and Ethynyl-Substituted Polycyclic Aromatic Hydrocarbons in Benzene Droplet Combustion Products," *Polycyclic Aromatic Compounds*, **13**(4), 379-402 (2000).
- Marsh, N. D., E. B. Ledesma, M. J. Wornat, M. P. Tan, D. L. Zhu and C. K. Law, "Newly Identified Products of Benzene Droplet Combustion: Polycyclic Aromatic Hydrocarbons of Three to Ten Rings," *Polycyclic Aromatic Compounds*, **25**(3), 227-244 (2005).
- McBride, B. J., M. Zehe and S. Gordon, "NASA Glenn Coefficients for Calculating Thermodynamic Properties of Individual Species," [NASA TP-2002-215556](#) (2002).
- Melia, P. F. and C. T. Bowman, "A three-zone model for coal particle swelling," *Combustion Science and Technology*, **31**(3-4), 195-201 (1983).
- Merrick, D., "Mathematical Models of the Thermal Decomposition of Coal: 2. Specific Heats and Heats of Reaction," *Fuel*, **62**(5), 540-546 (1983).
- Messenböck, R. C., D. R. Dugwell and R. Kandiyoti, "CO₂ and steam-gasification in a high-pressure wire-mesh reactor: the reactivity of Daw Mill coal and combustion reactivity of its chars," *Fuel*, **78**(7), 781-793 (1999).
- Messenböck, R. C., N. P. Paterson, D. R. Dugwell and R. Kandiyoti, "Factors governing reactivity in low temperature coal gasification. Part 1. An attempt to correlate results from a suite of coals with experiments on maceral concentrates," *Fuel*, **79**(2), 109-121 (2000).
- Mikolajczak, C. J., M. J. Wornat, F. L. Dryer, O. B. Fringer and T. J. Held, "A Flow Reactor Study of 1-Methylnaphthalene Pyrolysis Using a New Condensed Species Sampling Probe," *Chemical and Physical Processes in Combustion*, 183-186 (1996).

- Mitchell, R. E., "A Theoretical Model of Chemically Reacting Recirculating Flow," Livermore, CA, USA, Sandia National Laboratories, **SAND79-8236** (1980).
- Mitchell, R. E., "Variations in the temperatures of coal-char particles during combustion: a consequence of particle-to-particle variations in ash-content," *Symposium (International) on Combustion*, **23**, 1297-304 (1991).
- Mitchell, R. E., R. H. Hurt, L. L. Baxter and D. R. Hardesty, "Compilation of Sandia Coal Char Combustion Data and Kinetic Analyses. Milestone Report," Livermore, CA, USA, Sandia National Laboratories, **SAND92-8208**: 615 pages (1992).
- Mitchell, R. E., "An Intrinsic Kinetics-Based, Particle-Population Balance Model for Char Oxidation during Pulverized Coal Combustion," *Proceedings of the Combustion Institute*, **28**(2), 2261-2270 (2000).
- MKS, "Gas Correction Factors for Thermal-Based Mass Flow Controllers," <http://www.mksinst.com/docs/UR/MFCGasCorrection.aspx> (2011).
- Monson, C. R., "Char Oxidation at Elevated Pressure," Ph.D. Dissertation, Mechanical Engineering, Brigham Young University (1992).
- Mühlen, H.-J., K. H. van Heek and H. Jüntgen, "Kinetic Studies of Steam Gasification of Char in the Presence of H₂, CO₂ and CO," *Fuel*, **64**(7), 944-949 (1985).
- Niksa, S., "FLASHCHAIN Theory For Rapid Coal Devolatilization Kinetics. 2. Impact of Operating-Conditions," *Energy & Fuels*, **5**(5), 665-673 (1991a).
- Niksa, S., "FLASHCHAIN Theory For Rapid Coal Devolatilization Kinetics. 3. Modeling the Behavior of Various Coals," *Energy & Fuels*, **5**(5), 673-683 (1991b).
- Niksa, S. and A. R. Kerstein, "FLASHCHAIN Theory For Rapid Coal Devolatilization Kinetics. 1. Formulation," *Energy & Fuels*, **5**(5), 647-665 (1991).
- Niksa, S., G. S. Liu and R. H. Hurt, "Coal Conversion Submodels for Design Applications at Elevated Pressures. Part I. Devolatilization and Char Oxidation," *Progress in Energy and Combustion Science*, **29**(5), 425-477 (2003).
- Oh, M. S., W. A. Peters and J. B. Howard, "An Experimental and Modeling Study of Softening Coal Pyrolysis," *Aiche Journal*, **35**(5), 775-792 (1989).
- Omega, "Gas Correction Factors," http://www.omega.com/green/pdf/fma_gas_conv_ref.pdf (2011).
- Parkinson, A. R. and R. J. Balling, "The OptdesX design optimization software," *Structural and Multidisciplinary Optimization*, **23**(2), 127-139 (2002).
- Paul, P. H., "DRFM: A New Package for the Evaluation of Gas-Phase-Transport Properties," Livermore, CA, USA, Sandia National Laboratories, **SAND98-8203** (1997).

- Peng, F. F., I. C. Lee and R. Y. K. Yang, "Reactivities of in situ and ex situ Coal Chars during Gasification in Steam at 1000-1400°C," *Fuel Processing Technology*, **41**(3), 233-251 (1995).
- Perry, S. T., E. M. Hambly, T. H. Fletcher, M. S. Solum and R. J. Pugmire, "Solid-State ¹³C NMR Characterization of Matched Tars and Chars from Rapid Coal Devolatilization," *Proceedings of the Combustion Institute*, **28**(2), 2313-2319 (2000).
- Pickett, B. M., "Effects of Moisture on Combustion of Live Wildland Forest Fuels," Ph.D. Dissertation, Chemical Engineering, Brigham Young University (2008).
- Poddar, N. B., S. Thomas and M. J. Wornat, "Polycyclic Aromatic Hydrocarbons from the Co-Pyrolysis of Catechol and Propyne," *Proceedings of the Combustion Institute*, **33**(1), 541-548 (2011).
- Price, R. J., "Modeling Three Reacting Flow Systems with Modern Computational Fluid Dynamics," Ph.D. Dissertation, Chemical Engineering, Brigham Young University (2007).
- Pugmire, R., S. Yan, Y. J. Jiang, M. S. Solum, I. Preciado, E. G. Eddings and A. F. Sarofim, "Characterization of Free Radicals in Multi-Source Particular Emissions," *Abstracts of Papers, 231st ACS National Meeting, Atlanta, GA, United States, March 26-30, 2006*, FUEL-102 (2006).
- Ranz, W. E. and W. R. Marshall, "Evaporation From Drops," *Chemical Engineering Progress*, **48**, 141-146, 173-180 (1952).
- Roberts, D. G. and D. J. Harris, "Char Gasification with O₂, CO₂, and H₂O: Effects of Pressure on Intrinsic Reaction Kinetics," *Energy & Fuels*, **14**(2), 483-489 (2000).
- Roberts, D. G., D. J. Harris and T. F. Wall, "Total pressure effects on chemical reaction rates of chars with O₂, CO₂ and H₂O," *Fuel*, **79**(15), 1997-1998 (2000).
- Roberts, D. G., D. J. Harris and T. F. Wall, "On the Effects of High Pressure and Heating Rate during Coal Pyrolysis on Char Gasification Reactivity," *Energy & Fuels*, **17**(4), 887-895 (2003).
- Roberts, D. G. and D. J. Harris, "A Kinetic Analysis of Coal Char Gasification Reactions at High Pressures," *Energy & Fuels*, **20**(6), 2314-2320 (2006).
- Roberts, D. G. and D. J. Harris, "Char gasification in mixtures of CO₂ and H₂O: Competition and inhibition," *Fuel*, **86**(17-18), 2672-2678 (2007).
- Roberts, D. G., E. M. Hodge, D. J. Harris and J. F. Stubington, "Kinetics of Char Gasification with CO₂ under Regime II Conditions: Effects of Temperature, Reactant, and Total Pressure," *Energy & Fuels*, **24**, 5300-5308 (2010).

- Rowley, R. L., W. V. Wilding, J. L. Oscarson, Y. Yang and N. F. Giles, "DIPPR® Data Compilation of Pure Chemical Properties," Design Institute for Physical Properties, AIChE, New York, NY (2010).
- Sarofim, A. F., J. P. Longwell, M. J. Wornat and J. Mukherjee, "The Role of Biaryl Reactions in PAH and Soot Formation," *Springer Series in Chemical Physics*, **59**(Soot Formation in Combustion), 485-499 (1994).
- Sarofim, A. F., J. Lighty and E. G. Eddings, "Keynote address. Combustion Generated Aerosols: Health effects, Characterization, Mechanisms of Formation, and Modeling," *Abstracts of Papers of the American Chemical Society*, **224**, 080-FUEL (2002).
- Seber, G. A. F. and C. J. Wild, Nonlinear Regression, New York, Wiley & Sons (2003).
- Serio, M. A., D. G. Hamblen, J. R. Markham and P. R. Solomon, "Kinetics of Volatile Product Evolution in Coal Pyrolysis: Experiment and Theory," *Energy & Fuels*, **1**(2), 138-152 (1987).
- Shaddix, C. R., "Correcting Thermocouple Measurements for Radiation Loss: A Critical Review," 33rd National Heat Transfer Conference, Albuquerque, New Mexico, ASME (1999).
- Sheng, C. D. and J. L. T. Azevedo, "Modeling the Evolution of Particle Morphology During Coal Devolatilization," *Proceedings of the Combustion Institute*, **28**(2), 2225-2232 (2000).
- Simons, G. A., "The Role of Pore Structure in Coal Pyrolysis and Gasification," *Progress in Energy and Combustion Science*, **9**(4), 269-290 (1983).
- Skjoth-Rasmussen, M. S., P. Glarborg, M. Ostberg, J. T. Johannessen, H. Livbjerg, A. D. Jensen and T. S. Christensen, "Formation of polycyclic aromatic hydrocarbons and soot in fuel-rich oxidation of methane in a laminar flow reactor," *Combustion and Flame*, **136**(1-2), 91-128 (2004).
- Smith, I. W., "The Combustion Rates of Coal Chars: A Review," *Symposium (International) on Combustion*, **19**(1), 1045-1065 (1982).
- Smith, K. L., L. D. Smoot, T. H. Fletcher and R. J. Pugmire, The Structure and Reaction Processes of Coal, New York, Plenum Press (1994).
- Smoot, L. D. and D. T. Pratt, Pulverized Coal Combustion and Gasification, New York, Plenum Press (1979).
- Smoot, L. D. and P. J. Smith, Coal Combustion and Gasification, New York, Plenum Press (1985).
- Solomon, P. R., D. G. Hamblen, R. M. Carangelo, M. A. Serio and G. V. Deshpande, "General Model of Coal Devolatilization," *Energy & Fuels*, **2**(4), 405-422 (1988a).

- Solomon, P. R., D. G. Hamblen, R. M. Carangelo, M. A. Serio and G. V. Deshpande, "Models of Tar Formation During Coal Devolatilization," *Combustion and Flame*, **71**(2), 137-146 (1988b).
- Solomon, P. R., D. G. Hamblen, Z. Z. Yu and M. A. Serio, "Network Models of Coal Thermal-Decomposition," *Fuel*, **69**(6), 754-763 (1990).
- Solomon, P. R. and T. H. Fletcher, "Impact of Coal Pyrolysis on Combustion," *Symposium (International) on Combustion*, **25**, 463-74 (1994).
- Solum, M. S., R. J. Pugmire and D. M. Grant, "¹³C Solid-State NMR of Argonne Premium Coals," *Energy & Fuels*, **3**(2), 187-193 (1989).
- Solum, M. S., A. F. Sarofim, R. J. Pugmire, T. H. Fletcher and H. Zhang, "¹³C NMR Analysis of Soot Produced from Model Compounds and a Coal," *Energy & Fuels*, **15**(4), 961-971 (2001).
- Solum, M. S., J. M. Veranth, Y.-J. Jiang, A. M. Orendt, A. F. Sarofim and R. J. Pugmire, "The Study of Anthracene Aerosols by Solid-State NMR and ESR," *Energy & Fuels*, **17**(3), 738-743 (2003).
- Sowa, J. M., "Studies of Coal Nitrogen Release Chemistry for Oxyfuel Combustion and Chemical Additives," M.S. Thesis, Chemical Engineering, Brigham Young University (2009).
- Spalding, D. B., Some Fundamentals of Combustion, London, Butterworths Scientific Publications (1955).
- Speight, J. G., Handbook of Coal Analysis, New York, NY, Wiley (2005).
- Sun, J.-K. and R. H. Hurt, "Mechanisms of extinction and near-extinction in pulverized solid fuel combustion," *Proceedings of the Combustion Institute*, **28**(2), 2205-2213 (2000).
- Sun, J. K., R. H. Hurt, S. Niksa, L. Muzio, A. Mehta and J. Stallings, "A Simple Numerical Model to Estimate the Effect of Coal Selection on Pulverized Fuel Burnout," *Combustion Science and Technology*, **175**(6), 1085-1108 (2003).
- Thomas, S. and M. J. Wornat, "Effects of Acetylene Addition on Yields of the C₁-C₁₀ Hydrocarbon Products of Catechol Pyrolysis," *Energy & Fuels*, **22**(2), 976-986 (2008a).
- Thomas, S. and M. J. Wornat, "The Effects of Oxygen on the Yields of Polycyclic Aromatic Hydrocarbons Formed during the Pyrolysis and Fuel-Rich Oxidation of Catechol," *Fuel*, **87**(6), 768-781 (2008b).
- Thomas, S. and M. J. Wornat, "C₂₄H₁₄ Polycyclic Aromatic Hydrocarbons from the Pyrolysis of Catechol," *International Journal of Environmental Analytical Chemistry*, **88**(12), 825-840 (2008c).

- Thomas, S. and M. J. Wornat, "Polycyclic Aromatic Hydrocarbons from the Co-Pyrolysis of Catechol and 1,3-Butadiene," *Proceedings of the Combustion Institute*, **32**, 615-622 (2009).
- Tomczyk, N. A., J. E. Hunt, R. E. Winans, M. S. Solum, R. J. Pugmire and T. H. Fletcher, "Model Compound Study of the Pathways for Aromatic Hydrocarbon Formation in Soot," *Abstracts of Papers, 224th ACS National Meeting, Boston, MA, United States, August 18-22, 2002*, FUEL-131 (2002).
- Tsai, C.-Y. and A. W. Scaroni, "The Structural Changes of Bituminous Coal Particles During the Initial Stages of Pulverized-Coal Combustion," *Fuel*, **66**, 200-206 (1987).
- Turkdogan, E. T. and J. V. Vinters, "Effect of Carbon Monoxide on the Rate of Oxidation of Charcoal, Graphite and Coke in Carbon Dioxide," *Carbon*, **8**(1), 39-53 (1970).
- Van Krevelen, D. W. and P. J. Hoftyzer, *Properties of Polymers*, New York, Elsevier (1976).
- Veranth, J. M., T. H. Fletcher, D. W. Pershing and A. F. Sarofim, "Measurement of soot and char in pulverized coal fly ash," *Fuel*, **79**(9), 1067-1075 (2000).
- Wakao, N. and J. M. Smith, "Diffusion in catalyst pellets," *Chem. Eng. Sci.*, **17**(11), 825-834 (1962).
- Wakao, N. and J. M. Smith, "Diffusion and Reaction in Porous Catalysts," *Industrial & Engineering Chemistry Fundamentals*, **3**(2), 123-127 (1964).
- Wall, T. F., G.-S. Liu, H.-W. Wu, D. G. Roberts, K. E. Benfell, S. Gupta, J. A. Lucas and D. J. Harris, "The Effects of Pressure on Coal Reactions during Pulverized Coal Combustion and Gasification," *Progress in Energy and Combustion Science*, **28**(5), 405-433 (2002).
- Watt, M., T. H. Fletcher, S. Bai, M. S. Solum and R. J. Pugmire, "Chemical Structure of Coal Tar During Devolatilization," *Symposium (International) on Combustion*, **26**(2), 3153-3160 (1996).
- Wheeler, A., "Reaction Rates and Selectivity in Catalyst Pores," *Advances in catalysis*, V. I. K. E. K. R. P. H. E. W.G. Frankenburg and H. S. Taylor, Academic Press, **Volume 3**: 249-327 (1951).
- Winans, R. E., N. A. Tomczyk, J. E. Hunt, M. S. Solum, R. J. Pugmire, Y. J. Jiang and T. H. Fletcher, "Model Compound Study of the Pathways for Aromatic Hydrocarbon Formation in Soot," *Energy & Fuels*, **21**(5), 2584-2593 (2007).
- Winans, R. E., "Argonne Premium Coal Samples Home Page," Argonne, IL, Argonne National Laboratory: <http://www.anl.gov/PCS/pcshome.html> (2010).
- Wornat, M. J., A. F. Sarofim and J. P. Longwell, "Changes in the Degree of Substitution of Polycyclic Aromatic Compounds from Pyrolysis of a High-Volatile Bituminous Coal," *Energy & Fuels*, **1**(5), 431-7 (1987).

- Wornat, M. J., A. F. Sarofim, J. P. Longwell and A. L. Lafleur, "Effect of Pyrolysis Conditions on the Composition of Nitrogen-Containing Polycyclic Aromatic Compounds from a Bituminous Coal," *Energy & Fuels*, **2**(6), 775-82 (1988).
- Wornat, M. J., A. F. Sarofim and A. L. Lafleur, "The Pyrolysis of Anthracene as a Model Coal-Derived Aromatic Compound," *Symposium (International) on Combustion*, **24**, 955-63 (1992).
- Wornat, M. J., F. J. J. Vriesendorp, A. L. Lafleur, E. F. Plummer, A. Necula and L. T. Scott, "The Identification of New Ethynyl-Substituted and Cyclopenta-Fused Polycyclic Aromatic Hydrocarbons in the Products of Anthracene Pyrolysis," *Polycyclic Aromatic Compounds*, **13**(3), 221-240 (1999).
- Wu, H., G. Bryant, K. Benfell and T. Wall, "An Experimental Study on the Effect of System Pressure on Char Structure of an Australian Bituminous Coal," *Energy & Fuels*, **14**(2), 282-290 (2000).
- Yang, H. P., H. P. Chen, F. D. Ju, R. Yan and S. H. Zhang, "Influence of pressure on coal pyrolysis and char gasification," *Energy & Fuels*, **21**(6), 3165-3170 (2007).
- Yang, J. and M. Lu, "PAHs/Soot Formation from Pyrolysis of Methylnaphthalenes," *Proceedings - Annual International Pittsburgh Coal Conference*, **20**, 1921-1932 (2003).
- Yoshizawa, N., K. Maruyama, T. Yamashita and A. Akimoto, "Dependence of Microscopic Structure and Swelling Property of DTF Chars upon Heat-Treatment Temperature," *Fuel*, **85**(14-15), 2064-2070 (2006).
- Yu, J., D. Harris, J. Lucas, D. Roberts, H. Wu and T. Wall, "Effect of Pressure on Char Formation during Pyrolysis of Pulverized Coal," *Energy & Fuels*, **18**(5), 1346-1353 (2004a).
- Yu, J., J. Lucas, T. Wall, G. Liu and C. Sheng, "Modeling the Development of Char Structure During the Rapid Heating of Pulverized Coal," *Combustion and Flame*, **136**(4), 519-532 (2004b).
- Yu, J., J. A. Lucas and T. F. Wall, "Formation of the Structure of Chars during Devolatilization of Pulverized Coal and its Thermoproperties: A Review," *Progress in Energy and Combustion Science*, **33**(2), 135-170 (2007).
- Zelepouga, S. A., A. V. Saveliev, L. A. Kennedy and A. A. Fridman, "Relative Effect of Acetylene and PAHs Addition on Soot Formation in Laminar Diffusion Flames of Methane with Oxygen and Oxygen-Enriched Air," *Combustion and Flame*, **122**(1-2), 76-89 (2000).
- Zeng, D., "Effects of Pressure on Coal Pyrolysis at High Heating Rates and Char Combustion," Ph.D. Dissertation, Chemical Engineering Department, Brigham Young University (2005).

- Zeng, D., M. Clark, T. Gunderson, W. C. Hecker and T. H. Fletcher, "Swelling Properties and Intrinsic Reactivities of Coal Chars Produced at Elevated Pressures and High Heating Rates," *Proceedings of the Combustion Institute*, **30**(2), 2213-2221 (2005).
- Zeng, D. and T. H. Fletcher, "Effects of Pressure on Coal Pyrolysis and Char Morphology," *Energy & Fuels*, **19**(5), 1828-1838 (2005).
- Zhang, H., "Nitrogen Evolution and Soot Formation during Secondary Coal Pyrolysis," Ph.D. Dissertation, Chemical Engineering, Brigham Young University (2001).
- Zhang, H. and T. H. Fletcher, "Nitrogen Transformations During Secondary Coal Pyrolysis," *Energy & Fuels*, **15**, 1512-1522 (2001).
- Zolin, A., A. Jensen and K. Dam-Johansen, "Coupling thermal deactivation with oxidation for predicting the combustion of a solid fuel," *Combustion and Flame*, **125**(4), 1341-1360 (2001).
- Zygourakis, K., "Effect of Pyrolysis Conditions on the Macropore Structure of Coal-Derived Chars," *Energy & Fuels*, **7**(1), 33-41 (1993).

APPENDIX A. SOOT STUDIES

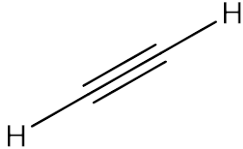
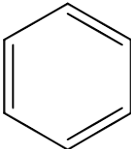
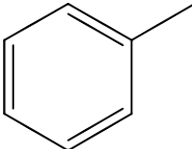
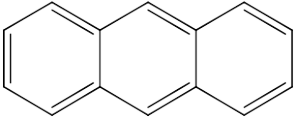
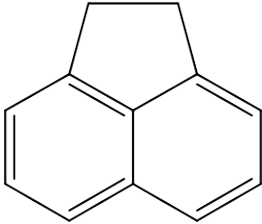
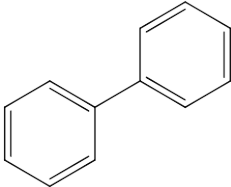
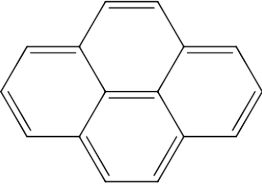
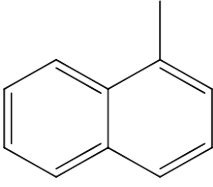
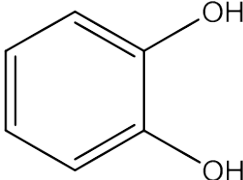
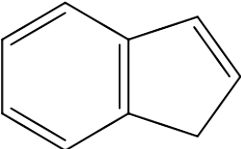
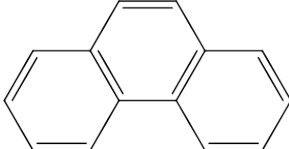
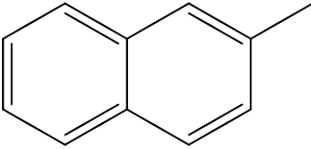
Previous studies on coal tar have shown that its chemical structure differs significantly from the parent coal as evaluated by ^{13}C -NMR (Watt et al., 1996; Perry et al., 2000). The average molecular weight of tar produced at atmospheric pressure is ~350 amu (Freihaut et al., 1989). The number of carbons per cluster and the cluster molecular weight are lower in the tar than in the parent coal due to the preferential evaporation of lighter constituents of the metaplast, especially at elevated pyrolysis pressures. The breakdown of bridges and side chains to form light gases causes the coordination number to decrease and the aromaticity to increase as the coal metaplast generates tar.

Soot formation mechanisms from light hydrocarbons have been investigated and models have been developed to describe the various stages. In the hydrogen-abstraction/carbon-addition (HACA) mechanism the aromatic structure is built “from scratch” by acetylene addition (Frenklach and Wang, 1991; Frenklach, 2002). The stability of aromatic structures at high temperatures under reducing conditions suggests that the mechanism of soot formation from coal tar differs; it is unreasonable to suppose that the aromatic clusters in the tar break down and then re-form. Pyrolysis studies with model aromatic compounds have shown that acetylene addition does occur, but polymerization events such as the formation of bi-aryl linkages also make important contributions to soot formation from existing aromatic structures (Sarofim et al., 1994; Sarofim et al., 2002; Winans et al., 2007).

Acetylene, small paraffinic hydrocarbons, and benzene derivatives are relatively common candidates for secondary pyrolysis studies (Marsh et al., 1999; Eiteneer and Frenklach, 2003; Skjoth-Rasmussen et al., 2004). Pyrolysis studies of compounds that are more representative of coal tar are less common. Catechol, which is functionally similar to compounds identified in lignites (Lynch and Durie, 1960), has recently been studied in combination with several simpler compounds (Thomas and Wornat, 2008a; Thomas and Wornat, 2009; Poddar et al., 2011). Compounds that have been investigated as model soot precursors are identified in Table A.1. Further pyrolysis studies with coals and model compounds are needed to determine the mechanisms by which the large aromatic structure of soot forms from the smaller aromatic clusters in coal tar. These surrogates should include oxygen and in some cases nitrogen. A variety of functional groups should be explored. The effect of pressure on soot formation should be investigated and quantified with coals and model coal-tar surrogate compounds.

Detailed soot formation models developed from such studies could be used to improve and validate simpler models designed for CFD applications, including existing models (Brown and Fletcher, 1998). The development of advanced soot models would require that more extensive data be collected to identify and quantify the most important chemical changes that occur in the transformation of coal tar into soot. Models that accurately predict the quantity, location, and size of soot formed would greatly improve the accuracy of heat transfer calculations in boilers and gasifiers. Advanced models of secondary pyrolysis would also be highly useful in tracking the release of fuel nitrogen. The impact of soot on carbon conversion has not received much attention in the literature even though much of the volatile matter becomes soot (Liu and Niksa, 2004).

Table A.1. Model compounds previously investigated in soot formation studies

 <p>Acetylene (Zelepouga et al., 2000; Hessler et al., 2001)</p>	 <p>Benzene (Marsh et al., 1999; Marsh et al., 2000; Marsh et al., 2005)</p>	 <p>Toluene (Hessler et al., 2001; Ledesma et al., 2005; Pugmire et al., 2006)</p>	 <p>Anthracene (Wornat et al., 1992; Wornat et al., 1999; Solum et al., 2003)</p>
 <p>Acenaphthene (Zelepouga et al., 2000)</p>	 <p>Biphenyl (Solum et al., 2001; Tomczyk et al., 2002; Winans et al., 2007)</p>	 <p>Pyrene (Zelepouga et al., 2000; Solum et al., 2001; Winans et al., 2007)</p>	 <p>1-Methylnaphthalene (Mikolajczak et al., 1996; Yang and Lu, 2003; Leininger et al., 2006)</p>
 <p>Catechol (Ledesma et al., 2002; Thomas and Wornat, 2008b, c)</p>	 <p>Indene (Lu and Mulholland, 2001)</p>	 <p>Phenanthrene (Zelepouga et al., 2000; Pugmire et al., 2006)</p>	 <p>2-Methylnaphthalene (Yang and Lu, 2003)</p>

Soot Formation under Gasification Conditions

Secondary pyrolysis processes cause soot to form from coal tar in combustion and gasification systems. Soot is of interest in these industrial settings because of its critical role in radiation heat transfer, its impact on the extent of conversion, and its role in the formation of pollutants such as particulates and NO_x. It is likely that soot oxidation and gasification reactivities vary with coal type and preparation conditions. The ability to predict the location and

characteristics of soot as it develops and gasifies is important for the development of advanced gasification models.

Low-Temperature Atmospheric Pyrolysis of Model Coal Tar Surrogates

The model compound 2,6-dimethylnaphthalene was studied as a precursor for soot in the atmospheric flat-flame burner (FFB). This compound was chosen to study the effect of aliphatic attachments on soot formation chemistry. Acetylene, methane, and a species functionally similar to naphthalene were identified in the FTIR spectrum of pyrolysis products derived from 2,6-dimethylnaphthalene at a peak temperature of 1400 K and a residence time of ~19 ms. However, these species could not be quantified due to irregularities in the particle feed rate. Changes in aromatic cluster size and aliphatic groups were quantified using ^{13}C -NMR analysis, which was conducted by the research groups of Dr. Pugmire and Dr. Solum at the University of Utah. The NMR spectra show that at a peak flame temperature of 1447 K the methyl groups had largely disappeared and CH_2 and/or CH groups had formed (Figure A.1). By 1500 K these new aliphatic groups had largely disappeared. At about 1550 K the NMR spectrum was too noisy to extract meaningful information due to the high conductivity of the large aromatic clusters.

It was found that 2,6-dimethylnaphthalene was difficult to feed into the FFB without clogging the feeder tube. The low melting point (108°C) of this compound is an indicator of its stickiness. When other compounds were selected for study, higher melting points were sought. Silica gel was mixed with the model compounds in high ratios of 3:1 or higher to reduce stickiness. Initially, the model compounds were ground and sieved to a particle size range of 45-75 μm , and then mixed with 32-63 μm silica gel.

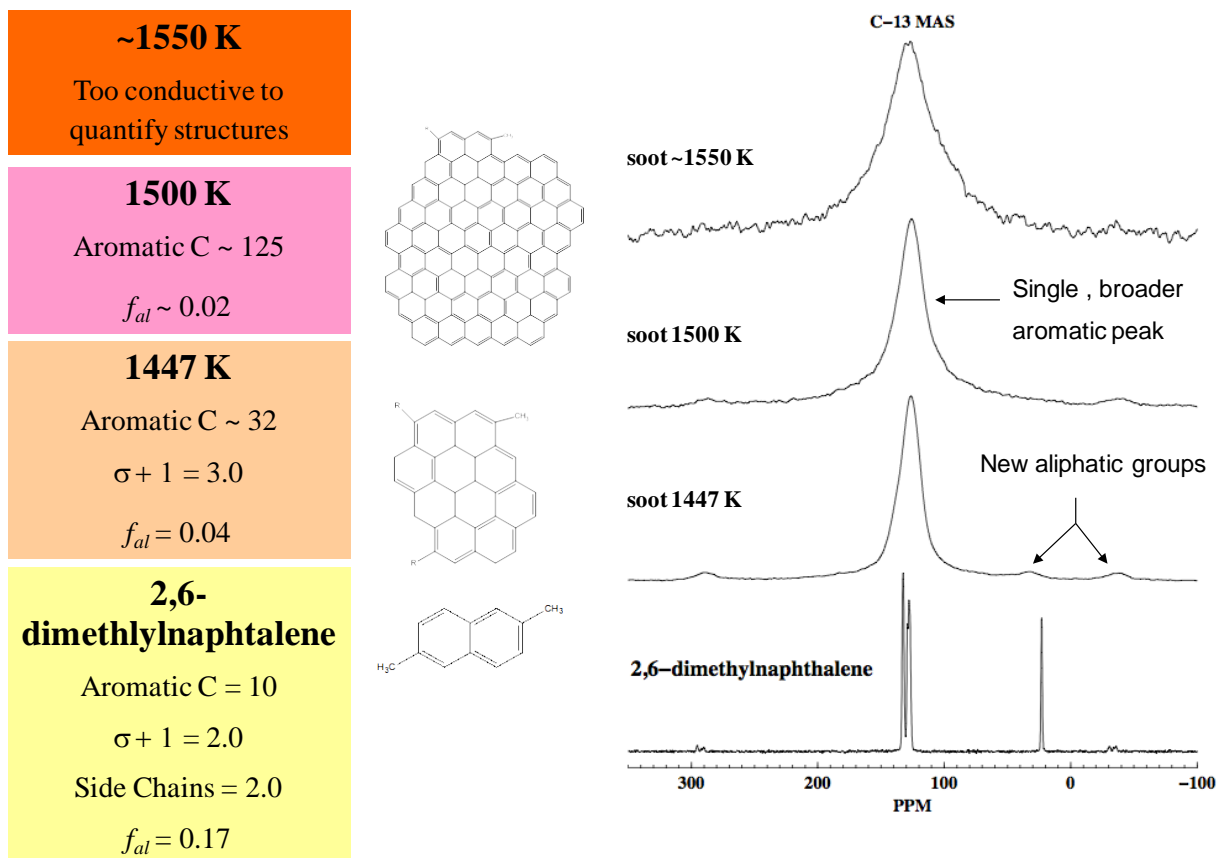


Figure A.1. NMR spectra of soots produced on the FFB from 2,6-dimethylnaphthalene (dmn).

In the final work on the model compound biphenyl, a more careful reading of the previous studies conducted with this compound (with a melting point of 70°C) indicated that model compounds were first ground together with the silica gel and then sieved (Solum et al., 2001). In retrospect, it made sense that this procedure would produce particles that are more intimately mixed and more uniform in size. This procedure also allowed the fine particles produced during grinding to be used. Application of this preparation procedure with the final biphenyl experiments resulted in more consistent particle feeding in the FFB and the HPFFB. It appears that the correct compound preparation procedure affected the feeding consistency at least

as much as the melting point. Earlier adoption of the correct compound preparation procedure probably would have resulted in more consistent particle feeding, which could have allowed acquisition of larger quantities of data from model compounds.

A search for new model compounds was initiated when very low yields of tar/soot from 2,6-dimethylnaphthalene were encountered. It was difficult to find a condition with a yield of soot high enough for practical analysis while using a temperature low enough to keep the aromaticity from growing too quickly. Since the aim of this research was to study the chemistry of soot development in the early stages, it was important to obtain polycyclic aromatic hydrocarbons (PAH) formed at low flame temperatures and residence times. Also, the ^{13}C -NMR technique that has been used in these types of studies previously does not work well for highly conductive aromatic clusters of large size. The useful “window” of temperatures and residence times was small for the model compounds studied in this work on the FFB.

A review of the structure of coal tar was conducted to aid in the selection of future model compounds. Attempts to illustrate chemical structures (Figure A.2) based on measured coal tar properties (Perry et al., 2000) are quantitatively compared in Table A.2. Several characteristics became apparent through these attempts to create representative illustrations of tar structure. Aliphatic chains with more than 2 carbon atoms are probably rare. Between 1 and 3 oxygen atoms occur in almost every aromatic cluster, and nitrogen atoms occur once in every 2 to 3 clusters. On average, a coal tar molecule would be expected to have 1 or 2 clusters, each consisting of 3 to 4 aromatic rings.

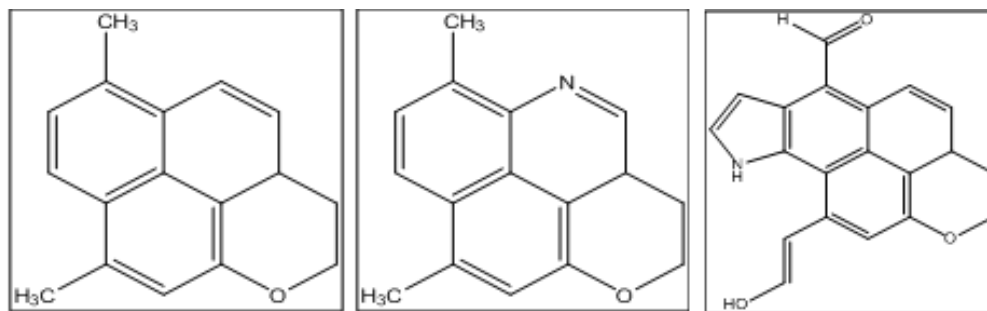


Figure A.2. Illustrations A, B, and C (from left to right) of suggested average tar molecules.

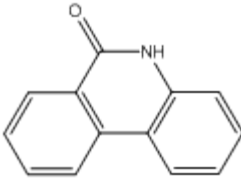
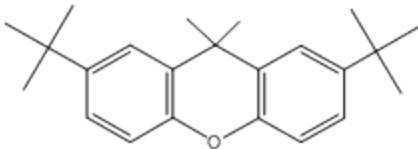
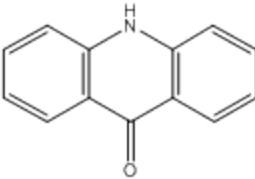
Table A.2. Average measured tar properties (Freihaut et al., 1989; Perry et al., 2000) compared to properties of suggested average tar molecules (see Figure A.2)

Structural Parameter	Measured Average Range	Illustration A Values	Illustration B Values	Illustration C Values
Molecular Weight (amu)	350	235	236	316
Aromatic Rings	3-4	3	3	4
Carbon Aromaticity	0.63-0.76	0.76	0.75	0.75
Side Chains	~2	2	2	2
Bridges	~2	2	2	2
Carbon Mass Percent	78%-82%	87%	81%	76%
Hydrogen Mass Percent	~4%	7%	6%	4%
Oxygen Mass Percent	5%-16%	6%	7%	15%
Nitrogen Mass Percent	~1.7%	0%	6%	4%
Cluster MW (amu)	240 - 290	235	236	316
Attachments MW (amu)	20-31	74	74	116

Unfortunately, it was found that compounds with molecular weights and functionalities similar to the hypothetical tar molecules in (Figure A.2) were not available for purchase from vendors of chemicals. Of necessity, new model compounds (Table A.3) that were selected typically had low molecular weights and high aromaticities or high molecular weights and low aromaticities compared to coal tar (Table A.2). 6-(5H)-Phenanthridinone was chosen for pyrolysis experiments because it had both oxygen and nitrogen functional groups. Attempts to use the other two compounds in Table A.3 were not successful due to clogging and low product

yields. Another compound (xanthene) was acquired, but was not used in experiments because of its low melting point of 102°C.

Table A.3. Additional compounds used as coal-tar surrogates in pyrolysis experiments

6-(5H)-phenanthridinone	2,7-di-tert-butyl-9,9-dimethylxanthene	9(10H)-acridanone
		
Molecular Weight = 195.22 amu	Molecular Weight = 322.48 amu	Molecular Weight = 195.22 amu
Melting Point = 290°C	Melting Point = 188°C	Melting Point > 300°C
Aromaticity = 0.923	Aromaticity = 0.522	Aromaticity = 0.923

It was found that the phenanthridinone (with a melting point of 290°C) was easier to feed than the dimethylnaphthalene. A higher yield of tar/soot was observed in phenanthridinone experiments on the FFB. Experiments were conducted with peak flame temperatures of 1450 K, 1500 K, and 1550 K and residence times of ~19 ms (corresponding to a collection height of 1.375 inches above the burner). At 1450 K the ¹³C-NMR spectrum showed a quadruple peak in the aromatic region, indicating little change from phenanthridinone to tar/soot (see Figure A.3). The elemental composition of the tar/soot at 1450 K changed by less than 1.3 wt% for carbon, hydrogen, and nitrogen, and by 3.2% for oxygen (which was calculated by difference). These very minor changes indicate that either the phenanthridinone is quite stable at 1450 K or else there was some error associated with the measured temperature profile. The experiments at the two higher temperatures were conducted to increase the extent of reaction so that more information could be extracted from NMR spectra featuring a single aromatic peak. FTIR scans of the gas species made during pyrolysis of 6-5(H)-phenanthridinone at 1450 K were acquired

(Figure A.8). For the phenanthridinone, the mass yields of gaseous species were 1.5% CH₄, 1.8% C₂H₂, and 1.2% HCN.

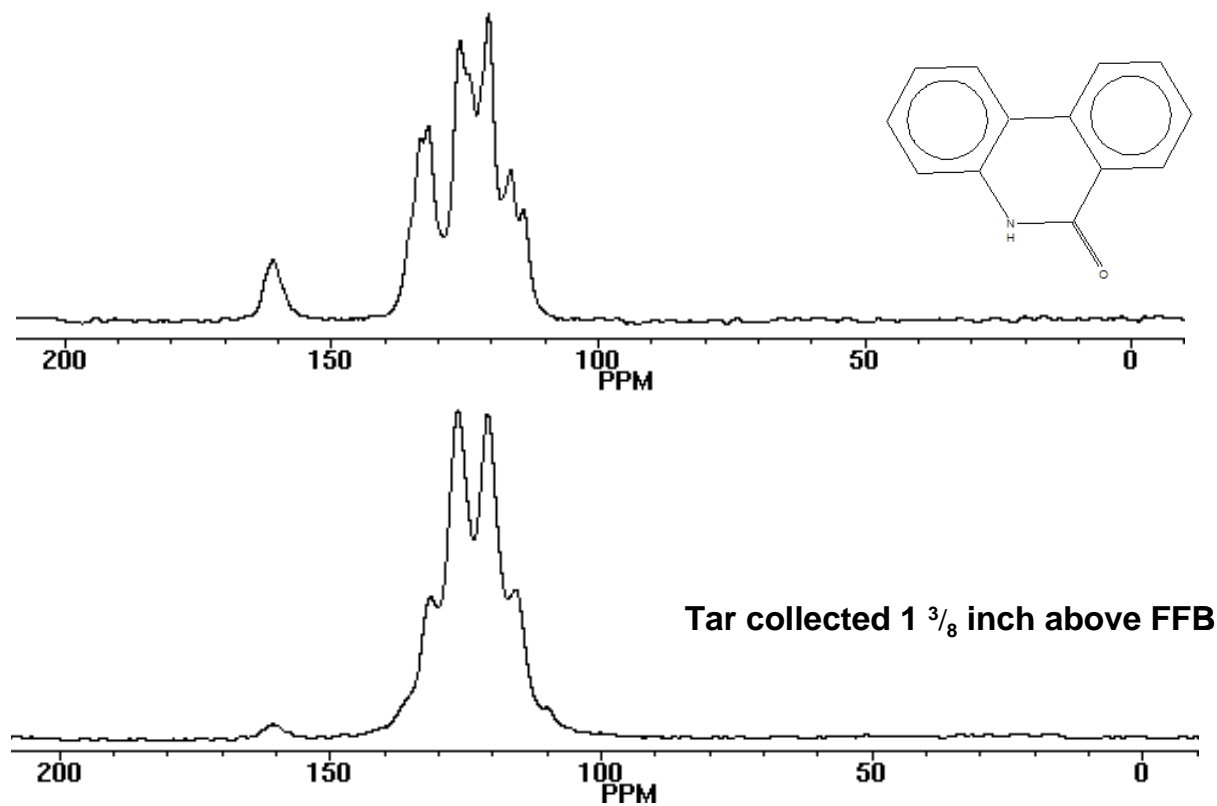


Figure A.3. ¹³C-NMR spectra of 6-5(H)-phenanthridinone and its solid pyrolysis products at 1450 K and 19 ms.

Low-Temperature Atmospheric Coal Pyrolysis Experiments

Eastern Bituminous A (EBA) and Wyodak subbituminous coal were subjected to pyrolysis conditions with peak flame temperatures of 1150 K, 1300 K, and 1450 K and residence times of ~19 ms. Gaseous products were measured using FTIR spectroscopy. For Wyodak coal the mass yields of gaseous species were 3.0% CH₄, 5.5% C₂H₂, and 0.6% C₂H₄. For EBA the

mass yields of gaseous species were 3.0% CH₄, 10.2% C₂H₂, and 2.8% C₂H₄. For Wyodak coal 30% of the nitrogen was released as HCN, compared to 35% for Eastern Bituminous A. No NH₃ was detected among the pyrolysis products for either coal. The tar/soot from the coals was collected for analysis.

The ¹³C-NMR studies of the tars and chars produced in the BYU FFB were conducted at the University of Utah under the direction of Dr. Ronald J. Pugmire and Dr. Mark S. Solum. Details of the techniques used have been published previously (Solum et al., 1989). Gas Chromatography-Mass Spectrometry (GC/MS) was used to characterize some of the tar samples.

The measured aromaticities of the two coals were practically identical (65-67%, see following figures and tables), but the shape of the aromatic peaks indicates that the structure of the aromatic carbon was very different. This explains the difference in pyrolysis behavior; carbon aromaticity increased to 83% for the Wyodak tar/soot and the Eastern Bituminous A tar/soot is practically 100% aromatic. The aliphatic peaks are observed to decrease dramatically for the Wyodak sample and disappear entirely for the Eastern Bituminous A sample. The average number of carbons per cluster increased 70% for the Wyodak coal and 244% for the Eastern Bituminous A coal.

The aromaticity of the tar/soot from the EBA coal at a collection height of 3 inches increased with increasing temperature (1150 to 1300 K), but the cluster size changed very little. The cluster size in the tar is typically smaller than in the parent coal, so the fact that the cluster size did not change suggests that secondary reactions occurred. The phenolic groups were lost selectively with increasing temperature. Aliphatic peaks disappeared by 1300 K.

At a lower residence time corresponding to a collection height of 1 3/8 inches, fewer secondary occur. The aromaticity of the EBA tar at 1350 K was 90%, which is much higher than

the parent coal. The aromatic cluster size is smaller in the tar than in the coal and is largest in the char. This suggests that the tar/soot sample is mostly tar for which most of the aliphatic material has been lost as light gases. The EBA tar soot sample collected at 1450 K is highly conductive. For mature soots such as these, NMR techniques are not as useful.

For the low temperature (1150 K and 1300 K) Wyodak experiments with a 3-inch collection height, much of the carbonyl and aliphatic groups disappeared as the coal turned into tar. The average number of attachments for the tar was lower than in the coal. The aromaticity increased with increasing temperature. The tar cluster size at 1150 K was slightly lower than in the coal, and the cluster size increased at 1300 K.

At a collection height of 1 3/8 inches, the Wyodak coal produced char at 1350 K with a larger cluster size than the coal, and the tar cluster size was about the same as the coal. At both 1350 K and 1450 K, phenolic groups have been lost and the aromaticity is 89%. The cluster size of the char at 1450 K was very low, indicating that gas temperature during the experiment was considerably lower than when the measurement was made with a thermocouple.

Table A.4. Measured NMR parameters for 2 coals from this study

Coal	M_δ	MW	p_o	$\sigma + I$
Wyodak 2010	37.7	333.3	0.500	0.519
EBA	31.3	393.2	0.478	5.95

Eastern Bituminous Coal and Tar/Soots 3 "

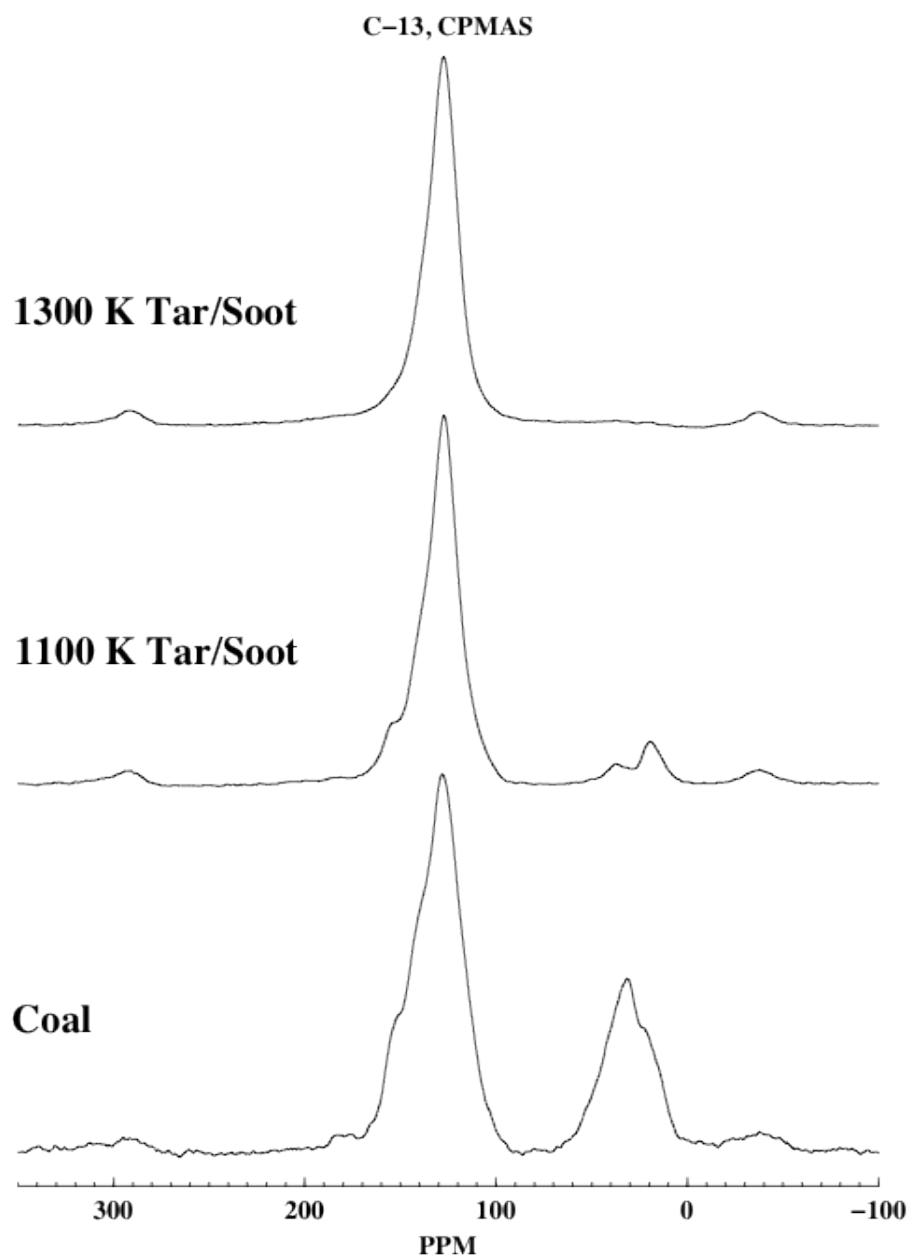


Figure A.4. C-13 CPMAS NMR spectra of the original EBA coal (bottom) and two tar/soots made at 1100 K (middle) and 1300 K (Top) from the coal.

Eastern Bituminous Coal and Products 1 3/8 "

C-13 CPMAS

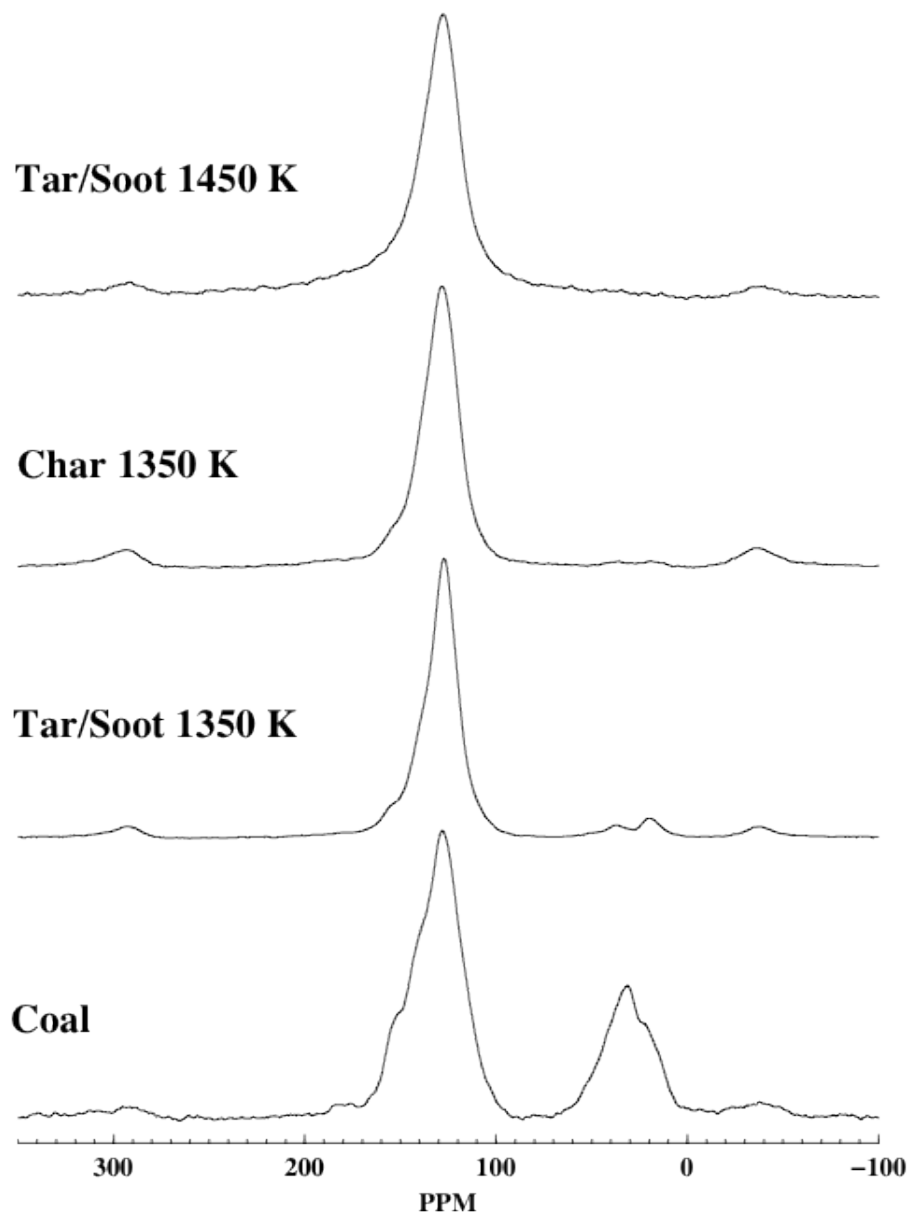


Figure A.5. C-13 CPMAS spectra of the EBA coal (bottom), a matched tar/soot and char pair in the two (middle) spectra and a tar/soot at 1450 K (top) spectrum.

Wyodak Coal and Tar/Soots 3 "

C-13 CPMAS

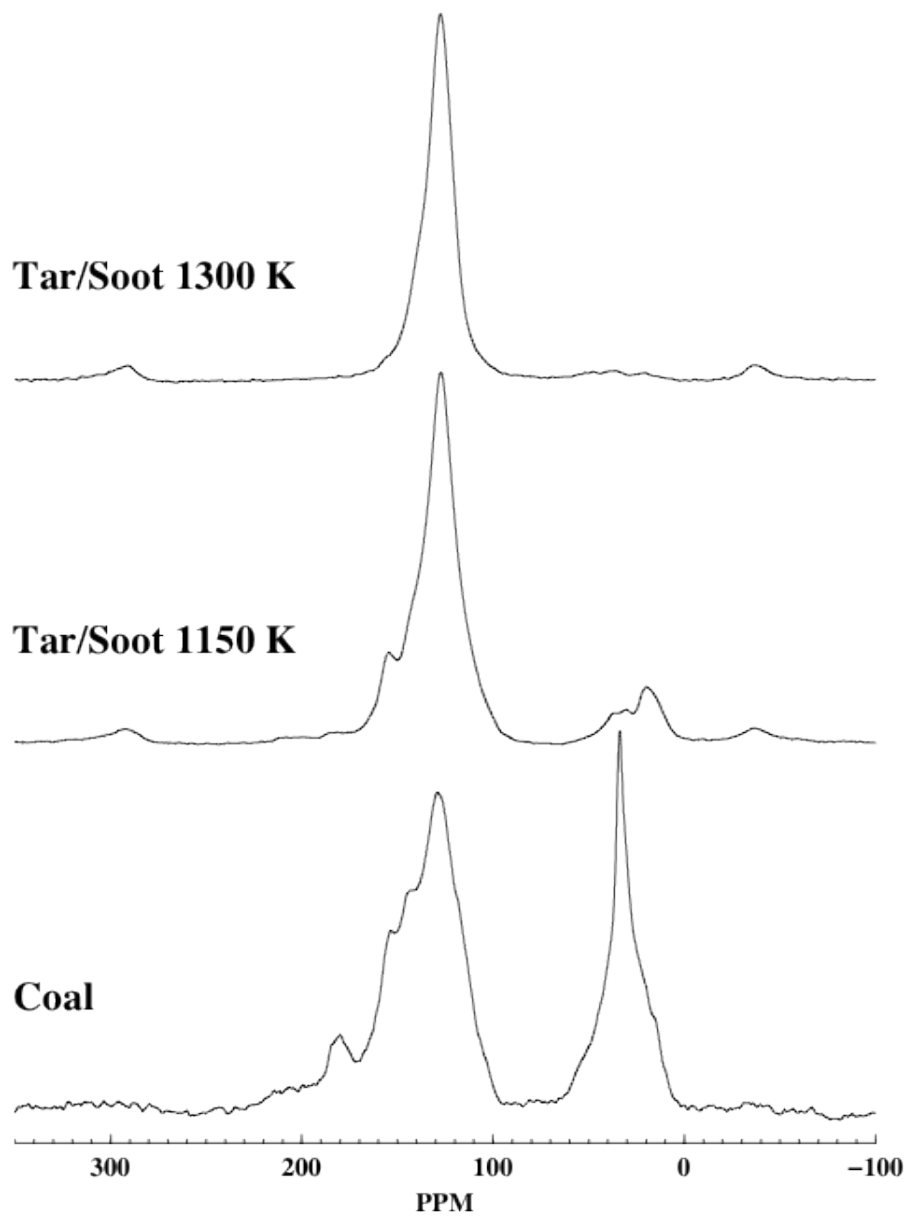


Figure A.6. C-13 CPMAS spectra the Wyodak coal (bottom) and tar/soots made at 1150 K (middle) and 1300 K (top).

Wyodak Coal and Pyrolysis Products 1 3/8 "

C-13 CPMAS

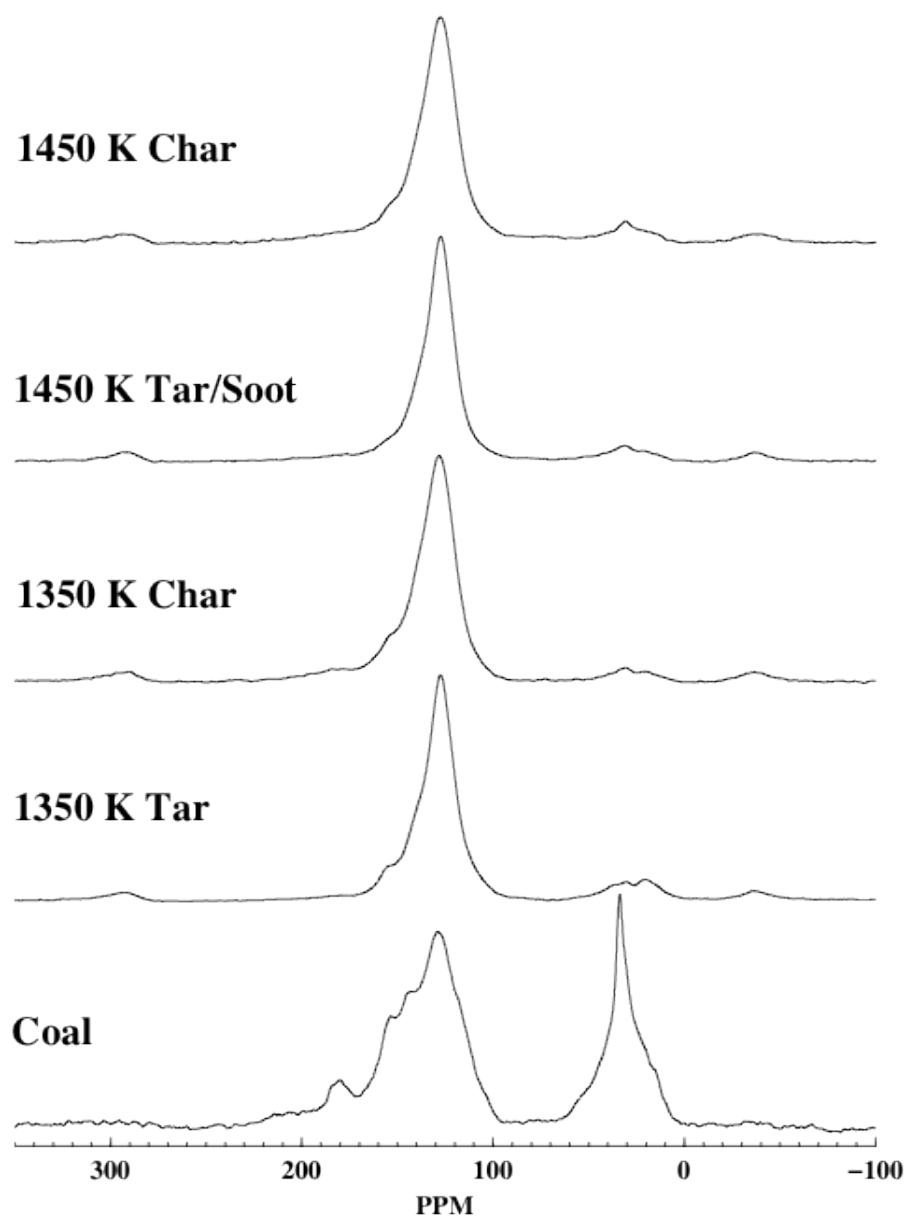


Figure A.7. C-13 CPMAS spectra of the Wyodak coal (bottom) and 1350 K tar/soot and char pairs (2 and 3 from bottom) and 1450 K tar/soot and char pairs (4 and 5 from bottom).

Table A.5. EBA coal and two tar/soot samples collected at 3 inches in the atmospheric FFB

Structural Parameters														
Compound	f_a	f_a^C	f_a^O	f_a^{OO}	f_{a^*}	f_a^H	f_a^N	f_a^P	f_a^S	f_a^B	f_{al}	f_{al}^H	f_{al}^*	f_{al}^O
Coal	0.67	0.02	0.005	0.015	0.65	0.20	0.45	0.06	0.17	0.22	0.33	0.21	0.12	0.04
Tar/Soot 1150 K	0.89	0.02	0.01	0.01	0.87	0.42	0.45	0.06	0.10	0.29	0.11	0.06	0.05	0.00
Tar/Soot 1300 K	0.95	0.03	0.01	0.02	0.92	0.38	0.54	0.04	0.19	0.31	0.05	0.04	0.01	0.02
Lattice Parameters														
Compound	χ_b	C	$\sigma+I$	P_0	$B.L.$	$S.C.$	$M.W.$	M_δ						
Coal	0.338	16.8	5.9	0.48	2.8	3.1	393	32						
Tar/Soot 1150 K	0.333	16.5	3.0	0.63	1.9	1.1	272	22						
Tar/Soot 1300 K	0.337	16.7	4.2	0.96	4.0	0.2	247	10						

Table A.6. EBA coal and pyrolysis products collected at 1 3/8 inches in the atmospheric FFB

Structural Parameters														
Compound	f_a	f_a^C	f_a^O	f_a^{OO}	f_{a^*}	f_a^H	f_a^N	f_a^P	f_a^S	f_a^B	f_{al}	f_{al}^H	f_{al}^*	f_{al}^O
Coal	0.67	0.02	0.005	0.015	0.65	0.20	0.45	0.06	0.17	0.22	0.33	0.21	0.12	0.04
Tar/Soot 1350 K	0.91	0.01	0.00	0.01	0.90	0.45	0.45	0.05	0.19	0.21	0.09	0.05	0.04	0.02
Char (2) 1350 K	0.92	0.02	0.01	0.01	0.90	0.30	0.60	0.05	0.21	0.34	0.08	0.06	0.02	0.04
Tar/Soot 1450 K	1.00	--	--	--	1.00	0.38	0.62	--	--	0.62 (Max)	0.0	--	--	--
Lattice Parameters														
Compound	χ_b	C	$\sigma+I$	P_0	$B.L.$	$S.C.$	$M.W.$	M_δ						
Coal	0.338	16.8	5.9	0.48	2.8	3.1	393	32						
Tar/Soot (2) 1350 K	0.233	11.2	3.0	0.83	2.5	0.5								
Char (2) 1350 K	0.378	18.7	5.4	0.92	5.0	0.4	--	--						
Tar/Soot 1450 K	0.620	41 (Max)	--	1.00	--	--	527	0						

Table A.7. Wyodak coal and tar/soots collected at 3 inches in the atmospheric FFB

Structural Parameters														
Compound	f_a	f_a^c	f_a^O	f_a^{OO}	f_a^*	f_a^H	f_a^N	f_a^P	f_a^S	f_a^B	f_{al}	f_{al}^H	f_{al}^*	f_{al}^O
Coal	0.65	0.09	0.03	0.06	0.56	0.17	0.39	0.10	0.16	0.13	0.35	0.22	0.13	0.03
Tar/Soot 1150 K	0.87	0.02	0.00	0.02	0.85	0.42	0.43	0.08	0.18	0.17	0.13	0.07	0.06	0.01
Tar/Soot 1300 K	0.93	0.02	0.01	0.01	0.91	0.44	0.47	0.04	0.19	0.24	0.07	0.05	0.02	0.03
Lattice Parameters														
Compound	χ_b	C	$\sigma+I$	P_0	$B.L.$	$S.C.$	$M.W.$	M_δ						
Coal	0.232	11.2	5.2	0.50	2.6	2.6	332	37						
Tar/Soot 1150 K	0.200	10.0	3.1	0.77	2.4	0.7	171	15						
Tar/Soot 1300 K	0.264	12.7	3.2	0.91	2.9	0.3	158	8						

Table A.8. Wyodak coal with tar/soots and chars collected at 1 3/8 inches on the atmospheric FFB

Structural Parameters														
Compound	f_a	f_a^c	f_a^O	f_a^{OO}	f_a^*	f_a^H	f_a^N	f_a^P	f_a^S	f_a^B	f_{al}	f_{al}^H	f_{al}^*	f_{al}^O
Coal	0.65	0.09	0.03	0.06	0.56	0.17	0.39	0.10	0.16	0.13	0.35	0.22	0.13	0.03
Tar (2) 1350 K	0.89	0.02	0.00	0.02	0.87	0.42	0.45	0.06	0.18	0.21	0.11	0.08	0.03	0.01
Char (2) 1350 K	0.89	0.03	0.01	0.02	0.86	0.31	0.55	0.06	0.18	0.31	0.11	0.07	0.04	0.03
Tar/Soot 1450 K	0.90	0.04	0.02	0.02	0.86	0.40	0.46	0.05	0.18	0.23	0.10	0.07	0.03	0.02
Char (2) 1450 K	0.83	0.04	0.02	0.02	0.79	0.39	0.40	0.05	0.17	0.18	0.17	0.12	0.05	0.06
1450 ch rpt	0.83	0.04	0.02	0.02	0.79	0.36	0.43	0.05	0.17	0.21	0.17	0.12	0.05	0.06
Lattice Parameters														
Compound	χ_b	C	$\sigma+I$	P_0	$B.L.$	$S.C.$	$M.W.$	M_δ						
Coal	0.232	11.2	5.2	0.50	2.6	2.6	332	37						
Tar (2) 1350 K	0.241	11.6	3.2	0.88	2.8	0.4	--	--						
Char (2) 1350 K	0.360	17.9	5.0	0.83	4.2	0.8	--	--						
Tar/Soot 1450 K	0.267	12.8	3.4	0.87	3.0	0.4	194	10						
Char (2) 1450 K	0.228	11.0	3.1	0.77	2.4	0.7	--	--						
1450 ch rpt	0.266	12.8	3.5	0.77	2.7	0.8	--	--						

FTIR Analysis of Pyrolysis Products

A Bomem MB-155 FTIR instrument with a 10-meter path length was used to study gaseous pyrolysis products of coals and coal tar surrogates in the atmospheric FFB. This instrument was used in a manner similar to previous studies (Zhang, 2001; Sowa, 2009). A reference spectrum of N₂ was collected to allow absorbance to be calculated for each of the subsequent samples. The quenched gases from the reaction zone passed through a filter where tar and soot were removed before entering the FTIR instrument gas cell. Quantification of yields of gas species per unit mass of solid fuel required the use of standards and a steady, well-characterized feeding rate.

An example of the technique for quantification of gases is shown in Figure A.8. A flame background was measured at the chosen experimental condition in the absence of products from solid fuels. Subtraction of the flame background absorbance facilitated identification and quantification of the species of interest. Spectra of standards were measured to allow quantification of species such as NH₃, HCN, C₂H₂, and CH₄. Each standard spectrum was multiplied by a scaling factor and subtracted from the original spectrum until the characteristic species peaks were removed. The optimized scaling factor was proportional to the concentration of the standard in the gas sample.

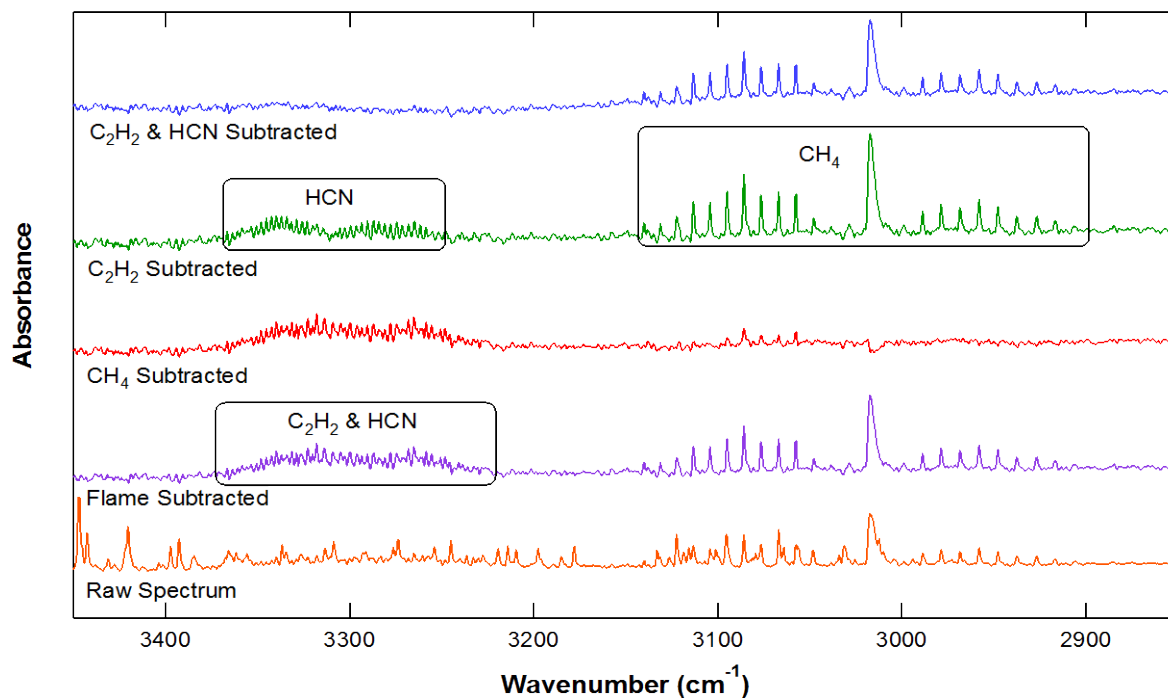


Figure A.8. FTIR spectra from pyrolysis of 6-5(H)-phenanthridinone, showing data reduction technique.

Secondary Coal Pyrolysis at Elevated Pressures

A gas condition at 5 atm with a peak temperature of 1539 K was developed for use in soot formation studies. The collection probe was set 2 inches above the burner, corresponding to a residence time of 86 ms. This condition was used with the model compound biphenyl and also for Eastern Bituminous A. The tar/soot samples were recovered on filters and sent with the bituminous char to Dr. Pugmire's group for analysis. Another condition at 10 atm, 1433 K with a residence time of 101 ms was also used to produce tar/soot from biphenyl, but the yield was very low. About 20 mg of product was given to Dr. Pugmire for more limited analysis. Other tar surrogate experiments were attempted at atmospheric pressure, but the yields of the selected compounds were too low for practical analysis.

The 5 atm biphenyl spectra indicate that some aromatic rings opened during pyrolysis, since aliphatic carbons were detected. The tar/soot sample was highly aromatic, so the amount of information available via NMR spectroscopy was limited. The EBA char sample was also very carbonized at this condition, but the tar was not. An upper limit estimate of the aromatic cluster size for the EBA tar was 200 carbons. The graphs of NMR spectra and the associated tables are taken from reports that are included on the CD that accompanies this dissertation.

Biphenyl 1484 K Tar/Soot

C-13, CPMAS

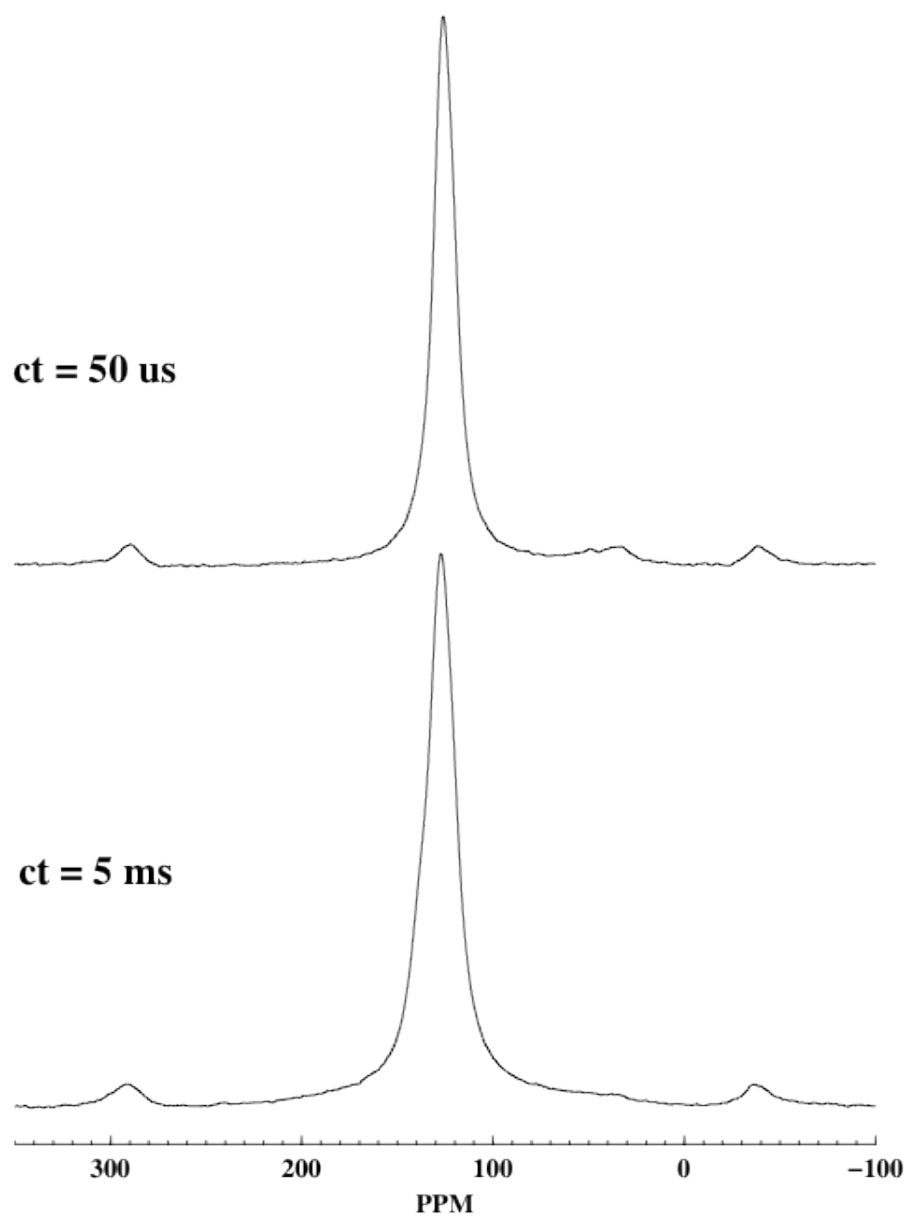


Figure A.9. Two spectra of a tar/soot made from biphenyl at 5 atm, 1539 K. The (bottom) spectrum shows all carbon types and the (top) short contact time spectrum shows mostly carbon types that are protonated.

Eastern Bituminous 1484 K Char

C-13 SPMAS

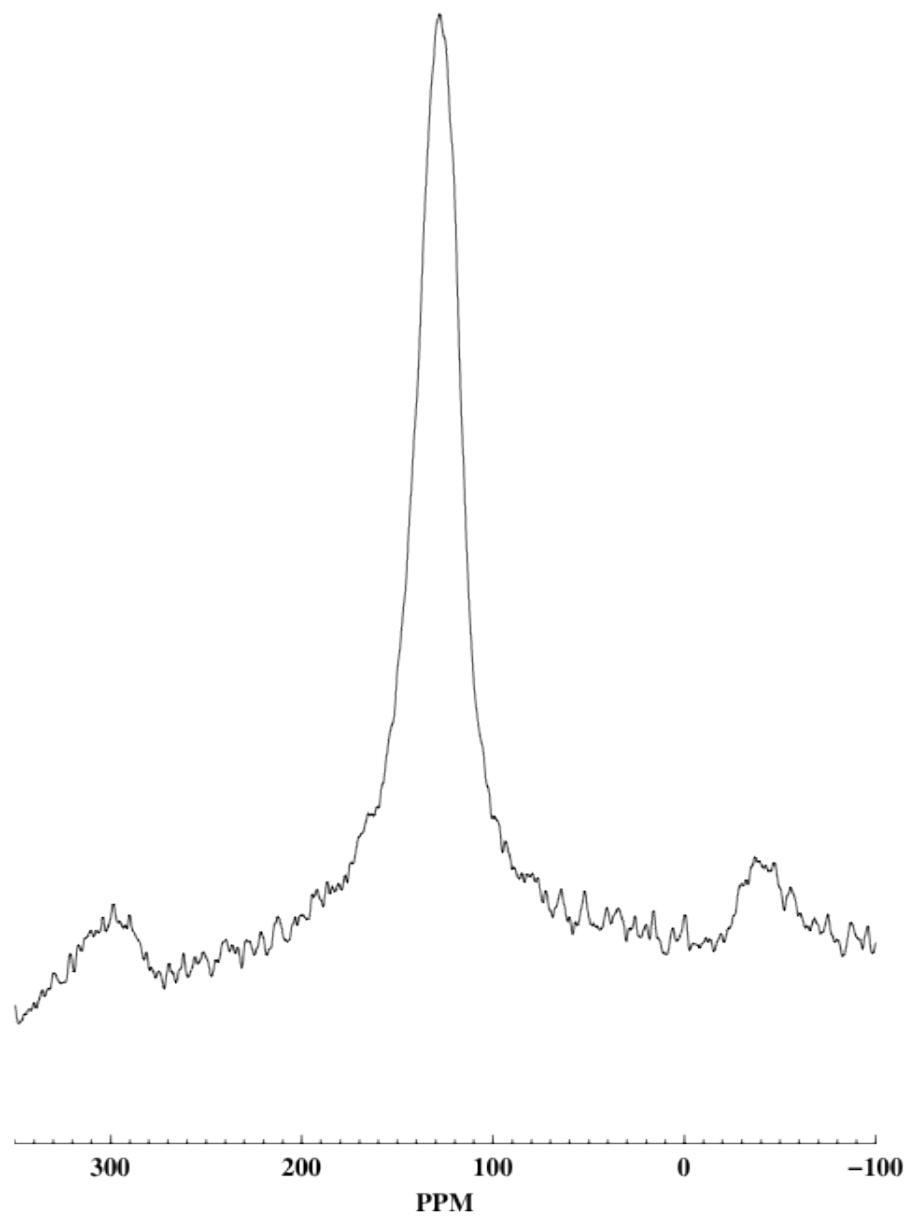


Figure A.10. A single pulse spectrum of a highly carbonized char made at 5 atm, 1539 K from the EBA.

Eastern Bituminous Tar/Soot 1484 K 2 "

C-13 CPMAS

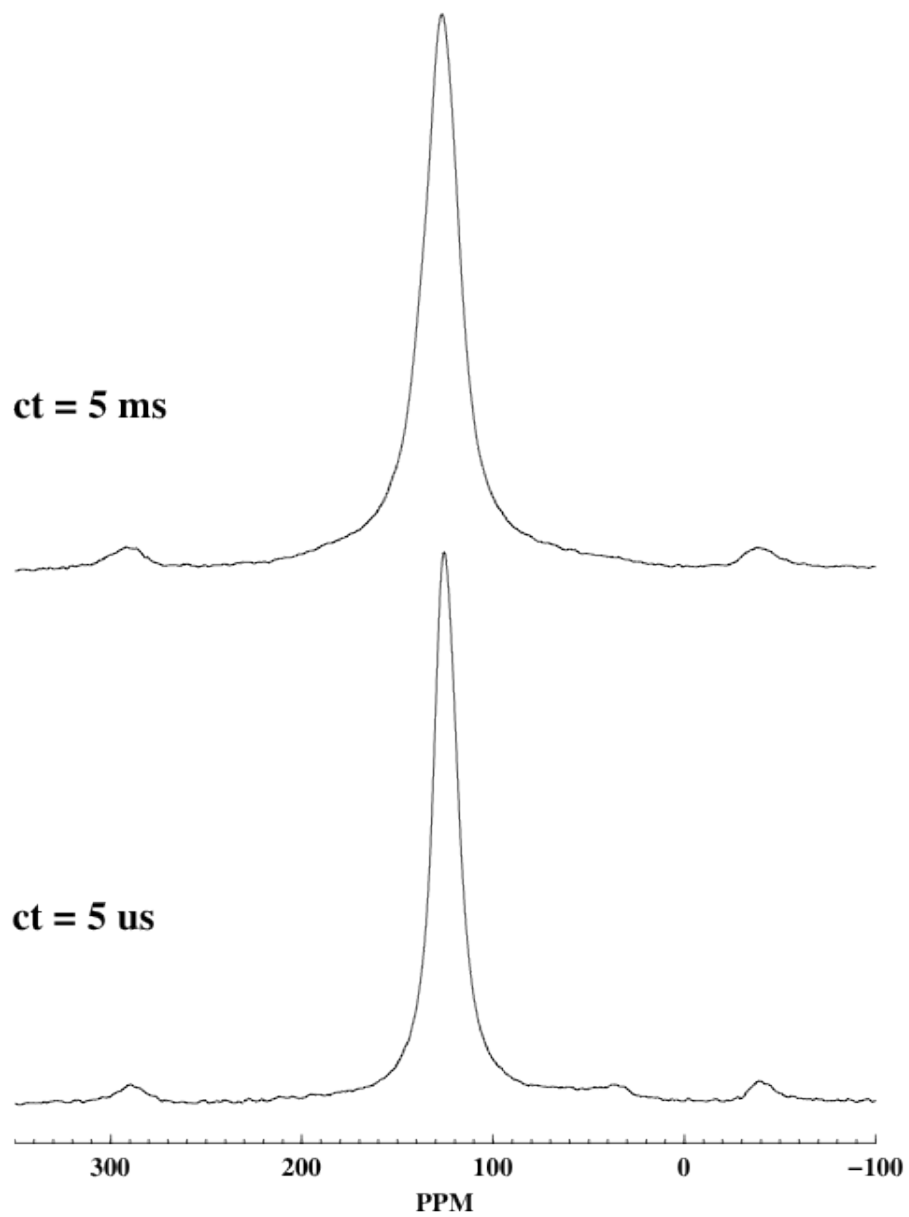


Figure A.11. C-13 CPMAS spectra of EBA tar/soot at 5 atm, 1539 K, collected at 2-inches above the burner. The short contact time (bottom) spectrum shows mostly protonated carbons and the (top) spectrum shows all carbon types.

FFB and HPFFB Gas Conditions for Soot Formation Studies

Table A.9. Gas flow rates and post-flame gas compositions for soot formation studies

Pressure and Peak Temperature	5 atm 1539 K	10 atm 1433 K	0.84 atm 1353 K	0.84 atm 1560 K	0.84 atm 1507 K	0.84 atm 1433 K	0.84 atm 1425 K	0.84 atm 1340 K	0.84 atm 1162 K
Adiabatic Temp (K)	1484	1405	1504	1866	1786	1750	1681	1625	1307
Φ (Equiv. Ratio)	1.3778	1.4330	2.3977	1.7987	1.9750	1.7990	1.9084	2.4516	3.6239
Carrier N ₂ (SLPM, coal entrainment)	0.075	0.10	0.0367	0.0367	0.0367	0.0367	0.0367	0.0367	0.0367
CO (SLPM)	3.30	5.72	10.50	11.40	10.50	8.85	8.85	9.75	10.20
H ₂ (SLPM)	0.17	0.21	0.45	0.40	0.30	0.45	0.45	0.30	0.60
Oxidizer N ₂ (SLPM)	4.40	7.28	13.50	15.00	12.50	12.50	12.50	7.81	7.75
Fuel N ₂ (SLPM)	-	-	6.00	5.00	5.00	5.70	5.70	6.50	5.93
Air (SLPM)	3.85	5.75	-	-	-	-	-	-	-
O ₂ (SLPM)	-	-	2.19	2.28	2.73	2.58	2.44	2.05	1.49
Equilibrium post-flame gas compositions									
CO ₂ mol %	13.64%	12.80%							
H ₂ O mol%	1.05%	0.70%							
CO mol %	16.40%	19.24%							
H ₂ mol %	0.50%	0.48%							
N ₂ mol %	68.08%	66.48%							
O ₂ mol %	0.00%	0.00%							

Table A.10. Radiation-corrected HPFFB temperature profiles for soot formation studies

Height above burner (inches)	5 atm, 1539 K peak	10 atm, 1433 K peak
0	1473	1412
0.2	1539	1433
0.4	1512	1431
0.6	1493	1424
0.8	1484	1415
1.0	1464	1397
1.2	1482	1378
1.4	1471	1353
1.6	1460	1332
1.8	1447	1280
2.0	1417	1222

Table A.11. Estimated particle velocity profiles and residence times for soot formation studies

Height above burner (mm)	5 atm, 1539 K v_p (cm/s)	10 atm, 1433 K v_p (cm/s)
0	10.7	1.5
3	35.4	31.7
6	46.3	41.5
9	53.9	48.9
12	60.5	54.8
15	66.2	59.3
20	70.6	64.1
25.4	72.9	65.7
Velocities are obtained for distances of $x > 25.4$ mm above the burner using the equation $v_p = v_p(25.4 \text{ mm}) \cdot T(x) / T(25.4 \text{ mm})$ where T is the centerline gas temperature at x .		
$T(25.4 \text{ mm})$	1464	1397
Residence time (ms) at 2-inches	86	101

For the remaining conditions in the atmospheric FFB, the residence times were calculated using the velocity profile in Table G.16. The collection height was normally about 1 inch, unless stated otherwise.

Table A.12. Radiation-corrected FFB temperature profiles for soot formation studies

Height above burner (inches)	0.84 atm, 1353 K peak "New PDN 1300"	0.84 atm 1560 K "PDN 1550"	0.84 atm 1507 K "PDN 1500"	0.84 atm 1433 K "PDN 1450"	0.84 atm 1425 K "DMN"	0.84 atm 1340 K "Old 1300"	0.84 atm 1162 K "1150"
0	1120	1346	1332	1314	1200	1212	1003
0.5	1339	1547	1493	1419	1395	1337	1152
1	1353	1560	1507	1433	1417	1340	1162
2	1348	1555	1496	1425	1424	1331	1158
3	1331	1536	1475	1408	1425	1315	1146
4	1314	1512	1450	1389	1422	1298	1133
5	1296	1485	1422	1363	1420	1275	1117

APPENDIX B. ADDITIONAL DETAILS REGARDING HPFFB DEVELOPMENT

The original HPFFB burner (Zeng, 2005) was water-cooled and had a total diameter of 2.5 inches, with a 2-inch diameter burner face. The face of the 2-inch burner was designed to connect to a tube that was too large to fit inside the heated cavity. Several systems composed of quartz collars and steel rings were devised to allow the burner to connect to the smaller tubes about 1 inch below the heated part of the cavity (Figure B.1). These systems were functional but cumbersome. The earlier system of quartz collars provided better visibility of the burner face, but the later system using a steel mounting ring provided better visibility of the hot coal stream.

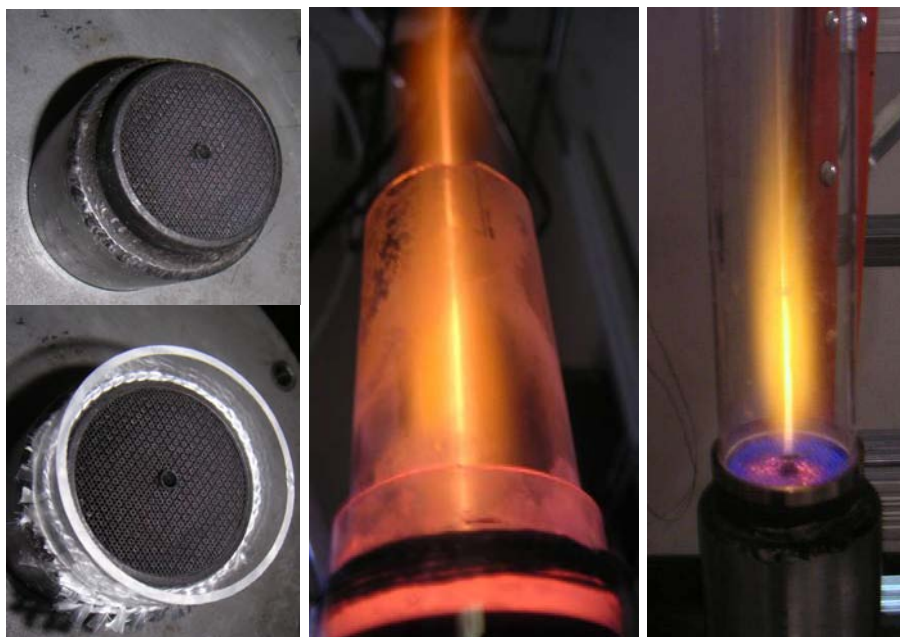


Figure B.1. Burner-to-quartz tube mounting systems: quartz collars (left and center) and steel ring (right).

A smaller burner (1-inch diameter) was found in the stock of spare parts in the HPFFB laboratory, as shown in Figure 4.1. The pressure vessel cap was adapted to accommodate either of the two burners, and the small burner was shortened. The 1-inch burner was originally developed as a prototype for the 2-inch burner and had seen service in very harsh environments; it was mostly worn out by the time it was put back into service in the new HPFFB. Within a few weeks the small burner broke down altogether, but a replacement was built because operation was observed to improve significantly compared to the large burner. Stable operation was observed with the rebuilt small burner due to the up-flow configuration.

The rebuilt 1-inch diameter burner was only $\frac{1}{4}$ the length of the 2-inch burner, allowing the coal feeder tube to be shortened by 2 feet; this reduced the occurrence of clogs while feeding particles. The small burner allowed for greater flexibility in gas velocities with the existing flow control system. Gas flow rates and hence operating costs were significantly reduced compared to the large burner.

The original 2-inch burner was built with a large (0.156 inch ID) central particle entrainment tube. Using this burner in an up-flow configuration proved to be difficult; a large amount of nitrogen was required to keep the coal entrained in the relatively large tube, particularly at high pressure. This reduced the heating rate and maximum temperature of the coal particles. Calculations of settling velocity revealed that a gas velocity of 0.18-0.26 m/s was required to entrain the coal particles with diameters of 100 μm at pressures of 2.5 to 15 atm (Appendix C). Since the gas density was proportional to the pressure, a higher mass flow rate of N_2 was needed at higher pressures to maintain this velocity. However, undesired turbulence was observed when the momentum of the N_2 used for entrainment was significantly different from the momentum of the gases flowing through the rest of the burner. Figure B.2 shows an observed

turbulent particle streak, and Figure B.1 includes a laminar particle streak that is suitable for pyrolysis and gasification experiments. This problem of turbulence was particularly prevalent with CH₄/H₂ flames at high pressures. It was found that a turbulent particle stream could be avoided by using an entrainment velocity that was within a factor of 3 of the cold burner gas velocity.

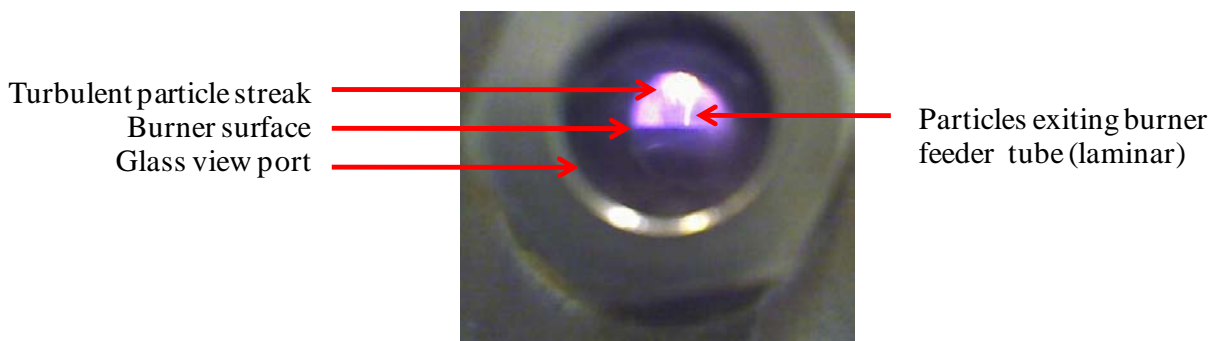


Figure B.2. Photograph of reacting coal stream exhibiting undesired transition to turbulence with 2-inch burner.

In flat-flame burners, flow rates of fuel and oxidizer are varied to adjust the post-flame temperature and species concentrations (i.e. O₂, CO₂, and/or H₂O). Burner flow settings using mixtures of CH₄ with H₂ for fuel were tried first. Soot production from the CH₄ fuel was found to occur at very low equivalence ratios at any pressure greater than 2 atm, even when a 50/50 mix of CH₄ with H₂ was used. Several flow settings were investigated at different pressures to find conditions appropriate for experiments. Any soot collected and analyzed should originate from coal tar rather than the gaseous CH₄ fuel. Partial premixing was attempted for a short period, but the reduction in soot was not complete enough to justify the risks associated with premixing fuels and oxidizers in a pressurized environment. These challenges were overcome initially by increasing the H₂ to 84 mole % of the total fuel content. These settings produced a

H₂O-rich gasification environment and eliminated soot formation at equivalence ratios of up to 1.2 and pressures of up to 15 atm.

These H₂O-rich settings were characterized at 2.5 atm and used for a set of pyrolysis and gasification experiments on subbituminous Wyodak coal (0). However, the work done was inefficient because the old coal entrainment apparatus suffered from frequent clogging. Controlling the condensation of steam was also an issue; liquid water on the polycarbonate soot filters created a large pressure drop, which caused the vessel pressure to increase faster than the controller could respond. Pressure swings caused interruption of feeding and contamination of the coal feeder system with moisture from the flame, thereby increasing the probability of clogging in the coal entrainment tube.

The H₂O-rich settings caused other problems in the particle collection system. Wet coal and soot did not separate correctly in the aerodynamic separation system. It was necessary to use heating tape on the collection system and carefully observe the temperatures of the filters while varying the heat input. An alternate method of heating the collection system by scaling up the total burner flow rate was also tried, but the increased flow rates made operation very expensive and the temperatures in the collection system rose high enough to melt o-rings and polycarbonate filters.

The H₂O-rich gasification settings could not be used with bituminous coals. The high H₂ content of the gaseous fuel caused a very high flame speed. The high-pressure flame was closer to the burner surface than was typical for flat-flame burners, causing high temperature corrosion of the burner surface and preheating of the entrained coal to occur before exiting the central burner tube. In fact, the burner surface was hot enough to glow. When attempts were made to use bituminous coals, the coal entrainment tube clogged a few millimeters below the burner surface

due to premature pyrolysis of the coal. The decision was therefore made to upgrade the facility to allow the safe use of CO as a fuel.

New flow settings were initially developed for a CO flame on the 2-inch burner, but operation was prohibitively expensive. CO is far more expensive on a heating value basis than either CH₄ or H₂. By that point in time, the surface of the 2-inch burner had suffered from extensive high temperature corrosion due to months of operation with high H₂ content. The decision was made to try the 1-inch burner. Operation with the 1-inch burner proved to be far more cost effective and reliable once the flow path was redesigned and stable flow settings were developed.

Collection Probe Quench System

Measurements of the centerline temperature inside the collection probe showed that the temperature did not drop very quickly after entering the probe. Larger and more numerous holes were bored in the tip of a new sintered steel tube. It was found that 70-80% of the N₂ supplied to the repaired probe passed through the larger quench jets, compared to 40-50% previously. The temperature dropped 500 K in the first 0.25 inch, which was much more effective than the 200 K drop in 1 inch measured previously. The total amount of N₂ used was reduced because the initial temperature drop was found to be relatively insensitive to N₂ flow beyond a certain minimum level; the standard amount of quench N₂ fed to the probe was specified as twice the total volumetric flow rate to the burner. The effectiveness of the quench jets was also indicated by the reduced heat damage to the sintered steel (including discoloration and warping) even at very high flame temperatures (Figure B.3).

Another attempt to improve the gas quench and particle collection efficiency included the construction of an extra probe with an alternate design. This alternate design included a concave tip with extra N₂ jets. However, the new design was not effective because the extra N₂ jets had diameters that were much too large; very little drop in temperature was observed within the probe because the low-velocity jets did not penetrate to the center of the hot gas flow. The shape of the tip also made it more difficult to insert into the top cap of the vessel. The concave-tipped probe design was abandoned in favor of the convex-tipped design based on the one used with the atmospheric flat-flame burner (Ma, 1996).

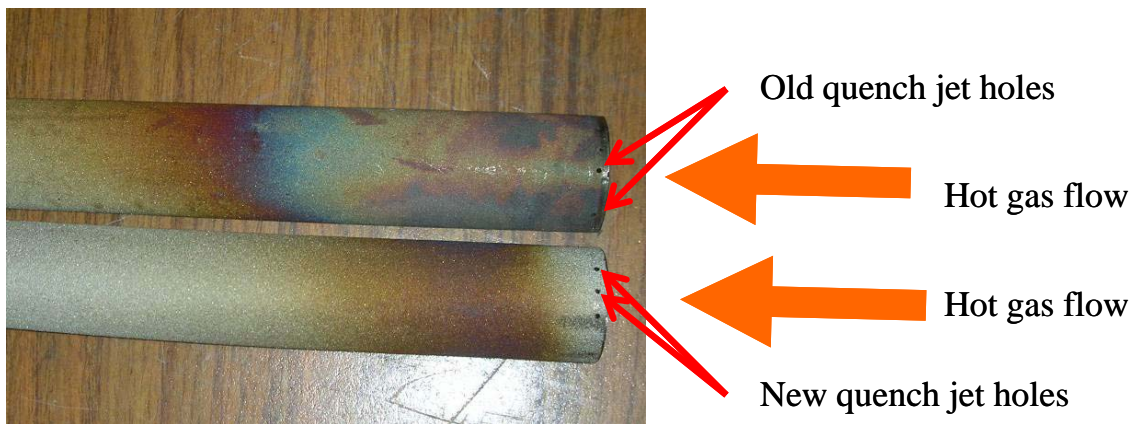


Figure B.3. Heat damage to sintered steel tubes: old tube (top) and new tube with more large holes (bottom).

APPENDIX C. PARTICLE VELOCITY CALCULATIONS

The flow rate of carrier N₂ must be specified at a proper level for each operating pressure to ensure consistent entrainment of the coal. A force balance between gravity, buoyancy, and drag was used to estimate the velocity required to entrain the coal (Figure C.1).

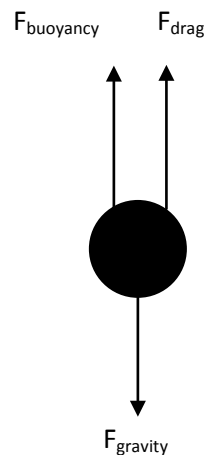


Figure C.1. Force balance on particle entrained with upward-flowing gas (Lewis, 2011).

The force balance takes the form:

$$0 = m_p a_{net} = \frac{4}{3} \pi r_p^3 (\rho_g - \rho_p) g + \pi r_p^2 \left(\frac{1}{2} \rho_g v_t^2 \right) C_D \quad (\text{C.1})$$

where the product of particle mass m_p and net acceleration a_{net} is the net force that sums to zero at the terminal velocity v_t (also referred to as the slip or settling velocity). The term with the difference between the particle density ρ_p and the gas density ρ_g is the sum of the buoyant and

gravity forces, where g is the acceleration due to gravity and r_p is the particle radius. The drag force term includes a drag coefficient C_D , which has the form (Bird et al., 2002):

$$C_D = \left(\sqrt{\frac{24}{\text{Re}_D}} + 0.5407 \right)^2 \quad (\text{C.2})$$

which is valid for spheres of diameter $D = 2r_p$ and Reynolds numbers of $\text{Re}_D < 6000$. The Reynolds number was calculated using the expression:

$$\text{Re}_D = \frac{\rho_g v_t D}{\mu} \quad (\text{C.3})$$

and the gas density was calculated from the ideal gas law using the expression:

$$\rho_g = \frac{PM_w}{R_g T_g} \quad (\text{C.4})$$

where μ is the gas viscosity, P is the total pressure, M_w is the molecular weight of the gas, R_g is the universal gas constant, and T_g is the gas temperature.

Reynolds numbers between 4 and 18 were calculated for 100 μm particles with densities of 1.3 g/cm^3 at pressures of 2.5 atm to 15 atm at the terminal velocity. N_2 gas properties at 300 K were used. This exceeds the Reynolds number limit of 0.1 that would be required to assume Stokes flow, which would allow an analytical solution for v_t to be found (the Stokes flow drag coefficient is identical to Equation C.2 without the term 0.5407). Therefore, the force balance was solved numerically for v_t , yielding values of 0.26 m/s at 2.5 atm and 0.18 m/s at 15 atm. Assuming Stokes flow would produce velocities of about 0.39 m/s at all pressures.

For entrained flow to exist in the feeder tube, the settling velocity must be exceeded. Due to increasing gas density with increasing pressure, larger mass flow rates of N_2 are needed with increasing pressure to maintain sufficient velocities. Using the calculated velocities and a margin of safety, standard entrainment gas flow rates of 0.06 SLPM, 0.075 SLPM, 0.1 SLPM, and 0.15

SLPM were adopted at 2.5 atm, 5 atm, 10 atm, and 15 atm, respectively. After injection into the hot post-flame zone, the particles accelerate. A transient version of the force balance is required to estimate particle velocities in this regime:

$$\frac{4}{3}\pi r_p^3 \rho_p \frac{dv_p}{dt} = \frac{4}{3}\pi r_p^3 (\rho_g - \rho_p)g + \pi r_p^2 \left(\frac{1}{2} \rho_g (v_g - v_p)^2 \right) C_D \quad (\text{C.5})$$

where the derivative of the particle velocity v_p with respect to time t is equivalent to a_{net} . In Equation C.5 the particle mass m_p has been expressed as the product of particle volume and density and the slip velocity v_t has been expressed in terms of the gas velocity v_g and the particle velocity. Using the measured gas temperature profile and the relationship

$$\frac{dz}{dt} = v_p \quad (\text{C.6})$$

allows these two differential equations to be solved with a Runge-Kutta method. The initial velocity calculated from the solution of Equation C.1 serves as the initial condition for Equation C.5, and the initial distance and time are defined as zero. The integration yields relationships between velocity, residence time, and location. Gas properties were calculated from correlations in the DIPPR[®] Database (Rowley et al., 2010).

APPENDIX D. HPFFB STEPPER MOTOR ELECTRONICS AND SOFTWARE

A stepper motor was used in conjunction with a pneumatic vibrator to feed coal from a plunger into a funnel, where it was entrained in N_2 through a steel tube that led to the burner surface. An electronic driver system was connected to the parallel port of a desktop computer running the Windows XP operation system. The electronic driver allowed pulses 5.9 VDC power to be delivered from a separate power supply to the appropriate coils on the stepper motor. A schematic of the stepper motor driver circuit is shown in Figure D.1. The ULN 2003 chip shown in Figure D.1 could only accommodate a 500 mA output, so 10 chips were used in parallel to supply up to 5 A to the stepper motor. This driver and the associated software were based on a design used for a home movie film digitizer (Brunner, 2007) and is also similar to the stepper motor used for the atmospheric FFB (Ma, 1996).

A Visual Basic program was written to run the stepper motor driver circuit. A special software driver was added to the computer to allow the VB program to send a signal through the computer parallel port (Logix4u, 2008). The program accepts the user's inputs of direction, fuel bulk density, distance, and inverse velocity. The bulk density is used to output an estimated feed rate to the screen, and the other parameters are processed to create a sequence of pulses to drive the stepper motor screw in the desired direction at the specified velocity to the specified distance. The graphical user interface is shown in Figure D.1.

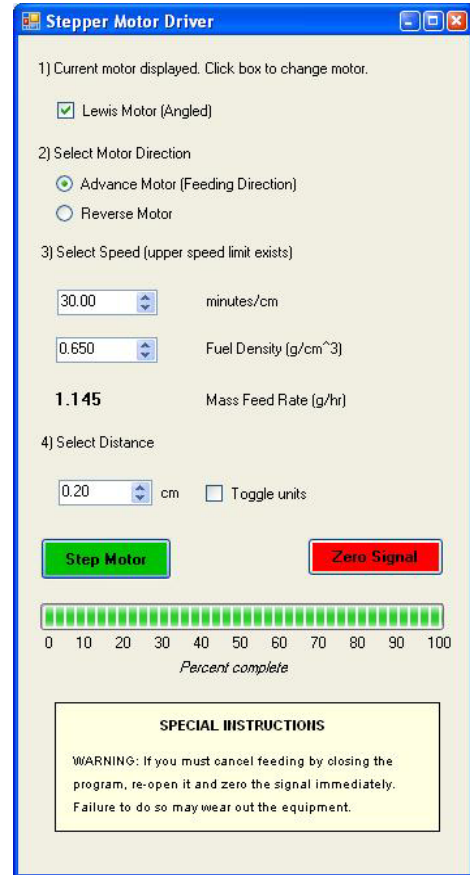
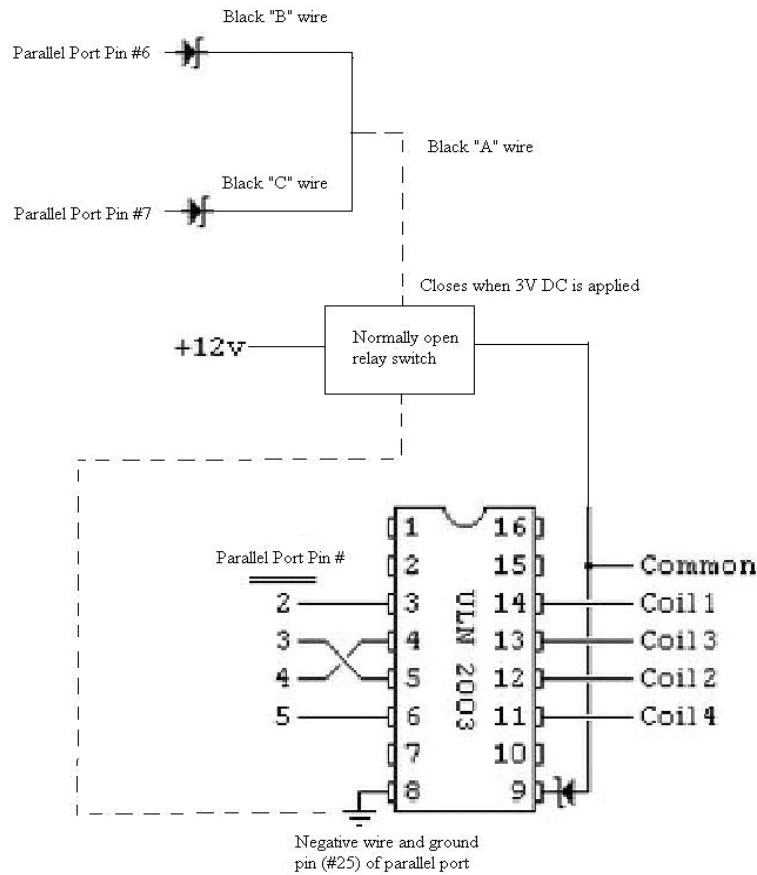


Figure D.1. HPFFB stepper motor driver circuit diagram and graphical user interface.

The VB code was implemented in Microsoft Visual Studio 2008. The source code that runs the electronic driver is included on the CD that accompanies this dissertation.

APPENDIX E. CHAR SEPARATION PROCEDURE

A challenge encountered with using bituminous coals in the HPFFB was that a significant portion of the collected char was fragmented. This made it very difficult to determine the original particle sizes. Some of the char collected was less fragmented, apparently due to small variations in the char collection method. Many of the char samples collected were also contaminated with large soot agglomerates. The soot reduced the quality of the data collected because char containing a significant quantity of soot cannot be accurately analyzed for mass change via elemental or ash tracer techniques. Also, accurate determination of swelling by the tap density technique is hindered by the presence of large, low density soot agglomerates. The presence of fragments also interferes with swelling measurements by increasing the observed density.

Density separation of the char was attempted. In a previous study, soot was separated from fly ash using a liquid-suspension gravity separation technique (Veranth et al., 2000). In the previous study, soot floated to the top of an ethanol supernatant and ash settled to the bottom. Such was not the case with the samples from the HPFFB; many of the cenospherical char particles floated. In early separation attempts, soot agglomerates remained intact and settled to the bottom of the liquid with the dense fraction of the char. Soot agglomerates were often compacted in these attempts. After trials with several different liquids, a mixture of 2 parts ethanol with 3 parts water (by volume) was adopted for the separation procedure (density = 0.94 g/mL). A low-intensity custom vibrator was used because fragmentation of the char particles

occurred when sonication was attempted. The vibrator was made by gluing a nut to a CPU fan; off-balance fans of this type are also used to help keep coal entrained in the HPFFB coal feeder system.

Char samples split into two fractions, which were filtered separately and dried. Paper filters with a pore size of $\sim 5 \mu\text{m}$ were used. The top fraction contained whole cenospherical char particles and the bottom fraction contained smaller cenospheres, denser particles (from high-ash and/or non-swelling coal particles), and particle fragments. With 2 hours of vibration, negligible amounts of soot were observed in SEM images of both the top and bottom fractions (Figures E.1 and E.2). It appears that the soot agglomerates broke down into fragments smaller than $5 \mu\text{m}$ and passed through the filter; the waste liquid had a cloudy gray color and the sum of the dried char sample weights was on the order of 10 mg less than the original sample weight of $\sim 300 \text{ mg}$. The top fraction was then dried and subjected to bulk density and ash tests to determine extent of reaction and swelling. The extent of reaction determined from ash content of the top fraction can be considered a lower bound, because particles with high ash content should be too heavy to collect in the top fraction. Similarly, the density determined from the top fraction can be viewed as a lower bound on the sample density.

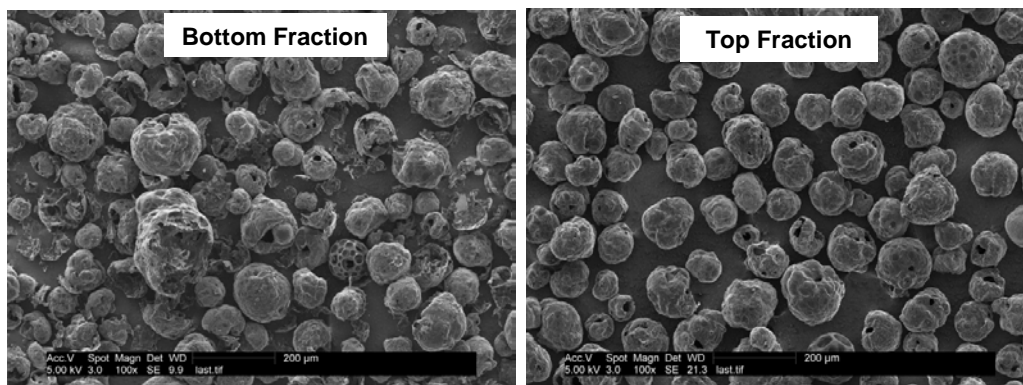


Figure E.1. SEM images of a separated Eastern Bituminous A char produced at 5 atm, 1702 K, 38 ms.

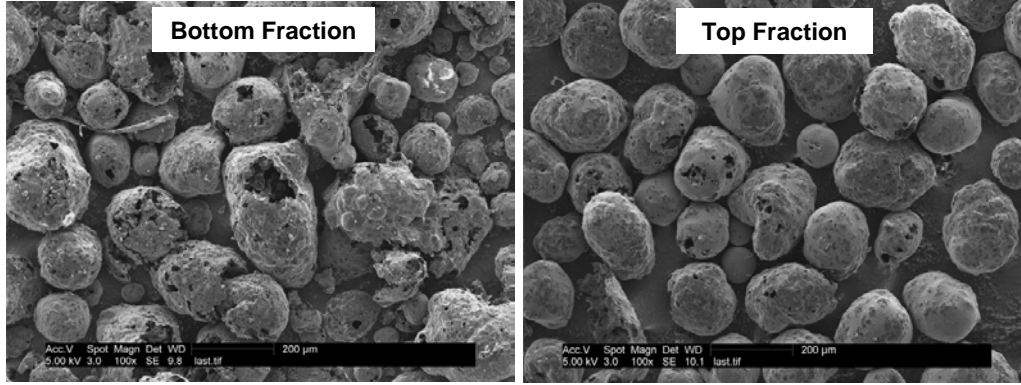


Figure E.2. SEM images of separated Eastern Bituminous B char produced at 15 atm, 1918 K, 660 ms.

The bottom fraction was also subjected to an ash test to determine an upper bound for the extent of reaction. When sufficient material was present in both top and bottom fractions, a mass-weighted average ash content was calculated from the ash content of the two fractions:

$$\begin{aligned}
 x_{ash,avg} &= \frac{m_{ash}}{m_{total}} = \frac{\sum_i^N m_{ash,i}}{\sum_i^N m_{particles,i}} = \frac{\sum_i^N (x_{ash,i} \cdot m_{particles,i})}{\sum_i^N m_{particles,i}} \\
 &= \frac{\sum_i^N \left(x_{ash,i} \cdot \frac{m_{particles,i}}{m_{total}} \right)}{\sum_i^N \left(\frac{m_{particles,i}}{m_{total}} \right)} = \frac{\sum_i^N \left(x_{ash,i} \cdot \frac{m_{particles,i}}{m_{total}} \right)}{1} = \sum_i^N (x_{ash,i} \cdot x_{particles,i})
 \end{aligned} \tag{E.1}$$

where the index i refers to some fraction of the material (top or bottom); $N = 2$ in this case. The variable m refers to mass and x refers to mass fraction, respectively. The bulk densities were not measured for the bottom fraction of the separated char because the presence of char fragments changes the packing factor. A swelling ratio determined from a bulk density on a sample with a high extent of fragmentation and an unknown packing factor has little or no physical meaning.

The upper and lower bounds on the swelling ratio determined using this technique were semi-quantitative in nature because many significant sources of error were present. First, the extent of fragmentation in the reaction zone versus in the collection system was unknown. However, comparison of SEM images before and after changing the collection procedures suggests that most particles reached the collection system intact. Second, fragmentation in the collection system was more likely for the largest (most swollen) char particles because they usually had thinner walls. Third, some of the largest non-fragmented cenospheric char particles were not retained by the cyclone due to their very low density and high surface area; they ended up on the soot filter, as shown in SEM images. Fourth, soot residues retained with the char after separation would artificially increase m/m_0 and hence the swelling ratio. However, based on SEM images, this effect was probably negligible. Fifth, the ash tracer technique assumes that the mass of ash remains constant throughout the experiment, but this was not strictly true at high experimental temperatures. Some compounds and elements in the ash vaporized and later condensed on surfaces where they were not collected, or else passed out of the system through the soot filters. Ash vaporization lowers the measured ash fraction and artificially increases the derived value of m/m_0 , which increases the observed swelling ratio.

The mass release calculated from the ash tracer yielded very noisy trends. Due to the large number of unquantified uncertainties, this char separation technique was abandoned. The decision was made to pursue new experiments with an altered collection system and a reinjection strategy to eliminate both the soot and fragmentation. This new approach allowed meaningful density and ash measurements to be made on the whole sample. Additionally, the changes in the collection system and operating procedures permitted a direct mass balance to be measured and compared to the ash tracer.

APPENDIX F. RADIATION TEMPERATURE CORRECTION

The centerline temperature was measured with a moveable B-type thermocouple. The thermocouple wires were encased in a ceramic sheath which was inserted into the central axis of the reactor through a water-cooled gasket at the top of the collection system. At high temperatures a significant amount of heat is radiated away from the thermocouple junction, or bead. The true gas temperature is higher and can be estimated using an energy balance on the bead. This was done by equating the convective heat flux and the radiation heat flux at the surface of the thermocouple bead:

$$h(T_g - T_b) = \sum_i^N [F_i \varepsilon \sigma (T_b^4 - T_i^4)] \quad (\text{F.1})$$

where h is the convective heat transfer coefficient, T_g is the gas temperature, T_b is the measured thermocouple bead temperature, F_i is one of N sphere-to-disk based view factors from the bead to a portion of the surroundings at temperature T_i (denoted T_{surr} when $N = 1$), ε is the emissivity of the thermocouple bead, and σ is the Stefan-Boltzman constant. Due to the temperature dependence of h , this equation was solved iteratively for the true gas temperature, T_g . A spreadsheet was written with VBA macros to accomplish this calculation. This radiation correction spreadsheet is included on the CD that accompanies this dissertation. Transport properties were taken from coefficients in the DIPPR[®] Database (Rowley et al., 2010). Thermodynamic properties were taken from coefficients used in the NASA-CEA code (McBride

et al., 2002). The convective heat transfer coefficient h was calculated from the spherical Nusselt number Nu_{sphere} (Ranz and Marshall, 1952):

$$Nu_{sphere} = 2.0 + 0.6Re_{d,sphere}^{1/2} Pr^{1/3} \quad (\text{F.2})$$

where $Re_{d,sphere}$ is the Reynolds number based on the approximately spherical bead diameter (measured optically with a microscope) and Pr is the Prandtl number, with gas properties evaluated at the bulk temperature $T_{\infty}=T_g$. Thermocouples are easily broken when inserted into a pressure vessel; several were used over the course of the measurements. When 0.005-inch diameter wire was used the bead diameter measured with a microscope was typically 350-400 μm . A cylindrical Nusselt number with the wire diameter was also used for comparison using the equation (Collis and Williams, 1959):

$$Nu_{cylinder} = (0.24 + 0.56Re_{d,cylinder}^{0.45})(T_m/T_{\infty})^{0.17} \quad (\text{F.3})$$

where gas properties are evaluated at the mean film temperature T_m . This Nusselt number was recommended for use with thermocouples in a previous review (Shaddix, 1999). When $Nu_{cylinder}$ is used the predicted value of T_g is higher compared to the case using Nu_{sphere} . Differences between the two correction methods are greatest at low Reynolds numbers, which occur at high temperatures and low pressures, especially near the burner surface. At 2.5 atm with peak flame temperatures near 1700 K, the maximum difference between the methods was 30 K. At 15 atm with peak flame temperatures of up to 1900 K, the maximum difference between the two methods was less than 5 K. This is considered acceptable agreement considering the error associated with the raw measurements, the error associated with the use of any Nusselt number correlation, and the magnitude of the impact expected on reaction processes. The Ranz-Marshall correlation (Equation F.2) was therefore used to correct all thermocouple measurements.

K-type thermocouples were installed on the surfaces of the original heaters surrounding the quartz tube that served as the reaction zone. B-type thermocouples were used with the newer molybdenum disilicide heating elements. These thermocouples provided temperatures of the surroundings T_i to be used in correcting the centerline temperature. Cool surfaces, including vessel walls, the burner, and the quench probe were assigned a uniform temperature of 500 K. For cases with 3 inches or less between the burner and the quench probe, no heaters were used and all T_i were assigned a value of 500 K. For cases with longer residence times, the portion of the heater surfaces visible from the centerline of the reactor was divided into 10 equal cylindrical sections. View factors were calculated for each heater section with respect to each measurement position and temperatures were assigned to each section by interpolating between the temperatures obtained from the thermocouples on the heater surfaces. The maximum heated surface temperature normally occurred towards the middle of the exposed heated region. Aaron Lewis has described and illustrated the geometric considerations associated with the use of view factors in the HPFFB (Lewis, 2011).

A thin coating of alumina was applied to the thermocouple junction via chemical vapor deposition to suppress catalytic heating of the thermocouple junction (Bahlawane et al., 2007). The apparatus developed to apply the coating has been described elsewhere (Lewis, 2011). A temperature-dependent emissivity developed for S-type thermocouple wire was used (Shaddix, 1999):

$$\varepsilon = 1.74(-0.1 + 3.24 \cdot 10^{-4} T_b - 1.25 \cdot 10^{-7} T_b^2 + 2.18 \cdot 10^{-11} T_b^3) \quad (\text{F.4})$$

The factor of 1.74 in this expression accounts for the alumina coating (Bahlawane et al., 2007). This emissivity varies from a value of 0.21 at 1000 K to 0.39 at 2000 K, which is consistent with values that have been measured in the literature (Shaddix, 1999). The magnitude of the

temperature correction is very sensitive to the value of the emissivity. It is possible that in some cases the coating was damaged. In the near-burner region, this would result in high raw temperature measurements due to catalytic heating. However, the catalytic reaction rate should be negligible above the location of the peak temperature (0.75 inch to 1 inch above the burner) because the gas composition should be close to equilibrium. A damaged alumina coating would also decrease the emissivity and hence decrease the temperature correction required. The spherical Nusselt number was chosen in part because it yields the smallest temperature correction; the conservative trend is better if imperfections in the thermocouple coating are considered probable.

The centerline gas temperature was measured using different heights between the burner and the collection probe. At heights of 3 inches and below, the heaters were not used. At the maximum height of 16.25 inches, power supplied to the Nichrome wire was reduced to keep the heater surface temperature below 1200°C, as specified by the manufacturer. At intermediate distances the maximum heater power was used while monitoring the heater surface temperatures for consistency; a partially inserted probe is a heat sink that prevents the heater surfaces from reaching 1200°C even at full power. An apparent consequence of this variation in heater power was that some of the gas temperatures near the probe were higher when the probe was set 10” above the burner than when it was set 16.25 inches above the burner (Figure F.1).

For some of the larger probe heights, it was difficult to obtain centerline temperatures with physically realistic trends due to thermocouple alignment issues. However, there were a sufficient number of good measurements to show that the temperatures near the burner were identical for large and small probe heights (see Figure F.1). When necessary, measurements taken far from the burner at probe heights of 10 inches and 16.25 inches were spliced with

measurements taken near the burner with the probe at 3 inches to produce physically realistic profiles. Intermediate points that interfered with the splicing procedure were omitted; temperatures in this regime were obtained through interpolation.

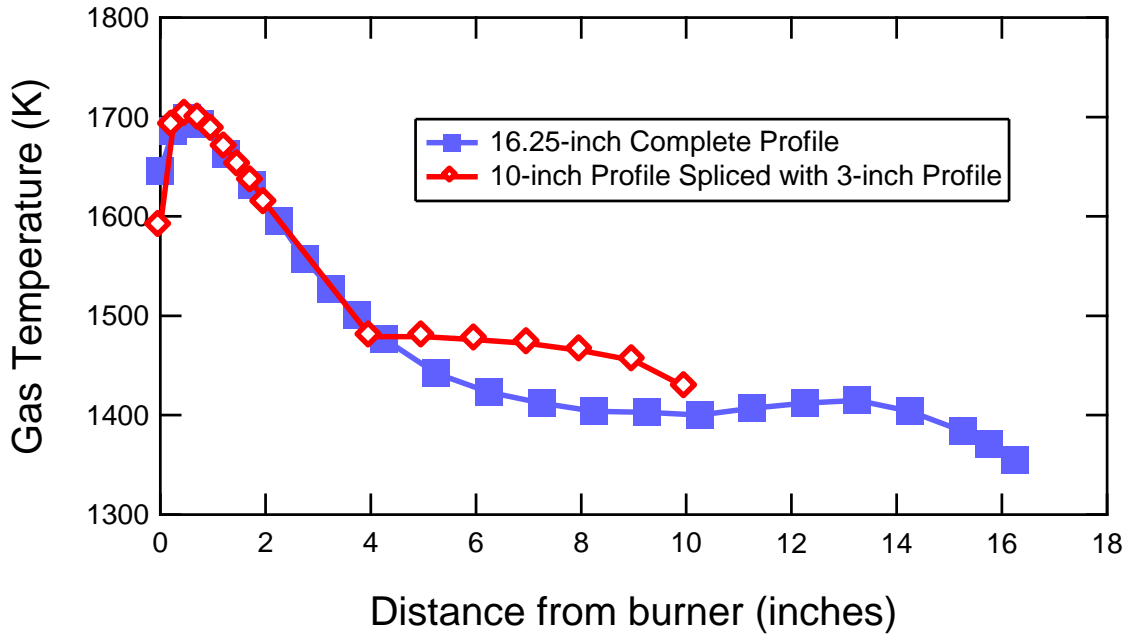


Figure F.1. Radiation-corrected centerline gas temperatures in the HPFFB at 5 atm with a maximum temperature of 1702 K at two probe heights. The 16.25-inch profile consists of a single collection of measurements and the 10-inch profile uses measurements from a 3-inch profile near the burner.

A useful intermediate quantity available in the spreadsheet used for the radiation temperature correction is the weighted sum of the surroundings temperatures to the fourth power:

$$T_{surr}^4 = \sum_i^N [F_i T_i^4] \quad (\text{F.5})$$

This summation over $N = 11$ view factors (F_i) was carried out at each measurement height. The heater surface temperature was fit in a piecewise linear fashion versus the height above the burner, and this correlation was used to provide the 10 T_i values required. The surfaces that did

not include the hot portion of the heaters were assumed to be at 500 K, which was used for the T_i associated with the remaining view factor.

T_{surr} is required for the energy balances used in the gasification models. T_{surr}^4 and the measurement height were fit to a 4th-order polynomial. T_{surr} versus residence time was derived from this correlation and the particle velocity profile for use in CCK and CCK^N. However, the 1st-order gasification model was designed to use a single surroundings temperature. The mean value theorem of calculus was used to derive an average T_{surr} for use in the 1st-order model:

$$T_{surr,avg}^4 = \frac{\int_{z_{min}}^{z_{max}} T_{surr}^4 dz}{z_{max} - z_{min}} \quad (\text{F.6})$$

where z is the height above the burner and z_{max} and z_{min} are the maximum and minimum between the burner and the collection probe corresponding to gasification experiments at high and low residence times. The integration in Equation F.6 was straightforward because T_{surr}^4 was fit to a 4th-order polynomial versus z .

APPENDIX G. EXPERIMENTAL GAS CONDITIONS AND PARTICLE SIZES

HPFFB Gas Conditions with ~20% CO₂

Table G.1. Gas flow rates and post-flame gas compositions with ~20% CO₂

Pressure and Peak Temperature	2.5 atm 1683 K	5 atm 1702 K	5 atm 1867 K	10 atm 1722 K	10 atm 1967 K	15 atm 1681 K	15 atm 1918 K
Gas flow (kg/s)	$1.544 \cdot 10^{-4}$	$2.229 \cdot 10^{-4}$	$2.232 \cdot 10^{-4}$	$3.625 \cdot 10^{-4}$	$3.633 \cdot 10^{-4}$	$4.854 \cdot 10^{-4}$	$4.863 \cdot 10^{-4}$
Adiabatic Temperature (K)	1666	1677	1921	1687	1936	1690	1939
Φ (Equiv. Ratio)	1.2735	1.2574	1.1677	1.2461	1.1553	1.2410	1.1510
Carrier N ₂ (SLPM, coal entrainment)	0.06	0.075	0.075	0.1	0.1	0.15	0.15
CO (SLPM)	2.08	3.0	3.00	4.90	4.90	6.56	6.56
H ₂ (SLPM)	0.17	0.17	0.17	0.17	0.17	0.17	0.17
Oxidizer N ₂ (SLPM)	2.75	3.99	3.08	6.50	5.00	8.70	6.69
Air (SLPM)	3.15	4.55	5.45	7.40	8.90	9.90	11.90
Equilibrium post-flame gas compositions							
CO ₂ mol %	15.7%	16.3%	20.0%	16.9%	20.78%	17.1%	21.0%
H ₂ O mol%	1.8%	1.3%	1.5%	0.8%	0.91%	0.6%	0.7%
CO mol %	11.9%	11.4%	8.2%	11.1%	7.72%	10.9%	7.5%
H ₂ mol %	0.4%	0.3%	0.1%	0.2%	0.08%	0.1%	0.0%
N ₂ mol %	70.2%	70.7%	70.2%	71.0%	70.03%	71.3%	70.8%

Table G.2. Residence times with ~20% CO₂

Collection height (inches)	2.5 atm 1683 K RT (ms)	5 atm 1702 K RT (ms)	5 atm 1867 K RT (ms)	10 atm 1722 K RT (ms)	10 atm 1967 K RT (ms)	15 atm 1681 K RT (ms)	15 atm 1918 K RT (ms)	15 atm 2160 K RT (ms)
0.75	33	38	38	42	46	46	41	46
3	-	113	116	122	114	122	111	115
10	-	367	388	-	-	414	389	-
16.25	-	611	662	-	-	692	660	-

Table G.3. Particle velocity profiles with ~20% CO₂

Height above burner (mm)	2.5 atm, 1683 K v_p (cm/s)	5 atm, 1702 K v_p (cm/s)	5 atm, 1867 K v_p (cm/s)	10 atm, 1722 K v_p (cm/s)	10 atm, *1967 K v_p (cm/s)	15 atm, 1681 K v_p (cm/s)	15 atm, 1918 K v_p (cm/s)
0	27.5	10.7	10.7	1.5	1.5	1.5	1.5
3	45.8	39.2	40.6	38.1	37.6	33.6	37.6
6	56.7	51.2	51.6	49.9	51.4	45.8	51.4
9	64.3	59.6	59.5	58.8	60.5	55.5	60.5
12	70.2	66.9	65.8	65.9	69.6	63.3	69.6
15	74.6	73.2	70.9	71.3	77.2	69.2	77.2
20	79.0	78.1	75.7	77.0	84.6	75.2	84.6
25.4	80.6	80.6	78.1	79.0	87.2	78.3	87.2
Velocities are obtained for distances of $x > 25.4$ mm above the burner using the equation $v_p = v_p(25.4 \text{ mm}) \cdot T(x) / T(25.4 \text{ mm})$ where T is the centerline gas temperature at x . Use $T_{data}(25.4 \text{ mm})$ if the measured T is being used to scale velocity and use $T_{fitted}(25.4 \text{ mm})$ if the polynomial fit of T is used. *The 15 atm 1918 K velocity profile was used to estimate the residence time for the 10 atm 1967 K condition because so many of the other measured velocities were similar.							
$T_{data}(25.4 \text{ mm})$	1675 K	1687 K	1858 K	1653 K	1919	1637 K	1906 K
$T_{fitted}(25.4 \text{ mm})$	1677 K	1694 K	1868 K	1661 K	N/A	1649 K	1897 K

Table G.4. Radiation-corrected HPFFB temperature profiles with ~20 % CO₂ with probe at 3 inches above burner

Height above burner (inches)	2.5 atm, 1683 K peak	5 atm, 1702 K peak	5 atm, 1867 K peak	10 atm, 1722 K peak	10 atm, 1967 K peak	15 atm, 1681 K peak	15 atm, 1918 K peak	15 atm, *2160 K peak
0	1448	1590	1735	1722	1961	1643	1841	2160
0.25	1616	1691	1845	1713	1967	1681	1883	2065
0.5	1667	1702	1864	1672	1952	1655	1898	2044
0.75	1683	1698	1867	1655	1937	1643	1918	2025
1	1675	1687	1858	1653	1919	1637	1906	1994
1.25	1664	1669	1843	1646	1896	1632	1854	1980
1.5	1642	1651	1824	1630	1869	1613	1836	1956
1.75	1613	1635	1773	1605	1827	1608	1810	1921
2	1582	1613	1689	1576	1788	1590	1777	1901
2.25	1556	1588	1594	1578	1763	1559	1744	1876
2.5	1528	1507	1554	1519	1708	1521	1742	1847
2.75	1500	1467	1530	1499	1669	1487	1697	1804
3	1468	1442	1524	1464	1631	1388	1606	1751
*The 15 atm 2160 K condition was only used for one experiment with Kentucky #9. It was too hot for sustained use; the quartz tube broke, and there was a concern about the possibility of burner damage. The 15 atm 1918 K condition with a scaling temperature of 2020 K was used to estimate the velocity profile for the 2160 K condition. The 2160 K condition had 24.05% CO ₂ , 9.02% CO, and 0.69% H ₂ O, with $\Phi = 1.1567$								

Table G.5. Radiation-corrected HPFFB temperature profiles with ~20 % CO₂ and curve-fits with probe at 10 inches

Height above burner (inches)	5 atm 1702 K peak	5 atm 1867 K peak	15 atm 1681 K peak	15 atm 1918 K peak
0	1590	1735	1643	1841
0.25	1691	1845	1681	1883
0.5	1702	1864	1655	1898
0.75	1698	1867	1643	1918
1	1687	1858	1637	1906
1.25	1669	1843	1632	1854
1.5	1651	1824	1613	1836
1.75	1635	1773	1608	1810
2	1613	-	1590	1777
2.25	-	-	1559	1744
2.5	-	-	1521	1742
2.75	-	-	-	1697
3	-	1617	-	1606
4	1479	1591	1376	1510
5	1479	1584	1334	1464
6	1476	1576	1292	1407
7	1472	1563	1257	1370
8	1465	1550	1227	1316
9	1455	1533	1198	1285
9.5	-	1522	1185	1269
10	1428	1501	1135	1227
Coefficients for equation $T = A \cdot z^6 + B \cdot z^5 + C \cdot z^4 + D \cdot z^3 + E \cdot z^2 + F \cdot z + G$ where T is the centerline temperature in Kelvin and z is the distance above the burner in meters				
A	-4.9639E+07	-1.6351E+08	2.7801E+06	-5.0619E+07
B	4.6488E+07	1.4266E+08	1.1813E+05	4.9071E+07
C	-1.7045E+07	-4.8228E+07	-1.6982E+06	-1.8960E+07
D	3.0043E+06	7.8253E+06	7.0267E+05	3.6162E+06
E	-2.4376E+05	-5.9845E+05	-9.7795E+04	-3.3152E+05
F	5.4604E+03	1.5587E+04	1.8967E+03	8.4731E+03
G	1.6647E+03	1.7440E+03	1.6504E+03	1.8416E+03
Average T_{surr} (K)	1291	1315	923	978
Coefficients for equation $T_{surr}^4 = A \cdot z^4 + B \cdot z^3 + C \cdot z^2 + D \cdot z + E$ where T_{surr} is the surroundings temperature in Kelvin and z is the distance above the burner in meters				
A	-5.4922E15	-5.9837E15	-1.2432E15	-3.3281E15
B	2.5292E15	2.8259E15	4.5644E14	1.4055E15
C	-4.8338E14	-5.5232E14	-6.3952E13	-1.8719E14
D	5.1723E13	5.8066E13	8.3783E12	1.3823E13
E	6.9148E11	7.6690E11	1.6438E11	1.4952E11

Table G.6. Radiation-corrected HPFFB temperature profiles with ~20 % CO₂ with probe at 16.25 inches

Height above burner (in)	5 atm 1702 K peak	5 atm 1867 K peak	15 atm 1681 K peak	15 atm 1918 K peak
0	1646	1735	1643	1841
0.25	1686	1845	1681	1883
0.5	1699	1864	1655	1898
0.75	1693	1867	1643	1918
1	-	1858	1637	1906
1.25	1663	1843	1632	1854
1.5	-	1824	1613	1836
1.75	1632	1773	1608	1810
2	-	1713	1590	1777
2.25	1595	1662	1559	1744
2.5	-	-	1521	1742
2.75	1557	1615	-	1697
3	-	-	1487	1606
3.25	1527	1585	-	-
3.75	1501	1560	-	1488
4.25	1477	1526	-	1471
4.75	-	-	1315	1442
5.25	1442	1500	1293	1421
6.25	1423	1482	1267	1377
7.25	1412	1466	1245	1349
8.25	1404	1457	1225	1319
9.25	1403	1452	1212	1297
10.25	1400	1453	1208	1288
11.25	1407	-	1205	1281
12.25	1412	1454	1208	1278
13.25	1415	1452	1210	1278
14.25	1404	1441	1215	1276
15.25	1384	1420	1218	1277
15.75	1371	1407	1219	1275
16.25	1355	1388	1214	1275
Coefficients for equation $T = A \cdot z^6 + B \cdot z^5 + C \cdot z^4 + D \cdot z^3 + E \cdot z^2 + F \cdot z + G$ where T is the centerline temperature in Kelvin and z is the distance above the burner in meters				
A	-3.3077E+06	-8.3500E+06	-4.7859E+06	-1.2118E+07
B	4.5021E+06	1.1031E+07	6.8309E+06	1.6477E+07
C	-2.3925E+06	-5.5883E+06	-3.7921E+06	-8.6084E+06
D	6.0281E+05	1.3285E+06	1.0080E+06	2.1314E+06
E	-6.4721E+04	-1.3796E+05	-1.2017E+05	-2.3864E+05
F	3.6982E+02	2.2812E+03	2.5484E+03	6.2416E+03
G	1.6973E+03	1.8556E+03	1.6467E+03	1.8527E+03
Average T_{surr} (K)	N/A	1318	1132	1168
Coefficients for equation $T_{surr} = A \cdot z^4 + B \cdot z^3 + C \cdot z^2 + D \cdot z + E$ where T_{surr} is the surroundings temperature in Kelvin and z is the distance above the burner in meters				
A	N/A	3.6484E13	-2.3836E14	-2.2364E14
B	N/A	-1.3675E14	2.4027E13	-1.4850E13
C	N/A	8.8018E12	3.0735E13	4.5955E13
D	N/A	1.8967E13	2.9277E12	2.5196E12
E	N/A	6.9518E11	1.8595E11	2.1594E11

HPFFB Gas Conditions with Enhanced CO₂ (40% and 90%)

Table G.7. Gas flow rates and post-flame gas compositions with enhanced CO₂

Pressure	10 atm	10 atm	10 atm	15 atm	15 atm	15 atm
Peak Temperature	1899 K	2093 K	1764 K	1835 K	2011 K	2023 K
Approximate CO ₂ %	~40 %	~40 %	~90 %	~40 %	~40 %	~90 %
Adiabatic Temp (K)	1770	1972	1917	1773	1968	1919
Φ (Equiv. Ratio)	1.1392	1.1182	1.0448	1.1366	1.1215	1.0431
Carrier N ₂ (SLPM, coal entrainment)	0.10	0.10	0.10	0.15	0.15	0.15
CO (SLPM)	6.00	5.90	5.20	8.02	8.02	6.98
H ₂ (SLPM)	0.17	0.17	0.17	0.17	0.17	0.17
Oxidizer CO ₂ (SLPM)	3.90	2.91	8.64	5.22	3.88	11.62
Air (SLPM)	8.90	10.00	0.00	11.90	13.35	0.00
O ₂ (SLPM)	0.00	0.00	2.09	0.00	0.00	2.80
Equilibrium post-flame gas compositions						
CO ₂ mol %	43.45%	40.87%	89.64%	42.77%	40.91%	90.17%
H ₂ O mol %	0.91%	0.94%	1.18%	0.68%	0.70%	0.88%
CO mol %	14.11%	11.02%	8.45%	13.89%	11.36%	8.14%
H ₂ mol %	0.08%	0.06%	0.03%	0.06%	0.04%	0.02%
N ₂ mol %	40.97%	46.56%	0.71%	41.11%	46.43%	0.79%

Table G.8. Particle velocity profiles with enhanced CO₂

Height above burner (mm)	10 atm 1899 K ~40 % CO ₂ v _p (cm/s)	10 atm 2093 K ~40 % CO ₂ v _p (cm/s)	10 atm 1764 K ~90 % CO ₂ v _p (cm/s)	15 atm 1835 K ~40 % CO ₂ v _p (cm/s)	15 atm 2011 K ~40 % CO ₂ v _p (cm/s)	15 atm 2023 K ~90 % CO ₂ v _p (cm/s)
0	1.5	1.5	1.5	1.5	1.5	1.5
3	30.7	33.3	30.0	23.9	29.2	27.1
6	40.2	43.6	39.4	32.6	40.0	37.1
9	47.4	51.4	46.4	39.6	47.0	43.6
12	53.1	57.6	52.0	45.1	54.1	50.2
15	57.5	62.3	56.2	49.3	60.0	55.7
20	62.1	67.3	60.7	53.6	65.8	61.0
25.4	63.7	69.0	62.3	55.8	67.8	62.9
Velocities are obtained for distances of $x > 25.4$ mm above the burner using the equation $v_p = v_p(25.4 \text{ mm}) \cdot T(x) / T(25.4 \text{ mm})$ where T is the centerline gas temperature at x . Use $T_{data}(25.4 \text{ mm})$ if the measured T is being used to scale velocity and use $T_{fitted}(25.4 \text{ mm})$ if the polynomial fit of T is used.						
$T_{data}(25.4 \text{ mm})$	1756 K	1900 K	1709 K	1793 K	1976 K	1907 K
$T_{fitted}(25.4 \text{ mm})$	1663 K	1894 K	1740 K	1776 K	1955 K	1895 K

Table G.9. Residence times with enhanced CO₂

Collection height (inches)	10 atm 1899 K ~40 % CO ₂ RT (ms)	10 atm 2093 K ~40 % CO ₂ RT (ms)	10 atm 1764 K ~90 % CO ₂ RT (ms)	15 atm 1835 K ~40 % CO ₂ RT (ms)	15 atm 2011 K ~40 % CO ₂ RT (ms)	15 atm 2023 K ~90 % CO ₂ RT (ms)
0.75	52	48	53	64	53	57
1.00	62	58	64	76	62	67
2.00	103	95	106	122	101	110
3.00	147	135	150	172	142	156
8.00	425	378	424	485	410	456
9.50 Heaters at 1250°C	-	424	462	-	-	-
9.50 Heaters at 1350°C	-	401	439	-	-	-

Table G.10. Radiation-corrected HPFFB temperature profiles with enhanced CO₂, 7.5-inch probe height, no heaters

Height above burner (inches)	10 atm 1899 K ~40 % CO ₂	10 atm 2093 K ~40 % CO ₂	10 atm 1764 K ~90 % CO ₂	15 atm 1835 K ~40 % CO ₂	15 atm 2011 K ~40 % CO ₂	15 atm 2023 K ~90 % CO ₂
0.1	1658	1816	1317	1752	1771	2004
0.3	1899	2093	1485	1835	2036	2023
0.5	1838	2021	1750	1811	2011	2023
0.7	1805	1992	1764	1809	1994	1906
0.9	1756	1930	1727	1793	1976	1907
1.1	-	-	1691	-	-	1874
1.3	-	-	1687	-	-	1871
1.5	1695	-	1718	1753	1927	1848
1.9	-	-	1690	-	-	1751
2.5	1660	1824	1648	1621	1764	1655
3.5	1544	1701	1503	1496	1602	1494
4.5	1419	1534	1393	1387	1488	1369
5.5	1334	1434	1300	1300	1380	1272
6.5	1258	1345	1212	1212	1286	1182
6.7	1232	1311	1197	1193	1263	1166
7.1	1191	1275	1151	1161	1233	1136
*7.5	1089	1154	1019	1076	1155	957
*Entrance to gas-quenched particle collection probe						
Coefficients for equation $T = A \cdot z^2 + B \cdot z + C$ where T is the centerline temperature in Kelvin and z is the distance above the burner in meters. These correlations were used to extrapolate the temperature profile to 8 inches.						
A	0	0	0	0	0	1.2351E04
B	-3.9967E03	-4.4451E03	-3.7624E03	-4.1062E03	-4.9287E03	-7.4670E03
C	1.7651E03	2.0695E03	1.8352E03	1.8795E03	2.0798E03	2.0764E03

Table G.11. Radiation-corrected HPFFB temperature profiles with enhanced CO₂ and heaters

Height above burner (inches)	10 atm 2093 K Peak ~40% CO ₂ 1250°C Heater	10 atm 2093 K Peak ~40% CO ₂ 1350°C Heater	10 atm 1764 K Peak ~90% CO ₂ 1250°C Heater	10 atm 1764 K Peak ~90% CO ₂ 1350°C Heater
0.2	1951	1951	1984	1984
0.4	1936	1936	1930	1930
0.6	1917	1917	1888	1888
0.8	1913	1913	1848	1848
1.0	1900	1900	1821	1821
1.6	1842	1842	1716	1716
2.0	1782	1782	1631	1631
2.4	1720	1720	-	-
2.6	1696	-	-	-
2.8	1663	-	-	-
3.0	1641	-	-	-
3.5	-	-	1479	1583
4.5	1577	1710	1458	1580
5.5	1585	1703	1458	1576
6.5	1586	1696	1478	1606
7.5	1581	1703	1496	1624
8.1	1580	1699	1503	1632
8.5	1577	1693	1501	1630
8.9	1571	1687	1498	1625
9.1	1569	1682	1495	1620
9.3	1558	1670	1484	1610
*9.5	1536	1647	1447	1588
*Entrance to gas-quenched particle collection probe				
Coefficients for equation $T = A \cdot z^4 + B \cdot z^3 + C \cdot z^2 + D \cdot z + E$ where T is the centerline temperature in Kelvin and z is the distance above the burner in meters. The splice point indicates the height above the burner to switch from short to long residence time correlations.				
A short RT	0	0	-2.1809E08	-2.1809E08
B short RT	0	0	3.7541E07	3.7541E07
C short RT	-3.3680E04	-3.3680E04	-2.1548E06	-2.1548E06
D short RT	-1.7226E03	-1.7226E03	3.9388E04	3.9388E04
E short RT	1.9592E03	1.9592E03	1.7052E03	1.7052E03
Splice point (m)	0.0850	0.0618	0.0750	0.0657
A long RT	0	0	0	0
B long RT	0	0	0	0
D long RT	0	0	0	0
D long RT	7.4533E01	-2.3435E02	1.2175E02	2.6549E02
E long RT	1.5586E03	1.7384E03	1.4653E03	1.5570E03
Average T_{surr} (K)	1348	1441	1356	1439
Coefficients for equation $T_{surr} = A \cdot z^2 + B \cdot z + C$ where T_{surr} is the surroundings temperature in Kelvin and z is the distance above the burner in meters. The average T_{surr} was used in the 1 st -order model and the coefficients were used to calculate T_{surr} versus residence time in CCK and CCK ^N .				
A	-2.7593E14	-3.5227E14	-2.7400E14	-3.5308E14
B	7.4963E13	9.2708E13	7.3379E13	9.3334E13
C	-9.2208E11	-6.4929E11	-6.6456E11	-7.4853E11

HPFFB Pyrolysis Gas Conditions with ~2% O₂

Table G.12. Gas flow rates and post-flame gas compositions with ~2% O₂

Pressure and Peak Temperature	5 atm 1798 K	10 atm 1907 K	15 atm 1834 K
Adiabatic Temp (K)	1771	1767	1770
Φ (Equiv. Ratio)	0.9181	0.9168	0.9201
Carrier N₂ (SLPM, coal entrainment)	0.075	0.10	0.15
CO (SLPM)	1.94	3.14	4.34
H₂ (SLPM)	0.17	0.17	0.17
Oxidizer N₂ (SLPM)	3.00	4.86	6.20
Fuel N₂ (SLPM)	1.00	1.50	2.50
Air (SLPM)	5.90	9.30	12.60
Equilibrium post-flame gas compositions			
CO₂ mol %	17.60%	18.04%	18.32%
H₂O mol%	1.54%	0.97%	0.72%
CO mol %	0.01%	0.01%	0.01%
H₂ mol %	0.00%	0.00%	0.00%
N₂ mol %	78.66%	78.74%	78.78%
O₂ mol %	1.59%	1.63%	1.57%

Table G.13. Particle velocity profiles and residence times with ~2% O₂

Height above burner (mm)	5 atm, 1798 K v_p (cm/s)	10 atm, 1907 K v_p (cm/s)	15 atm, 1834 K v_p (cm/s)
0	10.7	1.5	1.5
3	39.2	38.1	33.6
6	51.2	49.9	45.8
9	59.6	58.8	55.5
12	66.9	65.9	63.3
15	73.2	71.3	69.2
20	78.1	77.0	75.2
25.4	80.6	79.0	78.3
30.5	77.7	76.9	75.6
40.6	72.0	73.1	70.2
50.8	66.8	70.1	67.9
Residence time (ms) at 1.5-inch collection height	65	78	83

Table G.14. Radiation-corrected HPFFB temperature profiles with ~2 % O₂

Height above burner (inches)	5 atm, 1798 K peak	Height above burner (inches)	10 atm, 1907 K peak	15 atm, 1834 K peak
0.1	1693	0.0	1310	1277
0.3	1776	0.2	1907	1736
0.5	1798	0.4	1881	1834
0.7	1781	0.6	1880	1823
0.9	1735	0.8	1856	1734
1.5	1533	1.0	1810	1620
1.9	1413	1.2	1762	1562
2.5	1297	1.6	1674	1452
		2.0	1605	1405
		2.4	-	1369
		2.6	1450	1355

FFB Gas Conditions for Atmospheric Coal Pyrolysis Studies

Table G.15. Gas flows, compositions, and temperatures for atmospheric FFB coal swelling experiments

Pressure and Peak Temperature	0.84 atm 1546 K	0.84 atm 1662 K
Φ (Equiv. Ratio)	1.2737	0.9576
Carrier N ₂ (SLPM, coal entrainment)	0.0367	0.0367
CO (SLPM)	9.00	5.10
H ₂ (SLPM)	0.30	0.68
N ₂ with fuel (SLPM)	5.60	4.50
O ₂ (SLPM)	2.68	3.13
N ₂ with oxidizer (SLPM)	12.50	17.00
Equilibrium post-flame gas compositions		
CO ₂ mol %	18.65%	18.41%
H ₂ O mol %	0.91%	2.45%
CO mol %	14.15%	0.09%
H ₂ mol %	0.18%	0.00%
N ₂ mol %	66.10%	78.06%
Height above burner (inches)	EBA Heating Rate Study Gas Temperature (K)	Swelling Model Pressure Study Gas Temperature (K)
0.0	1503	1213
0.25	-	1592
0.5	1546	1637
0.75	-	1657
1.0	1520	1662
1.5	-	1655
2.0	1483	1646
3.0	1448	1615
4.0	1409	1580
5.0	1377	1541

Table G.16. Standard particle velocity profile used for 0.84 atm FFB pyrolysis experiments

Height above burner (mm)	v_p (cm/s)
0.0	3.4
0.02	13.0
0.33	49.0
1.04	88.0
2.33	128.0
4.66	168.0
7.56	197.0
10.01	212.0
13.07	223.0
18.8	233.0
*25.4	233.0

*Velocity assumed constant at 233 cm/s for larger heights. Residence time for coal swelling experiments at the 1662 K condition was 26 ms at a 2-inch collection height.

Particle Size Distributions from Coulter Counter Measurements

Table G.17. Particle size distributions for coals

Diameter Bin (μm)	Wyodak 2010 Mass Fraction	Wyodak 2011 Mass Fraction	Spliced Wyodak Mass Fraction (use this)	Kentucky #9 Mass Fraction	EBA Mass Fraction	EBB Mass Fraction
18.974	0	0	0	0.012306	0	0
21.121	0.001171	0	0.001492	0.013903	0	0.006214
23.511	0.001347	0	0.001717	0.015600	0.002515	0.009043
26.171	0.001146	0	0.001460	0.018758	0.003948	0.012284
29.133	0.002665	0	0.003395	0.023777	0.006583	0.015977
32.430	0.00641	0	0.008167	0.029912	0.010536	0.023432
36.099	0.01056	0.017346	0.013456	0.038105	0.016903	0.039202
40.184	0.020777	0.011649	0.026473	0.051825	0.029065	0.067073
44.732	0.043544	0.048265	0.055481	0.073099	0.052849	0.107189
49.794	0.069885	0.106009	0.089044	0.097956	0.093570	0.150687
55.428	0.099557	0.156784	0.126850	0.117675	0.145956	0.177200
61.701	0.124605	0.160912	0.158766	0.127146	0.191014	0.164659
68.683	0.135869	0.210532	0.173118	0.129923	0.208785	0.115187
76.455	0.137227	0.132511	0.174849	0.124202	0.168695	0.064827
85.107	0.104312	0.114678	0.132910	0.091207	0.064463	0.034191
94.738	0.082924	0.032108	0.032822	0.032189	0.005118	0.011859
105.460	0.082529	0	0	0.002417	0	0.000976
117.390	0.075473	0	0	0	0	0

Table G.17 (continued)

Diameter Bin (µm)	Pittsburgh #8 Mass Fraction	Lower Kittanning Mass Fraction	Dietz Mass Fraction	Illinois #6 Mass Fraction
3.4137	0.005238	0	0	0
3.8	0.005897	0	0	0
4.23	0.006593	0	0	0
4.7087	0.007326	0	0	0
5.2415	0.00806	0	0	0
5.8346	0.008878	0	0	0
6.4949	0.009838	0	0	0
7.2298	0.010981	0	0	0
8.048	0.012265	0	0	0
8.9587	0.013614	0	0	0
9.9725	0.014981	0	0	0
11.101	0.016405	0	0	0
12.357	0.017979	0	0	0
13.755	0.019834	0	0	0
15.312	0.022037	0	0	0
17.045	0.024662	0.00086	0	0
18.974	0.027792	0.000972	0.000589	0
21.121	0.031568	0.000968	0.000984	0
23.511	0.036272	0.001238	0.001507	0.001235
26.171	0.04221	0.001687	0.001882	0.00217
29.133	0.049754	0.002061	0.00174	0.003705
32.43	0.059311	0.002822	0.001398	0.006768
36.099	0.070648	0.004948	0.002359	0.0202
40.184	0.082498	0.009592	0.008362	0.021366
44.732	0.091757	0.021107	0.026187	0.03918
49.794	0.093579	0.049789	0.060355	0.072514
55.428	0.084635	0.106737	0.107561	0.130784
61.701	0.064917	0.175915	0.154614	0.192639
68.683	0.039063	0.212029	0.183792	0.203746
76.455	0.016745	0.182336	0.180883	0.187061
85.107	0.004166	0.114714	0.146191	0.118632
94.738	0.000501	0.060768	0.09026	0
105.46	0	0.031732	0.029193	0
117.39	0	0.018218	0.002142	0

Table G.18. Particle size distributions for reinjected chars sieved to 75-106 μm

Diameter Bin (μm)	Illinois #6 10 atm 1907 K Char Mass Fraction	Diameter Bin (μm)	Illinois #6 15 atm 1834 K Char Mass Fraction	Diameter Bin (μm)	Kentucky #9 10 atm 1907 K Char Mass Fraction	Diameter Bin (μm)	Kentucky #9 15 atm 1834 K Char Mass Fraction
71.3668	0.046805	68.2726	0.032361	71.5275	0.110808	69.1165	0.110808
79.4440	0.085831	75.9997	0.059344	79.6230	0.156295	76.9390	0.156295
88.4341	0.158853	84.6000	0.109831	88.6333	0.209442	85.6457	0.209442
98.4401	0.286503	94.1722	0.198089	98.6618	0.251603	95.3362	0.251603
109.5810	0.422008	104.8300	0.291777	109.8278	0.271853	106.1257	0.271853
		116.6924	0.308599				
<p>These size distributions were obtained by applying the measured swelling ratios to the coal size distribution, omitting the sizes that were more than 1 bin outside the sieve size range, and rescaling the mass fractions so that they summed to 1. The temperatures in the top row indicate the pyrolysis conditions with 2% O_2.</p>							

APPENDIX H. PYROLYSIS DATA FOR PRESSURIZED SWELLING MODEL

Table H.1. Wyodak pyrolysis data with 0% O₂

Pressure (atm)	Peak Gas Temperature (K)	Collection Height (inches)	Residence Time (ms)	Mass Release (daf wt %, Ash Tracer)	Mass Release (as rec'd wt %, Direct)	Ash (dry wt %)	Apparent Density ρ (g/cc)	Swelling Ratio d/d_0
15	1681	0.75	46	46.12	N/A	9.95	0.796	0.931
10	1722	0.75	42	44.50	N/A	9.69	0.766	0.952
5	1702	0.75	38	46.61	54.96	10.03	0.701	0.969
2.5	1683	0.75	33	46.83	56.48	10.07	0.702	0.967
Pressure		2.5	5	10	15			
Heating Rate (K/s)		7.36×10^4 K/s	7.28×10^4 K/s	6.91×10^4 K/s	6.26×10^4 K/s			

Table H.2. Dietz pyrolysis data with ~2% O₂

Pressure (atm)	Peak Gas Temperature (K)	Collection Height (inches)	Residence Time (ms)	Mass Release (daf wt %, Ash Tracer)	Mass Release (as rec'd wt %, Direct)	Ash (dry wt %)	Apparent Density ρ (g/cc)	Swelling Ratio d/d_0
15	1834	1.5	83	66.34	84.04	13.10	0.298	1.075
10	1907	1.5	78	53.96	74.40	9.93	0.430	1.056
5	1798	1.5	65	67.24	84.18	13.41	0.302	1.058
*0.84	1662	2	26	44.66	62.72	8.40	0.546	0.948
*Experiment performed in FFB rather than HPFFB								
Pressure		0.84	5	10	15			
Heating Rate (K/s)		1.64×10^5 K/s	9.53×10^4 K/s	1.05×10^5 K/s	9.58×10^4 K/s			

Table H.3. Illinois #6 pyrolysis data with ~2% O₂

Pressure (atm)	Peak Gas Temperature (K)	Collection Height (inches)	Residence Time (ms)	Mass Release (daf wt %, Ash Tracer)	Mass Release (as rec'd wt %, Direct)	Ash (dry wt %)	Apparent Density ρ (g/cc)	Swelling Ratio d/d_0
15	1834	1.5	83	47.32	59.32	15.02	0.129	1.699
10	1907	1.5	78	47.34	54.59	14.93	0.113	1.776
5	1798	1.5	65	47.48	66.27	15.06	0.264	1.337
*0.84	1662	2	26	52.16	54.91	16.29	0.506	1.024
*Experiment performed in FFB rather than HPFFB								
Pressure		0.84	5	10	15			
Heating Rate (K/s)		1.54×10^4 K/s	1.18×10^5 K/s	1.59×10^5 K/s	1.37×10^5 K/s			

Table H.4. Kentucky #9 pyrolysis data with ~2% O₂

Pressure (atm)	Peak Gas Temperature (K)	Collection Height (inches)	Residence Time (ms)	Mass Release (daf wt %, Ash Tracer)	Mass Release (as rec'd wt %, Direct)	Ash (dry wt %)	Apparent Density ρ (g/cc)	Swelling Ratio d/d_0
15	1834	1.5	83	44.84	55.66	13.73	0.137	1.721
10	1907	1.5	78	45.21	55.32	13.81	0.123	1.782
5	1798	1.5	65	52.89	N/A	15.71	0.108	1.784
*0.84	1662	2	26	57.04	11.60	16.97	0.650	0.955
*Experiment performed in FFB rather than HPFFB								
Pressure		0.84	5	10	15			
Heating Rate (K/s)		1.51×10^5 K/s	1.21×10^5 K/s	1.42×10^5 K/s	1.24×10^5 K/s			

Table H.5. Pittsburgh #8 pyrolysis data with ~2% O₂

Pressure (atm)	Peak Gas Temperature (K)	Collection Height (inches)	Residence Time (ms)	Mass Release (daf wt %, Ash Tracer)	Mass Release (as rec'd wt %, Direct)	Ash (dry wt %)	Apparent Density ρ (g/cc)	Swelling Ratio d/d_0
15	1834	1.5	83	44.05	60.94	11.16	0.120	1.835
10	1907	1.5	78	45.64	66.57	11.45	0.130	1.772
5	1798	1.5	65	43.75	66.67	11.11	0.143	1.732
*0.84	1662	2	26	50.56	56.85		0.652	0.974
*Experiment performed in FFB rather than HPFFB, used average of direct and ash tracer mass release.								
Pressure		0.84	5	10	15			
Heating Rate (K/s)		2.24×10^5 K/s	9.84×10^4 K/s	1.17×10^5 K/s	1.01×10^5 K/s			

Table H.6. Lower Kittanning pyrolysis data with ~2% O₂

Pressure (atm)	Peak Gas Temperature (K)	Collection Height (inches)	Residence Time (ms)	Mass Release (daf wt %, Ash Tracer)	Mass Release (as rec'd wt %, Direct)	Ash (dry wt %)	Apparent Density ρ (g/cc)	Swelling Ratio d/d_0
15	1834	1.5	83	31.92	56.36	24.11	0.142	1.829
10	1907	1.5	78	32.53	N/A	24.00	0.125	1.900
5	1798	1.5	65	11.83	**38.30	19.46	0.203	1.615
*0.84	1662	2	26	N/A	**34.19	16.56	0.704	1.090
*Experiment performed in FFB rather than HPFFB								
**Used direct mass balance instead of ash tracer for mass release								
Pressure	0.84			5		10	15	
Heating Rate (K/s)	1.03×10 ⁵ K/s			1.03×10 ⁵ K/s		1.25×10 ⁵ K/s	1.11×10 ⁵ K/s	

APPENDIX I. GASIFICATION DATA

Some of the CO₂ gasification data with in-situ pyrolysis were unsuitable for kinetic modeling because the apparent extents of gasification decreased with increasing residence time. This was probably due to increased soot contamination of the char with increasing temperature and residence time. There may also have been contributions from vaporization of ash and measurement noise effects attributable to the large magnitude of pyrolysis mass loss compared to gasification mass loss. The data that exhibited such unrealistic trends were not used for kinetic analysis.

Most of the data with unrealistic mass loss trends were from early work with the two Eastern Bituminous coals and the Kentucky #9 bituminous coal, where the ash tracer technique was used nearly exclusively. Direct mass balances were not conducted as regularly in the earlier HPFFB experiments because complete shutdown of the system after each experiment for measurement of the coal plunger mass was considered wasteful in terms of time and clogging of the feeder tube was frequent. In later experiments it was determined to be essential to do the direct mass balance for verification.

The CD that accompanies this dissertation contains the gasification data that were used for kinetic analysis in the form of spreadsheets. The individual worksheets were pasted into text files for use in OptdesX with CCK and CCK^N. The 1st-order gasification model spreadsheets are

also included on the CD. The data in the tables that follow should be compared to the coal data in Table 4.1. The gas conditions are identified by the pressure and peak gas temperature, which correspond to the headers used in the tables of gas conditions found in Appendix G.

Table I.1. Wyodak 2010 gasification data with ~20% CO₂ used for kinetic modeling

Pressure (atm)	Peak Gas Temperature (K)	Collection Height (inches)	Residence Time (ms)	Mass Release (daf wt %, Ash Tracer)	Ash (dry wt %)	Apparent Density ρ (g/cc)	Swelling Ratio d/d_0
*15	1918	0.75	46	44.63	9.71	0.751	0.957
15	1918	3	115	60.24	13.03	0.581	0.946
15	1918	3	115	60.43	13.08	0.659	0.905
15	1918	10	393	73.29	18.23	0.416	0.944
15	1918	10	393	72.40	17.75	0.518	0.886
*15	1681	0.75	46	46.12	9.95	0.796	0.931
15	1681	3	122	55.12	11.71	0.781	0.887
15	1681	3	122	55.58	11.82	0.595	0.969
15	1681	10	414	60.1	12.98	0.785	0.856
*10	1967	0.75	46	42.27	9.35	0.754	0.968
10	1967	3	114	53.66	11.39	0.646	0.954
*5	1702	0.75	38	46.61	10.03	0.701	0.969
5	1702	3	112	50.42	10.72	0.801	0.906
5	1702	3	112	53.72	11.40	0.765	0.902
5	1702	10	366	62.53	13.71	0.619	0.910
*5	1867 (really 1702)	0.75	38	46.61	10.03	0.701	0.969
5	1867	3	112	53.89	11.44	0.619	0.967
5	1867	3	112	56.50	12.04	0.619	0.969
5	1867	10	371	73.77	18.50	0.404	0.949
5	1867	10	371	80.51	23.40	0.385	0.892
5	1867	16.25	632	80.25	23.17	0.247	1.037
*Initial Condition							
Data Excluded from Kinetic analysis							
*10	1722	0.75	42	44.50	9.69	0.766	0.952
10	1722	3	118	45.14	9.79	0.776	0.944

Table I.2. Wyodak 2011 gasification data used for kinetic modeling, mostly with enhanced CO₂

Pressure (atm)	Peak Gas Temperature (K)	Collection Height (inches)	Residence Time (ms)	Mass Release (daf wt %, Ash Tracer)	Mass Release (daf wt %, Direct)	Ash (dry wt %)	Apparent Density ρ (g/cc)	Swelling Ratio d/d_0
*10	1764	2	106	59.29	74.29	11.52	0.624	0.802
10	1764	8	424	68.48	87.33	14.40	0.285	0.839
*10	2093	0.75	48	55.82	N/A	10.71	0.746	0.920
10	2093	3	135	64.31	82.59	12.93	0.532	0.967
*10	1899	0.75	52	50.05	N/A	9.59	0.797	0.934
10	1899	3	147	60.64	81.98	11.87	0.712	0.903
*15	2023	2	110	58.59	76.65	11.35	0.552	0.815
15	2023	8	456	75.21	90.24	17.62	0.339	0.736
*15	2011	0.75	53	54.89	N/A	10.52	0.610	0.990
15	2011	3	142	75.61	84.40	17.86	0.718	0.786
*15	1835	0.75	64	51.86	N/A	9.92	0.710	0.959
15	1835	3	172	57.02	N/A	10.98	0.664	0.948
15	1835	8	485	67.66	85.06	14.08	0.472	0.944
The direct mass balance was only used when it was available for all the residence times in a series. No direct mass balance was possible when multiple experiments were performed on the same day without shutting down.								
The last condition (below) was used for kinetic analysis only with the combined Wyodak series. Since the bad density data for this series corrupted the swelling ratio, the swelling ratios from the same condition in the Wyodak 2010 series were used for kinetic modeling for this condition.								
*15	1918	0.75	46	68.95	71.94	14.58	0.695	0.743
15	1918	3	115	58.70	77.54	11.38	0.344	1.532
*Initial condition								

Table I.3. Illinois #6 reinjection gasification data with enhanced CO₂.

Pressure (atm)	Peak Gas Temperature (K)	Collection Height (inches)	Residence Time (ms)	Mass Release (daf wt %, Ash Tracer)	Mass Release (daf wt %, Direct)	Ash (dry wt %)	Apparent Density ρ (g/cc)	Swelling Ratio d/d_0
The first 2 conditions below are the freshly pyrolyzed chars. The swelling ratios and mass release for these two conditions are based on the coal. The next two conditions are the 75-106 μm fractions of the sieved chars that were used for reinjection experiments that are presented in the rest of the table. The char mass release and swelling ratios in the main part of the table are based on these sieved char reference states rather than the coal.								
10	1907	1.5	78	47.41	N/A	14.95	0.109	1.776
15	1834	1.5	83	47.32	N/A	15.02	0.128	1.699
10	1907 sieved	1.5	78	Ref. State	Ref. State	10.18	0.164	Ref. State
15	1834 sieved	1.5	83	Ref. State	Ref. State	10.53	0.150	Ref. State
* 10	2093 No Heaters	2	95	** 16.50	13.12	11.95	0.166	0.944
10	2093 No Heaters	8	378	25.97	34.74	13.27	0.152	0.894
10	2093 K Gas 1250°C Heat	9.5	424	** 49.49	47.66	18.32	0.136	0.875
10	2093 K Gas 1350°C Heat	9.5	401	** 65.90	63.16	24.94	0.128	0.806
* 10	1764 No Heaters	2	106	** 19.92	15.52	12.40	0.169	0.927
+10	1764 No Heaters	2	106	11.30	24.25	11.33	0.161	0.920
10	1764 No Heaters	8	424	26.70	38.93	13.39	0.159	0.865
10	1764 K Gas 1250°C Heat	9.5	462	** 64.99	64.81	24.45	0.123	0.822
10	1764 K Gas 1350°C Heat	9.5	439	** 78.65	85.04	34.67	0.107	0.768
* 15	2011	2	101	27.80	21.89	14.02	0.153	0.917
15	2011	8	410	39.91	40.97	16.38	0.148	0.853
* 15	2023	2	110	22.70	23.36	13.21	0.149	0.915
+ 15	2023	2	110	3.16	20.77	10.84	0.140	0.945
15	2023	8	456	38.26	48.98	16.01	0.149	0.810
+ 15	2023	8	456	18.75	50.15	12.65	0.135	0.817
* Initial condition ** Ash tracer recommended for kinetic analysis instead of default direct mass balance due to small char quantity + Unused replicate								
The ash tracer was considered to be more reliable for these reinjection experiments compared to gasification with in-situ pyrolysis because most ash vaporization should happen during pyrolysis. The ash tracer was considered to have lower reliability if less than ~8 mg of ash was measured in the ash test or if the char was produced in a different batch from the listed reference state. The highest confidence was normally placed in the direct mass balance, especially when two consistent measurements were taken with different methods, or one of the two direct methods was consistent with the ash tracer.								

Table I.4. Kentucky #9 CO₂ gasification data with in-situ pyrolysis

Pressure (atm)	Peak Gas Temperature (K)	Collection Height (inches)	Residence Time (ms)	Mass Release (daf wt %, Ash Tracer)	Mass Release (as rec'd wt %, Direct)	Ash (dry wt %)	Apparent Density ρ (g/cc)	Swelling Ratio d/d_0
*15	1681	0.75	46	42.35	N/A	12.65	0.124/0.134	** 1.81/1.76 +1.89
15	1681	10	414	47.23	80.10	13.66	0.197/0.207	1.51/1.48
15	1681	10	414	46.34	76.71	13.46	0.162/0.223	1.62/1.45
*15	1918	0.75	41	42.58	73.81	12.69	0.196/0.257	** 1.55/1.42 +1.79
15	1918	10	389	49.37	92.54	14.15	0.174/0.176	1.55/1.55
15	1918	10	389	43.98	81.58	12.97	0.166/0.220	1.63/1.48
15	1918	16.25	660	51.55	N/A	14.70	0.213/0.221	1.44/1.42
*15	2160 (really 1918)	0.75	46	42.58	N/A	12.69	0.196/0.257	** 1.55/1.42 +1.75
15	2160	3	115	46.67	N/A	13.53	0.142/0.184	1.69/1.55
*10	1722	0.75	42	47.17	N/A	13.64	0.152/0.195	** 1.65/1.52 +1.93
10	1722	3	122	51.09	69.52	14.58	0.127/0.273	1.71/1.32
*5	1702	0.75	38	52.27	N/A	14.88	0.137/0.345	** 1.66/1.22 +1.61
5	1702	0.75	38	52.54	75.12	14.96	0.189/0.316	1.48/1.25
5	1702	10	367	55.91	N/A	15.91	0.146/0.187	1.59/1.46
5	1702	10	367	54.55	N/A	15.52	0.183/0.185	1.48/1.48

The mass release and swelling ratios for these data with in-situ pyrolysis are reported on a coal basis. The char separation procedure was used for these data. The ash and mass release numbers reported here are weighted averages of the separated top and bottom fractions unless noted otherwise. The densities and swelling ratios are reported in terms of top/bottom.

* Initial condition

** Indicates the swelling ratio that was used for kinetic modeling in this study

+ Indicates swelling ratio from the swelling model developed in this work

Table I.5. Kentucky #9 CO₂ gasification data with char reinjection

Pressure (atm)	Peak Gas Temperature (K)	Collection Height (inches)	Residence Time (ms)	Mass Release (daf wt %, Ash Tracer)	Mass Release (daf wt %, Direct)	Ash (dry wt %)	Apparent Density ρ (g/cc)	Swelling Ratio d/d_0
The first 2 conditions below are the freshly pyrolyzed chars. The swelling ratios and mass release for these two conditions are based on the coal. The next two conditions are the 75-106 μm fractions of the sieved chars that were used for reinjection experiments that are presented in the rest of the table. The char mass release and swelling ratios in the next part of the table are based on these sieved char reference states rather than the coal.								
10	1907	1.5	78	45.21	60.22	13.81	0.112	1.782
15	1834	1.5	83	44.84	57.58	13.73	0.137	1.721
10	1907 sieved	1.5	78	Ref. State	Ref. State	14.49	0.184	Ref. State
15	1834 sieved	1.5	83	Ref. State	Ref. State	13.51	0.173	Ref. State
*10	1764	2	106	7.18	22.19	15.44	0.194	0.901
10	1764	8	424	20.45	42.51	17.56	0.151	0.893
*15	2023	2	110	28.30	23.37	17.88	0.193	0.891
15	2023	8	456	39.83	40.37	20.60	0.187	0.838
*Initial condition								

Table I.6. Kentucky #9 CO₂ gasification data omitted from kinetic analysis

Pressure (atm)	Peak Gas Temperature (K)	Collection Height (inches)	Residence Time (ms)	Mass Release (daf wt %, Ash Tracer)	Mass Release (as rec'd wt %, Direct)	Ash (dry wt %)	Apparent Density ρ (g/cc)	Swelling Ratio d/d_0
10	1764	2	106	16.78	24.24 (daf)	16.92	0.199	0.890
A different batch of char was made for the reinjection experiment above without re-measuring ash content, hence the ash tracer yield unreasonable mass release numbers. However, the direct numbers were consistent with replicate experiments. The densities and swelling ratios below are reported in terms of top/bottom.								
15	2160	0.75	46	45.18 (bottom)	N/A	13.21	0.127/0.239	(N/A)/1.43
10	1722	3	122	45.04	82.47	13.18	(N/A)/0.241	(N/A)/1.43
5	1702	3	113	45.54	N/A	13.29	0.126/0.191	1.77/1.54
5	1702	3	113	51.33	N/A	14.64	0.152/0.287	1.61/1.30
5	1867	3	116	49.59	N/A	14.21	0.226/0.234	1.42/1.41
5	1867	3	116	49.67	N/A	14.22	0.234/0.239	1.40/1.40
5	1867	10	388	49.38	N/A	14.15	0.170/0.248	1.57/1.38
10	1967	0.75	46	53.75 or 54.87 bottom	64.98	15.29	0.171/0.232	1.52/1.38**
10	1967	3	114	54.40 bottom	60.16	15.47	0.128/0.284	(N/A)/1.28

Table I.7. EBA CO₂ gasification data with in-situ pyrolysis.

Pressure (atm)	Peak Gas Temperature (K)	Collection Height (inches)	Residence Time (ms)	Mass Release (daf wt %, Ash Tracer)	Mass Release (daf wt %, Al/Si avg tracer)	Ash (dry wt %)	Top Apparent Density ρ (g/cc)	Swelling Ratio d/d_0
*15	1681	0.75	46	45.77 51.49 NS	60.62, or 61.41 (as rec'd direct)	12.02	0.156	1.62 ++1.89
+15	1681	0.75	46	75.98	N/A	23.58	0.156	1.30 1.49/1.09
15	1681	3	122	48.06 51.23 ^{NS}	60.62, or 68.24 (as rec'd direct)	12.49	0.228	1.41 1.58/1.31
15	1681	10	414	50.68 53.35 ^{NS}	N/A	13.06	0.185	1.49 1.55/1.44
*15	1918 (really 1681)	0.75	46	45.77	N/A	12.02	0.156	1.62 ++1.75
15	1918	3	111	49.67 48.80 ^{NS}	59.39	12.84	0.221	1.42
?15	1918	16.25	660	48.55	N/A	12.59	0.203	1.47
*5	1867	3	116	53.13 52.55 ^{NS}	56.32	13.65	N/A	++1.51
5	1867	10	388	59.37 47.85 ^{NS}	65.12 (as rec'd direct)	15.43	0.293	1.21 1.25/1.10
+5	1867	10	388	50.11 49.22 ^{NS}	N/A	12.93	0.230	1.39 1.47/1.30
+5	1867	16.25	662	45.42 43.19 ^{NS}	64.94 (as rec'd direct)	11.95	0.220	1.45 1.52/1.34
+5	1702	0.75	38	53.35	63.49 (as rec'd direct)	13.71	0.158	1.55 1.65/1.49 ++1.55
+5	1702	3	113	50.17 52.56 ^{NS}	61.02	12.95	N/A	N/A
+5	1702	10	367	50.11 49.22 ^{NS}	N/A	12.93	0.230	1.39

*Initial condition

+Omitted from kinetic analysis

++ Indicates swelling ratio from the swelling model developed in this work

^{NS} Indicates a portion of the sample was ashed for tracer analysis prior to using the separation procedure

The densities and swelling ratios are reported as top/bottom; a weighted average was provided when possible

Table I.8. EBB CO₂ gasification data with in-situ pyrolysis.

Pressure (atm)	Peak Gas Temperature (K)	Collection Height (inches)	Residence Time (ms)	Mass Release (daf wt %, Ash Tracer)	Mass Release (daf wt %, Al/Si avg tracer)	Ash (dry wt %)	Top Apparent Density ρ (g/cc)	Swelling Ratio d/d_0
*15	1681	0.75	46	40.88	N/A	9.34	0.150	**1.73/1.45 ++1.79
15	1681	3	122	45.06	N/A	9.98	0.201	1.54/1.43
15	1681	3	122	49.16 47.06 ^{NS}	N/A	10.70	0.218	1.51/1.40
15	1681	10	414	54.46	N/A	11.80	0.137	1.68/1.58
15	1681	16.25	692	48.47	N/A	10.58	0.227	1.45/1.30
*15	1918 (really 1681)	0.75	46	40.88	N/A	9.34	0.150	1.73/1.45 **++1.59
15	1918	3	111	45.45 44.80 ^{NS}	N/A	10.05	0.197	1.53/1.44
+15	1918	16.25	662	45.36	N/A	10.03	0.200	1.52/1.47
*5	1702	0.75	38	39.38	N/A	9.13	0.210	**1.50/1.51 ++1.49
+5	1702	0.75	38	41.80	N/A	9.48	0.196	1.59/1.49
+5	1702	3	113	53.40	45.01	11.57	0.227	1.31/1.59
5	1702	10	367	42.88	N/A	9.64	0.242	1.45/1.39
+5	1702	16.25	611	38.30 44.07 ^{NS}	N/A	8.99	N/A	N/A
*5	1867 (really 1702)	0.75	38	39.38	N/A	9.13	0.210	**1.50/1.51 ++1.46
5	1867	3	116	40.36 43.38 ^{NS}	42.35	9.27	N/A	N/A
5	1867	10	388	44.06	N/A	9.82	0.243	1.39/1.41
+5	1867	16.25	662	32.59	N/A	8.29	N/A	N/A
*Initial condition +Omitted from kinetic analysis ++ Indicates swelling ratio from the swelling model developed in this work ^{NS} Indicates a portion of the sample was ashed for tracer analysis prior to using the separation procedure								

APPENDIX J. 1ST-ORDER MODEL WITH STEAM GASIFICATION DATA

The Wyodak 2010 coal was gasified in an H₂O-rich environment using the 2-inch burner and the nichrome wire heaters. Due to high costs in terms of time and damage to the burner, only one gas condition was used at 2.5 atm. An overall gas flame equivalence ratio of 1.07 was used with 84 mol % H₂ and 16 mol % CH₄ in the fuel line. The peak centerline gas temperature was 1653 K and the equilibrium composition of the post-flame gas was 27.4% H₂O, 3.0% CO₂, and 1.1% CO, with the remainder being N₂. Pyrolysis was conducted in-situ, but a fully pyrolyzed case at a lower residence time subsequently became available when the CO₂ gasification conditions came into use using the 1-inch burner. The nichrome wire heaters were used to maintain gas temperatures above 1400 K. The conversion profile is shown with the 1st-order model in Figure J.1 and the predicted χ factors (~0.07) are included in Figure 6.5.

The 1st-order model was not able to optimize the activation energy for the H₂O gasification data set due to the narrow range of experimental temperatures at residence times below 150 ms. Therefore, only a constant rate was derived for this condition. The 1st-order model predicts complete conversion by 170 ms. Even when the activation energy was fixed at 100 kJ/mol, no significant change in the residence time required for full conversion occurred. This data set is too small to fit to a kinetic model, and the 1st-order model is not capable of modeling low rates that are typically observed at high conversion levels (Hurt et al., 1998). It is probable that annealing and ash inhibition reduced the overall rates at residence times above 150 ms.

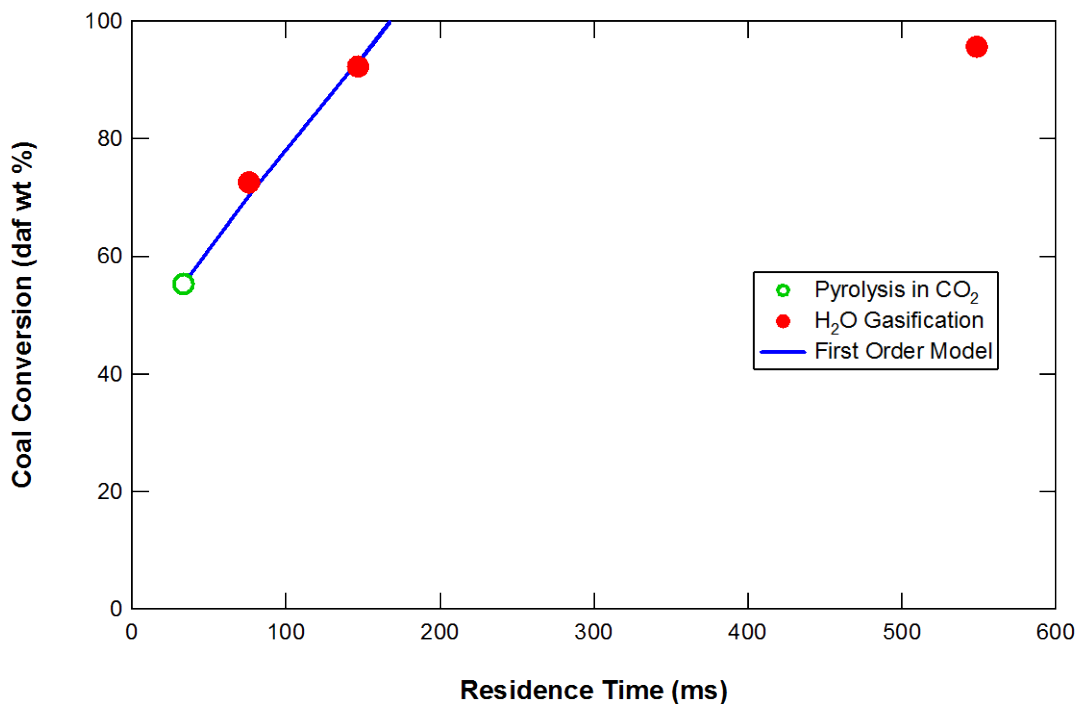


Figure J.1. Gasification of Wyodak 2010 coal in 0.68 atm steam with predicted 1st-order rate.

The single rate derived from this data set was more than 2 orders of magnitude higher than the Wyodak 2010 rate constant for CO₂ gasification at the same temperature. This difference in rates seems excessively large, since H₂O gasification rates have previously been found to exceed CO₂ gasification rates for bituminous coals by a factor of 3 to 4 (Mühlen et al., 1985).

It seems probable that a small amount of O₂ was present in the reaction zone due to incomplete mixing of the gaseous fuel and oxidizer at the surface of the 2-inch burner. This would result in the measurement of coal conversion rates that were influenced by both combustion and H₂O gasification. Oxidizing conditions could also have occurred if the H₂ mass flow controller was poorly calibrated, yielding an actual flow rate lower than the measured flow rate. Flows of H₂ can yield nonlinear signals when measured with electronic mass flow meters,

especially when a conversion factor is used for a meter that was calibrated for a different gas (Honeywell, 2011; MKS, 2011; Omega, 2011).

It was found that the peak centerline gas temperature occurred 4 inches above the surface of the 2-inch diameter burner. The peak centerline temperature always occurred at less than 1 inch above the burner when CO flames were used in the 1-inch diameter burner and also the atmospheric FFB. The high H₂ content of the flame used in these experiments should have caused a higher flame speed, for which there was ample evidence (see glowing burner surface in Figure B.1). Imperfect mixing in the large burner could have caused a lengthened combustion zone, which would explain the anomalous location of the peak temperature. These findings serve to endorse the change to the 1-inch diameter burner with a CO flame.

The elemental analysis of the Wyodak coal used and the chars produced are shown in Table J.1. The mass release (MR), density and swelling data are shown in Table J.2. SEM images of the coal and chars are shown in Figure J.2.

Table J.1. Ultimate analysis of Wyodak coal and chars produced at 2.5 atm and 1698 K (daf wt%)

Sample	C	H	N	S	O (diff)
Wyodak Coal	72.25	5.30	0.94	0.50	21.01
76 ms char	91.14	1.11	1.06	0.27	6.42
147 ms char	92.50	1.16	0.86	0.39	5.10
548 ms char	92.69	1.22	0.94	0.53	4.62

Table J.2. Mass release, apparent particle densities and swelling ratios of Wyodak coal and chars

Sample	Wyodak Coal	76 ms char	147 ms char	548 ms char
MR (% daf)	0.00	67.2	87.1	90.5
ρ_D (g/cc)	1.49	0.76	0.63	0.59
d/d_0	1.00	0.86	0.72	0.71

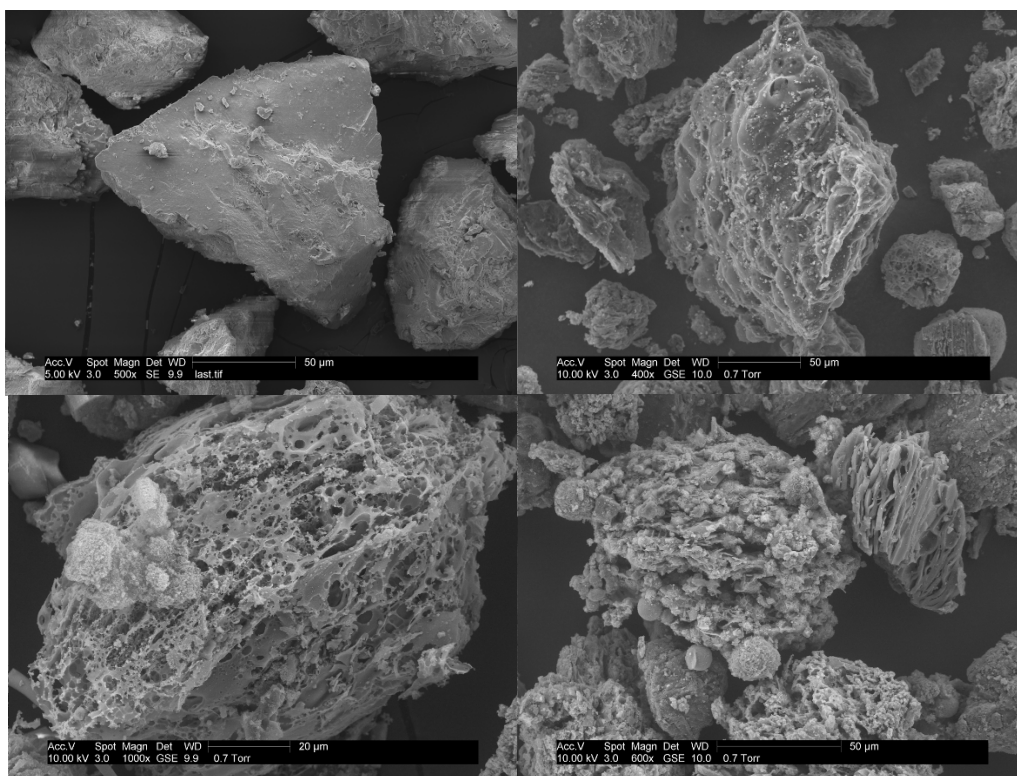


Figure J.2. Wyodak coal (top left) and chars produced at peak centerline temperature of 1698 K, pressure of 2.5 atm, residence times of 76 ms (top right) 147 ms (bottom left) and 548 ms (bottom right).

HPFFB Gas Conditions for Steam Gasification of Wyodak

Table J.3. Steam gasification gas flow rates and post-flame gas compositions from the NASA-CEA code

Pressure and Peak Temperature	2.5 atm 1698 K
Adiabatic Temp (K)	2341
Φ (Equiv. Ratio)	1.0747
Carrier N₂ (SLPM, coal entrainment)	0.046
CH₄ (SLPM)	0.90
H₂ (SLPM)	4.8
Air (SLPM)	19.1
Equilibrium post-flame gas compositions	
CO₂ mol %	3.02%
H₂O mol%	27.36%
CO mol %	1.14%
H₂ mol %	1.80%
N₂ mol %	65.37%
O₂ mol %	0.06%

Table J.4. Residence times for 2.5 atm HPFFB steam gasification experiments

Height above burner (in)	Residence times (ms)
*0.75	33
2.25	76
4.75	147
18.25	548

*From a 20% CO₂ condition at the same pressure
A velocity of 87.7 cm/s was used at 1 inch with a scaling temperature of 1600 K.

Table J.5. Radiation-corrected HPFFB temperature profiles with steam and Nichrome wire heaters at 2.5 atm

Height above burner (inches)	Long Profile with Heaters	Height above burner (inches)	Short Profile with Heaters
0.125	1386	0	1549
0.375	1556	0.25	1557
0.625	1596	0.5	1566
1.125	1619	0.75	1586
2.125	1667	1	1594
3.125	1690	1.5	1623
4.125	1698	2	1643
5.125	1679	2.5	1650
6.125	1659	3	1653
7.125	1634	3.5	1644
8.125	1608	4	1627
9.125	1577	4.5	1611
10.125	1571	4.75	1593
11.125	1556		
12.125	1543		
13.125	1529		
14.125	1513		
15.125	1494		
16.125	1468		
16.625	1448		
17.125	1431		
17.625	1409		
18.125	1400		

Coefficients for equation $T_{surr} = A \cdot z^2 + B \cdot z + C$ where T_{surr} is the surroundings temperature in Kelvin and z is the distance above the burner in inches.

A	-3.0386E+00		-3.2325E+01
B	5.1685E+01		1.6846E+02
C	1.1997E+03		1.1519E+03

APPENDIX K. EFFECTIVENESS FACTORS FROM CCK^N

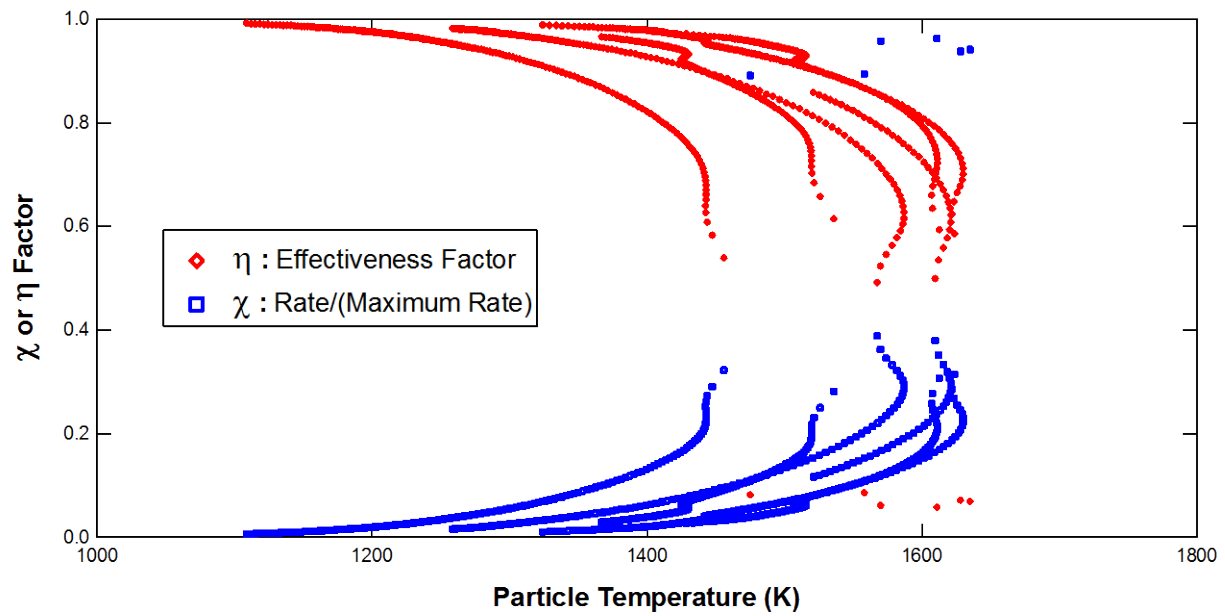


Figure K.1. Wyodak 2010 η and χ factors from CCK^N with $n = 0.5$, indicating Zone II behavior.

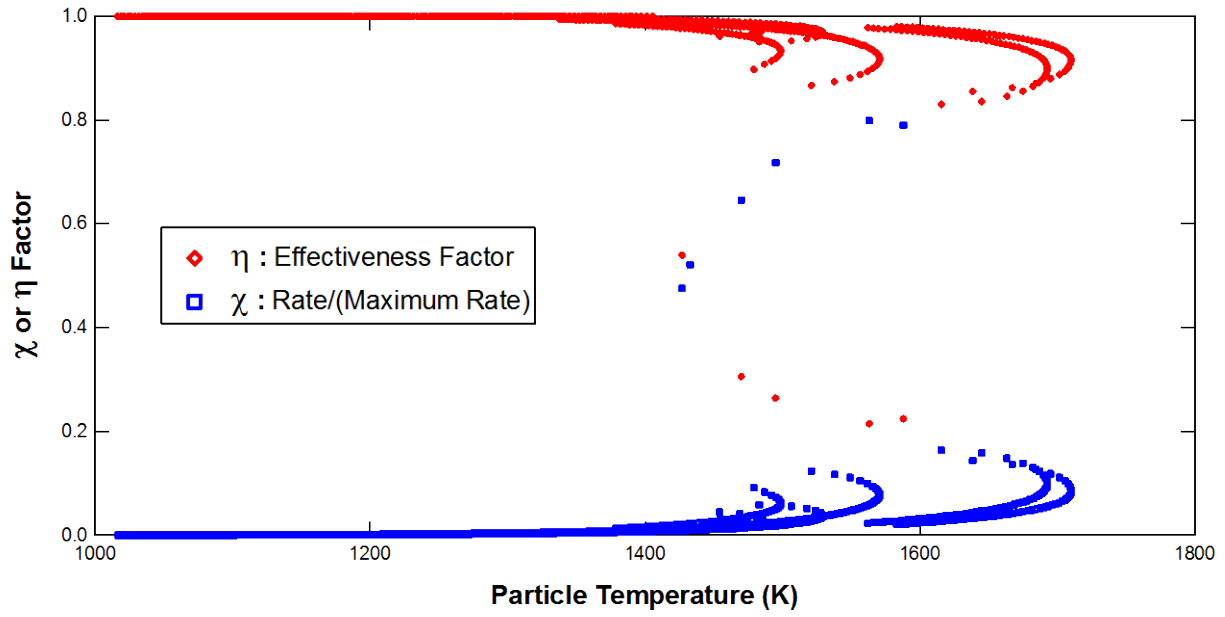


Figure K.2. Wyodak 2011 η and χ factors from CCK^N with $n = 0.5$, indicating Zone II behavior above ~ 1400 K.

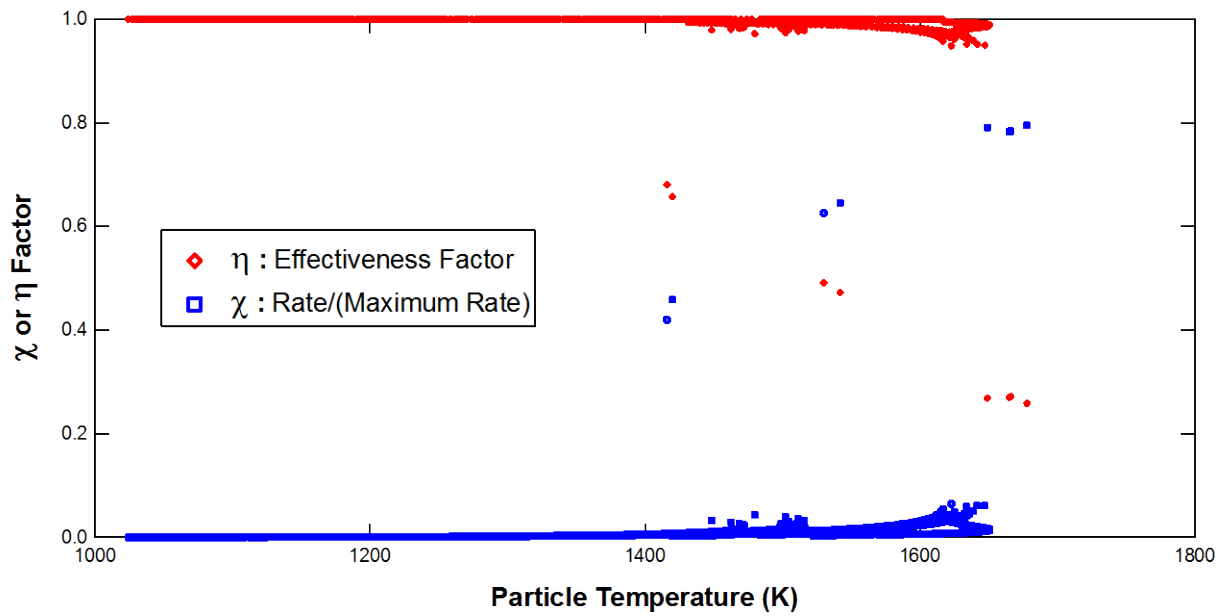


Figure K.3. Illinois #6 η and χ factors from CCK^N with $n = 0.5$, indicating Zone II behavior above ~ 1500 K.

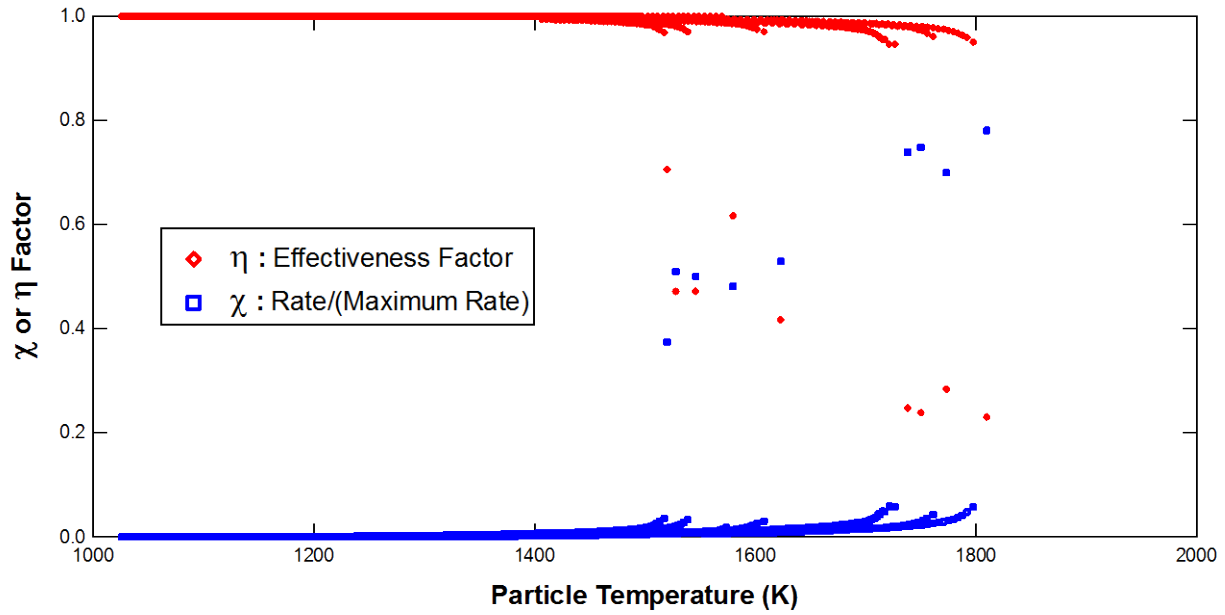


Figure K.4. Kentucky #9 η and χ factors from CCK^N with $n = 0.5$, indicating Zone II behavior above ~ 1500 K.

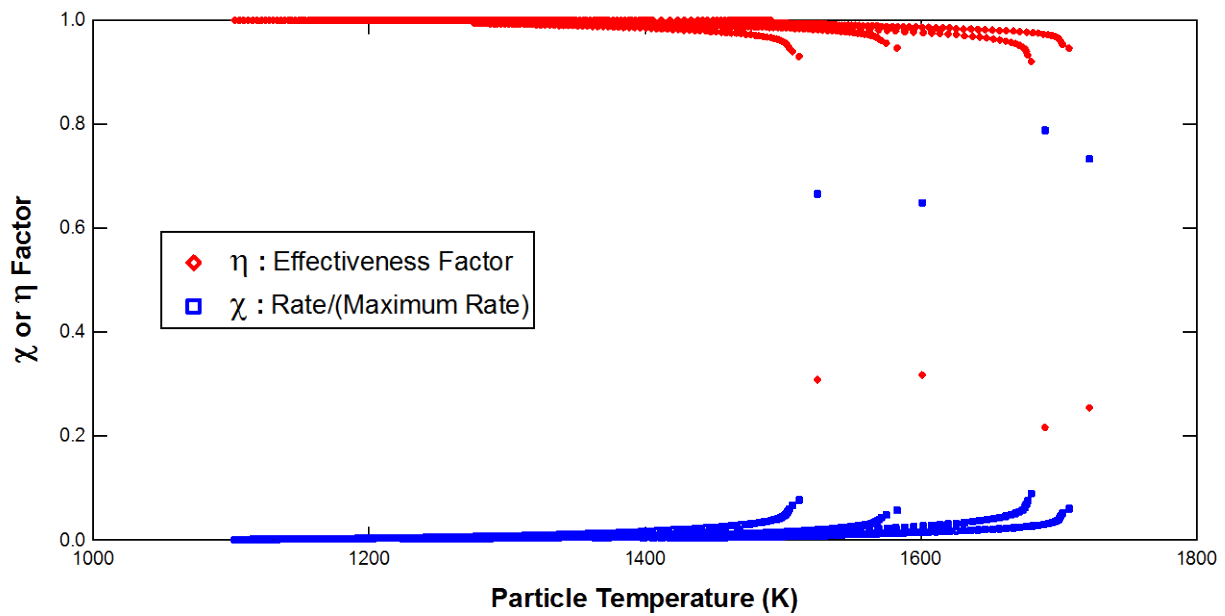


Figure K.5. EBA η and χ factors from CCK^N with $n = 0.5$, indicating Zone II behavior above ~ 1500 K.

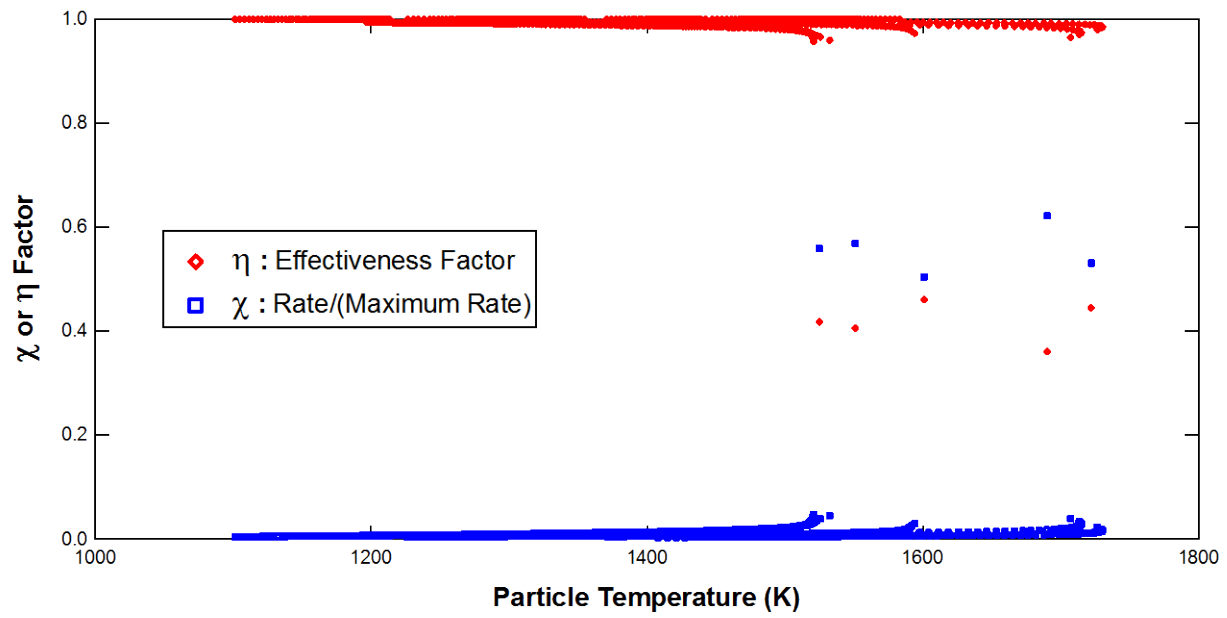


Figure K.6. EBB η and χ factors from CCK^N with $n = 0.5$, indicating Zone II behavior above ~ 1500 K.

APPENDIX L. CORRELATIONS FOR NMR PARAMETERS

The ^{13}C -NMR parameters used in this work are defined in Table 2.1. For convenience, these parameters were predicted from correlations with the ultimate and proximate analyses for use in the swelling and CO_2 reactivity correlations in this work. These correlations were developed for use with the CPD model (Fletcher et al., 1992) by Dominic Genetti (Genetti et al., 1999). The correlations for the NMR parameters are included in spreadsheet format on the CD that accompanies this dissertation. These correlations have the form:

$$y = c_1 + c_2x_C + c_3x_C^2 + c_4x_H + c_5x_H^2 + c_6x_O + c_7x_O^2 + c_8x_{VM} + c_9x_{VM}^2 \quad (\text{L.1})$$

where y is one of the correlated NMR structural properties, x represents a mass fraction on a dry, ash-free (daf) basis, and the subscripts C , H , O , and VM refer to carbon, hydrogen, oxygen, and volatile matter (from the ASTM Volatiles test). The coefficients are shown in Table L.1. Additionally, the CPD code uses the empirical parameter c_0 to account for the effect of thermally stable bridges on pyrolysis behavior. The correlation for c_0 at high heating rates is:

$$c_0 = \min[0.36, \max\{(0.118x_C - 10.1), 0.0\}] + \min[0.15, \max\{(0.014x_C - 0.175), 0.0\}] \quad (\text{L.2})$$

Table L.1. Coefficients used to predict NMR parameters (Genetti et al., 1999)

y	M_δ	MW	p_0	$\sigma + I$
c_1	4.220E+2	1.301E+3	4.898E-1	-5.2105E+1
c_2	-8.647E+0	1.639E+1	-9.816E-3	1.639E+0
c_3	4.639E-2	-1.875E-1	1.330E-4	-1.076E-2
c_4	-8.473E+0	-4.548E+2	1.555E-1	-1.237E+0
c_5	1.182E+0	5.171E+1	-2.439E-2	9.319E-2
c_6	1.154E+0	-1.007E+1	7.052E-3	-1.657E-1
c_7	-4.340E-2	7.608E-2	2.192E-4	4.096E-3
c_8	5.568E-1	1.360E+0	-1.105E-2	9.261E-3
c_9	-6.546E-3	-3.136E-2	1.009E-4	-8.267E-5

APPENDIX M. ADDITIONAL DETAILS REGARDING CCK DEVELOPMENT

It was assumed that any typographical errors found in the CBK/G publication (Liu and Niksa, 2004) were not present in the code itself, meaning the published correlations for rate constants are still valid for use with the correct equations in CCK. A typographical error in the coded annealing mechanism was corrected in CCK. This error in the implementation of the log-normal distribution caused some of the highest activation energies in the distribution to be omitted and dates back to the earliest versions of CBK (Figure M.1). A test of the fixed annealing distribution in CBK/E using the default coal and gas input parameters showed a difference of only 0.3% in char conversion (daf mass %) at 100 ms, compared to a total of 58%. Therefore, the annealing correction does not require regression of new kinetic parameters for any of the CBK or CCK codes.

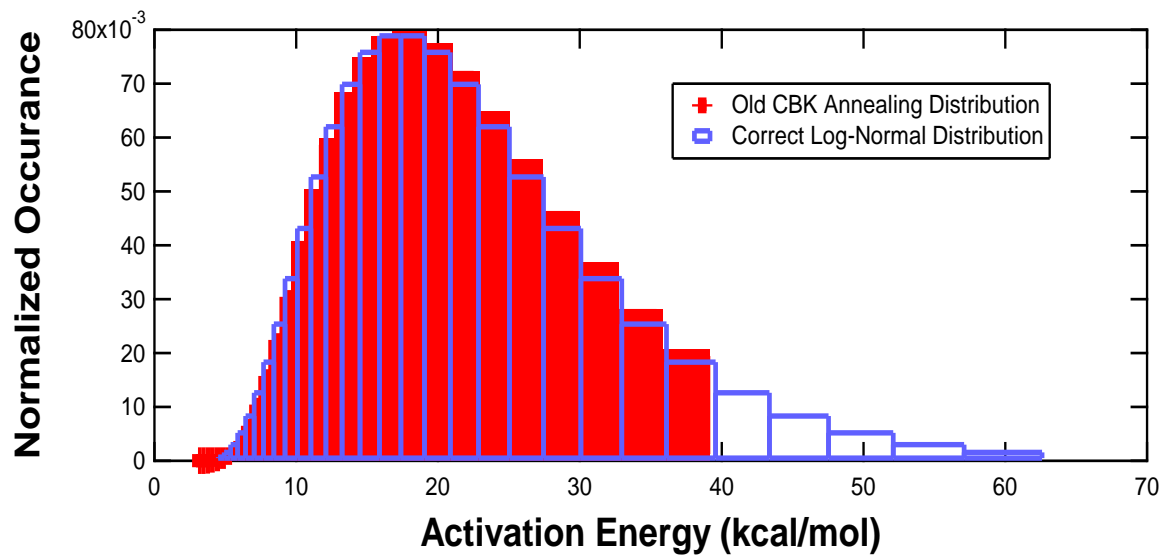


Figure M.1. Log-normal annealing distribution from CBK and corrected CCK version.

APPENDIX N. THERMOGRAVIMETRIC ANALYSIS

Thermogravimetric Analyzers (TGAs) heat coal or char at low heating rates (0.1 K/s-100 K/s). TGAs operate in regimes that are free of mass transfer limitations if the heating rates, temperatures, and sample sizes are sufficiently low and the gas flow rates are sufficiently high. The BYU High Pressure TGA (HPTGA) has been used previously to measure intrinsic O₂ reactivities of chars produced in flat-flame burners (Hecker et al., 2003; Zeng et al., 2005). In this study, the HPTGA was used to compare or rank the intrinsic CO₂ reactivities of the chars that were produced in the HPFFB for high temperature CO₂ gasification studies via reinjection.

A linear temperature ramp at 10°C/min to 900°C was used in this study. The maximum temperature was maintained for 60 minutes after the ramp. The CO₂ reaction was found to be sufficiently slow to prevent full conversion in the course of a practical experiment. The reactivities of the coal chars were compared at different conditions by determining the temperatures at which the mass started to decrease and the initial rate of decrease in mass.

As in previous HPTGA studies, a sample mass of ~4 mg was used and a total flow rate of 4 SLPM through the reactor was used to minimize mass transfer effects (Hecker et al., 2003; Zeng et al., 2005). CO₂ made up either 42 mole % or 90 mole % of the total flow rate at 10 and 15 atm, with helium making up the balance of the gas flow. These gas compositions were selected to be similar to those used in the HPFFB.

Buoyancy makes a significant contribution to the mass measurements made in the HPTGA (Hillier, 2011), so a correction procedure was applied to the HPTGA data. An empty

basket was used under the experimental conditions of interest to measure the effects of buoyancy in the absence of chemical reactions. A curve-fit of the basket mass versus temperature was made over the temperature range of experimental interest. Sometimes the fit was a polynomial, as was the case for Hillier (2011). However, at the high temperatures used in this study, it was found that polynomials did not always provide a good fit over the whole temperature range. Logarithmic fits of the buoyancy data were found to yield better fits with fewer coefficients in most cases.

After the buoyancy curve was subtracted from measurements of the char mass, the offset and any residual buoyancy effects were removed by fitting a linear portion of the mass versus temperature curve (generally 250-500°C) to a straight line. The mass data were then rescaled by subtracting off the fitted line and adding the independently measured initial sample mass and subtracting the ash content. Data collected at temperatures below ~150°C often had residual buoyancy and/or moisture vaporization effects and were generally omitted for the purposes of this study.

The TGA data are included in spreadsheet format on the CD that accompanies this dissertation. The chars studied include Kentucky #9, Illinois #6, and Wyodak 2011. The bituminous chars were the same samples that were used for gasification experiments via reinjection in the HPFFB. The Wyodak 2011 char was from the low residence time experiments with 90% CO₂. The Wyodak data appeared to be comparable in reactivity to the bituminous coals, which was surprising. This might mean that the conditions used were not free of mass transfer limitations. The Illinois #6 chars appeared to be the most reactive.

APPENDIX O. HPFFB OPERATING MANUAL

Thanks are due to the students who helped develop and document these procedures. Most of this version was written by Gregory Sorensen, Kade Fowers, and Joseph Hogge.

Start-Up Procedures: Cleaning the Vessel

1. Turn on the blue box that controls the heaters and displays temperatures.
2. Lower the burner from the vessel and cover the vessel hole with duct tape. Undo the oxidizer line's quick-connect and blow out the burner with air through the oxidizer line.
3. Clean the feeder tube out by running a wire through, then blow through it from both ends, using the small bent tube on the burner end.
4. Remove the probe from the vessel and cover the vessel hole with duct tape. Brush out the probe with the brush hanging next to the house air.
5. Cover the probe with duct tape, then climb up the platform and blow through the filters. Proceed by opening filters 2 and 3 and closing filter 1 and the char trap, blowing through from filter 3, then close filter 2 and opening the char trap, blowing through from filter 3, and finally closing the char trap and removing the duct tape from the probe, again blowing through filter 3.
6. Cover the burner with duct tape, then remove the duct tape from the top and bottom of the vessel and blow through it, from the top down.
7. Get a wet paper towel and clean the o-rings where the burner enters the vessel
8. Center the quartz tube, insert the burner two inches, and verify that the inner quartz tube is centered, both visually (with the mirror) and with the measuring tape.
9. Lower the probe to ignition position.
10. Weigh filters and install them. (See *Changing Filters During the Run*)
11. Verify that all the valves are appropriately open or closed. The green valves for filters 2 and 3 should be open, the green valve for filter 1 closed, the secondary should be closed, the 3-way valve that purges the burner or the wall should be set to the wall, the valve from the cyclone to the char-trap should be open, but the valve leaving the char trap should be closed. The three valves on the platform should all be directing flow to the board (not facing the plastic lines).

Conducting a Pressure Test

12. Close Filter 1, 2, & 3 valves on the board and make sure the cranks on the probe and burner are secured. Close the manual vent valve on the board.
13. Make sure all flows are set to zero.
14. Open the N₂ tanks
15. Open the Quench N₂ valve until the pressure reads about 15 psi above operating pressure. Once it has reached this pressure, close the Quench N₂ valve.
16. Snoop connections to make sure there are no leaks, particularly the filter assemblies and the coal feeder vessel.

Igniting the Flame

17. Open filter 2 until vessel is about 5 psi below operating pressure, allowing the pressure regulator to kick in.
18. Turn on cooling water and adjust the cooling water to the appropriate flows.
19. Make sure the CO/ N₂ three-way valve is set to flow N₂
20. Open Filters 2 and 3 on the board

21. Set the Carrier, Quench N₂ and CO (running nitrogen) to the desired flows.
22. Crack open the manual vent
23. Turn on the air tanks and the N₂ Oxidizer line, then set them to the ignition settings.
24. Turn on the glow plug.
25. Verify pressure, water, and all flow rates.
26. Verify that the H₂ set point is zero on the mass flow controllers, double check pressure, water, flow rates and the glow plug, and then
27. Open the H₂ and CO tanks
28. Switch the CO/ N₂ valve to CO and set the H₂ to the ignition settings
29. After lighting, set all flows **except carrier** to experimental conditions, especially the quench flow rate.
 - a. For pyrolysis:
 - i. Turn H₂ to the run setting
 - ii. Turn on the N₂ in the fuel line slowly, checking to see if the burner is flat
 - iii. Turn on the N₂ in the oxidizer line 10% at a time making sure the burner is still lit
 - iv. Turn the air and CO to the run settings
30. If the burner is still lit, turn off the glow plug
31. If using, make sure the heaters are set to 'manual' mode and set them to 100 using ▲ key. This can be done before ignition.

*the A/M button toggles between manual and automatic
32. Open the 'secondary to wall' valve, which introduces N₂ as you lower the probe to prevent thermal shock to the quartz tube.
33. Lower the probe to the desired operating height
34. Close the 'secondary to wall' valve about a minute after lowering the probe.
35. Adjust the burner to the desired operating height.
36. Adjust filters 2 and 3 as desired. Typically, we want about three times as much flow through filter 2 as through filter 3.
37. Once the pressure has stabilized, lower the carrier to the set point and double check all other flows.
38. Turn on the electric vibrators
39. Turn on the pneumatic vibrator
40. Step the motor forward slowly until particles begin to drop in the funnel. Set the speed to the desired feeding rate and length, and then commence feeding.

Shutting Down

41. Make sure all char is collected (see next section)
42. Close the H₂ and then the CO tanks.
43. Once CO has drained, switch the three-way valve so N₂ flows, then close the air and N₂ oxidizer tanks.
44. Once air has drained, increase the H₂ to about 20% so it drains faster.
45. While the H₂ is draining, pump the char trap until all char is removed, weigh and store the char in a bottle under argon.
46. Once H₂ is drained, purge the system by opening the secondary valve. While secondary is flowing, raise the probe to ignition position, depressurize slowly, and reduce quench to about 0.2
47. After purging for 10 minutes, turn off secondary, close the N₂ tanks, and let the system and line depressurize.
48. Weigh and scrape the filters.

Collecting Char

1. Stop stepper motor
2. Stop pneumatic vibrator
3. Tap feeder line to help residual coal to feed through
4. Turn off electric vibrators
5. Make sure burner is in a visible position (2" or lower) to verify that it is clean
6. Turn up CO ~15% to prevent flame from blowing out
7. Open Filter 1
8. Close Filter 3
9. While stabilizing the char trap with one hand, tap the cyclone with a hammer to help char drop into char trap
10. Isolate char trap from the process with large green valve
11. Cycle small green vent valve open and closed after assuring that the needle valve downstream is closed
12. Partially vent the pressurized vent line with the needle valve (usually vent half the pressure or less), then close the needle valve.
13. Open the small green vent valve. The pressure gauge should go back up most of the way.
14. Open the large green valve quickly to blow extra char into the trap. The pressure gauge should go up to the operating pressure.
15. Close the large green valve
16. Close the small green vent valve
17. Repeat steps 12 to 16 several times
18. Isolate the char trap from the process by closing the large green valve
19. Open both the small green vent valve and the needle valve to depressurize the char trap
20. Remove char trap, weigh char, clean trap, and replace char trap
21. Close small green vent valve and needle valve
22. Slowly open large green valve to make the char trap part of the process again; most char should drop straight in from the cyclone

23. Open Filter 3
24. Close Filter 1
25. Turn CO back to operating set point
26. Make sure burner is at its proper operating height
27. Check balance of flows between Filters 2 and 3
28. Turn electric vibrators on
29. Turn pneumatic vibrator on
30. When appropriate, start stepper motor.

Changing Filters During the Run*

1. Stop feeding (stop stepper motor, pneumatic vibrator, electric vibrators)
2. Attach the personal CO monitor to your person
3. Open the valve on filter 1 (make sure it is also open on the board)
4. Close the valve on desired filter (one or the other, but not both)
5. Turn on the vacuum
6. Turn the valve for the desired filter ON THE PLATFORM to let the line for the filter vent
7. Unscrew the filter clamps
8. Remove filter carefully with tweezers
9. Turn off vacuum
10. Clean filter assembly with a wipe
11. Turn on vacuum
12. Replace filter on flange
13. Screw the filter back onto collection system
14. Turn the valve for the filter on the platform back to starting point
15. Turn off vacuum
16. Open valve for the filter
17. Close the valve for filter 1
18. Recheck the flow balances on the board
19. Resume feeding

*If not during a run, only steps 4-16 are necessary

Replacing the Small Quartz Tube

1. Make sure the vessel is cold and unplug the power cords to the heaters
2. Remove probe and burner from the vessel
3. Feed a wire with a hook at the end down the top of the vessel
4. Hook the end of the wire under the bottom of the small quartz tube
5. Pull the wire and tube out carefully* †
6. Hook the end of the wire under the bottom of the new quartz tube
7. Lower the tube gently down into the vessel
8. Unhook the wire from the tube
9. Remove wire

*If the small tube is broken, you may have to do the procedure for replacing the large quartz tube to remove the pieces

†If the small tube is longer than 4", it may be necessary to remove the top cap in order to pull the tube out using this method

Replacing the Large Quartz Tube

WARNING: THIS IS A 2 PERSON JOB

1. Make sure the vessel is cold and unplug the power cords to the heaters
2. Remove probe from the vessel
3. Undo all lines running into and out of the lower cap (cooling water, secondary, thermocouples, etc.)
4. Unscrew the lower cap of the vessel (including the support plate running diagonally across the cap)
5. Lower the cap of the vessel by lowering the burner stand
6. Lift the large tube and gently remove the small tube from underneath
7. While holding the burner in place, unscrew the two allen wrench screws
8. Raise the large quartz tube up to the vessel, and remove the burner and clamp from the system
9. Lower the quartz tube out of the vessel
10. Insert new large quartz tube
11. Screw burner and clamp back onto stand
12. Insert small quartz tube like before
13. Redo lower cap and diagonal support

Making/Removing the Feeder Tube

1. Cut the large diameter tube to about 34" in length (one length of tube makes 2 feeder tubes with an inch or two to spare)
2. Insert the small diameter tube into the large diameter tube
3. Epoxy the ends of the small tube to the inside of the large tube (one side should be flush with the large tube, the other poking out about 14")
4. Let set overnight
5. Widen the mouth of the large diameter side using the Dremel Tool. You may want to wrap that end in Teflon tape to ensure a snug fit with the glass funnel.
6. Polish the tube to remove extra epoxy that would make insertion difficult using red polishing material
7. Remove the old feeder tube by unscrewing the ferrule on the feeder vessel side first, followed by the burner side, then gently removing the tube without bending the small tube in the burner
8. Insert small-tube end of the new feeder tube into the burner until the large tube portion touches the bottom of the burner
9. Screw the feeder tube into the burner using an 1/8" steel ferrule
10. Bend the feeder tube *gently* towards the feeder vessel to reduce strain
11. Apply several layers of duct tape onto the head of the burner, allowing the extra portion of feeder tube to poke through
12. Cut the feeder tube flush with the burner head using the Dremel Tool (BE CAREFUL to not harm the burner head)
13. Put ferrule pieces onto the other end of the feeder tube
14. Undo and remove the carrier N2 flow line into the feeder tube
15. Insert feeder tube into the feeder vessel and glass funnel. Try to center the funnel using a tube or pipe inserted through the hole for the carrier N2 flow. If the funnel starts cracking and breaking before the tube is in, you'll have to take off the feeder vessel (see next section)
16. Screw the ferrule onto the underside of the feeder vessel
17. Be sure to snoop both of the ferrules during pressure tests

Removing/Replacing the Feeder Vessel

1. Make sure that the plunger and carrier N2 flow line are out of the vessel
2. Remove the duct tape from the nuts on top of and below the feeder vessel
3. Loosen the nuts immediately below the vessel
4. Loosen and remove the nuts on top of the vessel
5. Lift the top of the vessel off of the plastic cylinder
6. Lift the plastic cylinder off of the stand while being careful to not let the glass funnel fall
7. Clean off the floor of the vessel using air/wipes
8. Insert the feeder tube into the funnel *carefully*
9. Slightly tighten the ferrule on the feeder tube, holding the feeder tube and funnel in place
10. Clean the bottom o-ring off and place in groove along edge of the vessel floor
11. Clean the top and bottom of the plastic cylinder

12. Spread silicone grease onto bottom and top of cylinder
13. Place cylinder on top of o-ring in the groove
14. Place o-ring on top of cylinder
15. Place top of vessel onto cylinder, making sure the o-ring lines up with the groove in the top
16. Align plunger hole with the stepper motor (it may help to move the stepper forward and place an old plunger in the vessel)
17. Screw the nuts back onto the top of the vessel, then keep screwing while holding the nuts immediately below the vessel in place (this provides the pressure seal for the vessel)
18. Align the plunger with the stepper by screwing the nuts on the underside of the frame while holding the very top nuts in place. Tighten each nut a little at a time, while moving from nut to nut in a circle
19. Finish tightening the ferrule on the feeder tube

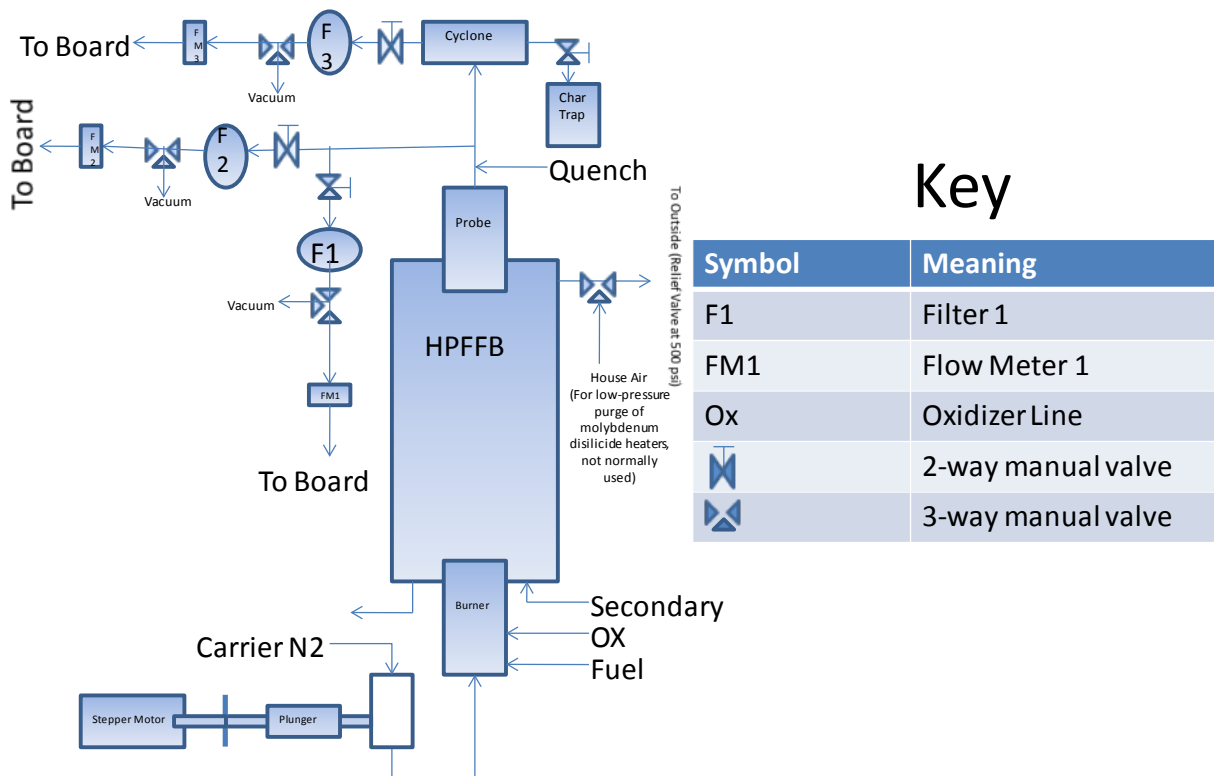
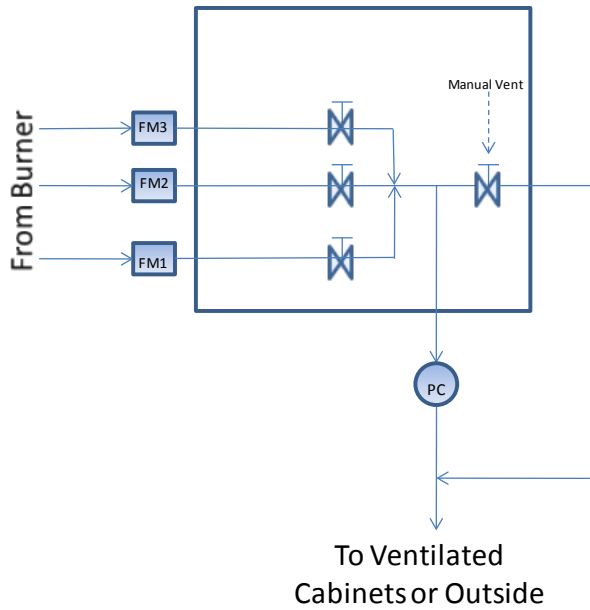


Figure O.1. Piping flow diagram of HPFFB.

Board

Key





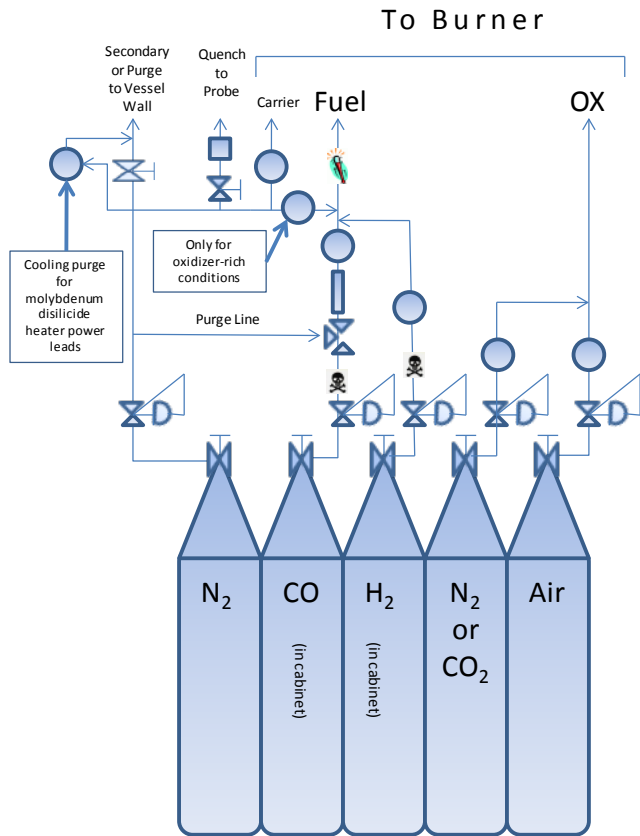
Symbol	Meaning
FM1	Flow Meter 1
Ox	Oxidizer Line
	2-way Manual Valve
	Pressure Control Valve

Figure O.2. Piping diagram for gas outlets on HPFFB.



Key

Symbol	Meaning
Ox	Oxidizer Line
	2-way manual valve
	3-way manual valve
	Mass Flow Controller
	Back Pressure Regulator
	Mass Flow Meter
	Fe Carbonyl Trap
	Shut-off valve triggered by toxic/flammable gas detectors
	Shut-off valve triggered by high temperature or thermocouple failure in lower vessel chamber

Figure O.3. Gas supply system for the HPFFB.